microorganisms

Special Issue Reprint

Diagnosis, Characterization and Treatment of Emerging Pathogens, Second Edition

Edited by
Shengxi Chen

mdpi.com/journal/microorganisms

MDPI

Diagnosis, Characterization and Treatment of Emerging Pathogens, Second Edition

Diagnosis, Characterization and Treatment of Emerging Pathogens, Second Edition

Guest Editor

Shengxi Chen

MDPI
Basel • Beijing • Wuhan • Barcelona • Belgrade • Novi Sad • Cluj • Manchester

Guest Editor
Shengxi Chen
Biodesign Center for
Bioenergetics
Arizona State University
Tempe
USA

Editorial Office
MDPI AG
Grosspeteranlage 5
4052 Basel, Switzerland

This is a reprint of the Special Issue, published open access by the journal *Microorganisms* (ISSN 2076-2607), freely accessible at: https://www.mdpi.com/journal/microorganisms/special_issues/1SEJ159ZNH.

For citation purposes, cite each article independently as indicated on the article page online and as indicated below:

Lastname, A.A.; Lastname, B.B. Article Title. *Journal Name* **Year**, *Volume Number*, Page Range.

ISBN 978-3-7258-5973-3 (Hbk)
ISBN 978-3-7258-5974-0 (PDF)
https://doi.org/10.3390/books978-3-7258-5974-0

Contents

About the Editor

Shengxi Chen

Shengxi Chen is a researcher at the Biodesign Center for Bioenergetics, Arizona State University, Tempe, AZ, USA. His research focuses on the molecular mechanisms of cancer progression, viral infections, and emerging pathogens, with an emphasis on developing innovative strategies for their diagnosis and treatment. Dr. Chen's work integrates approaches from molecular biology, bioenergetics, and translational medicine to better understand host–pathogen interactions and identify novel therapeutic targets. He has contributed to 60 publications in peer-reviewed journals and continues to advance research at the intersection of infectious disease and biomedical innovation.

microorganisms

Editorial

Diagnosis, Characterization, and Treatment of Emerging Pathogens, Second Edition

Shengxi Chen

Biodesign Center for Bioenergetics, Arizona State University, Tempe, AZ 85287, USA; shengxi.chen.1@asu.edu

Emerging and re-emerging pathogens continue to pose significant challenges to global health, because of the limits of current diagnostic, therapeutic, and preventive strategies [1–5]. Building upon the success of the first collection on this topic (contribution 1), the second volume of the Special Issue, "Diagnosis, Characterization, and Treatment of Emerging Pathogens, Second Edition" presents a comprehensive selection of original studies and case reports that advance our understanding of pathogenic mechanisms, molecular characterization, innovative diagnostic approaches, and the clinical management of infectious diseases. In summary, these contributions underscore the ongoing need for interdisciplinary collaboration that bridges microbiology, molecular biology, clinical medicine, and public health to effectively confront the evolving landscape of infectious threats.

In this Special Issue, tuberculosis (TB) remains a central focus, reflecting its ongoing significance as a leading cause of infectious mortality worldwide. Wumaier et al. investigate the role of G-protein-coupled receptor 84 (GPR84) in the interaction between *Mycobacterium tuberculosis* (Mtb) and macrophages (contribution 2). Their findings reveal that GPR84 modulates pro-inflammatory cytokine expression and promotes lipid droplet accumulation, thereby facilitating bacterial persistence within host cells. This work provides new insight into host–pathogen interactions and identifies GPR84 as a potential therapeutic target for host-directed TB treatment strategies. Complementing this, Cuthbert et al. report the structural characterization of the Mtb encapsulin in complex with dye-decolorizing peroxidase (DyP) (contribution 3). The study presents high-resolution crystallographic data that elucidate the structural features of this encapsulated complex and its relevance to oxidative stress resistance, adding an important layer to our understanding of Mtb's adaptive mechanisms within macrophages.

Technological advancements in microbial diagnostics are also well represented. Handigund and Lee evaluate the Novaplex™ multiplex real-time PCR assay for the detection of *Streptococcus agalactiae* serotypes, demonstrating its accuracy, efficiency, and potential utility for routine clinical use in serotype identification (contribution 4). Chen et al. further contribute to diagnostic innovation through the integration of artificial intelligence and machine learning into an automated microscopy platform for acid-fast bacilli detection in sputum smears (contribution 5). Their results show that this intelligent microscopy system achieves high sensitivity and specificity, offering a promising approach for improving diagnostic throughput in TB laboratories, particularly in high-burden settings.

Viral and fungal pathogens are also addressed through molecular and epidemiological investigations. Tikute et al. describe the emergence of the recombinant Coxsackievirus A6 subclade D3/Y during a hand–foot–and–mouth disease outbreak in India, underscoring the rapid genomic evolution and epidemiological dynamics of enteroviruses (contribution 6). Similarly, van Steen et al. present a fatal case of necrotizing pneumonia caused by exfoliative toxin etE2-producing *Staphylococcus aureus* belonging to sequence type ST152, highlighting

https://doi.org/10.3390/microorganisms13112586

the pathogenic potential of emerging *S. aureus* lineages harboring novel virulence factors (contribution 7). In a parallel line of inquiry, Stolfa et al. report the first case of *Candida auris* sepsis in Southern Italy, integrating antifungal susceptibility testing and whole-genome sequencing to characterize this multidrug-resistant yeast (contribution 8). Their findings emphasize the importance of genomic surveillance and stringent infection control measures in preventing nosocomial transmission.

In the field of pediatric infectious diseases, Di Meglio et al. provide two case reports and a systematic review of *Streptococcus pyogenes* meningitis, a rare but severe condition (contribution 9). Their analysis identifies key prognostic indicators, including bacteremia and a high Phoenix Sepsis Score, which are associated with poor outcomes. This work contributes valuable clinical evidence to guide management and prognosis in pediatric patients. Lastly, Cheng and Chen review the application of in vitro models for studying the complex interactions between environmental exposures and the human microbiota (contribution 10). Their review highlights how these systems can serve as ethically viable and mechanistically informative tools to investigate exposure–microbiota dynamics, offering an important framework for future research on environmental determinants of microbial ecology and human health.

Collectively, the studies presented in this Special Issue illustrate the multidimensional progress being made in pathogen diagnosis, molecular characterization, and treatment innovation. From molecular insights into host–pathogen interactions to the development of advanced diagnostic platforms and genomic surveillance tools, these contributions underscore the importance of cross-disciplinary collaboration in addressing the ongoing and emerging challenges posed by infectious diseases.

Funding: This research received no external funding.

Institutional Review Board Statement: Not applicable.

Informed Consent Statement: Not applicable.

Data Availability Statement: No new data were created or analyzed in this study. Data sharing is not applicable to this article.

Acknowledgments: The Guest Editor would like to express sincere appreciation to all the authors who contributed their valuable research to this Special Issue. We also extend our gratitude to the reviewers for their insightful evaluations and constructive feedback, which have greatly enhanced the quality of the published articles. Finally, we acknowledge the editorial staff of *Microorganisms* for their professional support and commitment in facilitating the successful completion of this Special Issue.

Conflicts of Interest: The author declares no conflicts of interest.

List of Contributions

1. Chen, S. Diagnosis, characterization and treatment of emerging pathogens. *Microorganisms* **2023**, *11*, 2032.
2. Wumaier, R.; Zhang, K.; Zhou, J.; Wen, Z.; Chen, Z.; Luo, G.; Wang, H.; Qin, J.; Du, B.; Ren, H.; et al. Mycobacteria exploit host GPR84 to dampen pro-inflammatory responses and promote infection in macrophages. *Microorganisms* **2025**, *13*, 110.
3. Cuthbert, B.J.; Chen, X.; Burley, K.; Batot, G.; Contreras, H.; Dixon, S.; Goulding, C.W. Structural characterization of *Mycobacterium tuberculosis* encapsulin in complex with dye-decolorizing peroxide. *Microorganisms* **2024**, *12*, 2465.
4. Handigund, M.; Lee, J. Performance evaluation of Novaplex™ multiplex real-time PCR assay for detection of *Streptococcus agalactiae* serotypes. *Microorganisms* **2024**, *12*, 2043.
5. Chen, W.-C.; Chang, C.-C.; Lin, Y.E. Pulmonary tuberculosis diagnosis using an intelligent microscopy scanner and image recognition model for improved acid-fast bacilli detection in smears. *Microorganisms* **2024**, *12*, 1734.

6. Tikute, S.; Deshmukh, P.; Chavan, N.; Shete, A.; Shinde, P.; Yadav, P.; Lavania, M. Emergence of recombinant subclade D3/Y in *Coxsackievirus A6* strains in hand-foot-and-mouth disease (HFMD) outbreak in India, 2022. *Microorganisms* **2024**, *12*, 490.
7. van Steen, W.J.; Fliss, M.A.; Metz, E.; Filoda, K.; van den Berg, C.H.S.B.; Sinha, B.; Bathoorn, E. Case report: Fatal necrotizing pneumonia by exfoliative toxin etE2-producing *Staphylococcus aureus* belonging to MLST ST152 in The Netherlands. *Microorganisms* **2025**, *13*, 1618.
8. Stolfa, S.; Caggiano, G.; Ronga, L.; Dalfino, L.; Centrone, F.; Sallustio, A.; Sacco, D.; Mosca, A.; Stufano, M.; Saracino, A.; et al. First case of *Candida auris* sepsis in Southern Italy: Antifungal susceptibility and genomic characterisation of a difficult-to-treat emerging yeast. *Microorganisms* **2024**, *12*, 1962.
9. Di Meglio, L.; De Luca, M.; Cursi, L.; Romani, L.; Pisani, M.; Musolino, A.M.; Mercadante, S.; Cortazzo, V.; Vrenna, G.; Bernaschi, P.; et al. Unraveling pediatric group A *Streptococcus* meningitis: Lessons from two case reports and a systematic review. *Microorganisms* **2025**, *13*, 1100.
10. Cheng, Q.; Chen, S. Using in vitro models to study the interactions between environmental exposures and human microbiota. *Microorganisms* **2025**, *13*, 247.

References

1. Church, D.L. Major factors affecting the emergence and re-emergence of infectious diseases. *Clin. Lab. Med.* **2004**, *24*, 559. [CrossRef] [PubMed]
2. Morens, D.M.; Folkers, G.K.; Fauci, A.S. The challenge of emerging and re-emerging infectious diseases. *Nature* **2004**, *430*, 242. [CrossRef] [PubMed]
3. Muteeb, G.; Rehman, M.T.; Shahwan, M.; Aatif, M. Origin of antibiotics and antibiotic resistance, and their impacts on drug development: A narrative review. *Pharmaceuticals* **2023**, *16*, 1615. [CrossRef] [PubMed]
4. Hitchcock, N.M.; Devequi Gomes Nunes, D.; Shiach, J.; Valeria Saraiva Hodel, K.; Dantas Viana Barbosa, J.; Alencar Pereira Rodrigues, L.; Coler, B.S.; Botelho Pereira Soares, M.; Badaró, R. Current clinical landscape and global potential of bacteriophage therapy. *Viruses* **2023**, *15*, 1020. [CrossRef] [PubMed]
5. Wang, S.; Li, W.; Wang, Z.; Yang, W.; Li, E.; Xia, X.; Yan, F.; Chiu, S. Emerging and reemerging infectious diseases: Global trends and new strategies for their prevention and control. *Signal Transduct. Target. Ther.* **2024**, *9*, 223. [CrossRef] [PubMed]

microorganisms

Article

Mycobacteria Exploit Host GPR84 to Dampen Pro-Inflammatory Responses and Promote Infection in Macrophages

Reziya Wumaier [1,†], Ke Zhang [2,†], Jing Zhou [3], Zilu Wen [3], Zihan Chen [3,4], Geyang Luo [3], Hao Wang [3], Juliang Qin [5], Bing Du [5], Hua Ren [5], Yanzheng Song [3], Qian Gao [1,*] and Bo Yan [3,*]

[1] Key Laboratory of Medical Molecular Virology (MOE/NHC/CAMS), School of Basic Medical Sciences, Shanghai Medical College, Shanghai Public Health Clinical Center, Fudan University, Shanghai 200433, China; 16111010063@fudan.edu.cn

[2] Shanghai Institute of Infectious Disease and Biosecurity, Fudan University, Shanghai 200032, China; 23111010092@m.fudan.edu.cn

[3] Shanghai Public Health Clinical Center, Fudan University, Shanghai 201508, China; zhoujing@shaphc.org (J.Z.); wenzilu@shaphc.org (Z.W.); czhan2020@163.com (Z.C.); luogeyang@fudan.edu.cn (G.L.); wh94zz@163.com (H.W.); songyanzheng@shaphc.org (Y.S.)

[4] Pathology Department, The First Affiliated Hospital of Shenzhen University, Shenzhen Second People's Hospital, Shenzhen 518035, China

[5] Shanghai Frontiers Science Center of Genome Editing and Cell Therapy, Shanghai Key Laboratory of Regulatory Biology and School of Life Sciences, East China Normal University, Shanghai 200241, China; jlqin@bio.ecnu.edu.cn (J.Q.); bdu@bio.ecnu.edu.cn (B.D.); huaren@bio.ecnu.edu.cn (H.R.)

[*] Correspondence: qiangao@fudan.edu.cn (Q.G.); bo.yan@shphc.org.cn (B.Y.)

[†] These authors contributed equally to this work.

Abstract

Tuberculosis (TB) remains the major cause of mortality and morbidity, causing approximately 1.3 million deaths annually. As a highly successful pathogen, *Mycobacterium tuberculosis* (*Mtb*) has evolved numerous strategies to evade host immune responses, making it essential to understand the interactions between *Mtb* and host cells. G-protein-coupled receptor 84 (GPR84), a member of the G-protein-coupled receptor family, contributes to the regulation of pro-inflammatory reactions and the migration of innate immune cells, such as macrophages. Its role in mycobacterial infection, however, has not yet been explored. We found that GPR84 is induced in whole blood samples from tuberculosis patients and *Mycobacterium marinum* (*Mm*)-infected macrophage models. Using a *Mm-wasabi* infection model in mouse tails, we found that GPR84 is an important determinant of the extent of tissue damage. Furthermore, from our studies in an in vitro macrophage *Mm* infection model, it appears that GPR84 inhibits pro-inflammatory cytokines expression and increases intracellular lipid droplet (LD) accumulation, thereby promoting intracellular bacterial survival. Our findings suggest that GPR84 could be a potential therapeutic target for host-directed anti-TB therapeutics.

Keywords: tuberculosis (TB); G-protein-coupled receptors 84 (GPR84); pro-inflammatory cytokines

1. Introduction

Tuberculosis (TB), caused by the *Mycobacterium tuberculosis* (*Mtb*), has re-emerged as the leading cause of death from infectious diseases worldwide, posing a significant public health threat [1]. Because *Mtb* can develop resistance to all currently used drugs, and because of the current scarcity of new candidate anti-TB drugs, there is increasing interest in

https://doi.org/10.3390/microorganisms13010110

host-directed therapy (HDT) to target components of the host's immune response [2,3]. Several innovative host-directed agents target the membrane receptors that are characterized by high specificity for ligands and mediate signal recognition and transduction [4,5].

The G-protein-coupled receptors (GPCRs), as transmembrane proteins, include chemokine receptors, bioactive lipid receptors, and orphan receptors and play significant roles in the progression of mycobacterial infection [6–8]. The expression of chemokine receptor CCR5 is upregulated in *Mtb*-infected mouse bone marrow-derived macrophages (BMDMs) and activates the kinases Lyn and ERK to promote IL-10 production [6]. Similarly, the anti-lipolytic receptor GPR109A leads to a reduction in cyclic adenosine monophosphate (cAMP), which decreases perilipin phosphorylation. This process results in the formation of a protective layer around LDs that prevents lipolysis and facilitates the retention of *Mtb* within macrophages [7]. In contrast, certain GPCRs act against mycobacterial growth. The oxysterol-sensing receptor GPR183 inhibit *Mtb* and BCG proliferation by negatively regulating type I IFN production [9]. Additionally, in a peritoneal macrophage model of BCG infection, the deficiency of GPR160 impedes ERK signaling, reducing BCG entry and enhancing resistance in mice [8]. Collectively, these studies demonstrate that GPCRs modulate host immune pathways to either facilitate or inhibit mycobacterial growth. Moreover, a screening of host-targeted small molecules identified that 32% (41/133) of compounds that limit mycobacterial growth in macrophages are GPCR modulators [10]. This highlights the potential of GPCRs as therapeutic targets for tuberculosis treatment.

GPR84 falls within the rhodopsin-like branch of the GPCR family (Class A) and is expressed in various innate immune cell types, including neutrophils, monocytes, macrophages, and microglia [11,12]. It has been reported that GPR84 contributes to inflammatory disease processes including ulcerative colitis, acute lung injury, diabetes, and atherosclerosis [13–15]. In a dextran sulfate sodium (DSS)-induced acute colitis mouse model, lowered protein levels of pro-inflammatory cytokines, including IL-1β, IL-6, and TNF-α in colon tissue in *Gpr84*$^{-/-}$ mice at later stages and mitigated mucosal damage [13], were observed. Similarly, in an LPS-induced acute lung injury (ALI) model, Yin et al. observed that alveolar macrophages transitioned from a CD11b^{lo} to a CD11b^{hi} inflammatory state at later stages, whereas *Gpr84*$^{-/-}$ alveolar macrophages (AMs) reduced the mRNA expression of inflammatory cytokines such as IL-6, TNF, and IL-12β [14], ultimately leading to milder tissue damage. These studies indicate that GPR84 exacerbates inflammation-induced tissue damage and enhances the expression of pro-inflammatory cytokines in the later stages of disease. Furthermore, GPR84 has been implicated in the immune responses to both bacterial and viral infections [16]. For instance, BMDMs pretreated with a GPR84 agonist (6-OAU) demonstrated increased phagocytic activity against *E. coli* [15]. In a zebrafish–*Shigella* model, Torraca et al. illustrated that *gpr84* remained differentially expressed during both early (4 h) and late (24 h) stages of infection, with *gpr84*-deficient zebrafish exhibiting heightened susceptibility to *Shigella* infection [17]. In the context of viral infection, GPR84 expression was upregulated in neutrophils from COVID-19 patients, as revealed by the RNA sequencing of bronchoalveolar lavage fluid [18]. Collectively, these findings underscore the complex role of GPR84 in immune responses to pathogenic infections. GPCRs are important targets for drug development, and identifying the specific GPCR targets involved in the progression of TB is crucial for drug development [10]. Through the analysis of publicly available RNA-seq datasets, we found that GPR84 is upregulated in the very early stages of mycobacteria infection (2h or 4h), suggesting that GPR84 may play a key role in the establishment of mycobacteria infection [19,20]. However, no studies have yet reported on the function of GPR84 in mycobacterium infection. Therefore, we conducted an initial exploration of the role and mechanism of GPR84 in mycobacterium infection, providing new insights into the host–pathogen interaction in mycobacterium infection.

We report that *GPR84* expression is markedly upregulated during mycobacterial infections. Utilizing *Mm* infections in both an in vivo mouse model and an in vitro macrophage model, we show an association between GPR84 and mycobacterial proliferation, infection-induced tissue damage, and the expression of pro-inflammatory cytokines. These findings suggest that GPR84 is integral to the pathophysiology of mycobacterial infection and represents a potential target for host-directed therapeutic strategies in the treatment of tuberculosis.

2. Materials and Methods

2.1. Collection of Blood Samples from TB Patients

Blood samples were obtained from 45 healthy controls (HC) and 48 TB patients (TB), through the Tuberculosis Department and the Physical Examination Center of Shanghai Public Health Clinical Center. Whole blood samples were collected in EDTA anticoagulant tubes, and RNA was extracted using Qiagen kit (QIAGEN, Dusseldorf, Germany). Furthermore, 1 μL of the RNA samples was used to determine the concentration and purity with the Nanodrop 2000, which was subsequently utilized for subsequent qRT-PCR analysis. The sample collection was approved and followed ethical guidelines by Shanghai Public Health Clinical Center Ethics Committee, Fudan University (Number: 2019-S009-02). Informed consent was obtained during the collection process.

2.2. Bacteria Strain

The *Mm-wasabi* and *Mm-tdTomato* were generously provided by Lalita Ramakrishnan from the University of Washington [21] and Professor Stefan H. Oehlers [22], respectively. The *Mm-wasabi* and *Mm-tdTomato* strains were cultivated in 7H9 medium supplemented with 10% OADC and 50 μg/mL hygromycin (Hyg) at a temperature of 32 °C. Upon reaching the logarithmic growth phase, indicated by an OD_{600} of 0.6 to 0.8, the bacterial cultures were subjected to sonication using a disperser. The ultrasound parameters employed included sonication for 15 s, separated by a 10 s pause, with a total treatment duration of 1 min [23].

2.3. Cell Culture

In this study, three distinct types of macrophages were utilized: the mouse macrophage cell line RAW264.7, the human macrophage cell line THP-1, and mouse bone marrow-derived macrophages (BMDMs). RAW264.7 cells were cultured in a DMEM medium containing 10% fetal bovine serum (FBS) and 1% penicillin/streptomycin (P/S). THP-1 cells were maintained in 1640 medium, also supplemented with 10% FBS and 1% P/S, and were differentiated with PMA for 48 h prior to experimentation. All cell cultures were incubated at 37 °C in a 5% CO_2 atmosphere [24].

BMDMs were isolated from the tibias and femurs of 6- to 8-week-old female C57BL/6 WT and $Gpr84^{-/-}$ mice. In brief, fresh bone marrow cells were extracted and cultured in the DMEM medium containing 10% FBS, 1% P/S, and 100 ng/mL M-CSF for a duration of 7 days. Following this incubation period, the mature BMDMs were harvested and subsequently seeded into various culture dishes or plates as required for the experimental procedures [25].

2.4. Infection of Macrophages

The bacterial inoculum for the infection of macrophages was determined according to the specific experimental design [26]. For the collection of RNA samples, macrophages were seeded 6 × 10^5 cells/well in a 12-well plate and infected with *Mm-wasabi* at a MOI of 10. For intracellular bacterial proliferation, BMDMs were seeded 6 × 10^5 cells/well in a 12-well plate and infected at an MOI of 1. Following infection, BMDMs were treated with 200 µg/mL of gentamicin at 4 hpi to eliminate extracellular bacteria. BMDMs were then lysed with 0.1% Triton X-100 at 6 hpi, 24 hpi, and 48 hpi, respectively. The released bacteria were plated onto 7H10 agar plates and were counted for 2 weeks.

2.5. qRT-PCR Detection of GPR84 mRNA Expression

Total RNA was isolated using TRIzol reagent [24], and RNA concentration was measured using a Nanodrop spectrophotometer. The RNA was then stored at −80 °C. Reverse transcription was performed using a reverse transcription kit according to the manufacturer's instructions to convert RNA into cDNA. Quantitative RT-PCR was then performed using SYBR Green Supermix on the CFX96 Real-Time System (BioRad, Hercules, CA, USA). The sequences of the primers used are shown in Table 1.

Table 1. Primers used for qPCR. Related to Figure 1.

Gene Name	GeneBank (No.)	Forward and Reverse Primer Sequence (5′-3′)
Human *GPR84*	MT536737.1	F: TGAAGCCTAACTGTCCACCAG R: CCACATGATAGAGGCTGAGT
Human *β-actin*	PQ040393.1	F: TCACCATGGATGATGATATCGC R: ATAGGAATCCTTCTGACCCATGC
Mouse *Gpr84*	AF272948.1	F: CCACCGCTTTTGCAAGGATGT R: AACGGTAGCCCTCAACAGAG
Mouse *β-actin*	BC138611.1	F: GCCGGGACCTGACAGACTAC R: TGGCCA TCTCCTGCTCGAAG

The relative expression of the target gene was calculated using the comparative threshold cycle (CT) method, specifically the $2^{-\Delta\Delta CT}$ method. The formula is as follows [24]:

$$\Delta\Delta CT = \text{Experimental sample } (CT_{\text{target gene}} - CT_{\beta\text{-actin}}) - \text{Control sample } (CT_{\text{target gene}} - CT_{\beta\text{-actin}}).$$

2.6. Animals

Female wild-type (WT) mice were purchased from Shanghai Jihui Co., Ltd. (Shanghai, China). The *Gpr84* knockout (*Gpr84*$^{-/-}$) mice were kindly provided by Professor Hua Ren from East China Normal University [27]. Mice were maintained under standard specific pathogen-free (SPF) conditions, with a temperature of 24 °C, humidity levels ranging from 45% to 55%, and a 12 h light/dark cycle, allowing for ad libitum access to food and water. All female mice utilized in the experiments were aged between 6 and 8 weeks and were randomly selected and maintained into different mouse cages. Three experiment members joined the mouse tail vein infection process, and Member A randomly selected a mouse, Member B numbered the group "WT group" and "*Gpr84*$^{-/-}$ group", and Member C conducted tail veins injection. The animal infection experiments were approved by Shanghai Public Health Clinical Center Laboratory Animal Welfare & Ethics Committee, Fudan University (Number: 2021-A051-01).

2.7. Mouse Infected with Mm-Wasabi, Histopathological Analysis, Nile-Red Staining, and Acid-Fast Staining

2.7.1. Mouse Infected with Mm-Wasabi

The tail veins of 6 to 8-week-old mice were injected with 4 × 10^7 colony-forming units (CFU) of *Mm-wasabi*, with phosphate-buffered saline (PBS) as a negative control.

Tissue damage in the tails of the mice was evaluated visually every other day over a total of 14 days, after which the mice were euthanized and the tails were harvested and examined for tissue pathology. The total area of tail ulcers (mm^2) was calculated as length (mm) × width (mm) [24].

2.7.2. Histopathological Analysis

The collected mouse tail samples were fixed in 4% paraformaldehyde and embedded in paraffin. Then, 5 μm thick sections were stained with hematoxylin and eosin (H&E) and examined by light microscopy [24]. The *Mm* burdens in the mouse tail were calculated by acid-fast staining according to standard Ziehl–Neelsen method, and they were visualized by light microscopy [28].

2.7.3. Nile Red Staining

The collected mouse tail samples were fixed in 4% paraformaldehyde and subsequently embedded in paraffin. Tissue sections were deparaffinized in xylene for 10 min, repeated three times, and then rehydrated using a gradient of ethanol (100%, 85%, and 75%) with each concentration maintained for 5 min, followed by a wash with distilled water. The sections were then incubated with Nile Red dye (1 μg/mL) (AbMole, M5118) (37 °C, 30 min), and the nuclei were stained with DAPI (RT, 10 min) [29,30]. Fluorescent images were acquired using a Nikon inverted fluorescence microscope.

2.7.4. Immunofluorescence Assay

Mouse tail sections, deparaffinized and rehydrated as above, were treated with an EDTA antigen retrieval solution for 30 min at 100 °C and at a pH of 9.0. Following this, the sections were blocked with 3% BSA, incubated with primary antibodies (5 μg/mL, overnight), and incubated with secondary antibodies. Finally, DAPI was applied for nuclei stained [31]. Fluorescent images were observed and captured using a Nikon inverted fluorescence microscope.

2.8. Immunofluorescence Microscopy Imaging

For immunofluorescence assays, cells were seeded into glass-bottom dish (Thermo Scientific™, Waltham, MA, USA, 150682). After completion of the infection assay, the dishes were fixed with 4% paraformaldehyde, permeabilized with 0.2% Triton X-100, and then blocked with 5% goat serum in PBS. The dishes were then incubated with BODIPY and counterstained with DAPI. Images were visualized using a Leica SP8 confocal microscope (Laica, Wetzlar, Germany).

2.9. Flow Cytometry

Mm-tdTomato (MOI = 10) were added to BMDM for 4 h, and non-infected bacteria were eliminated with 200 μg/mL of gentamicin for 2 h. The BMDM were then treated with 1 mg/mL BODIPY 493/503 (Invitrogen D3922, Carlsbad, CA, USA) (RT, 15 min) and stained with a dead/live dye (FVD eFluor 780, Invitrogen 65-0865) (1:1000, RT, 10 min). Subsequently, BMDM were washed and fixed with 3% paraformaldehyde (RT, 30 min), resuspended in 100 μL PBS, and further analyzed for LDs accumulation using the BD LSRFortessa flow cytometer (BD, Franklin Lakes, NJ, USA) [32].

2.10. RNA Sequencing and Transcriptome Analysis

WT-BMDM and *Gpr84*$^{-/-}$ BMDM infected with *Mm-wasabi* were collected at 4 hpi and 36 hpi, and RNA extracted using TRIzol reagent. Transcriptome sequencing and analysis were performed by Shanghai OE Biotechnology Co., Ltd. (Shanghai, China). In brief, libraries were sequenced on the Illumina Novaseq 6000 platform (Illumina, San Diego, CA, USA), and the principal component analysis (PCA) of gene counts was conducted using R (v3.2.0) to assess biological replication across samples.

HISAT2 software (v2.1.0) was used for alignment to the reference genome (NCBI_GRCm39) [33]. Differentially expressed genes (DEGs) were identified using DESeq2 (v1.22.2) with a q-value < 0.05 and fold change > 2 or <0.5 [34]. Gene Ontology (GO) [35] and Kyoto Encyclopedia of Genes and Genomes (KEGG) [36] pathway analyses were performed using hypergeometric distributions to identify significantly enriched functional categories. Gene Set Enrichment Analysis (GSEA) [37] was conducted using predefined gene sets, and genes were ranked based on their differential expression between sample groups.

2.11. Data Analysis

GraphPad Prism 9 software was used to analyze the data, presented as Mean ± SEM. Image J (v1.8.0) software was used to analyze the fluorescence images. Student's *t*-test (two-tailed), one-way ANOVA with Tukey's multiple comparisons test, and two-way ANOVA with multiple comparisons were performed to test the statistical significance. $p < 0.05$ was considered significant.

3. Results

3.1. Mycobacterial Infection Induces Upregulation of GPR84 Expression

To investigate the role of GPR84 in TB, we compared the amino acid sequence of the GPR84 homolog in mice with that of human GPR84. The results showed that the amino acid sequences of the seven transmembrane regions are highly conserved among these species (Figure 1A). Next, we explored GPR transcript changes during *Mtb* infections with publicly available data, and GPR84 is significantly upregulated among RAW264.7 infected with different MOIs [19] and H37Rv-infected AM [20] at early time points of infection (4 h or 2 h). Subsequently, we assessed the expression of GPR84 mRNA in whole blood samples obtained from patients diagnosed with tuberculosis. The results indicated a significant upregulation of *GPR84* mRNA in the blood of these patients (Figure 1B), suggesting the potential involvement of GPR84 in the progression of mycobacterial infection. Following this, we validated these results in vitro using mice and human macrophage cell lines infected with *Mm-wasabi*, which similarly demonstrated a significant increase in *Gpr84* mRNA expression post-infection (Figure 1C,D). These findings corroborate that the upregulation of GPR84 is positively correlated with mycobacterial infection, implying that GPR84 may play a critical role in the mycobacterial infection process within the host.

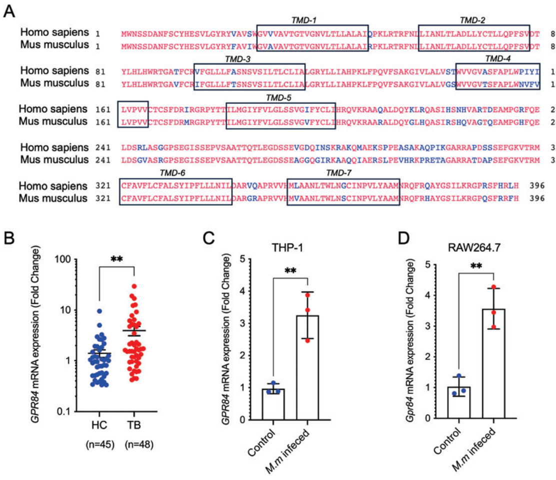

Figure 1. Mycobacterial infection induces a significant increase in *GPR84* mRNA expression. (**A**): comparison of mouse GPR84 homologous proteins with human GPR84. The differential amino

acid is marked in blue, and the seven transmembrane sequences are marked in the black box. (**B**): *GPR84* mRNA expression in the blood of 48 tuberculosis patients (TB, n = 48) and 45 healthy controls (HC, n = 45). (**C**): *GPR84* mRNA expression in PMA-differentiated THP- 1 macrophages infected with *Mm-wasabi* (MOI = 10) compared to non-infected controls at 6 hpi. Total RNA was isolated and subjected to RT-PCR. (**D**): *Gpr84* mRNA expression in RAW264.7 macrophages infected with *Mm-wasabi* (MOI = 10) compared to non-infected controls at 6hpi. Total RNA was isolated and subjected to RT-PCR. Values were normalized to *β-actin*. Data were analyzed with GraphPad Prism 9 software and are presented as mean ± SEM. Data are representative of three independent experiments. Statistical analysis was conducted using Student's *t*-test for (**B**–**D**). **: $p < 0.01$.

3.2. GPR84 Aggravates Mycobacterium-Induced Tissue Damage

We subsequently employed an in vivo mouse tail vein infection model to evaluate the effects of $Gpr84^{-/-}$ mice on tissue pathology following *Mm-wasabi* injection into the tail vein (Figure 2A) [24]. Ulceration was observed on the tails of all mice at 14 dpi; however, overall, tail lesions on $Gpr84^{-/-}$ mice were significantly reduced in comparison to the tail lesions of WT mice (Figure 2B,C). WT mice displayed elongated and continuous lesions with swelling, extensive skin ulceration, and white nodules. In contrast, $Gpr84^{-/-}$ mice exhibited only mild skin damage characterized by sparsely distributed lesions and minimal ulceration, resulting in significantly smaller areas of ulceration (Figure 2B,C). The histological analysis of tail tissue sections, along with counts of immune cells, indicated a decreased level of immune cell infiltration in $Gpr84^{-/-}$ mice (Figure 2D,E). Moreover, $Gpr84^{-/-}$ mice infected with *Mm-wasabi* exhibited lower *Mm* loads in their tails examined by acid-fast staining (Figure 2F,G). These results suggest that GPR84 plays an important role in mediating tissue damage and promoting infection.

3.3. GPR84 Promotes Intracellular Proliferation of Mm-Wasabi and LD Accumulation

BMDMs from $Gpr84^{-/-}$ and WT mice were infected with *Mm-tdTomato* at an MOI of 1, and intracellular bacterial proliferation was assessed at 6, 24, and 48 hpi. $Gpr84^{-/-}$ BMDMs demonstrated significantly lower bacterial loads in comparison to WT BMDMs (Figure 3A). Because LD accumulation can influence mycobacterial growth within macrophages [38], we hypothesized that *GPR84* deficiency might also affect LD accumulation in macrophages. Using BODIPY staining to visualize LD accumulation in BMDMs, we found that following *Mm-tdTomato* infection induced the formation of LDs, which co-localized with *Mm-tdTomato*. Compared to WT BMDM, $Gpr84^{-/-}$ BMDMs exhibited less co-localization of bacteria with LDs (Figure 3B) and a reduced BODIPY fluorescence intensity, indicating fewer LDs (Figure 3C). Furthermore, flow cytometry analysis confirmed a significant reduction in the number of BODIPY+ macrophages within the $Gpr84^{-/-}$ group (Figure 3D). Similarly, the histological examination of sections from the tail lesions revealed significantly less LD accumulation in the lesions of $Gpr84^{-/-}$ mice (Figure 3E,F) compared to WT mice.

3.4. $Gpr84^{-/-}$ BMDMs Promotes the Expression of Pro-Inflammatory Cytokine

To further explore the factors contributing to the limited proliferation of mycobacterium in $Gpr84^{-/-}$ BMDMs, we conducted a systematic analysis of differentially expressed genes (DEGs) in *Mm*-infected WT and $Gpr84^{-/-}$ BMDMs using RNA-seq technology. WT and $Gpr84^{-/-}$ BMDM samples were effectively differentiated through multidimensional scaling (Figure 4A,B). Compared to WT BMDMs, 25 genes were significantly upregulated in $Gpr84^{-/-}$ BMDMs at both 4 hpi and 36 hpi. Among these, *Adamts1* [39], *Bex1* [40], *Col5a3* [41], *Mid1* [42], and *Tie1* [43] have previously shown to be highly expressed during inflammatory responses and exhibit pro-inflammatory characteristics, which are closely associated with an enhanced host bactericidal function. Additionally, the genes *Mgll* [44], *Dgat2* [45], *Slc27a6* [45], and *Stard10* [45] have been implicated in lipid metabolism, indicating that lipid metabolism may be disrupted in *Gpr84*$^{-/-}$ BMDMs during mycobacterial infection. Notably, among the 66 upregulated genes identified in *Gpr84*$^{-/-}$ BMDMs at 36 hpi, there were genes associated with the NF-kappaB signaling pathway, including *Ccl4, Cxcl1, and Bcl2a1a* [46–48]. Other genes related to the macrophage inflammatory response, such as *Il6* and *Il12b*, also exhibited upregulation at 36 hpi but not 4 hpi. These findings suggest that *Gpr84*$^{-/-}$ BMDMs at 36 hpi may enhance the inflammatory response in macrophages, thereby facilitating the control of mycobacterium proliferation (Figures 2G and 4D). Subsequently, we utilized the KEGG database to categorize the functions of DEGs and conducted a further analysis of the variations in downstream signaling pathways. Compared to 4 hpi, BMDMs at 36 hpi exhibited enhanced enrichment in genes related to pathways seen in diseases (such as Amoebiasis, alcoholic liver disease, and COVID-19), receptor signaling (such as RIG-I-like receptor signaling pathway and C-type lectin receptor signaling pathway), IL-17 signaling pathway, and the positive regulation of nitric oxide biosynthetic pathway (Figure 4E). Genes such as *Il12b, Il6, Cxcl10, Tnf,* and *Cxcl1* are involved in multiple pathways, suggesting that the genes upregulated in *Gpr84*$^{-/-}$ BMDMs at 36 hpi may help to control mycobacterium proliferation. Furthermore, the gene expression analysis of cytokines associated with bactericidal activity found that the mRNA expression of pro-inflammatory cytokines *Tnf, Il6, Il12b, Cxcl10,* and *Cxcl1* were significantly upregulated compared to WT BMDMs at 4 hpi (Figure 5A–E).

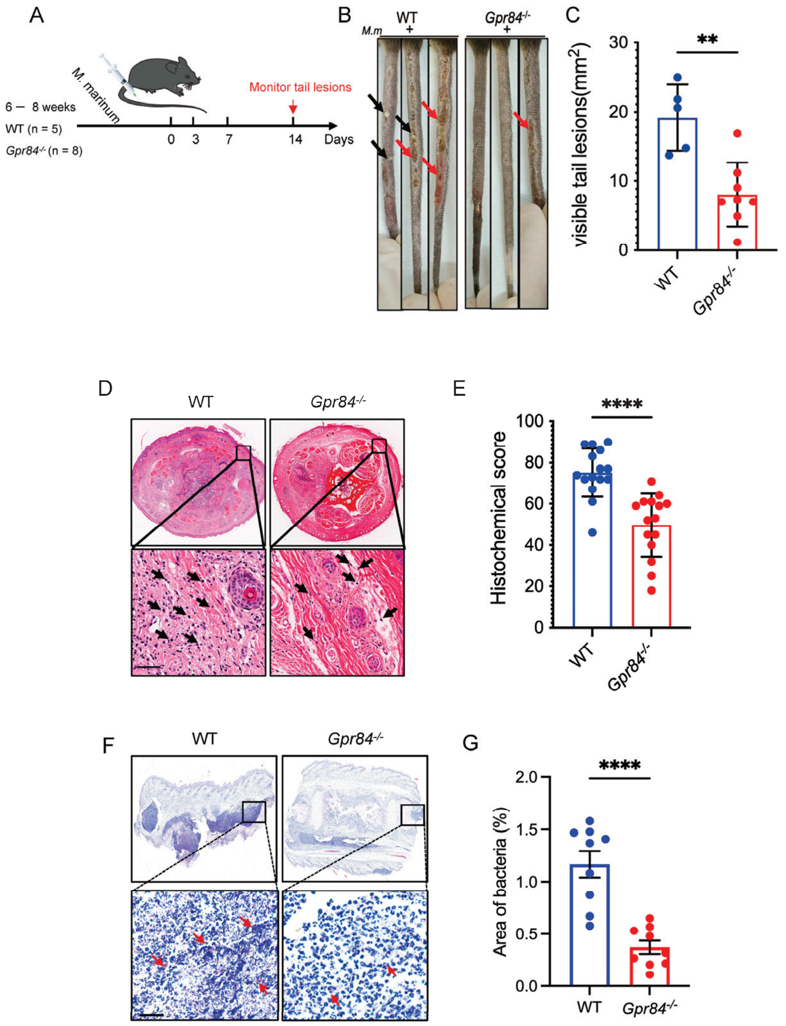

Figure 2. Tail pathology in mice following *Mm-wasabi* infection. (**A**): Schematic of the experimental procedure for tail vein infection with *Mm-wasabi* in mice. *Gpr84*$^{-/-}$ (n = 8) and WT (n = 5) mice

were infected via tail vein injection with 4 × 10^7 CFU of *Mm-wasabi*. Tail lesions were monitored and photographed every other day, with comprehensive tail images of the entire tail captured at 14 dpi. (**B**): Three representative images of tails of WT and *Gpr84*$^{-/-}$ mice at 14 dpi. Black arrows indicate nodules and red arrows indicate denote ulcerations. (**C**): Quantification of area of tail lesions, calculated by length (mm) × width (mm), as shown in panel (**B**). Each data point represents an individual mouse tail. (**D**): Representative histopathological images of H & E stained tail tissue from WT and *Gpr84*$^{-/-}$ mice at 14 dpi. The analysis was performed using five mice per group, with three sections examined per mice. Black arrows indicate infiltrated immune cells. Scale bar: 100 µm. (**E**): Quantification of immune cell infiltration in tail tissue sections. The analysis includes five mice per group, with three tissue sections examined per mice. (**F**): Representative images of acid-fast staining of *Mm-wasabi*. The analysis was performed using three mice per group, with three sections examined per mice. Red arrows indicate bacteria. Scale bar, 100 µm. (**G**): Quantification of area of red-marked bacteria by ImageJ (v1.8.0) software. Data were analyzed with GraphPad Prism 9 software and are presented as mean ± SEM. Statistical analysis was performed using Student's *t*-test for (**C**,**E**,**G**). ** $p < 0.01$, **** $p < 0.0001$.

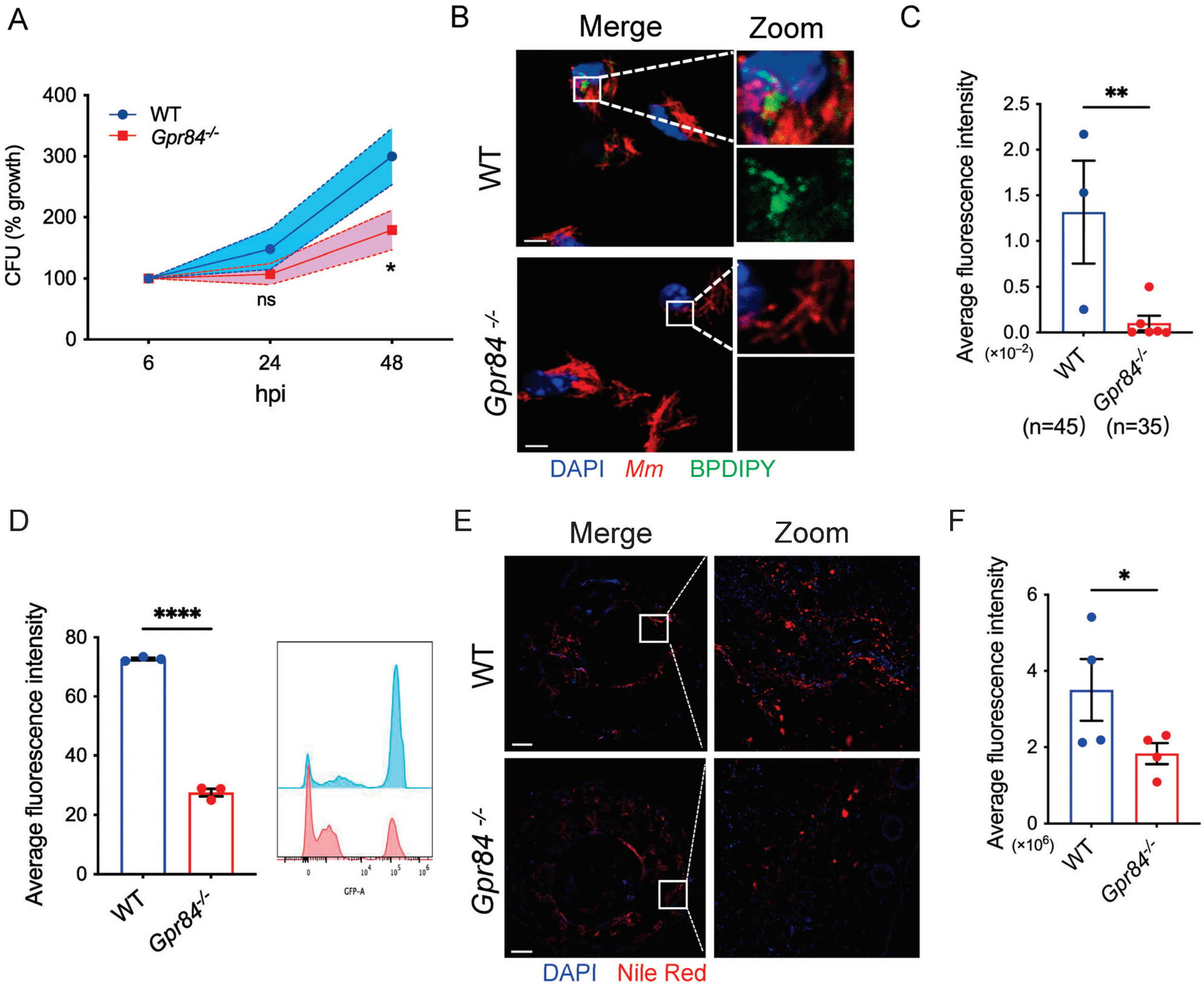

Figure 3. GPR84 deficiency reduces LDs accumulation in macrophages. (**A**): Colony-forming unit (CFU) counts of WT and *Gpr84*$^{-/-}$ BMDM infected *Mm-wasabi* at an MOI of 1, lysed at 6 hpi, 24 hpi, and 48 hpi; CFU were counted on plates. Data are representative of three independent experiments. (**B**): Confocal microscopy images of lipid content in WT and *Gpr84*$^{-/-}$ BMDMs at 6 hpi with

Mm-tdTomato (MOI = 10). *Mm-tdTomato* is shown in red, BODIPY-stained lipids in green, and DAPI-stained nuclei in blue. The images were representative of three independent experiments. Scale Bar: 5 µm. (**C**): Quantification of LDs in macrophages based on green BODIPY fluorescence intensity, analyzed by ImageJ (v1.8.0) software. (**D**): Flow cytometry analysis of LDs in macrophages 6 hpi with *Mm-tdTomato* (MOI = 10). The left panel shows the percentage of BODIPY-positive macrophages, and the right panel shows BODIPY-positive fluorescence intensity. (**E**): Representative multi-color immunofluorescence staining of tail tissue sections from mice at 14 dpi. LDs were stained with Nile Red (red) and cell nuclei with DAPI (blue). The images were representative of three independent experiments. Scale Bar: 100 µm. (**F**): Quantification of red fluorescence intensity of Nile Red-stained LDs by ImageJ (v1.8.0) software. Data were analyzed with GraphPad Prism 9 software and are presented as mean ± SEM. Statistical significance was determined by two-way ANOVA for (**A**) and Student's *t*-test for (**C**,**D**,**F**). * $p < 0.05$, ** $p < 0.01$, **** $p < 0.0001$.

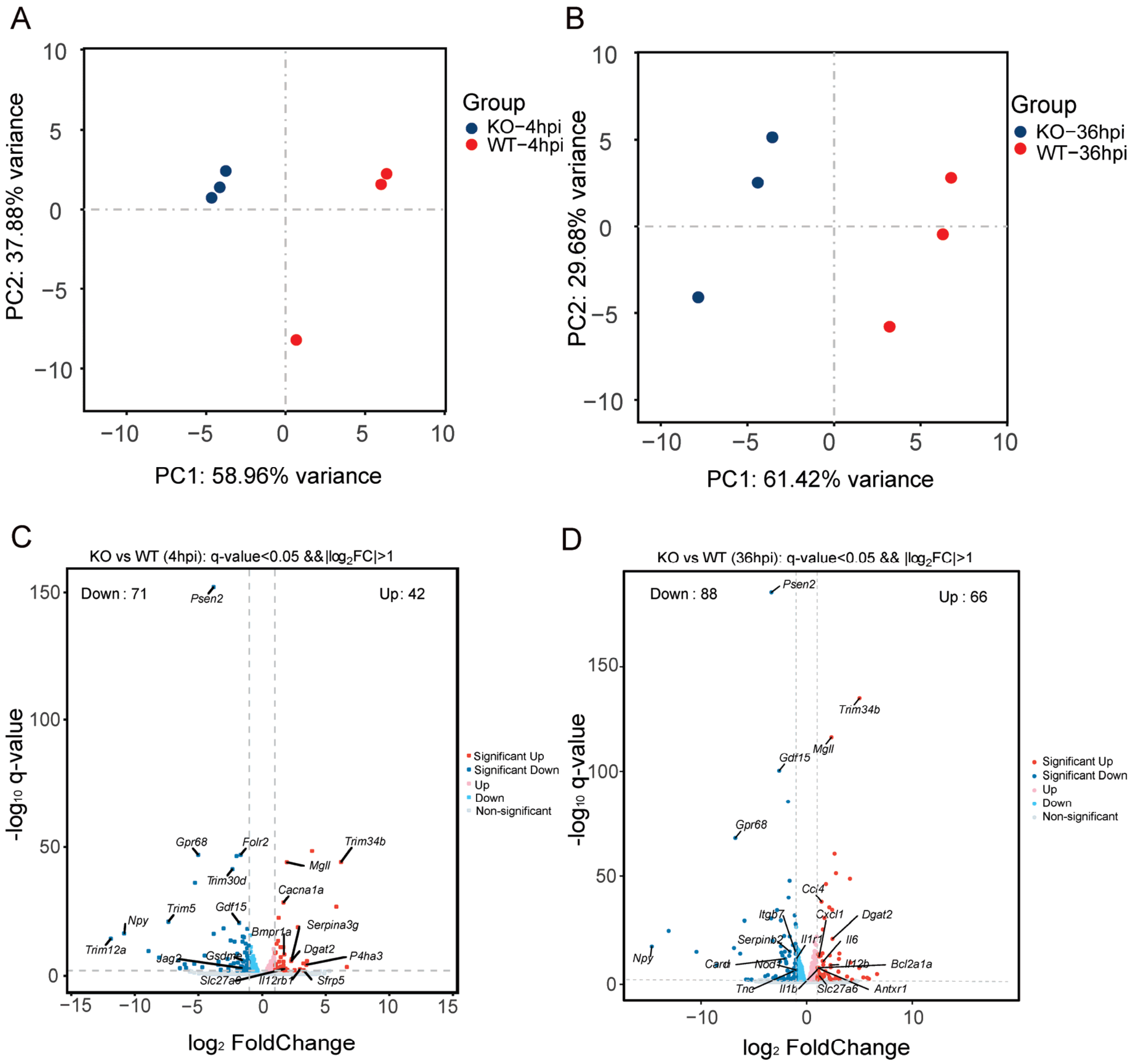

Figure 4. *Cont*.

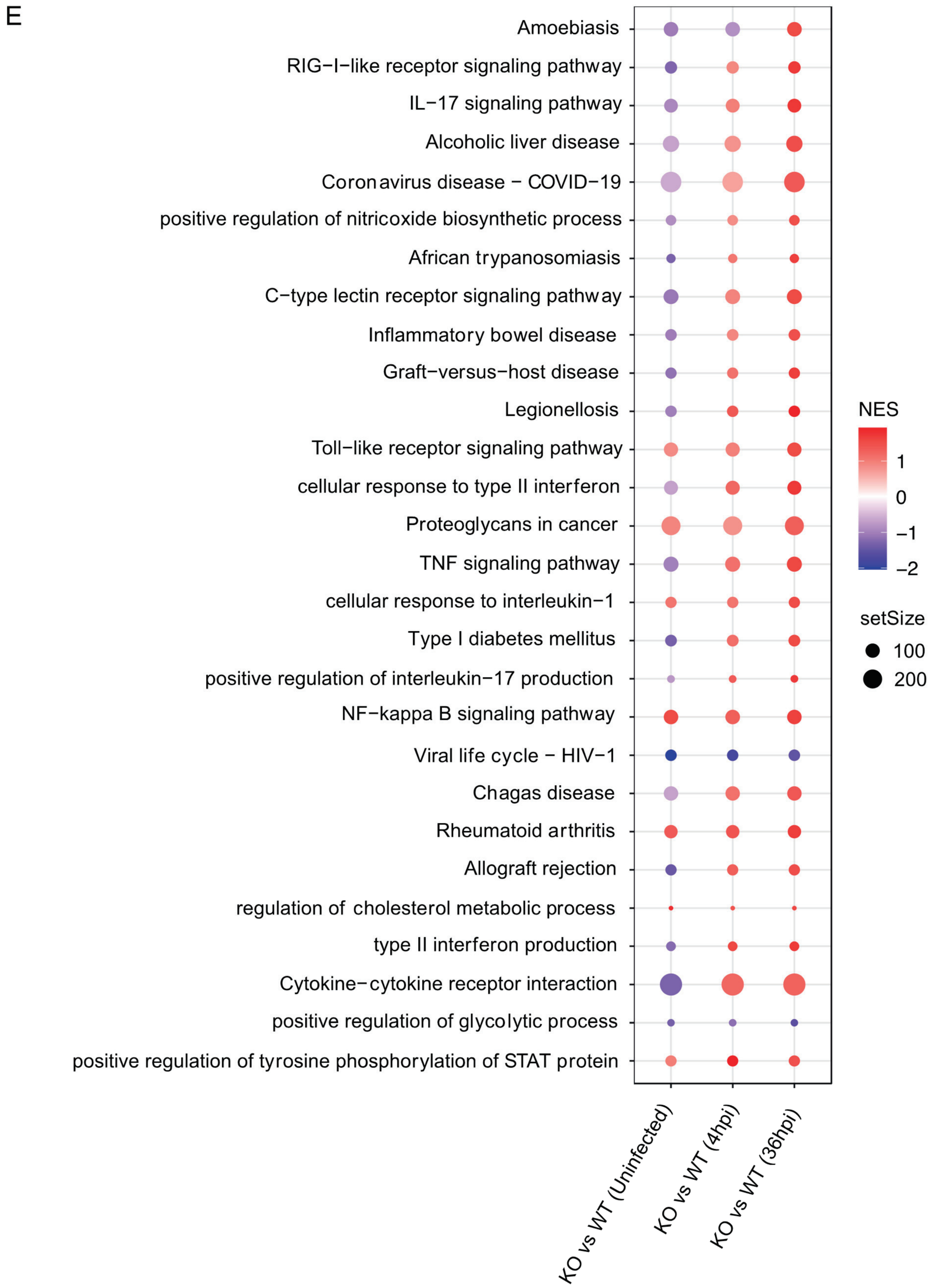

Figure 4. Results of RNA-seq analysis, differentially expressed genes and pathways. (**A**,**B**): Multi-dimensional scaling between *Gpr84*$^{-/-}$ BMDM and WT BMDM at 4 hpi (**A**) and 36 hpi (**B**). Each

group has three biological replicates. (**C**,**D**): Volcano plot of differentially expressed genes (DEGs). Genes with significant expression differences ($p < 0.05$) are listed, while red dots and blue dots are up- or downregulated genes in $Gpr84^{-/-}$ BMDM, respectively, compared to WT BMDM at 4 hpi (**C**) and 36 hpi (**D**). The x axis represents $\log_2$ of fold change and the y axis represents the $\log_{10}$ of p values. (**E**): KEGG pathway enrichment analysis of significant DEGs in uninfected and *Mm*-infected BMDM at 4 hpi and 36 hpi. KEGG pathway enrichment analysis of significant DEGs in datasets from uninfected BMDM, *Mm*-infected BMDM at 4 hpi and 36 hpi. Set size represents the number of DEGs. Normalized enrichment score (NES) represents the gene enriched degree, and higher |NES| represent more up- or downregulated genes in a given pathway.

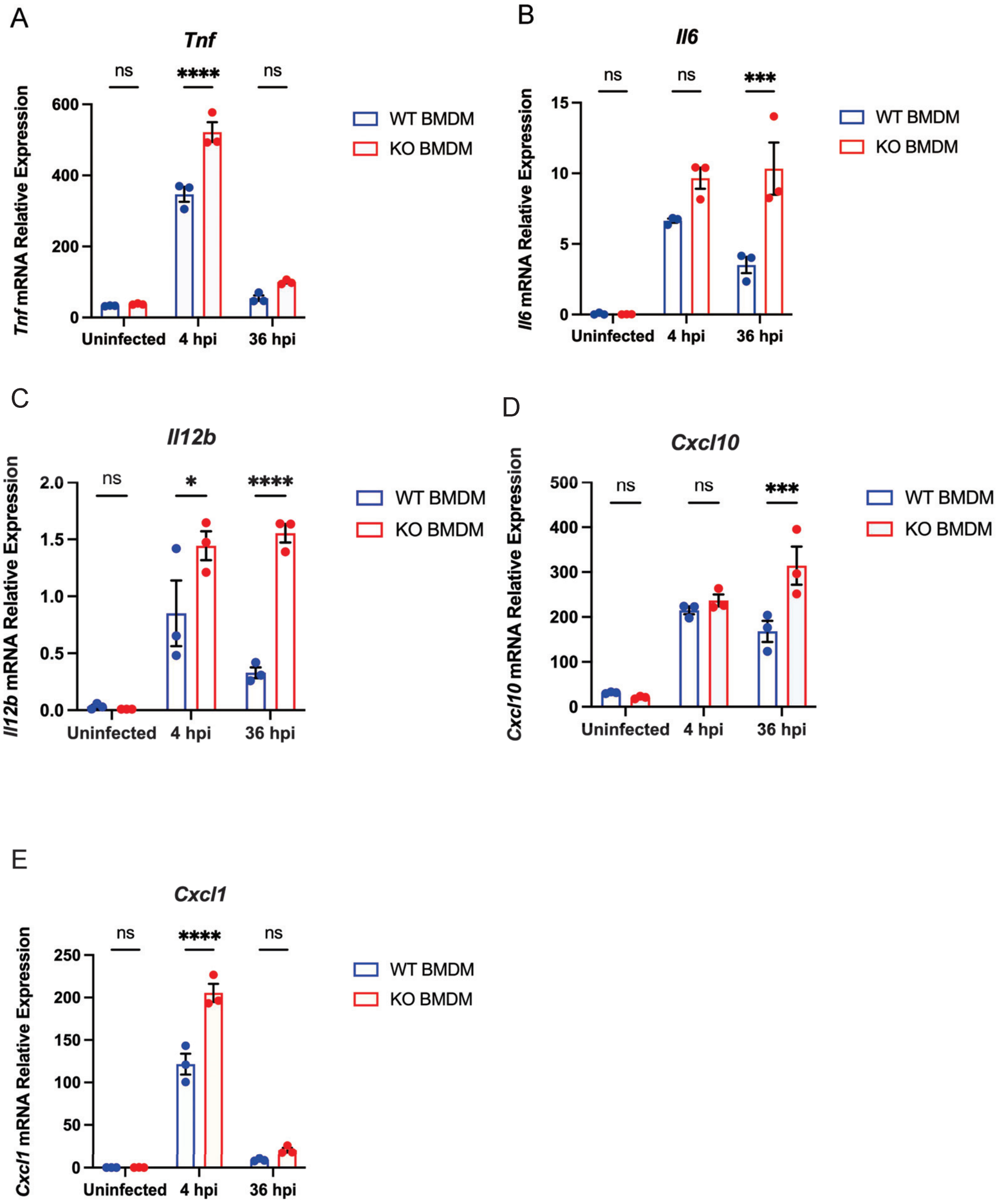

Figure 5. $Gpr84^{-/-}$ BMDMs promotes the expression of pro-inflammatory cytokines. (**A**–**E**): *Tnf*, *Il6*, *Il12b*, *Cxcl10*, and *Cxcl1* mRNA expression. Based on the RNA-seq analysis results, the expression of *Tnf* (**A**), *Il6* (**B**), *Il12b* (**C**), *Cxcl10* (**D**), and *Cxcl1* (**E**) mRNA was quantitated in WT and $Gpr84^{-/-}$ BMDM. Data were analyzed with GraphPad Prism 9 software and are presented as mean ± SEM. Statistical analysis was performed using two-way ANOVA for (**A**–**E**). * $p < 0.05$, *** $p < 0.001$, **** $p < 0.0001$, ns, not significant.

4. Discussion

In this study, we found that GPR84 plays a harmful role for hosts in mycobacterial infections. In both BMDM and mouse tail models, *Gpr84* deficiency was associated with the reduced accumulation of the intra-cellular LDs that facilitate bacterial survival within host cells. And GPR84 deficiency is beneficial to increase the expression of pro-inflammatory cytokines during mycobacterium infection.

Previous research has demonstrated that the deficiency of GPR84 mitigates host inflammatory responses [13,49–51]. For example, in a mouse model of ALI, *Gpr84*$^{-/-}$ mice significantly reduced pulmonary inflammation by decreasing neutrophil recruitment and the production of reactive oxygen species (ROS) [13]. Additionally, in a DSS-induced colitis model, *Gpr84*$^{-/-}$ mice reduced the infiltration of inflammatory cells and damage to the colonic mucosa [51]. These results are similar to our observation of decreased inflammatory cell infiltration and tissue damage in *Mm-wasabi* infected tails of *Gpr84*$^{-/-}$ mice (Figure 2) [13,51].

Our RNA-seq results indicate that in *Gpr84*$^{-/-}$ BMDMs following *Mm-wasabi* infection, the expression of pro-inflammatory cytokines such as *Tnf*, *Il12b*, *Il6*, *Cxcl10*, and *Cxcl1* is significantly elevated (Figure 5A–E). It is possible that the increased cytokines production enhances the ability of *Gpr84*$^{-/-}$ BMDMs to control bacterial proliferation (Figure 3A). However, this observation appears to contradict the previous notion that GPR84 promotes the M1 polarization of macrophages and increases the expression of pro-inflammatory cytokines, including TNF-α and IL-6 [13,14]. We propose several possible explanations for this discrepancy. First, the mechanisms by which GPR84 functions following infection may differ depending on the diseases being studied. In acute lung injury, acute colitis, or LPS-induced acute inflammation, GPR84 acts as a pro-inflammatory receptor that increases the release of late-stage pro-inflammatory cytokines, exacerbating pathological damage [13,14,51]. However, in chronic diseases such as osteoarthritis, non-alcoholic steatohepatitis, and *Brucella abortus* infection, GPR84 plays a role in modulating inflammation by reducing the expression of pro-inflammatory factors (such as TNF-α), thereby alleviating disease progression or promoting infection [16,52,53]. Consistent with the findings on the aforementioned *Brucella abortus* infection [16], we also observed that GPR84 negatively regulates the inflammatory response to promote infection. Therefore, our results further emphasize the importance of disease models when studying GPR84's function, as GPR84 may play distinctly opposite roles in different disease models. Additionally, the timing of the expression of inflammatory cytokines may differ depending on the disease models. In acute inflammatory models, the role of GPR84 in promoting pro-inflammatory functions typically manifests at later stages, where cytokine expression may indicate a secondary response in the progression of the disease [13,51]. We observed that at an early time point post infection, *Gpr84*$^{-/-}$ mice showed an increased expression of pro-inflammatory cytokines, suggesting that GPR84 may inhibit their expression in the early stages of infection (Figure 5A–E). Although variations in cytokine expression are noted at different time points, GPR84 consistently facilitates disease progression (Figure 2B) [13,51]. Furthermore, differences in cellular models may significantly influence the role of GPR84 in the production of pro-inflammatory cytokines. For example, GPR84-mediated signaling in microglia promotes cell migration through the Gi/o pathway, but does not elicit a pro-inflammatory response [54]. Consequently, while it appears that GPR84 plays an important role in the immune response to infections, its functions are complex and may vary depending on the pathogen [15,16], the disease model [13,53], the time of the response, and the specific cell type examined [51,54].

One way by which mycobacteria appear to evade the host immune response is by promoting the accumulation of LDs within macrophages [55,56]. In macrophages infected with *Mtb*, a reduction in the accumulation of LDs restores the macrophage antibacterial capacity, leading to a reduction in the intracellular burden of *Mtb* [56–58]. In our study, we observed that *Gpr84*$^{-/-}$ mice decreased LD accumulation in both BMDM and mouse tails with lower *Mm* loads (Figure 3). Similarly, previous studies have reported that the overexpression of GPR84 in RAW264.7 can promote LD formation [59]. Further analysis of our RNA-seq results revealed an upregulation of lipid metabolism-related genes, *Mgll* [44] and *Dgat2* [45], at both 4 hpi and 36 hpi (Figure 4C,D), suggesting that macrophages may attempt to compensate for lipid synthesis by upregulating the expression of *Mgll* and *Dgat2* to restore lipid homeostasis in infected *Gpr84*$^{-/-}$ macrophages. This compensatory mechanism could provide an energy reserve for the antimicrobial activity of macrophages. Meanwhile, the LD accumulation reduction in macrophages prevents the differentiation of foam cells (FM), allowing macrophages to maintain their original bactericidal function and release pro-inflammatory cytokines such as TNF-α and IL-6 to reduce intracellular bacterial load [60].

In conclusion, our study demonstrates that GPR84 exacerbates the progression of mycobacterial infection. Both in vivo findings from mouse models and in vitro results from macrophage infections indicate that the *Gpr84*$^{-/-}$ BMDM lead to an increased expression of inflammatory cytokines, accompanied by a decrease in LD accumulation, ultimately limiting the intracellular and in vivo proliferation of mycobacteria. Further exploration of the regulatory mechanisms by which GPR84 influences the host response to mycobacterial infection may offer novel avenues for the development of host-directed anti-tuberculosis therapeutics.

5. Limitations

Our study found that GPR84 deficiency restricts the progression of mycobacterial infection, but the delineation of the downstream signaling pathways activated by GPR84 during mycobacterial infections will require subsequent investigation. Furthermore, the ligand for GPR84 and whether mycobacterium harbors GPR84-specific pathogen-associated molecular patterns (PAMPs), like PDIM and Sulfolipids, or other virulence factors that may affect lipid metabolism pathways or macrophage polarization to promote infection remains to be determined. Moreover, using macrophage-specific Cre driver mice with the conditional knock out of GPR84 is necessary to eliminate changes in other cells, such as neutrophils and epithelial cells.

Author Contributions: Conceptualization, R.W., B.Y. and Q.G.; methodology, R.W., K.Z., J.Z., Z.W., Z.C., G.L., H.W., J.Q. and B.D.; formal analysis, R.W., K.Z., J.Z., Z.W., Z.C., G.L., H.W., J.Q., B.D., H.R., Y. S., Q.G. and B.Y.; resources, Z.W., J.Q., B.D., H.R., Y.S., H.R., Q.G. and B.Y.; data curation, R.W. and K.Z.; writing—original draft preparation, R.W., K.Z., Q.G. and B.Y.; writing—review and editing, all authors.; project administration, B.Y. and Q.G.; funding acquisition, B.Y., Q.G., J.Q. and B.D. All authors have read and agreed to the published version of the manuscript.

Funding: This research was funded by the National Key Research and Development Program (2023YFE0199200 to B.Y.), Shanghai Municipal Science and Technology Major Project (ZD2021CY001 to Q.G.), National Natural Science Foundation of China (82272376 and 32470186 to Q.G, 82372263 to B.Y.), and Science and Technology Commission of Shanghai Municipality (23141903300 to J.Q., 23141901800 to B.D.).

Institutional Review Board Statement: The study was conducted in accordance with the Declaration of Helsinki, and approved by Shanghai Public Health Clinical Center Ethics Committee, Fudan University (protocol code: 2019-S009-02; date of approval: 24 April 2019). The animal study protocol was approved by Shanghai Public Health Clinical Center Laboratory Animal Welfare & Ethics Committee, Fudan University (protocol code: 2021-A051-01; date of approval: 10 August 2021).

Informed Consent Statement: Informed consent was obtained from all subjects involved in the study. Written informed consent has been obtained from the patient(s) to publish this paper.

Data Availability Statement: The raw data supporting the conclusions of this article will be made available by the authors on request.

Acknowledgments: We would like to express our deepest gratitude to Howard Takiff for assistance in manuscript editing.

Conflicts of Interest: The authors declare no conflicts of interest.

References

1. WHO. *Global Tuberculosis Report 2024*; World Health Organization: Geneva, Switzerland, 2024.
2. Kumar, A.; Rani, M.; Ehtesham, N.Z.; Hasnain, S.E. Commentary: Modification of Host Responses by Mycobacteria. *Front. Immunol.* **2017**, *8*, 466. [CrossRef] [PubMed]
3. Young, C.; Walzl, G.; Du Plessis, N. Therapeutic host-directed strategies to improve outcome in tuberculosis. *Mucosal Immunol.* **2020**, *13*, 190–204. [CrossRef] [PubMed]
4. Baskakova, K.O.; Kuzmichev, P.K.; Karbyshev, M.S. Advanced applications of Nanodiscs-based platforms for antibodies discovery. *Biophys. Chem.* **2024**, *313*, 107290. [CrossRef] [PubMed]
5. Gulezian, E.; Crivello, C.; Bednenko, J.; Zafra, C.; Zhang, Y.; Colussi, P.; Hussain, S. Membrane protein production and formulation for drug discovery. *Trends Pharmacol. Sci.* **2021**, *42*, 657–674. [CrossRef]
6. Das, S.; Banerjee, S.; Majumder, S.; Chowdhury, B.P.; Goswami, A.; Halder, K.; Chakraborty, U.; Pal, N.K.; Majumdar, S. Immune subversion by Mycobacterium tuberculosis through CCR5 mediated signaling: Involvement of IL-10. *PLoS ONE* **2014**, *9*, e92477. [CrossRef]
7. Singh, V.; Jamwal, S.; Jain, R.; Verma, P.; Gokhale, R.; Rao, K.V. Mycobacterium tuberculosis-driven targeted recalibration of macrophage lipid homeostasis promotes the foamy phenotype. *Cell Host Microbe* **2012**, *12*, 669–681. [CrossRef]
8. Yang, H.; Liu, H.; Chen, H.; Mo, H.; Chen, J.; Huang, X.; Zheng, R.; Liu, Z.; Feng, Y.; Liu, F.; et al. G protein-coupled receptor160 regulates mycobacteria entry into macrophages by activating ERK. *Cell Signal* **2016**, *28*, 1145–1151. [CrossRef]
9. Bartlett, S.; Gemiarto, A.T.; Ngo, M.D.; Sajiir, H.; Hailu, S.; Sinha, R.; Foo, C.X.; Kleynhans, L.; Tshivhula, H.; Webber, T.; et al. GPR183 Regulates Interferons, Autophagy, and Bacterial Growth During Mycobacterium tuberculosis Infection and Is Associated With TB Disease Severity. *Front. Immunol.* **2020**, *11*, 601534. [CrossRef]
10. Stanley, S.A.; Barczak, A.K.; Silvis, M.R.; Luo, S.S.; Sogi, K.; Vokes, M.; Bray, M.A.; Carpenter, A.E.; Moore, C.B.; Siddiqi, N.; et al. Identification of host-targeted small molecules that restrict intracellular Mycobacterium tuberculosis growth. *PLoS Pathog.* **2014**, *10*, e1003946. [CrossRef]
11. Yousefi, S.; Cooper, P.R.; Potter, S.L.; Mueck, B.; Jarai, G. Cloning and expression analysis of a novel G-protein-coupled receptor selectively expressed on granulocytes. *J. Leukoc. Biol.* **2001**, *69*, 1045–1052. [CrossRef]
12. Wang, J.; Wu, X.; Simonavicius, N.; Tian, H.; Ling, L. Medium-chain fatty acids as ligands for orphan G protein-coupled receptor GPR84. *J. Biol. Chem.* **2006**, *281*, 34457–34464. [CrossRef] [PubMed]
13. Zhang, Q.; Chen, L.H.; Yang, H.; Fang, Y.C.; Wang, S.W.; Wang, M.; Yuan, Q.T.; Wu, W.; Zhang, Y.M.; Liu, Z.J.; et al. GPR84 signaling promotes intestinal mucosal inflammation via enhancing NLRP3 inflammasome activation in macrophages. *Acta Pharmacol. Sin.* **2022**, *43*, 2042–2054. [CrossRef]
14. Yin, C.; Cheng, L.; Pan, J.; Chen, L.; Xue, Q.; Qin, J.; Wang, S.; Du, B.; Liu, M.; Zhang, Y.; et al. Regulatory role of Gpr84 in the switch of alveolar macrophages from CD11b(lo) to CD11b(hi) status during lung injury process. *Mucosal Immunol.* **2020**, *13*, 892–907. [CrossRef] [PubMed]
15. Recio, C.; Lucy, D.; Purvis, G.S.D.; Iveson, P.; Zeboudj, L.; Iqbal, A.J.; Lin, D.; O'Callaghan, C.; Davison, L.; Griesbach, E.; et al. Activation of the Immune-Metabolic Receptor GPR84 Enhances Inflammation and Phagocytosis in Macrophages. *Front. Immunol.* **2018**, *9*, 1419. [CrossRef] [PubMed]
16. Reyes, A.W.B.; Kim, H.; Huy, T.X.N.; Vu, S.H.; Nguyen, T.T.; Kang, C.K.; Min, W.; Lee, H.J.; Lee, J.H.; Kim, S. Immune-metabolic receptor GPR84 surrogate and endogenous agonists, 6-OAU and lauric acid, alter Brucella abortus 544 infection in both in vitro and in vivo systems. *Microb. Pathog.* **2021**, *158*, 105079. [CrossRef]
17. Torraca, V.; White, R.J.; Sealy, I.M.; Mazon-Moya, M.; Duggan, G.; Willis, A.R.; Busch-Nentwich, E.M.; Mostowy, S. Transcriptional profiling of zebrafish identifies host factors controlling susceptibility to Shigella flexneri. *Dis. Model. Mech.* **2024**, *17*, dmm050431. [CrossRef]
18. Didangelos, A. COVID-19 Hyperinflammation: What about Neutrophils? *mSphere* **2020**, *5*, e00367-20. [CrossRef]
19. Ding, Y.; Bei, C.; Xue, Q.; Niu, L.; Tong, J.; Chen, Y.; Takiff, H.E.; Gao, Q.; Yan, B. Transcriptomic Analysis of Mycobacterial Infected Macrophages Reveals a High MOI Specific Type I IFN Signaling. *Infect. Immun.* **2023**, *91*, e0015523. [CrossRef]

20. Sadee, W.; Cheeseman, I.H.; Papp, A.; Pietrzak, M.; Seweryn, M.; Zhou, X.; Lin, S.; Williams, A.M.; Wewers, M.D.; Curry, H.M.; et al. Human alveolar macrophage response to Mycobacterium tuberculosis: Immune characteristics underlying large inter-individual variability. *bioRxiv* **2022**. [CrossRef]
21. Takaki, K.; Davis, J.M.; Winglee, K.; Ramakrishnan, L. Evaluation of the pathogenesis and treatment of Mycobacterium marinum infection in zebrafish. *Nat. Protoc.* **2013**, *8*, 1114–1124. [CrossRef]
22. Kam, J.Y.; Cheng, T.; Garland, D.C.; Britton, W.J.; Tobin, D.M.; Oehlers, S.H. Inhibition of infection-induced vascular permeability modulates host leukocyte recruitment to Mycobacterium marinum granulomas in zebrafish. *Pathog. Dis.* **2022**, *80*, ftac009. [CrossRef] [PubMed]
23. Mittal, E.; Roth, A.T.; Seth, A.; Singamaneni, S.; Beatty, W.; Philips, J.A. Single cell preparations of Mycobacterium tuberculosis damage the mycobacterial envelope and disrupt macrophage interactions. *eLife* **2023**, *12*, e85416. [CrossRef] [PubMed]
24. Ding, Y.; Tong, J.; Luo, G.; Sun, R.; Bei, C.; Feng, Z.; Meng, L.; Wang, F.; Zhou, J.; Chen, Z.; et al. Mycobacterial CpsA activates type I IFN signaling in macrophages via cGAS-mediated pathway. *iScience* **2024**, *27*, 109807. [CrossRef] [PubMed]
25. Tong, J.; Meng, L.; Bei, C.; Liu, Q.; Wang, M.; Yang, T.; Takiff, H.E.; Zhang, S.; Gao, Q.; Wang, C.; et al. Modern Beijing sublineage of Mycobacterium tuberculosis shift macrophage into a hyperinflammatory status. *Emerg. Microbes Infect.* **2022**, *11*, 715–724. [CrossRef]
26. Wang, Q.; Zhu, L.; Jones, V.; Wang, C.; Hua, Y.; Shi, X.; Feng, X.; Jackson, M.; Niu, C.; Gao, Q. CpsA, a LytR-CpsA-Psr Family Protein in Mycobacterium marinum, Is Required for Cell Wall Integrity and Virulence. *Infect. Immun.* **2015**, *83*, 2844–2854. [CrossRef]
27. Wang, S.; Chen, L.L.; Yin, C.C.; Du, B.; Qian, M.; Ren, H. Establishment of Gpr84 knockout mice and its effect on secretion of TNF-α of macrophage. *Highlights Sci. Online* **2017**, *10*, 242–247.
28. Kamber, R.A.; Nishiga, Y.; Morton, B.; Banuelos, A.M.; Barkal, A.A.; Vences-Catalan, F.; Gu, M.; Fernandez, D.; Seoane, J.A.; Yao, D.; et al. Inter-cellular CRISPR screens reveal regulators of cancer cell phagocytosis. *Nature* **2021**, *597*, 549–554. [CrossRef]
29. Greenspan, P.; Mayer, E.P.; Fowler, S.D. Nile red: A selective fluorescent stain for intracellular lipid droplets. *J. Cell Biol.* **1985**, *100*, 965–973. [CrossRef]
30. Sun, W.; Zhang, X.; Qiao, Y.; Griffin, N.; Zhang, H.; Wang, L.; Liu, H. Exposure to PFOA and its novel analogs disrupts lipid metabolism in zebrafish. *Ecotoxicol. Environ. Saf.* **2023**, *259*, 115020. [CrossRef]
31. Pedrosa, L.F.; Kouzounis, D.; Schols, H.; de Vos, P.; Fabi, J.P. Assessing high-temperature and pressure extraction of bioactive water-soluble polysaccharides from passion fruit mesocarp. *Carbohydr. Polym.* **2024**, *335*, 122010. [CrossRef]
32. Listenberger, L.L.; Studer, A.M.; Brown, D.A.; Wolins, N.E. Fluorescent Detection of Lipid Droplets and Associated Proteins. *Curr. Protoc. Cell Biol.* **2016**, *71*, 4–31. [CrossRef] [PubMed]
33. Kim, D.; Langmead, B.; Salzberg, S.L. HISAT: A fast spliced aligner with low memory requirements. *Nat. Methods* **2015**, *12*, 357–360. [CrossRef] [PubMed]
34. Love, M.I.; Huber, W.; Anders, S. Moderated estimation of fold change and dispersion for RNA-seq data with DESeq2. *Genome Biol.* **2014**, *15*, 550. [CrossRef] [PubMed]
35. The Gene Ontology, C. The Gene Ontology Resource: 20 years and still GOing strong. *Nucleic Acids Res.* **2019**, *47*, D330–D338. [CrossRef]
36. Kanehisa, M.; Araki, M.; Goto, S.; Hattori, M.; Hirakawa, M.; Itoh, M.; Katayama, T.; Kawashima, S.; Okuda, S.; Tokimatsu, T.; et al. KEGG for linking genomes to life and the environment. *Nucleic Acids Res.* **2008**, *36*, D480–D484. [CrossRef]
37. Subramanian, A.; Tamayo, P.; Mootha, V.K.; Mukherjee, S.; Ebert, B.L.; Gillette, M.A.; Paulovich, A.; Pomeroy, S.L.; Golub, T.R.; Lander, E.S.; et al. Gene set enrichment analysis: A knowledge-based approach for interpreting genome-wide expression profiles. *Proc. Natl. Acad. Sci. USA* **2005**, *102*, 15545–15550. [CrossRef]
38. Huang, Q.; Feng, D.; Liu, K.; Wang, P.; Xiao, H.; Wang, Y.; Zhang, S.; Liu, Z. A medium-chain fatty acid receptor Gpr84 in zebrafish: Expression pattern and roles in immune regulation. *Dev. Comp. Immunol.* **2014**, *45*, 252–258. [CrossRef]
39. Krampert, M.; Kuenzle, S.; Thai, S.N.; Lee, N.; Iruela-Arispe, M.L.; Werner, S. ADAMTS1 proteinase is up-regulated in wounded skin and regulates migration of fibroblasts and endothelial cells. *J. Biol. Chem.* **2005**, *280*, 23844–23852. [CrossRef]
40. Martens, C.R.; Dorn, L.E.; Kenney, A.D.; Bansal, S.S.; Yount, J.S.; Accornero, F. BEX1 is a critical determinant of viral myocarditis. *PLoS Pathog.* **2022**, *18*, e1010342. [CrossRef]
41. Ledoult, E.; Jendoubi, M.; Collet, A.; Guerrier, T.; Largy, A.; Speca, S.; Vivier, S.; Bray, F.; Figeac, M.; Hachulla, E.; et al. Simple gene signature to assess murine fibroblast polarization. *Sci. Rep.* **2022**, *12*, 11748. [CrossRef]
42. Collison, A.; Hatchwell, L.; Verrills, N.; Wark, P.A.; de Siqueira, A.P.; Tooze, M.; Carpenter, H.; Don, A.S.; Morris, J.C.; Zimmermann, N.; et al. The E3 ubiquitin ligase midline 1 promotes allergen and rhinovirus-induced asthma by inhibiting protein phosphatase 2A activity. *Nat. Med.* **2013**, *19*, 232–237. [CrossRef] [PubMed]
43. Woo, K.V.; Qu, X.; Babaev, V.R.; Linton, M.F.; Guzman, R.J.; Fazio, S.; Baldwin, H.S. Tie1 attenuation reduces murine atherosclerosis in a dose-dependent and shear stress-specific manner. *J. Clin. Investig.* **2011**, *121*, 1624–1635. [CrossRef] [PubMed]

44. Fader Kaiser, C.M.; Romano, P.S.; Vanrell, M.C.; Pocognoni, C.A.; Jacob, J.; Caruso, B.; Delgui, L.R. Biogenesis and Breakdown of Lipid Droplets in Pathological Conditions. *Front. Cell Dev. Biol.* **2021**, *9*, 826248. [CrossRef]
45. Jin, Y.; McFie, P.J.; Banman, S.L.; Brandt, C.; Stone, S.J. Diacylglycerol acyltransferase-2 (DGAT2) and monoacylglycerol acyltransferase-2 (MGAT2) interact to promote triacylglycerol synthesis. *J. Biol. Chem.* **2014**, *289*, 28237–28248. [CrossRef]
46. Cheng, Y.C.; Acedera, J.D.; Li, Y.J.; Shieh, S.Y. A keratinocyte-adipocyte signaling loop is reprogrammed by loss of BTG3 to augment skin carcinogenesis. *Cell Death Differ.* **2024**, *31*, 970–982. [CrossRef]
47. Li, Y.; Chen, L.; Sottas, C.; Raul, M.C.; Patel, N.D.; Bijja, J.R.; Ahmed, S.K.; Kapelanski-Lamoureux, A.; Lazaris, A.; Metrakos, P.; et al. The mitochondrial TSPO ligand Atriol mitigates metabolic-associated steatohepatitis by downregulating CXCL1. *Metabolism* **2024**, *159*, 155942. [CrossRef]
48. Okuda, J.; Arikawa, Y.; Takeuchi, Y.; Mahmoud, M.M.; Suzaki, E.; Kataoka, K.; Suzuki, T.; Okinaka, Y.; Nakai, T. Intracellular replication of Edwardsiella tarda in murine macrophage is dependent on the type III secretion system and induces an up-regulation of anti-apoptotic NF-kappaB target genes protecting the macrophage from staurosporine-induced apoptosis. *Microb. Pathog.* **2006**, *41*, 226–240. [CrossRef]
49. Mikkelsen, R.B.; Arora, T.; Trost, K.; Dmytriyeva, O.; Jensen, S.K.; Meijnikman, A.S.; Olofsson, L.E.; Lappa, D.; Aydin, O.; Nielsen, J.; et al. Type 2 diabetes is associated with increased circulating levels of 3-hydroxydecanoate activating GPR84 and neutrophil migration. *iScience* **2022**, *25*, 105683. [CrossRef]
50. Marsango, S.; Milligan, G. Regulation of the pro-inflammatory G protein-coupled receptor GPR84. *Br. J. Pharmacol.* **2024**, *181*, 1500–1508. [CrossRef]
51. Wang, S.W.; Zhang, Q.; Lu, D.; Fang, Y.C.; Yan, X.C.; Chen, J.; Xia, Z.K.; Yuan, Q.T.; Chen, L.H.; Zhang, Y.M.; et al. GPR84 regulates pulmonary inflammation by modulating neutrophil functions. *Acta Pharmacol. Sin.* **2023**, *44*, 1665–1675. [CrossRef]
52. Ohue-Kitano, R.; Nonaka, H.; Nishida, A.; Masujima, Y.; Takahashi, D.; Ikeda, T.; Uwamizu, A.; Tanaka, M.; Kohjima, M.; Igarashi, M.; et al. Medium-chain fatty acids suppress lipotoxicity-induced hepatic fibrosis via the immunomodulating receptor GPR84. *JCI Insight* **2023**, *8*, e165469. [CrossRef] [PubMed]
53. Wang, F.; Ma, L.; Ding, Y.; He, L.; Chang, M.; Shan, Y.; Siwko, S.; Chen, G.; Liu, Y.; Jin, Y.; et al. Fatty acid sensing GPCR (GPR84) signaling safeguards cartilage homeostasis and protects against osteoarthritis. *Pharmacol. Res.* **2021**, *164*, 105406. [CrossRef] [PubMed]
54. Wei, L.; Tokizane, K.; Konishi, H.; Yu, H.R.; Kiyama, H. Agonists for G-protein-coupled receptor 84 (GPR84) alter cellular morphology and motility but do not induce pro-inflammatory responses in microglia. *J. Neuroinflamm.* **2017**, *14*, 198. [CrossRef] [PubMed]
55. Russell, D.G.; Huang, L.; VanderVen, B.C. Immunometabolism at the interface between macrophages and pathogens. *Nat. Rev. Immunol.* **2019**, *19*, 291–304. [CrossRef]
56. Guerrini, V.; Gennaro, M.L. Foam Cells: One Size Doesn't Fit All. *Trends Immunol.* **2019**, *40*, 1163–1179. [CrossRef]
57. Guerrini, V.; Prideaux, B.; Blanc, L.; Bruiners, N.; Arrigucci, R.; Singh, S.; Ho-Liang, H.P.; Salamon, H.; Chen, P.Y.; Lakehal, K.; et al. Storage lipid studies in tuberculosis reveal that foam cell biogenesis is disease-specific. *PLoS Pathog.* **2018**, *14*, e1007223. [CrossRef]
58. Ouimet, M.; Koster, S.; Sakowski, E.; Ramkhelawon, B.; van Solingen, C.; Oldebeken, S.; Karunakaran, D.; Portal-Celhay, C.; Sheedy, F.J.; Ray, T.D.; et al. Mycobacterium tuberculosis induces the miR-33 locus to reprogram autophagy and host lipid metabolism. *Nat. Immunol.* **2016**, *17*, 677–686. [CrossRef]
59. Wang, M.; Zhang, X.; Zhang, S.; Liu, Z. Zebrafish fatty acids receptor Gpr84 enhances macrophage phagocytosis. *Fish. Shellfish. Immunol.* **2019**, *84*, 1098–1099. [CrossRef]
60. Li, C.; Wang, J.; Xu, J.F.; Pi, J.; Zheng, B. Roles of HIF-1alpha signaling in Mycobacterium tuberculosis infection: New targets for anti-TB therapeutics? *Biochem. Biophys. Res. Commun.* **2024**, *711*, 149920. [CrossRef]

microorganisms

MDPI

Article

Structural Characterization of *Mycobacterium tuberculosis* Encapsulin in Complex with Dye-Decolorizing Peroxide

Bonnie J. Cuthbert [1,*], Xiaorui Chen [1], Kalistyn Burley [2], Gaëlle Batot [1], Heidi Contreras [1], Shandee Dixon [1] and Celia W. Goulding [1,2,*]

[1] Department of Molecular Biology and Biochemistry, University of California Irvine, Irvine, CA 92697, USA
[2] Department of Pharmaceutical Sciences, University of California Irvine, Irvine, CA 92697, USA
* Correspondence: bjcuthbe@uci.edu (B.J.C.); celia.goulding@uci.edu (C.W.G.)

Abstract: *Mycobacterium tuberculosis* (Mtb) is the causative agent of tuberculosis, the world's deadliest infectious disease. Mtb uses a variety of mechanisms to evade the human host's defenses and survive intracellularly. Mtb's oxidative stress response enables Mtb to survive within activated macrophages, an environment with reactive oxygen species and low pH. Dye-decolorizing peroxidase (DyP), an enzyme involved in Mtb's oxidative stress response, is encapsulated in a nanocompartment, encapsulin (Enc), and is important for Mtb's survival in macrophages. Encs are homologs of viral capsids and encapsulate cargo proteins of diverse function, including those involved in iron storage and stress responses. DyP contains a targeting peptide (TP) at its C-terminus that recognizes and binds to the interior of the Enc nanocompartment. Here, we present the crystal structure of the Mtb-Enc•DyP complex and compare it to cryogenic-electron microscopy (cryo-EM) Mtb-Enc structures. Investigation into the canonical pores formed at symmetrical interfaces reveals that the five-fold pore for the Mtb-Enc crystal structure is strikingly different from that observed in cryo-EM structures. We also observe DyP-TP electron density within the Mtb-Enc shell. Finally, investigation into crystallographic small-molecule binding sites gives insight into potential novel avenues by which substrates could enter Mtb-Enc to react with Mtb-DyP.

Keywords: *Mycobacterium tuberculosis*/pathogenicity; *Mycobacterium tuberculosis*/enzymology; bacterial proteins; crystallography; X-ray; peroxidase

1. Introduction

Mycobacterium tuberculosis (Mtb), the causative agent of tuberculosis (TB), is the deadliest infectious killer of humans. In 2023, TB resulted in an estimated 1.3 million deaths and 10.6 million new infections [1]. While TB is treatable, the currently used drug regimens require 4–5 antibiotics, are long in duration, and have numerous side effects [2]. Due to these issues, treatment noncompliance is common, fueling the emergence of multi-drug and extensively drug-resistant Mtb strains [2]. The discovery of novel anti-TB drug targets is an important step in the development of desperately needed new anti-TB therapeutics [3,4]. Deciphering how Mtb interacts with and evades its host is one approach to revealing novel drug targets.

Mtb encapsulin (Enc) has been implicated in the Mtb oxidative stress response, which is critical for Mtb's survival in the host [5,6]. Enc nanocompartments have also been implicated in a number of metabolic pathways in other bacteria, including iron mineralization and storage [7–12], anaerobic ammonium oxidation [13], and sulfur metabolism [14–16], in addition to the oxidative stress response [5,6,17,18]. Enc nanocompartments self-assemble to form a protein shell with icosahedral symmetry. The Enc protein is a homolog of a single subunit viral capsid protein and adopts a HK97 (bacteriophage Hong Kong 97)-like fold [19]. Enc nanocompartments are formed from 60 (Triangulation (T) number = 1 [7,9,11,12,17–23], 180 (T = 3, [7,10,24,25]), or 240 (T = 4, [8,26]) subunits, resulting in protein shells from 21 to 42 nm in diameter [27]. Each Enc has a dedicated protein cargo encapsulated within the Enc shell, where the cargo protein dictates the function of the complex.

To date, a number of different cargo proteins have been identified, including dye-decolorizing peroxidase (DyP), ferritin-like protein (FLP), iron-mineralizing Enc-associated firmicute (IMEF), hemerythrin and rubrerythrin [8,13,16,19,28]. At the N- or C-terminus of the cargo protein there is a targeting domain or targeting peptide (TP) which is between 10 to 40 residues in length and is required for cargo loading [16,19,27]. Cargo loading is generally believed to rely on efficient coexpression and cotranslation of the cargo and encapsulin proteins, where the TP localizes its cargo to the interior of the Enc shell as the nanocompartment assembles [27].

Enc systems have remarkable promise for biotechnology and for drug design and delivery [29,30]. Several characteristics make Enc uniquely attractive for these purposes: (1) the simplicity of the system and potential for genetic engineering, (2) Enc systems can be utilized to encapsulates highly diverse cargo, and (3) the system self-assembles in both prokaryotic and eukaryotic cells [29,30]. Ultimately, Enc can be engineered to deliver non-native enzymes to specific targets. Thus, furthering our understanding of these systems could empower the design of therapeutics.

In Mtb, the operon encoding Enc (Rv0798c) also encodes for DyP (Rv0799c) [5], with the stop codon for Rv0799c overlapping the start codon for Rv0798c. DyP is a heme-containing enzyme that oxidizes and degrades a wide range of synthetic dyes and, importantly, reduces hydrogen peroxide (H_2O_2) to water [5]. It has been shown that Mtb-DyP is a hexamer [6], where the C-terminus of Mtb-DyP contains the TP sequence that targets Mtb-DyP to the interior of the Mtb-Enc 60-mer shell [5].

Mtb-Enc•DyP is critical for resisting oxidative stress at low pH, as a Mtb *enc-dyp* deletion strain (MtbΔ*enc-dyp*) exhibits diminished survival at pH 4.5 in the presence of H_2O_2 [6]. Mtb requires the expression of both Enc and DyP for full protection against oxidative stress [6], allowing for Mtb's survival in human macrophages. Notably, MtbΔ*enc-dyp* also shows increased susceptibility to the antibiotic pyrazinamide (PZA) [6], indicating that Mtb-Enc may be a good combination drug target. Despite the clear biological importance of the Mtb-Enc•DyP complex, the biologically relevant substrate of Mtb-DyP has not yet been identified nor has its point of entry into the nanocompartment nor its mechanism of delivery to Mtb-DyP. However, as discussed above, Enc nanocompartments have vast promise for therapeutics and drug delivery, and thus understanding Mtb-Enc•DyP could empower novel mechanisms for therapeutic delivery to Mtb.

Here, we have solved the crystallographic structure of the Mtb-Enc•DyP complex to 3.15 Å resolution. A comparison of the Mtb-Enc crystal structure (PDB ID 9BKX) with previously determined Mtb-Enc cryogenic electron microscopy (cryo-EM) structures (PDB IDs 7PHM, 7P1T, 8IKA, 8PYS) reveals dramatic differences in the pores formed at and around the five-fold symmetry point. While DyP was cocrystallized with Enc, there is only observable electron density for Mtb-DyP-TP. In addition to Mtb-DyP-TP, we also observed density across the Mtb-Enc shell for glycerol, polyethylene glycol (PEG), and nickel ions; small molecules that were introduced to the complex during purification and crystallization. Notably, the observed symmetric pores with bound solvent molecules that traverse the shell may indicate channels by which Mtb-DyP substrate/product(s) could enter or exit the Mtb-Enc interior.

2. Materials and Methods

Mtb-Enc$_{\mathrm{His}}$ and Mtb-DyP were coexpressed and copurified in BL21 Gold (DE3) cells (Agilent, Santa Clara, CA, USA) as described previously [5]; however, neither the catalytic activity nor the heme content was determined for the crystallized complex. Purified Mtb-Enc•DyP was concentrated to ~11 mg/mL and screened against 600 sparse matrix crystallization conditions using a Mosquito nanoliter dispensing robot (SPT Labtech, Covina, CA, USA) and hanging-drop vapor diffusion techniques. Initial crystals were grown in

Qiagen PEGs Suite condition 24: 0.1 M TRIS-HCl pH 8.5, 25% PEG 2000 MME (Germantown, MD, USA). Crystals were further optimized using the Hampton Research additive screen (Aliso Viejo, CA, USA) and crystallization was aided by 3% Trimethlyamine *N*-oxide (TMN). Diffraction data from a single, diffracting crystal grown in 0.1 M TMN, 0.1 M Tris-HCl pH 8.5, and 20% PEG MME 2000 were collected at Stanford Synchrotron Radiation Laboratory (SSRL) beamline 7-1. No cryoprotectant was used.

Diffraction data were processed in iMosflm 7.2.2 to 3.15 Å resolution (Table 1) [31]. Phases were provided by an Enc structure from *Thermatoga maritima* (PDB ID 3DKT, [19]) and solved by molecular replacement (MR) in Phaser (PHENIX 1.9-1692) [32]. The initial model was improved by PHENIX 1.21-5207 AutoBuild [33]. Reiterative rounds of manual refinement in coot (0.8.9.1-1.10.08) and phenix.refine (PHENIX 1.21-5207) resulted in a final R_{work}/R_{free} of 20.2/23.3 [34,35]. Electron density maps were produced in Polder (PHENIX 1.21-5207) (Figure S1) [36].

Table 1. Data collection and refinement statistics for Mtb-Enc●DyP crystal structure.

Wavelength of collection	1 Å
Data collection	SSRL 7-1
Space group	P 21 3
Cell dimensions	
a, b, c (Å)	313.5, 313.5, 313.5
α, β, γ (°)	90, 90, 90
Resolution (Å)	54.56–3.15 (3.20–3.15) [1]
R_{merge} [2]	0.284 (0.887)
$I/\sigma I$	7.4 (1.4)
Completeness (%)	99.4 (99.8)
Redundancy	4.5 (4.5)
Refinement	
Resolution (Å)	49.0–3.15 (3.26–3.15)
Total reflections	790,230 (38,895)
Unique reflections	174,711 (8661)
R_{work}/R_{free} [3]	20.2/23.3 (28.2/32.8)
Ramachandran favored (%)	96.8
Ramachandran outliers (%)	0.2
Enc subunits in ASU	20
DyP peptides in ASU	9
No. atoms	42,837
Protein	41,266
Ligands	1179
Water	392
B-factors (Å^2)	
Protein	41.9
Ligands	61.3
Water	26.3
Root mean square deviations	
Bond lengths (Å)	0.003
Bond angles (°)	0.6
PDB ID	9BKX

[1] Values within parentheses refer to the highest resolution shell; [2] $R_{merge} = \sum\sum|I_{hkl} - I_{hkl}(j)|/\sum I_{hkl}$, where $I_{hkl}(j)$ is observed intensity and I_{hkl} is the final average value of intensity. [3] $R_{work} = \sum||F_{obs}| - |F_{calc}||/\sum|F_{obs}|$ and $R_{free} = \sum||F_{obs}| - |F_{calc}||/\sum|F_{obs}|$, where all reflections belong to a test set of 5% data randomly selected in Phenix 1.21-5207.

3. Results and Discussion

3.1. Crystallographic Structure of Mtb-Enc in Complex with DyP

Despite several available cryo-EM structures of Mtb-Enc alone and in complex with DyP, many questions remain regarding the interactions between the two proteins and the Mtb-Enc●DyP system more generally. To address some of these questions, Mtb-Enc was coexpressed and copurified with Mtb-DyP and the Mtb-Enc●DyP complex was crystallized.

The crystal structure of the Mtb-Enc•DyP complex was solved by MR to 3.15 Å resolution and refined to a final R_{work}/R_{free} of 20.2/23.3 (Table 1).

The resulting structure of Mtb-Enc•DyP (PDB ID 9BKX) contains 20 Mtb-Enc subunits in the asymmetric unit (ASU) (Figure S1A). Application of crystallographic symmetry generated an intact 60-subunit capsule with T1 icosahedral symmetry (Figure 1A). The Mtb-Enc subunit adopts the HK97 phage-like fold consisting of the canonical axial domain (A-domain), peripheral domain (P-domain), and extended loop (E-loop) (Figure 1B). A structural homology search using the Dali server [37] unsurprisingly yielded mycobacteria Enc structures as the top closest structural homologs to Mtb-Enc (Table S1). These included *Mycobacterium hassiacum* (PDB ID 6I9G, 0.4 Å root mean square deviation (rmsd)) and *Mycobacterium smegmatis* (Msm; PDB ID 7BOJ, 0.9 Å rmsd) Enc•DyP structures as the closest matches, both of which have upwards of 80% amino acid sequence similarity to Mtb-Enc, along with the cryo-EM Mtb-Enc structures (PDB IDs 7PHM, 8IKA, and 8PYS, and lastly 7P1T, which was solved in situ and will not be discussed due to unknown cargo, with 0.8–0.9 Å rmsd) (Table S1). The closest non-mycobacteria Mtb-Enc structural homologs were an Enc•DyP complex and apo-Enc from *Klebsiella pneumoniae* (Kpn; PDB ID 8U51 and 8U50, 0.9 Å rmsd) and apo-Enc from *Brevibacterium linens* (PDB ID 7BCV, 1.0 Å rmsd) (Table S1). Notably, the diameters of the mycobacteria and Kpn Enc structures did not vary drastically between DyP-loaded and unloaded structures, in contrast to the biophysical study of *Rhodococcus jostii* Enc [38].

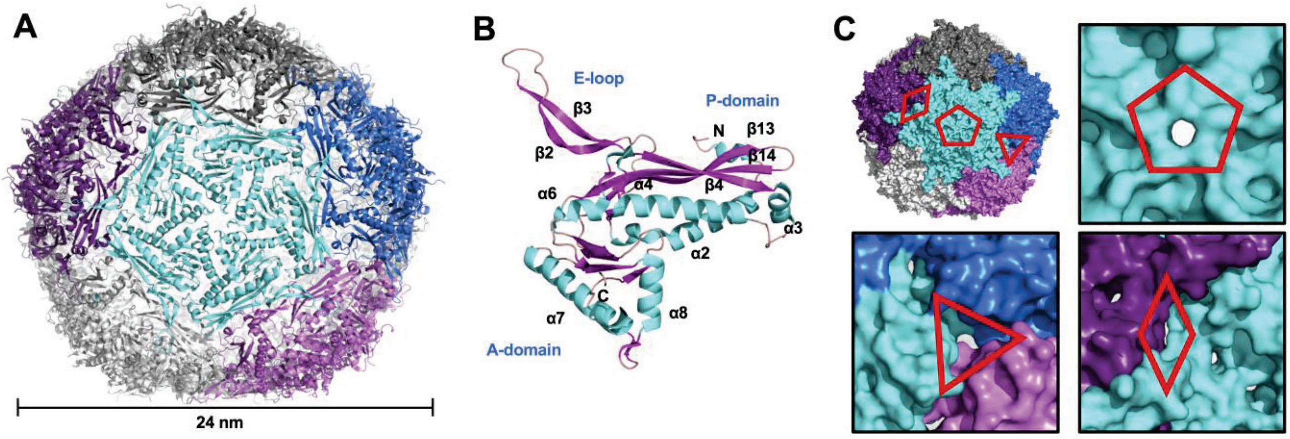

Figure 1. Crystallographic structure of Mtb-Enc•DyP. (**A**) The encapsulin shell generated by crystallographic symmetry is shown in cartoon representation and colored to highlight the five-fold axis. The nanocompartment has a diameter of ~24 nm as measured with Draw Protein Dimensions script [39]. (**B**) Structure of a single subunit of Mtb-Enc in cartoon representation colored by secondary structure: α-helices are in cyan, β-sheets in pink, and loops are wheat-colored. A- and P-domains, and E-loop are labelled, as are N- and C-termini and secondary structure elements. (**C**) Pores formed by two-fold, three-fold, and five-fold symmetry in the Mtb-Enc shell. The molecular surface of the protein is colored as in A. The two-fold, three-fold, and five-fold pores are indicated by diamond, triangle and pentamer symbols, respectively. A closer view of each pore is provided. Figures generated in PyMOL [39].

While the compact domain of Mtb-DyP (residues 1-314 based on the AlphaFold Mtb-DyP predicted structure [40]) lacks a corresponding electron density in the interior of the Mtb-Enc shell and cannot be modeled, the electron density for Mtb-DyP-TP was observed (Figure S1C). In the ASU, nine DyP-TPs were modeled (Figure S1). These peptides were bound to the interior of subunits D, G, H, I, P, Q, R, S, and T, and are referred to as d, g, h, i, p, q, r, s, and t, respectively. As is the case for other characterized Enc•DyP complexes [17–19], only residues near the conserved TP sequence could be modeled. Overall, the Mtb-DyP-TPs had electron density sufficient to build nine residues on average; however, a range of 6–12 residues were modeled for the Mtb-DyP-TPs (Figure S1D). Natively loaded DyP in the Enc shell generally results in one or two DyP hexamers per icosahedral unit [17–19,22]; thus, the nine bound DyP-TP per 20 Enc subunits are not biologically relevant. Instead, we are likely observing an averaging of DyP-TP sites across the entire unit cell. Notably, the *Thermatoga maritima* Enc●FLP crystal structure (PDB ID 3DKT) has a FLP-TP modeled at every Enc subunit in the ASU [19].

In addition to the Mtb-DyP-TPs, the Mtb-Enc●DyP structure displayed excess electron density that we modeled with molecules from the purification and crystallization process: glycerol, nickel (Ni^{2+}) ions, and PEG molecules (Figure S1A). Ni^{2+} ions were modeled when waters did not sufficiently fulfill the electron density. When the 20 subunits are superimposed, several locations with a high occurrence of small-molecule binding become apparent (Figure S1B). Notably, one of these locations occurs near the N-terminal region of the modeled DyP-TP (Figure S1E). The proximity of these molecules to bound DyP-TP indicates that these small molecules may be fulfilling poorly resolved electron density for DyP interacting with the interior Enc shell. Notably, a few other small-molecule "clustering" locations extend into and sometimes traverse the Enc shell (Figure S1A,B) and could represent solvent or ligand channels in Mtb-Enc.

3.2. Variability of the Five-Fold Pore Across Species

The Enc icosahedral structure has locations at the Enc subunit interfaces with five-fold, three-fold, and two-fold symmetry (Figure 1), and at these interfaces, we observe five-fold, three-fold, and two-fold pores, respectively (Figure 1C). While investigating these pores in the Mtb-Enc●DyP structure (PDB ID 9BKX), we found that the three-fold and two-fold pores were minimally open to solvent and that the five-fold pore is only slightly open (Figure 1C). In contrast, the five-fold pores in cryo-EM structures of Mtb-Enc (PDB IDs 7PHM, 8IKA, and 8PYS) are significantly more open (Figure 2A).

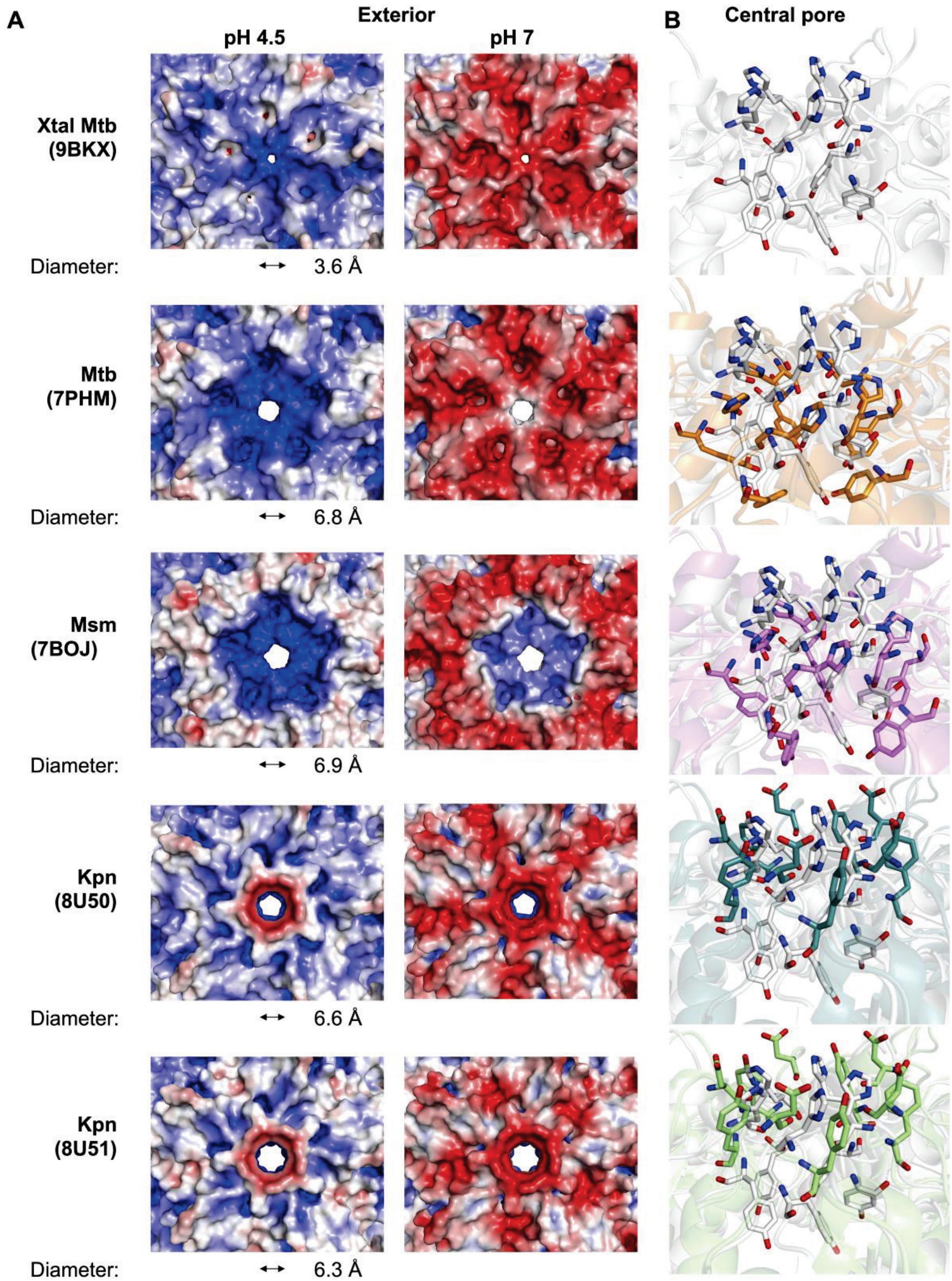

Figure 2. Five-fold major pore and surrounding exterior surface of Mtb-Enc shell. (**A**) The electrostatic exterior surfaces of the five-fold point of symmetry at pH 4.5 and pH 7.5, generated by pdb2qr and APBS [41,42]. Surfaces are colored according to charge, ranging from red (negatively charged) to blue (positively charged). Pore diameter determined by CAVER [43]. (**B**) Stick representation of the charged residues that line the central pore as viewed from the exterior. For comparison with cryo-EM structures, the crystal structure is shown in white.

We further investigated these features using MOLE (v. online) [44] and CAVER (v. 3.0 PyMOL plugin) [43], tools that allow for the characterization of channels, tunnels, and pores in macromolecular structures. Specifically, we compared the smallest diameter or bottleneck, hydropathy, and polarity of various pores in the different Enc structures. We used CAVER to determine the smallest diameter of each Enc pore [43] and found that Mtb-Enc structures solved without DyP cargo (PDB ID 7PHM and 8IKA) have bottlenecks in the pore with a diameter of 6.8 and 8.5 Å, respectively (Figure 2A). The Mtb-Enc structures solved with DyP cargo (PDB ID 9BKX and 8PYS) have bottleneck diameters of 3.6 Å and 7.3 Å, respectively, while the Msm-Enc●DyP structure (PDB ID 7BOJ) has a bottleneck 6.9 Å in diameter (Figure 2A). Interestingly, the *Haliangium ochraceum* Enc has been shown to adopt both closed and open five-fold pores in the presence of its native cargo, ferritin [11], and apo-Enc from *Acidipropionibacterium acidipropionici* Enc can also adopt both open and closed five-fold pore conformations [26]. For *H. ochraceum* Enc●ferritin, the five-fold pore expands from a closed conformation diameter of 5 Å to the open conformation diameter of 15 Å [11], and for *A. acidipropionici* Enc, the closed 5 Å diameter conformation opens to 20 Å in diameter [26]. While the five-fold pore of mycobacterial Enc has been captured in a variety of conformations, we do not know if mycobacterial Enc opens to a similar extent to *H. ochraceum* Enc●ferritin or apo *A. acidipropionici* Enc. Notably, the crystal structure of Mtb-Enc●DyP described here has the smallest mycobacterial five-fold pore described to date at 3.6 A (Figure 2A).

When investigating the five-fold pore, we also found that there are only two polar residues that face into the pore: His187 and Tyr189 (Figures 2B and S2). Strikingly, there is little variation in the position of these residues in the three cryo-EM Mtb-Enc structures (PDB IDs: 7PHM, 8IKA, and 8PYS). However, in our crystal structure we found a dramatic difference in the loop bearing these residues (Figure S3B). In the cryo-EM structures, His187 and Tyr189 are stacked on top of each other, symmetrically presenting His187-$N_\varepsilon 2$ and Tyr189-OH into the pore (Figure 2B). In the crystal structure, the C_α of His187 is translated ~5–6 Å upwards, resulting in the orientation of its carbonyl oxygen directly into the pore, and Tyr189 is angled ~45–50° along the pore and translated such that the hydroxyl group is ~6–7 Å away from its cryo-EM position. The result is a significant increase in polarity around the pore (25.5 vs. 3.9–18.6 as described by the Zimmerman scale, where the most polar amino acids have the highest value) for the crystal structure relative to the cryo-EM structures [44].

Recently, structures of Kpn-Enc were solved with and without non-native DyP-TP cargo (PDB IDs 8U50 and 8U51 [17]). As mentioned above, these structures represent some of the closest structural homologs of the Mtb-Enc●DyP crystal structure. When investigating the Kpn-Enc five-fold pores, we focused on the positions of their five-fold pore inward-facing polar residues, Asp187 and Tyr189 (Figures 2B and S2). The sidechains of Asp187 and Tyr189 are both directed up and out of the pore, similar to His187 from the Mtb-Enc crystal structure (Figure 2B). Thus, it appears the Mtb-Enc●DyP crystal structure has captured an intermediary state in between the cryo-EM structures of Mtb- and Kpn-Enc. It is likely that the five-fold pore can sample these three conformations in both species depending on the environment.

Notably, the positions of the two polar residues appear to be independent of cargo protein internalization, as we note similar positions for DyP-bound and apo cryo-EM Enc structures from Mtb and Kpn. Interestingly, MOLE analysis [44] revealed that the Kpn-Enc five-fold pore is dramatically less polar (2.7–2.8) than the Mtb five-fold pores (3.9–25.5), likely due to the orientation of Asp187 and Tyr189, which point away from the center of the five-fold pore in the Kpn-Enc structure. The structures of Kpn-Enc also show a change in the bottleneck diameter, from 6.6 Å to 6.3 Å, with non-native DyP-TP bound (Figure 2A) [43].

To date, the native substrate(s) for DyP-type Enc nanocompartments has not been identified, and questions remain about how DyP substrate(s) is delivered. Previous experiments have shown that the Enc shell is permeable to specific ligands such as H_2O_2, 2,2′-azino-bis(3-ethylbenzothiazoline-6-sulfonic acid) (ABTS), 7,8-dihydroneopterin, and ferrous ammonium sulfate, but is impermeable to guaiacol [5]. It is intriguing that the large molecule, ABTS (515 g/mol and 9 × 4 Å), can enter the nanocompartment, but guaiacol (124 g/mol and 6 × 2 Å) cannot. Neither ABTS nor guaiacol could fit through the five-fold pore in any of the Mtb-, Msm- or Kpn-Enc structures, but could easily traverse the open five-fold pores of *H. ochraceum* or *A. acidipropionici* Enc discussed above [11,26]. One potential reason behind the inability of guaiacol to enter Enc is the presence of a greasy surface on its central phenol ring that has no polar groups. In contrast, both ABTS and 7,8-dihydroneopterin are well decorated with hydrophilic chemical groups. Thus, it is likely that the native substrate will present a more polar surface than guaiacol, but also that the pore responsible for substrate entry has not been captured in an open state in any of the Mtb-Enc structures.

3.3. Minor Pores Surrounding the Five-Fold Central Pore May Allow Small Molecules to Enter Enc

Others have previously noted the presence of small pores on the surface of Enc beyond the pores formed along symmetry axes [22]. Indeed, while investigating the surface of the crystal structure of Mtb-Enc●DyP, we found small pores at numerous places across the surface of the nanocompartment. For example, near the three-fold and two-fold pores, small pores are present along the three-fold symmetry axis or internal to individual subunits at the two-fold axis (Figure 1C). Further, when investigating areas where small molecules from the purification buffer or crystallographic condition colocalize, we noted intriguing small pores formed at the interface of neighboring subunits along the five-fold symmetry axis, which will be referred to as five-fold minor pores, while the pore formed at the five-fold symmetry axis will be referred to as the five-fold major pore. Notably, all five minor pores surrounding each five-fold major pore in the ASU are occupied by solvent molecules (Figure 3A).

The five-fold minor pores in the Mtb crystal structure are formed by a vast array of residues at the interface between two subunits. Residues that are involved in every pore are Glu18, Leu21, Glu22, Arg25, Lys97, Asp98, Ser99, Asp100, Trp101, Gly220, Tyr255, Thr256, Ala257, and Glu258 (Figures 3B–D and S2). In addition to these residues, several pores also comprise Glu102, Lys105, and Ser136. The resulting pore has, on average, a bottleneck diameter of 3.4 ± 0.8 Å, with −1.8 ± 0.4 hydropathy and 26.6 ± 4.1 polarity (Table 2) [44]. DyP has peroxidase activity, converting H_2O_2 to water, when it degrades dye-colorizing-like substrates. H_2O_2 has a mean diameter of 2.5–2.8 Å and is able to traverse aquaporin through a pore with a diameter of 3 Å [45]. This suggests that these five-fold minor pores would allow for the passage of H_2O_2 through Enc to its cargo protein, DyP.

Table 2. Characteristic measurements for the five-fold minor pore—bottleneck diameter, hydropathy, and polarity—as calculated by MOLE for several Enc structures [44].

Structure	PDB ID	Bottleneck Diameter (Å)	Hydropathy [46]	Polarity [47]
Mtb-Enc with DyP	9BKX	3.4 ± 0.8	−1.8 ± 0.4	26.6 ± 4.1
Mtb-Enc with DyP	8PYS	2.8 ± 0.3	−2.3 ± 0.3	30.5 ± 2.9
Mtb-Enc	7PHM	3.4 ± 0.6	−2.2 ± 0.3	29.2 ± 3.9
Mtb-Enc	8IKA	3.5 ± 0.7	−0.6 ± 1.0	15.7 ± 11.8
Msm-Enc with DyP	7BOJ	2.2 ± 0	−0.7 ± 0.0	14.5 ± 0.0
Kpn-Enc	8U50	4.0 ± 0.8	−2.5 ± 0.9	20.0 ± 5.7
Kpn-Enc with SUMO-DyP-TP	8U51	4.0 ± 1.4	−2.3 ± 1.2	14.8 ± 1.5

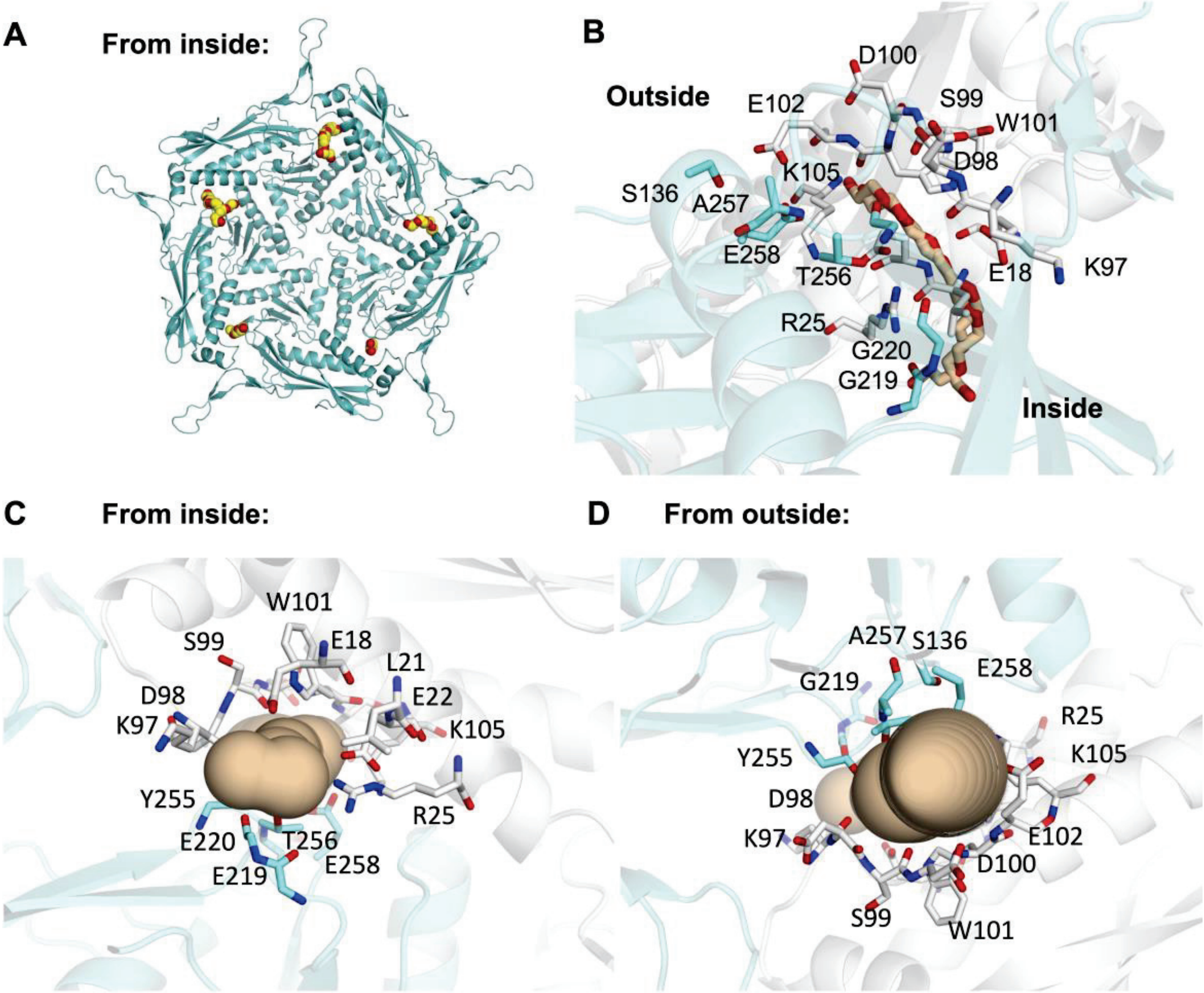

Figure 3. The five-fold minor pore is formed between Mtb-Enc subunits along the five-fold symmetry axis. (**A**) Mtb-Enc is shown as a cyan cartoon, and ligand occupying the minor pores are shown in sphere representation with yellow carbon and red oxygen atoms. (**B**–**D**) The minor pore at the interface of the C (cyan) and F (white) subunits. Protein is shown in cartoon and residues that line the pore are shown as sticks. The PEG molecule occupying the pore is shown as stick representation with wheat-colored carbons in (**B**), while a depiction of the pore generated in MOLE is shown in (**C**,**D**). The pore is viewed from the side in (**B**), from the interior in (**C**), and from the exterior in (**D**).

Indeed, five-fold minor pores are present in each Mtb-, Msm-, and Kpn-Enc structure (Figure 4, Table 2). In each, we see similar features in terms of diameter, hydropathy, and polarity, indicating these five-fold minor pores could also accommodate the passage of H_2O_2. Further, the majority of residues that line the minor five-fold pores are conserved across species; these include Glu22, Arg25, Asp98, Ser99, Asp100, Trp101, Gly220, Thr256, and Glu258 (Figure S2).

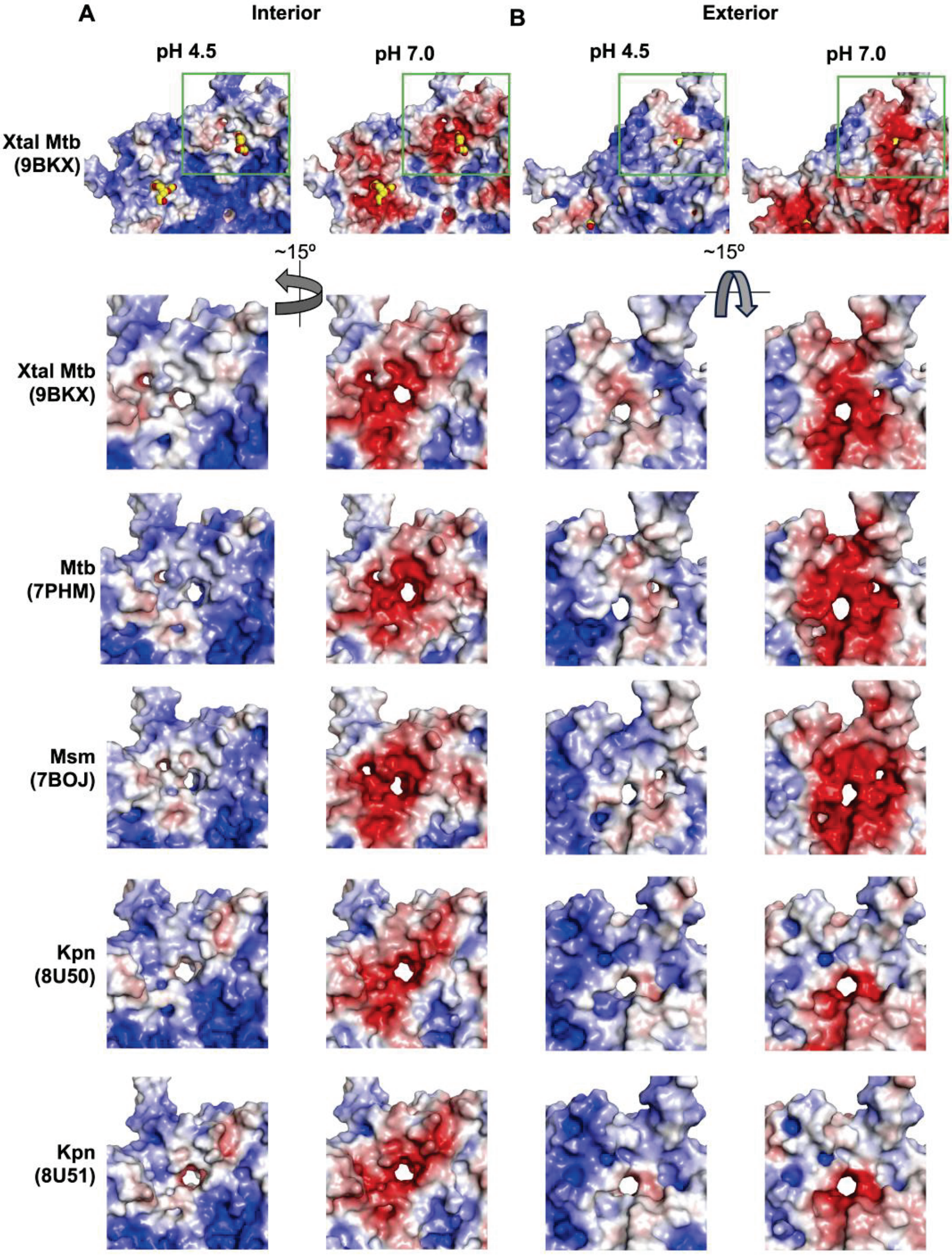

Figure 4. The five-fold minor pores across Enc structures. Shown here is the interior (**A**) and exterior (**B**) electrostatic surface of various Mtb, Msm, and Kpn cryo-EM structures in addition to the Mtb crystal structure at the five-fold minor pores. Notably, in the crystal structure the minor pores are occupied by small molecules (shown as spheres with yellow carbons). The green inset box indicates the region depicted below for comparison with the other structures. Surfaces are colored as in Figure 2A.

3.4. Biologically Relevant Electrostatic Surfaces Show Differences at the Five-Fold Major Pore Across Species

Previous discussions of the molecular surface of Enc predominately highlight surface electrostatics at neutral pH [7,8,15–20,24]. However, studies have shown that DyP is most active at low pH [48–50] and Mtb-Enc•DyP is part of the oxidative stress response and is also most active at low pH [5,6]. Thus, we decided to examine the electrostatic surface of Mtb-Enc at pH 4.5, which likely mimics physiological pH when Mtb encounters oxidative stress, as well as at neutral pH. Protein surfaces were modeled at pH 4.5 and 7 using PDB2PQR and the electrostatic surface was calculated in APBS [41,42].

When comparing mycobacterial Enc●DyP nanocompartments at pH 4.5 and pH 7, we observe an overall change around the five-fold major pore (Figures 2A and S3A). At pH 4.5, the exterior surface of the pore is positively charged for all available mycobacterial structures. Similarly, the interior surface of the pore is positively charged for the majority of structures, excluding the crystal structure, which has a neutral to slight negatively charged ring at the interior of the pore (Figure S3A). At pH 7, however, the exterior surface of the pore varies quite widely across mycobacterial species, presenting a strongly negative charge for the crystal structure, a neutral to negative surface for the cryo-EM Mtb structure, and a positively charged surface for the Msm structure (Figure 2A). In contrast to the exterior, the interior surface of the pore in the mycobacterial structures at pH 7 is strongly negatively charged or neutral (Figure S3A). The difference in His187 and Tyr189 orientation between the crystal and cryo-EM structures described above likely explains the altered electrostatic surface charge observed for the crystallographic five-fold major pore relative to the cryo-EM pores (Figures 2 and S3A).

Interestingly, when comparing the electrostatic surfaces between mycobacterial Enc structures and Kpn-Enc, we note marked differences (Figures 2A and S3A). Strikingly, in Kpn-Enc (PDB ID 8U50/8U51), the exterior surface of the pore is strongly negative at pH 7 and negative to neutrally charged at pH 4.5, while the interior surface of the pore is positively charged at both pHs (Figure S3A). Again, the varied charges at the electrostatic surfaces are likely a reflection of the differences in loop orientation (Figure S3B) and polar residues (Kpn-Asp187 vs. Mtb-His187) at the five-fold pore (Figure 2A). The species variation in the presented charge at the five-fold major pore likely indicates differences in the types of molecules that can traverse the five-fold major pore and could indicate that a common substrate such as H_2O_2 does not utilize the five-fold major pore across bacterial species.

If we compare the electrostatic surface at the five-fold minor pores amongst a series of Enc nanocompartment structures, we find that at pH 7, the mycobacterial structures all show strong negatively charged surfaces on the exterior and interior of the shell (Figure 4). Interestingly, for Kpn-Enc structures, we see a strong negatively charged surface at the interior, but a mixture of negatively charged and neutral surfaces on the exterior of the shell. However, at pH 4.5, the five-fold minor pores are more neutral; in some cases, the surface of the five-fold minor pore displays mixed charges (e.g., PDB IDs 7PHM, 7BOJ, and 8U50) and in others it is slightly negative (e.g., PDB IDs 9BKX and 8U51). Interestingly, this difference does not follow species or sequence variation, but rather DyP loading: the mixed-charge five-fold minor pores are found in *apo* Mtb- and Kpn-Enc structures, and the slightly negative five-fold minor pores are found in DyP-loaded Mtb-, Msm-, and Kpn-Enc structures. This difference could indicate the presence of the cargo protein signaling for, or directing, the internalization of the DyP substrate (i.e., H_2O_2) through the five-fold pore.

3.5. Recognition of Mtb-DyP-TP by Mtb-Enc

As mentioned above, nine Mtb-DyP-TPs were modeled in the ASU of the Mtb-Enc●DyP structure (Figure S1). On average, Mtb-Enc stabilizes bound Mtb-DyP-TP through 2.6 H-bonds. These H-bonds typically involve the carbonyl of Mtb-Enc-Arg34 with the backbone nitrogen of Mtb-DyP-TP-Leu330 (78% occurrence), the sidechain NH_2 nitrogen of Mtb-Enc-Arg34 with the carbonyl of Mtb-DyP-TP-Ile327 or Mtb-DyP-TP-Leu330 (78%), and the carbonyl of Mtb-Enc-Val230 with the backbone nitrogen of Mtb-DyP-TP-Leu325 or Mtb-DyP-TP-Ser326 (44%) (Figures 5A and S2).

H-bond coordination of Mtb-DyP-TP involves a peptide sidechain in only one occurrence, where the terminal nitrogen of Lys331 in peptide s is coordinated by a carboxyl oxygen of Mtb-Enc-Asp202. Notably, peptide s is the only peptide where electron density of the Lys331 sidechain is observed. Thus, apart from Mtb-DyP-TP-Lys331, it seems unlikely there is much sequence-specific recognition of the DyP-TP by Mtb-Enc through polar interactions.

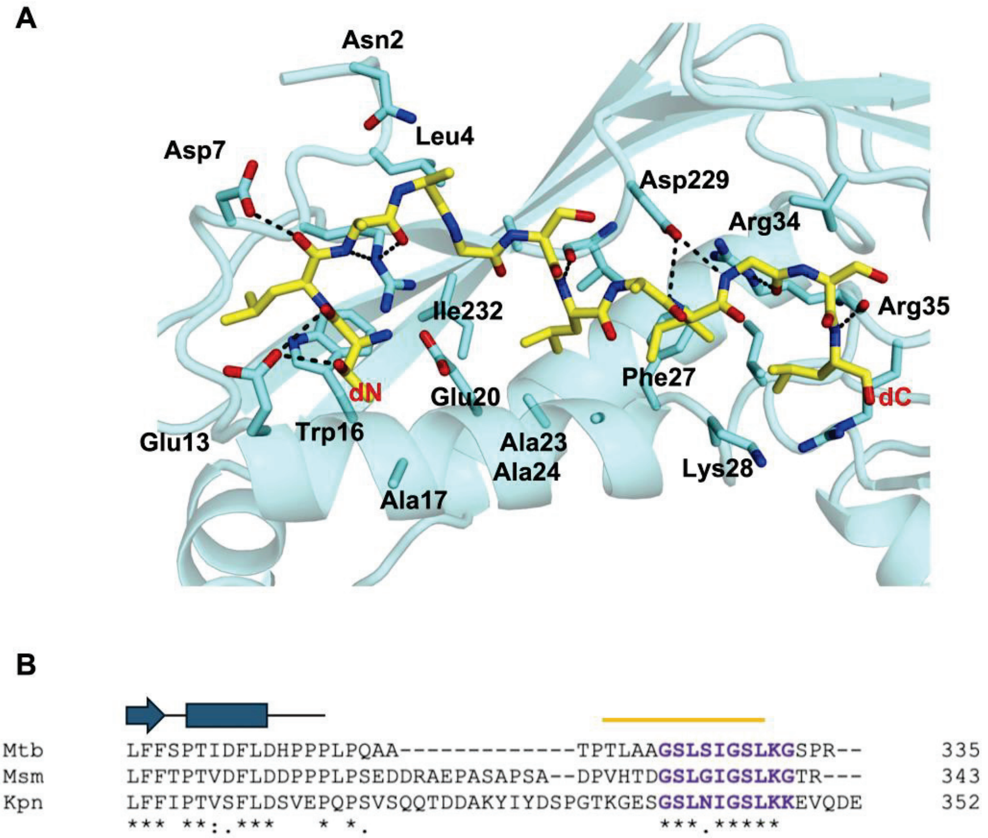

```
Mtb     LFFSPTIDFLDHPPPLPQAA-------------TPTLAAGSLSIGSLKGSPR--      335
Msm     LFFTPTVDFLDDPPPLPSEDDRAEPASAPSA--DPVHTDGSLGIGSLKGTR---      343
Kpn     LFFIPTVSFLDSVEPQPSVSQQTDDAKYIYDSPGTKGESGSLNIGSLKKEVQDE      352
        *** **:.***   * *.                     ***.*****
```

Figure 5. Enc recognition of the C-terminal targeting peptide (TP) of DyP. (**A**) Enc residues that coordinate the TP (subunit i, yellow stick) are shown. Enc (subunit I) is displayed as a cyan cartoon with residues involved in TP binding shown as sticks. H-bond contacts are highlighted as dashed black lines between Enc residues and DyP-TP. (**B**) A sequence alignment of the C-terminus of DyP for Mtb, Msm, and Kpn was generated by Clustal Omega [51]. A cartoon representation of the secondary structure elements for characterized DyP proteins is shown above the alignment, and a yellow line indicates the sequence modelled for DyP-TP-i (shown in (**A**)). Mtb-DyP is missing residues upstream of the DyP-TP when compared to DyP from other species. Symbols below the alignment indicate the degree of sequence conservation, where * denotes fully conserved residues, : strongly similar residues, and . weakly similar residues.

Mtb-Enc does, however, coordinate the Mtb-DyP-TP sequence through sidechain interactions. The terminal nitrogen atoms (NH_1/NH_2) of Mtb-Enc-Arg34 are involved in coordinating five of the nine peptides, while the N_ε atom coordinates the carbonyl of Mtb-DyP-TP-Gly328 in another two peptides (Figure 5A). A carboxyl oxygen atom of Mtb-Enc-Asp229 coordinates the backbone nitrogen of Mtb-DyP-TP-Gly328 and, as mentioned above, a carboxyl oxygen atom of Mtb-Enc-Asp202 coordinates Mtb-DyP-TP-Lys331-N_ζ.

While there are few H-bonds formed between Mtb-DyP-TP and Mtb-Enc, there is a vast network of nonbonded contacts, including hydrophobic and van der Waals interactions, ranging from 33 nonbonded contacts for peptide r to 87 for peptide i (the longest peptide modeled). Consistent nonbonded contacts are provided by Mtb-Enc Ala24, Phe27, Lys28, Ile31, Arg34, Arg35, Val39, Asp229, and Val230 (Figures 5A and S2).

Overall, the DyP-TPs bound in the Kpn- and Mtb-Enc structures align well. Specifically, Mtb-DyP-TP-g, i, p, r, s, and t all align quite closely to the Kpn-DyP-TPs (Figure S1D,E). As mentioned above, Mtb-DyP-TP-i extends past most of the peptides at its N-terminal end. A few Mtb-DyP-TPs diverge from the others in their conformation: peptides d, h and q.

Mtb-DyP-d diverges at the peptide’s C-terminus, while h and q are quite similar but diverge at their N-terminal end (Figure S1B,D). In summary, the majority of the Mtb-DyP-TPs are observed in a similar binding state to Kpn-DyP-TP; however, Mtb-DyP-TP-d, -h, and -q show alternative binding states.

The DyP-TP sequence is almost entirely conserved between Mtb-, Msm-, and Kpn-DyP, except for Mtb-DyP Ser326, which is a glycine (Gly335) in Msm, and an asparagine (Asn341) residue in Kpn (Figure 5B). A mutation analysis was carried out to test the residues required for recognition of the Kpn-DyP-TP (S^{337}GSLNIGSLKK^{347}) [17]. The results showed that the Kpn-DyP-TP bulky, hydrophobic residues (Leu340, Ile342, and Leu345), the C-terminal lysine residue (Lys346), the internal glycine residue (Gly343), and the serine residues (Ser339/Ser344 double mutant), when mutated to alanine, completely ablated binding of Kpn-DyP-TP to Kpn-Enc [17]. Notably, all these residues are conserved across Mtb-, Msm-, and Kpn-DyP (Figure 5); thus, we predict that these residues are important for DyP cargo loading in mycobacterial species as well.

Interestingly, Kpn-DyP-TP Asn341—the only nonconserved residue—is not an essential determinant of Kpn-DyP/Enc recognition, as Asn341Ala-DyP displayed only a 38% reduction in Kpn-Enc binding [17]. Mutations of Kpn-Enc residues within the Kpn-Dyp-TP recognition pocket were also evaluated [17]. It was observed that Kpn-Enc-Arg34 was essential, while Asp229 and Ile230 were important for Kpn-DyP-TP recognition. Notably, these Enc residues are conserved across species, although Kpn-Enc-Ile230 is a valine (Val230) residue in mycobacterial species, and are implicated in DyP-TP recognition in the crystal structure of Mtb-Enc●DyP (Figure S2). Thus, we would expect similar interaction impairments with the mutation of these three Enc residues in mycobacterial species.

Downstream of DyP-TP, there is no homology in the number or sequence of the final few residues (Figure 5B), suggesting that they are not important in Enc recognition. When comparing the amino acid sequence upstream of DyP-TP, there is a substantial gap in the alignment before Mtb-DyP-Thr317 (Kpn-Gly332). Here, Kpn-DyP has a string of charged and aromatic residues and Msm-DyP has a proline/alanine/serine-rich region which are absent from Mtb-DyP. Prior to this break in sequence similarity, the DyP proteins have high sequence conservation (Figure 5B). Notably, published structures of Enc-associated DyP do not extend to the C-terminal TP sequence nor do they contain the extra sequence present in Kpn- and Msm-DyP that is absent in Mtb-DyP: the Kpn-DyP structure ends at Pro315 (PDB ID 8U4Z; [17]) and Msm-DyP ends at Pro311 (PDB ID 7BOK; [18]). Thus, we do not know if sequence differences beyond the DyP compact domain will result in any differences in secondary structure. However, it is most likely that this region of DyP (downstream of Kpn-Pro315 and Msm-Pro311) is an unstructured loop. These differences in length and charge in these disparate stretches of the loop region between the DyP compact domain and the DyP-TP recognition sequence could be important for DyP/Enc interactions across species.

Interestingly, cryo-EM studies of Msm- and *B. linens* Enc with DyP cargo show localization of the DyP cargo to the Enc three-fold axis [22,52]. The authors of these papers speculate that the three-fold pore could be responsible for delivering substrate directly to DyP. It is interesting to speculate if such colocalization occurs in Mtb; however, it does not appear to as we do not see the colocalization of TP binding restricted to the three-fold Enc axis. Indeed, as the linker between the DyP compact domain and its TP is significantly shorter in Mtb (Figure 5B) than in other DyP proteins, we might hypothesize that this truncated linker prevents the tri-peptide interaction between the Enc three-fold axis and DyP-TP described for Msm and *B. linens* Enc [22,52].

4. Conclusions

Several structures of DyP-type Enc nanocompartments have been investigated to date, but many questions remain unanswered. The crystal structure of Mtb-Enc●DyP discussed herein represents the first mycobacterial structure of a native DyP-loaded compartment where DyP residues are resolved. Exactly how DyP is recognized by the nanocompartment will require further exploration. Intriguingly, the native substrate of DyP remains a mystery. Additionally, how this unknown substrate enters the Enc shell—using the five-fold major or three-fold pore, through the five-fold minor pores highlighted here, or using one of the uncharacterized pores in the surface of the shell—and how it is delivered to the DyP cargo also warrant further investigation. The crystal structure of Mtb-Enc●DyP presented here provides useful direction for these future research efforts. As Enc proteins represent attractive biotechnology systems for drug design and drug delivery [29,30], furthering our understanding of Enc proteins is important and ultimately may provide future avenues towards anti-mycobacterial therapeutics.

Supplementary Materials: The following supporting information can be downloaded at: https://www.mdpi.com/article/10.3390/microorganisms12122465/s1, Table S1: Structural homologs for Mtb-Enc subunit from Mtb-Enc●DyP using Dali; Figure S1: The crystallographic asymmetric unit (ASU) for the Mtb-Enc●DyP complex and comparison of bound Mtb-DyP-TP conformations; Figure S2: Sequence alignment for Enc proteins; Figure S3: Five-fold major pore of the Enc shell.

Author Contributions: Conceptualization, C.W.G.; methodology, B.J.C., X.C., K.B., G.B., H.C. and S.D.; validation, B.J.C.; formal analysis, B.J.C. and C.W.G.; writing and editing, B.J.C. and C.W.G.; visualization, B.J.C. and C.W.G.; supervision, C.W.G.; funding acquisition, C.W.G. All authors have read and agreed to the published version of the manuscript.

Funding: This work was supported by National Institutes of Health grants GM117930 (CWG).

Data Availability Statement: The data that support the findings of this study are openly available at the Protein Data Bank, PDB ID 9BKX.

Acknowledgments: The authors thank the Advanced Light Source at Berkeley National Laboratories and the Stanford Synchrotron Radiation Lightsource for help in data collection, Duilio Cascio and Michael Sawaya (University of California, Los Angeles) for help and discussions regarding structure determination, and Christine Hardy for critical reading of the manuscript.

Conflicts of Interest: The authors declare no conflicts of interest.

References

1. The World Health Organization. Global Tuberculosis Report 2023. Available online: https://www.who.int/teams/global-tuberculosis-programme/tb-reports/global-tuberculosis-report-2023 (accessed on 7 November 2023).
2. Rojano, B.; Caminero, J.A.; Hayek, M. Curving tuberculosis: Current trends and future needs. *Ann. Glob. Health* **2019**, *85*, 5. [CrossRef] [PubMed]
3. Gill, C.M.; Dolan, L.; Piggott, L.M.; McLaughlin, A.M. New developments in tuberculosis diagnosis and treatment. *Breathe* **2022**, *18*, 210149. [CrossRef]
4. Sharma, K.; Ahmed, F.; Sharma, T.; Grover, A.; Agarwal, M.; Grover, S. Potential Repurposed Drug Candidates for Tuberculosis Treatment: Progress and Update of Drugs Identified in over a Decade. *ACS Omega* **2023**, *8*, 17362–17380. [CrossRef]
5. Contreras, H.; Joens, M.S.; McMath, L.M.; Le, V.P.; Tullius, M.V.; Kimmey, J.M.; Bionghi, N.; Horwitz, M.A.; Fitzpatrick, J.A.J.; Goulding, C.W. Characterization of a Mycobacterium tuberculosis nanocompartment and its potential cargo proteins. *J. Biol. Chem.* **2014**, *289*, 18279–18289. [CrossRef] [PubMed]
6. Lien, K.A.; Dinshaw, K.; Nichols, R.J.; Cassidy-Amstutz, C.; Knight, M.; Singh, R.; Eltis, L.D.; Savage, D.F.; Stanley, S.A. A nanocompartment system contributes to defense against oxidative stress in mycobacterium tuberculosis. *eLife* **2021**, *10*, e74358. [CrossRef]
7. Eren, E.; Wang, B.; Winkler, D.C.; Watts, N.R.; Steven, A.C.; Wingfield, P.T. Structural characterization of the Myxococcus xanthus encapsulin and ferritin-like cargo system gives insight into its iron storage mechanism. *Structure* **2022**, *30*, 551–563.e4. [CrossRef]
8. Giessen, T.W.; Orlando, B.J.; Verdegaal, A.A.; Chambers, M.G.; Gardener, J.; Bell, D.C.; Birrane, G.; Liao, M.; Silver, P.A. Large protein organelles form a new iron sequestration system with high storage capacity. *eLife* **2019**, *8*, e46070. [CrossRef]
9. LaFrance, B.J.; Cassidy-Amstutz, C.; Nichols, R.J.; Oltrogge, L.M.; Nogales, E.; Savage, D.F. The encapsulin from *Thermotoga maritima* is a flavoprotein with a symmetry matched ferritin-like cargo protein. *Sci. Rep.* **2021**, *11*, 22810. [CrossRef]
10. McHugh, C.A.; Fontana, J.; Nemecek, D.; Cheng, N.; Aksyuk, A.A.; Heymann, J.B.; Winkler, D.C.; Lam, A.S.; Wall, J.S.; Steven, A.C.; et al. A virus capsid-like nanocompartment that stores iron and protects bacteria from oxidative stress. *EMBO J.* **2014**, *33*, 1896–1911. [CrossRef]
11. Ross, J.; McIver, Z.; Lambert, T.; Piergentili, C.; Bird, J.E.; Gallagher, K.J.; Cruickshank, F.L.; James, P.; Zarazúa-Arvizu, E.; Horsfall, L.E.; et al. Pore dynamics and asymmetric cargo loading in an encapsulin nanocompartment. *Sci. Adv.* **2022**, *8*, eabj4461. [CrossRef]

12. Wiryaman, T.; Toor, N. Cryo-EM structure of a thermostable bacterial nanocompartment. *IUCrJ* **2021**, *8*, 342–350. [CrossRef] [PubMed]
13. Giessen, T.W.; Silver, P.A. Widespread distribution of encapsulin nanocompartments reveals functional diversity. *Nat. Microbiol.* **2017**, *2*, 17029. [CrossRef] [PubMed]
14. Andreas, M.P.; Giessen, T.W. Large-scale computational discovery and analysis of virus-derived microbial nanocompartments. *Nat. Commun.* **2021**, *12*, 4748. [CrossRef] [PubMed]
15. Benisch, R.; Andreas, M.P.; Giessen, T.W. A widespread bacterial protein compartment sequesters and stores elemental sulfur. *Sci. Adv.* **2024**, *10*, eadk9345. [CrossRef] [PubMed]
16. Nichols, R.J.; Lafrance, B.; Phillips, N.R.; Radford, D.R.; Oltrogge, L.M.; Valentin-Alvarado, L.E.; Bischoff, A.J.; Nogales, E.; Savage, D.F. Discovery and characterization of a novel family of prokaryotic nanocompartments involved in sulfur metabolism. *eLife* **2021**, *10*, e59288. [CrossRef]
17. Jones, J.A.; Andreas, M.P.; Giessen, T.W. Structural basis for peroxidase encapsulation inside the encapsulin from the Gram-negative pathogen Klebsiella pneumoniae. *Nat. Commun.* **2024**, *15*, 2558. [CrossRef]
18. Tang, Y.; Mu, A.; Zhang, Y.; Zhou, S.; Wang, W.; Lai, Y.; Zhou, X.; Liu, F.; Yang, X.; Gong, H.; et al. Cryo-EM structure of Mycobacterium smegmatis DyP-loaded encapsulin. *Proc. Natl. Acad. Sci. USA* **2021**, *118*, e2025658118. [CrossRef]
19. Sutter, M.; Boehringer, D.; Gutmann, S.; Günther, S.; Prangishvili, D.; Loessner, M.J.; Stetter, K.O.; Weber-Ban, E.; Ban, N. Structural basis of enzyme encapsulation into a bacterial nanocompartment. *Nat. Struct. Mol. Biol.* **2008**, *15*, 939–947. [CrossRef]
20. Adamson, L.S.R.; Tasneem, N.; Andreas, M.P.; Close, W.; Jenner, E.N.; Szyszka, T.N.; Young, R.; Cheah, L.C.; Norman, A.; MacDermott-Opeskin, H.I.; et al. Pore structure controls stability and molecular flux in engineered protein cages. *Sci. Adv.* **2022**, *8*, eabl7346. [CrossRef]
21. Lončar, N.; Rozeboom, H.J.; Franken, L.E.; Stuart, M.C.A.; Fraaije, M.W. Structure of a robust bacterial protein cage and its application as a versatile biocatalytic platform through enzyme encapsulation. *Biochem. Biophys. Res. Commun.* **2020**, *529*, 548–553. [CrossRef] [PubMed]
22. Putri, R.M.; Allende-Ballestero, C.; Luque, D.; Klem, R.; Rousou, K.A.; Liu, A.; Traulsen, C.H.H.; Rurup, W.F.; Koay, M.S.T.; Castón, J.R.; et al. Structural Characterization of Native and Modified Encapsulins as Nanoplatforms for in Vitro Catalysis and Cellular Uptake. *ACS Nano* **2017**, *11*, 12796–12804. [CrossRef]
23. Xiong, X.; Sun, C.; Vago, F.S.; Klose, T.; Zhu, J.; Jiang, W. Cryo-EM structure of heterologous protein complex loaded thermotoga maritima encapsulin capsid. *Biomolecules* **2020**, *10*, 1342. [CrossRef] [PubMed]
24. Akita, F.; Chong, K.T.; Tanaka, H.; Yamashita, E.; Miyazaki, N.; Nakaishi, Y.; Suzuki, M.; Namba, K.; Ono, Y.; Tsukihara, T.; et al. The Crystal Structure of a Virus-like Particle from the Hyperthermophilic Archaeon Pyrococcus furiosus Provides Insight into the Evolution of Viruses. *J. Mol. Biol.* **2007**, *368*, 1469–1483. [CrossRef] [PubMed]
25. Kwon, S.; Andreas, M.P.; Giessen, T.W. Structure and heterogeneity of a highly cargo-loaded encapsulin shell. *J. Struct. Biol.* **2023**, *215*, 108022. [CrossRef]
26. Jones, J.A.; Andreas, M.P.; Giessen, T.W. Exploring the Extreme Acid Tolerance of a Dynamic Protein Nanocage. *Biomacromolecules* **2023**, *24*, 1388–1399. [CrossRef]
27. Jones, J.A.; Benisch, R.; Giessen, T.W. Encapsulin cargo loading: Progress and potential. *J. Mater. Chem. B* **2023**, *11*, 4377–4388. [CrossRef]
28. Tracey, J.C.; Coronado, M.; Giessen, T.W.; Lau, M.C.Y.; Silver, P.A.; Ward, B.B. The Discovery of Twenty-Eight New Encapsulin Sequences, Including Three in Anammox Bacteria. *Sci. Rep.* **2019**, *9*, 20122. [CrossRef]
29. Giessen, T.W. Encapsulins: Microbial nanocompartments with applications in biomedicine, nanobiotechnology and materials science. *Curr. Opin. Chem. Biol.* **2016**, *34*, 1–10. [CrossRef]
30. Quinton, A.R.; McDowell, H.B.; Hoiczyk, E. Chapter One—Encapsulins: Nanotechnology's future in a shell. In *Advances in Applied Microbiology*; Gadd, G.M., Sariaslani, S., Eds.; Academic Press: Cambridge, MA, USA, 2023; Volume 125, pp. 1–48.
31. Battye, T.G.G.; Kontogiannis, L.; Johnson, O.; Powell, H.R.; Leslie, A.G.W. iMOSFLM: A new graphical interface for diffraction-image processing with MOSFLM. *Acta Crystallogr. Sect. D Biol. Crystallogr.* **2011**, *67*, 271–281. [CrossRef] [PubMed]
32. McCoy, A.J.; Grosse-Kunstleve, R.W.; Adams, P.D.; Winn, M.D.; Storoni, L.C.; Read, R.J. Phaser crystallographic software. *J. Appl. Crystallogr.* **2007**, *40*, 658–674. [CrossRef]
33. Terwilliger, T.C.; Grosse-Kunstleve, R.W.; Afonine, P.V.; Moriarty, N.W.; Zwart, P.H.; Hung, L.W.; Read, R.J.; Adams, P.D. Iterative model building, structure refinement and density modification with the PHENIX AutoBuild wizard. *Acta Crystallogr. Sect. D Biol. Crystallogr.* **2007**, *64*, 61–69. [CrossRef] [PubMed]
34. Emsley, P.; Cowtan, K. Coot: Model-building tools for molecular graphics. *Acta Crystallogr. D Biol. Crystallogr.* **2004**, *60*, 2126–2132. [CrossRef] [PubMed]
35. Afonine, P.V.; Grosse-Kunstleve, R.W.; Echols, N.; Headd, J.J.; Moriarty, N.W.; Mustyakimov, M.; Terwilliger, T.C.; Urzhumtsev, A.; Zwart, P.H.; Adams, P.D. Towards automated crystallographic structure refinement with phenix.refine. *Acta Crystallogr. Sect. D Biol. Crystallogr.* **2012**, *68*, 352–367. [CrossRef] [PubMed]
36. Liebschner, D.; Afonine, P.V.; Moriarty, N.W.; Poon, B.K.; Sobolev, O.V.; Terwilliger, T.C.; Adams, P.D. Polder maps: Improving OMIT maps by excluding bulk solvent. *Acta Crystallogr. Sect. D Struct. Biol.* **2017**, *73*, 148–157. [CrossRef] [PubMed]
37. Holm, L.; Rosenstrom, P. Dali server: Conservation mapping in 3D. *Nucleic Acids Res.* **2010**, *38*, W545–W549. [CrossRef]

38. Rahmanpour, R.; Bugg, T.D.H. Assembly in vitro of Rhodococcus jostii RHA1 encapsulin and peroxidase DypB to form a nanocompartment. *FEBS J.* **2013**, *280*, 2097–2104. [CrossRef] [PubMed]
39. *The PyMOL Molecular Graphics System*, version 2.5; Schrödinger, LLC: New York, NY, USA, 2021.
40. Jumper, J.; Evans, R.; Pritzel, A.; Green, T.; Figurnov, M.; Ronneberger, O.; Tunyasuvunakool, K.; Bates, R.; Žídek, A.; Potapenko, A.; et al. Highly accurate protein structure prediction with AlphaFold. *Nature* **2021**, *596*, 583–589. [CrossRef]
41. Jurrus, E.; Engel, D.; Star, K.; Monson, K.; Brandi, J.; Felberg, L.E.; Brookes, D.H.; Wilson, L.; Chen, J.; Liles, K.; et al. Improvements to the APBS biomolecular solvation software suite. *Protein Sci.* **2018**, *27*, 112–128. [CrossRef]
42. Unni, S.; Huang, Y.; Hanson, R.M.; Tobias, M.; Krishnan, S.; Li, W.W.; Nielsen, J.E.; Baker, N.A. Web Servers and Services for Electrostatics Calculations with APBS and PDB2PQR SAMIR. *J. Comput. Chem.* **2011**, *32*, 1488–1491. [CrossRef]
43. Jurcik, A.; Bednar, D.; Byska, J.; Marques, S.M.; Furmanova, K.; Daniel, L.; Kokkonen, P.; Brezovsky, J.; Strnad, O.; Stourac, J.; et al. CAVER Analyst 2.0: Analysis and visualization of channels and tunnels in protein structures and molecular dynamics trajectories. *Bioinformatics* **2018**, *34*, 3586–3588. [CrossRef]
44. Pravda, L.; Sehnal, D.; Toušek, D.; Navrátilová, V.; Bazgier, V.; Berka, K.; Vařeková, R.S.; Koča, J.; Otyepka, M. MOLEonline: A web-based tool for analyzing channels, tunnels and pores (2018 update). *Nucleic Acids Res.* **2018**, *46*, W368–W373. [CrossRef]
45. Bienert, G.P.; Schjoerring, J.K.; Jahn, T.P. Membrane transport of hydrogen peroxide. *Biochim. Biophys. Acta Biomembr.* **2006**, *1758*, 994–1003. [CrossRef]
46. Cid, H.; Bunster, M.; Canales, M.; Gazitúa, F. Hydrophobicity and structural classes in proteins. *Protein Eng. Des. Sel.* **1992**, *5*, 373–375. [CrossRef]
47. Zimmerman, J.M.; Eliezer, N.; Simha, R. The characterization of amino acid sequences in proteins by statistical methods. *J. Theor. Biol.* **1968**, *21*, 170–201. [CrossRef]
48. Catucci, G.; Valetti, F.; Sadeghi, S.J.; Gilardi, G. Biochemical features of dye-decolorizing peroxidases: Current impact on lignin degradation. *Biotechnol. Appl. Biochem.* **2020**, *67*, 751–759. [CrossRef]
49. Sugano, Y.; Muramatsu, R.; Ichiyanagi, A.; Sato, T.; Shoda, M. DyP, a unique dye-decolorizing peroxidase, represents a novel heme peroxidase family: ASP171 replaces the distal histidine of classical peroxidases. *J. Biol. Chem.* **2007**, *282*, 36652–36658. [CrossRef] [PubMed]
50. Sugano, Y.; Yoshida, T. Dyp-type peroxidases: Recent advances and perspectives. *Int. J. Mol. Sci.* **2021**, *22*, 5556. [CrossRef] [PubMed]
51. Madeira, F.; Madhusoodanan, N.; Lee, J.; Eusebi, A.; Niewielska, A.; Tivey, A.R.N.; Lopez, R.; Butcher, S. The EMBL-EBI Job Dispatcher sequence analysis tools framework in 2024. *Nucleic Acids Res.* **2024**, *52*, W521–W525. [CrossRef] [PubMed]
52. Kirykowicz, A.M.; Woodward, J.D. Shotgun EM of mycobacterial protein complexes during stationary phase stress. *Curr. Res. Struct. Biol.* **2020**, *2*, 204–212. [CrossRef]

microorganisms

MDPI

Article

Performance Evaluation of Novaplex^{TM} Multiplex Real-Time PCR Assay for Detection of *Streptococcus agalactiae* Serotypes

Mallikarjun Handigund [1,2] and Jaehyeon Lee [1,2,*]

[1] Department of Laboratory Medicine, Jeonbuk National University Medical School and Hospital, Jeonju 54907, Republic of Korea; ecoarjun156@jbnu.ac.kr
[2] Research Institute of Clinical Medicine of Jeonbuk National University, Biomedical Research Institute of Jeonbuk National University Hospital, Jeonju 54907, Republic of Korea
* Correspondence: jlee@jbnu.ac.kr; Tel.: +82-63-250-2693; Fax: +82-63-250-1200

Abstract: *Streptococcus agalactiae*, or group B streptococcus (GBS), is a Gram-positive pathogen with an extended track record of colonization in the gastrointestinal and genitourinary tracts. GBS can induce disease in individuals across all age demographics, yet it predominantly triggers infections in neonates and the elderly. Identification of the serotype is vital for effective management of the disease as it provides critical information for clinicians on the cause of the disease. In this study, we evaluated the rapid, simple, and easy-to-adopt multiplex real-time PCR technique, Novaplex^{TM} (NovaPCR). A total of 131 clinical isolates of different serotypes were tested using NovaPCR. Observations revealed that 129 isolates showed the same observations as LA and conventional mPCR. NovaPCR accurately identified serotypes IV and V, which were first classified as serotype Ia in the LA test and mPCR, and the difference between the traditional (LA test and mPCR) and NovaPCR methods is only 1.52%. Accurate serotype identification is helpful for monitoring the epidemics and achieving optimal clinical outcomes, and NovaPCR showed a reliable, fast, easy-to-interpret, and cost-efficient performance in GBS serotyping.

Keywords: group B streptococcus; multiplex PCR; *Streptococcus agalactiae*; serotype; NovaPCR

1. Introduction

Streptococcus agalactiae, or group B streptococcus (GBS), is a long-familiar Gram-positive pathogen that frequently colonizes gastrointestinal and genitourinary tracts [1]. GBS can cause illness in individuals of all age groups but primarily causes infections in neonates and the elderly [2,3]. Moreover, it is an emerging infectious disease in adults with pre-existing medical conditions or immunocompromised conditions [4,5]. Hence, GBS is now considered an important pathogen among immunosuppressed individuals. Thus, it is crucial to perform screening tests to identify group B streptococcus (GBS) in pregnant women, as it poses a significant threat to both newborns and the elderly. GBS virulence ability is believed to be associated with its capsular polysaccharide. The genes in the *cps* locus determine the serotype of a GBS. Until now, 10 serotype variants that differ in their virulence patterns have been recognized. The serotypes Ia, Ib, II, III, IV, V, VI, VII, VIII, and IX are identified depending on the capsular polysaccharide [6]. Generally, these serotypes demonstrate varying prevalence, geographic distribution, and virulence. For instance, serotype III is linked to neonatal invasive diseases [7,8]. In contrast, serotype V is linked to various infections, particularly in older patients with skin and soft tissue infections [9,10]. Thus, detection and understanding of the distribution of serotypes may assist clinicians in identifying the risk factors and help them to treat patients accordingly. Furthermore, monitoring the serotype is crucial for vaccine development and clinical epidemic research. For example, immunization with capsular polysaccharide (CPS)-protein conjugates is one of the possible solutions to decrease the GBS infection, and GBS conjugate vaccines covering the majority of serotypes are at the developmental stage [11]. Notably, it is widely

Microorganisms **2024**, *12*, 2043. https://doi.org/10.3390/microorganisms12102043 https://www.mdpi.com/journal/microorganisms

recognized that serotypes can vary in their virulence characteristics, affecting the degree of the infection and the clinical outcomes [12–14]. Therefore, the identification of serotypes becomes clinically significant for clinicians for potential treatment.

Traditionally, the Lancefield precipitation test (LP test) has long been regarded as the standard method for GBS serotyping. In this method, specific antigens from the surface of GBS are extracted and allowed to react with serotype-specific antisera to detect the serotype. However, the extraction of specific antigens is a laborious process, which makes it impractical to analyze a large number of samples [15]. Also, the LP test can yield false-negative or false-positive results due to cross-reactivity or weak antigen-antibody interactions [16]. Additionally, the LP test has been rendered obsolete with the development of the latex agglutination test (LA test), flow cytometry [17], and PCR-based assay [3,18]. The flow cytometric technique uses fluorescent antibodies to identify the GBS serotypes. This method offers high sensitivity, specificity, multiplexing, and quantitative analysis. However, it requires technical expertise and involves complex sample preparation procedures. In contrast, the LA test is a rapid and less expensive technique, but it is laborious when analyzing a large number of samples. Thus, the high cost of consumables and equipment and the need for specialized technicians make both methods less applicable for large-scale testing. Therefore, rapid, economical, and precision-oriented methods are essential for the identification of GBS serotypes. Further, PCR-based techniques look promising, as they offer rapid results and adaptability for detecting multiple or emerging serotypes, as well as the simultaneous analysis of multiple samples, which enables short turnaround times. Still, several PCR assays demonstrated inconsistent results with the LA test, complicating the interpretation. Multiplex PCR, a technique that allows the simultaneous amplification of multiple target DNA sequences, is the preferred method by the Centers for Disease Control and Prevention (CDC) [19]. Precise design and optimization of primers are crucial for the performance of traditional multiplex PCR methods in detecting serotypes, but these steps also add variability. Additionally, the interpretation of multiplex PCR results is complex. In contrast, multiplex PCR kits deliver standardized and readily available reagents for the simultaneous detection of multiple targets, assuring consistent outcomes and user-friendly application. Thus, evaluation of newly developed rapid multiplex PCR kits is crucial for ensuring their accuracy, reliability, and clinical applicability. However, to our knowledge, there were no commercially available assays for simultaneous detection of the GBS serotypes. Even if such assays are available, they were intended for research purpose only. Herein, we evaluated the rapid, simple, and easy-to-adopt multiplex real-time PCR technique called Novaplex^{TM} (NovaPCR, Seegene Inc., Seoul, Republic of Korea) for clinically relevant serotypes.

2. Materials and Methods

2.1. Sample Collection

A total of 131 GBS isolates collected from clinical samples in the Department of Laboratory Medicine, JBNU hospital, between 2008 and 2018 were enrolled in this study to identify GBS serotypes using NovaPCR. These 131 samples were collected from various locations: urine (33), blood (26), spot urine (15), vaginal discharge (13), pus (12), tissues (6), closed pus (4), open pus (3), cerebrospinal fluid (2), NCT urine (2), urine catheter (2), eye discharge (1), sputum (1), and others (7). The collected samples were identified with automated culture systems Vitek 2 System (BioMérieux Inc., Hazelwood, MO, USA) and VitekMS (BioMérieux Inc., Marcy L'Étoile, France), and all the isolates were stored in skim milk at −80 °C. Subsequently, collected samples were cultured in blood agar plates (BAP) and incubated at 35 °C for 16–24 h before experiments. The bacterial strains used in this investigation were collected after clinical practice for diagnosis or for surveillance. Additionally, the samples used for the investigation are entirely de-identified, ensuring the non-traceability of their origin. All bacterial isolate collection and storage procedures were performed in accordance with the Micro Bank at Jeonbuk National University Hospital (JBUH) and the department of laboratory medicine in JBUH.

2.2. Serotyping bt Latex Agglutination (LA)

The *S. agalactiae* strains were cultured on BAP. All the selected GBS isolates were serotyped by LA test (ImmuLex^{TM} Streptococcus-B kit, SSI Diagnostica, Hillerød, Denmark) according to the manufacturer's instructions. Briefly, 10 µL of RNase-free water and a single bacterial colony were applied to a reaction card provided by manufacturers and mixed thoroughly with a drop (2 µL) of latex suspension. Then, the reaction card was rotated slowly and observed for agglutination. A positive reaction was noted when distinct and visible agglutination occurred within a time frame of 30 s.

2.3. Extraction of Nucleic Acid and Multiplex Polymerase Chain Reaction (mPCR)

Total DNA was extracted by the modified boiling method [20]. Briefly, two to three colonies from BAP were transferred to an Eppendorf tube containing 1 mL of distilled water. Then, samples were mixed thoroughly by vertexing and centrifuged at 13,000 rpm for 10 min to collect the pellet. Then, 100 µL of DNA extraction buffer (Seegene Inc., Seoul, Republic of Korea) was added, and the suspension was boiled at 95 °C for 20 min and centrifuged for 10 min. The supernatant was used as the template for PCR to detect the GBS serotype. Extracted DNA was stored at −80 °C or used immediately.

We performed the conventional multiplex PCR (mPCR) with extracted DNA using the same set of primers as described previously [21]. Briefly, samples were amplified by an initial denaturation step at 95 °C for 5 min. Then, the PCR protocol; 15 cycles of 95 °C for 60 s, 54 °C for 60 s, and 72 °C for 2 min, and following this, an additional 25 cycles of 95 °C for 60 s, 56 °C for 60 s, and 72 °C for 2 min were used. The final extension was performed at 72 °C for 10 min. All the products were evaluated using 1.5% agarose gel. All the primer sequences used in the study are listed in Table 1.

Table 1. List of primer sequences used for multiplex conventional PCR.

Primer	**Sense (5′-3′)**
cpsI-Ia-6-7-F	GAATTGATAACTTTTGTGGATTGCGATGA
cpsI-6-R	CAATTCTGTCGGACTATCCTGATG
cpsI-7-R	TGTCGCTTCCACACTGAGTGTTGA
cpsL-F	CAATCCTAAGTATTTTCGGTTCATT
cpsL-R	TAGGAACATGTTCATTAACATAGC
cpsG-F	ACATGAACAGCAGTTCAACGGT
cpsG-R	ATGCTCTCCAAACTGTTCTTGT
cpsG-2-3-6-R	TCCATCTACATCTTCAATCCAAGC
cpsN-5-F	ATGCAACCAAGTGATTATCATGTA
cpsN-5-R	CTCTTCACTCTTTAGTGTAGGTAT
cpsJ-8-F	TATTTGGGAGGTAATCAAGAGACA
cpsJ-8-R	GTTTGGAGCATTCAAGATAACTCT
cpsJ-2-4-F	CATTTATTGATTCAGACGATTACATTGA
cpsJ-2-R	CCTCTTTCTCTAAAATATTCCAACC
cpsJ-4-R	CCTCAGGATATTTACGAATTCTGTA
cpsI-7-9-F	CTGTAATTGGAGGAATGTGGATCG
cpsI-9-R	AATCATCTTCATAATTTATCTCCCATT
cpsJ-Ib-F	GCAATTCTTAACAGAATATTCAGTTG
cpsJ-Ib-R	GCGTTTCTTTATCACATACTCTTG

2.4. Multiplex Real-Time PCR

Nucleic acids were extracted from using 330 μL of diluted samples from two to three colonies using Microlab NIMBUS IVD platform (Seegene Inc., Seoul, Republic of Korea) with STARMag 96X4 Universal Cartridge kit (Seegene Inc., Seoul, Republic of Korea). All the extraction procedures were carried out in accordance with the manufacturer's instructions. The final elution volume was 100 μL. The multiplex real-time PCR was done with a Novaplex^{TM} multiplex real-time PCR kit (NovaPCR, Seegene) according to the manufacturer's instructions. The samples were amplified with a step for 15 min at 95 °C, followed by 45 cycles of 95 °C for 10 s, 60 °C for 15 s, and 72 °C for 10 s. Fluorescence was detected at 60 °C and 72 °C. All real-time PCR runs were performed on CFX96$^{\mathbf{TM}}$ (Bio-Rad Laboratories, Hercules, CA, USA). GBS type Ia and Ib were recognized by fluorophore FAM (Fluorescein amidite), GBS type II and VI by fluorophore HEX (Hexachlorofluorescein), GBS type III and V by fluorophore Cal Red 610, GBS type IV, VII, VIII, and IX by fluorophore Quasar 705, fluorophore Quasar 670 identified internal control (IC), and common GBS region. All the samples were done on 8-strip tubes and 96-well plates. All the data were analyzed by Seegene Viewer (Seegene Inc., Seoul, Republic of Korea), an automated data analysis application for multiplex real-time PCR. Primers/probes for Novaplex^{TM} multiplex PCR reactions are withheld, as this method is deemed a commercial product.

2.5. Sensitivity and Specificity of NovaPCR

In this study, 1000-fold diluted DNA was used to evaluate the sensitivity of the NovaPCR. Generally, DNA may exist in various concentrations and can degrade during storage. Thus, testing the NovaPCR performance with such diluted DNA indicates its robustness across different sample concentrations. Here, the study used LA and conventional multiplex PCR as reference methods to confirm the efficiency of NovaPCR. Also, for the analytical specificity, *Bacillus cereus*, *Enterobacter cloacae*, *Enterobacter hormaechei*, *E coli*, *Lactobacillus salivarius*, *Lactococcus garvieae*, *Staphylococcus epidermidis*, *Staphylococcus gordonii*, and *Streptococcus pneumoniae* isolates were tested, and those strains were received from Jeonbuk National University Hospital Culture collection for pathogens to verify the potential interferences by non-target species. This step was performed with the same primer and probe set under the conditions mentioned in NovaPCR with DNA from non-target clinical isolates.

2.6. Interpretation and Statistical Analysis

The observations acquired with mPCR were compared to those obtained from the LA test to validate the accuracy of the serotype identification. A comparison between the two methods assisted in obtaining consistent, accurate, and reliable serotype identification. A true serotype was considered when the isolates showed positive for a specific serotype in both methods. Next, we analyzed the sensitivity, specificity, and agreement of NovaPCR based on the true serotypes. When there were discrepancies between the mPCR, latex agglutination test, and NovaPCR, the strains were sequenced, and the serotypes were confirmed based on the sequence results. All statistical analyses were conducted with MedCalc Statistical Software ver.19.2.1. (MedCalc Software Ltd., Ostend, Belgium).

3. Results

3.1. Serotype Distribution by LA Test

The LA test is considered an efficient and standardized technique used for serotyping GBS. It has been demonstrated to be serotype-specific and can effectively detect most GBS strains. In this study, the LA test identified 8 serotypes. The distribution of the serotypes was as follows: Ia, 15.26% (20/131); Ib, 15.26% (20/131); II, 7.63% (10/131); III, 15.26% (20/131); V, 16.03% (21/131); VI, 15.26% (20/131); VIII, 15.26% (20/131); IX, 0.76% (1/131). However, we could not acquire serotypes IV and VII through the LA test because their incidences are extremely low. Figure 1 demonstrates a visible clumping (agglutination) in the respective serotype within 30 sec of beginning the card rotation. Specifically, serotypes

III, V, and VIII exhibited strong agglutination, while others demonstrated moderate agglutination. All the images were captured within the manufacturer's interpretation time frame. All the identified serotypes from different samples are listed in Table 2.

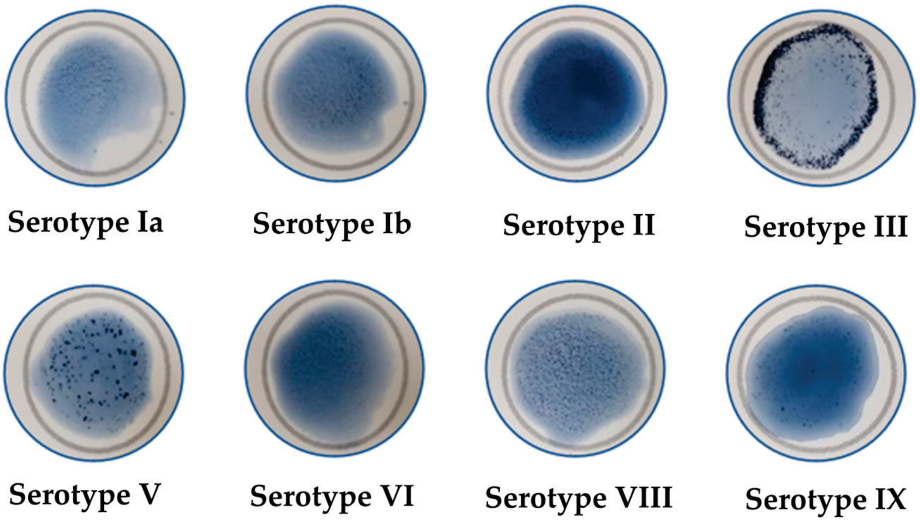

Figure 1. Representative images showing positive LA tests for specific serotypes.

Table 2. The latex agglutination test (LA test) observations on group B Streptococcus serotypes present in isolates.

Serotype/Specimen	Blood	Urine	Vaginal Discharge	Pus	Others	Total
Ia	2	4	4	4	6	20
Ib	1	7	1	4	7	20
II	2	4	2	0	2	10
III	7	7	3	0	3	20
IV	0	0	0	0	0	0
V	4	7	2	2	6	21
VI	1	9	2	5	3	20
VII	0	0	0	0	0	0
VIII	8	6	3	3	0	20
IX	0	1	0	0	0	1

The Table 2 observations demonstrate the distribution of various serotypes across different specimen types, with Serotypes V and VI being the most frequent (21 and 20 occurrences, respectively). At the same time, serotypes IV and VII are absent. Serotype V is found across all specimens, mainly in urine samples, while Serotype IX is the least frequent, with just 1 occurrence in urine. Serotypes Ia, Ib, and V are widely distributed, but their distribution is not even among samples. These observations suggest uneven distribution across multiple specimens.

3.2. Serotype Distribution by Conventional mPCR

mPCR was performed to validate its efficacy against the observations of the LA test. Here, we identified the same number of serotypes as identified in the LA test and observed 100% concordance between the mPCR and LA methods. The strong agreement between the two methods suggests their comparable reliability for serotype identification. Furthermore, these observations indicate that any of these approaches can be used based on the clinical needs. The perfect concordance also implies that there were no discrepancies or false results in either test, highlighting the accuracy and reliability of these techniques used by most diagnostic laboratories to detect serotypes.

3.3. Serotype Identification by NovaPCR

NovaPCR detected 9 serotypes. The distribution of the serotypes was as follows; Ia, 13.74% (18/131); Ib, 15.26% (20/131); II, 7.63% (10/131); III, 15.26% (20/131); IV, 0.76% (1/131); V, 16.79% (22/131); VI, 15.26% (20/131); VIII, 15.26% (20/131); IX, 0.76% (1/131). Interestingly, serotype IV was detected in one isolate from the urine sample, which was serotype Ia in both LA and mPCR. Thus, the total number of serotypes observed in the NovaPCR screening is 9. Furthermore, one isolate from the pus samples screened by NovaPCR revealed serotype V, whereas the LA test and mPCR identified the same sample as serotype Ia. Statistically, NovaPCR observations agree with the LA and mPCR tests, with a PPA (positive percent agreement) value of 1 and a kappa value of 1 in most samples. However, serotype Ia is the exceptional serotype, with a PPA of 0.94 and a kappa value of 0.98. Comparative observations of serotypes identified using different methods are presented in Table 3. In addition, positive percent agreement (PPA) values are shown in Table 3 to substantiate the efficacy of NovaPCR.

Table 3. Comparative observations of serotypes identified using different methods along with positive percentage agreement (PPA) and kappa value.

Serotype	LA Test	mPCR	NovaPCR	Kappa Value	Agreement	
				Observed Kappa (95% CI)	Positive (%) (95% CI)	Negative (%) (95% CI)
Ia	20	20	18	0.983	94	99
Ib	20	20	20	1	100	100
II	10	10	10	1	100	100
III	20	20	20	1	100	100
IV	0	0	1	NA	NA	NA
V	21	21	22	1	100	100
VI	20	20	20	1	100	100
VII	0	0	0	NA	NA	NA
VIII	20	20	20	1	100	100
IX	1	1	1	1	100	100

NovaPCR observation showed two discrepancies out of 131 samples compared to LA or mPCR serotyping. Specifically, the two samples were detected as serotype Ia in LA and mPCR tests. However, NovaPCR detected those samples as serotypes IV and V. To validate the NovaPCR observations, sequencing was performed. The sequencing results confirm those samples as serotypes IV and V, clearly indicating the efficiency of NovaPCR.

3.4. Sensitivity and Specificity of NovaPCR

To assess the sensitivity of the NovaPCR method, samples were serially diluted up to 1000-fold, and all dilutions across all serotypes and samples showed positive results. NovaPCR clearly detected serotypes in all the diluted samples, indicating its efficacy at lower concentrations. In a specificity test using bacteria other than GBS to verify the interference by non-target strains, NovaPCR results were observed to be negative for all the non-target strains.

4. Discussion

GBS is considered an asymptotic colonizer in healthy adults but can cause severe invasive infections in pregnant women, neonates, and immunosuppressed adults. The occurrence of GBS disease has seen a rise in incidence among nonpregnant adults, increasing from 3.6 to 7.3 cases per 100,000 people between 1990 and 2007 in the United States [22]. Interestingly, most affected adults have comorbidities such as heart disease, neurological disorders, diabetes, and immunocompromising conditions [23]. It is estimated to have a 2–10% fatality rate in premature neonates [24]. Also, GBS causes significant maternal morbidity and is responsible for severe infections in elderly individuals, diabetic patients, and immunocompromised individuals. The World Health Organization (WHO)-funded systematic review and meta-analysis revealed that, globally, 48.9% of invasive GBS disease was due to serotype III in neonates, followed by serotype Ia (22.9%), Ib (7%), II (6.2%), and V 9.1% [25]. Moreover, several reports suggest a correlation between different serotypes and diseases caused [26–28]. For instance, serotype III is frequently associated with invasive illnesses in newborns, such as sepsis and meningitis [29,30]. Furthermore, serotypes Ia, Ib, II, III, and V have been implicated with severe invasive illness. Interestingly, previous reports suggest that serotypes V, III, and Ia collectively constitute 67% of the prevalent serotypes responsible for invasive soft tissue infections [10]. Each serotype, with its unique characteristics, seemed to play a crucial role in determining and exhibiting distinct characteristics in its virulence, prevalence, and the populations it affects. The reliability and accuracy of detecting serotypes are essential for developing effective vaccines, guiding antibiotic prophylaxis, and understanding the association of serotypes with transmission patterns of specific pathogens. Accurate serotype detection becomes particularly crucial when considering epidemics. Thus, the accuracy of detection is crucial in understanding the pathogenesis and prevention of GBS infections. In this study, efforts were made to validate the novel mPCR called NovaPCR for rapid and reliable detection of GBS serotypes.

Despite advances in molecular techniques, and in the era of whole-genome sequencing [31], the diagnosis and serotyping of GBS continue to rely heavily on traditional methods such as LA and mPCR, which can be time-consuming and labor-intensive [32,33]. Although LA is widely used and considered the standard method for serotyping, it has significant limitations. The major limitations include cross-reactivity between serotypes, subjective interpretation, and the inability to type certain isolates, resulting in a substantial proportion of non-typeable strains [33,34]. Slotved et al. reported that 12.5% of isolates could not be serotyped using LA [35]. Also, LA is unsuitable for processing large volumes, it cannot be used directly with clinical samples, and its reagents are expensive, adding to the burden of detection [15]. Multiplex PCR offers improved accuracy but requires specialized equipment, expertise, and complex workflows, making it less accessible for routine clinical use. While mPCR has been developed to address some limitations of LA, it still involves labor-intensive tasks such as gel loading and aliquoting of multiple tubes, which can lead to human error and reduced cost-efficiency [36–39]. The tedious nature of these methods can delay appropriate treatment and epidemiological surveillance [40]. Breeding et al. reported that serotyping by LA can take up to 24 h, while PCR-based methods, though faster, still require several hours for results. Furthermore, discrepancies between phenotypic and genotypic methods complicate interpretation. Imperi et al. found only 71.1% agreement between LA- and PCR-based serotyping [41]. Some GBS strains show weak reactions in LA assays, leading to incorrect identification despite mPCR confirmation, possibly due to cross-reactivity or weak antigen expression among serotypes. Consequently, the analysis of LA test results may require substantial knowledge of potential cross-reactions. These challenges underscore the growing demand for streamlined, high-throughput, and automated methods to improve the speed and accuracy of GBS detection and serotyping in clinical diagnostics, particularly when rapid diagnosis is crucial for neonatal and maternal health. Real-time multiplex PCR emerges as a promising alternative, offering a straightforward, rapid, and reliable strategy to detect GBS serotypes in an easy, simple, and effective manner.

In this study, a total of 131 clinical isolates of different serotypes were tested using NovaPCR. Observations revealed that 129 isolates showed the same observations as LA and conventional mPCR. However, the two isolates in NovaPCR are distinctively different from LA and conventional mPCR. Specifically, two isolates in serotype Ia were detected as serotype IV and V in NovaPCR. To solve the discrepancies, sequencing was performed, and the results of two isolates revealed the same serotype by sequencing as observed in NovaPCR. These observations suggest that there could be potential ambiguity issues with the LA test and conventional mPCR. The serotype Ia is one of the most common and widely distributed GBS serotypes. It is frequently associated with neonatal GBS early-onset disease (EOD), which occurs within the first week of life and often leads to severe conditions such as sepsis, pneumonia, and meningitis [42–44]. The difference between the traditional (LA test and mPCR) and NovaPCR methods is only 1.52%, but clinically, we cannot define or measure its clinical impact on treatment and its outcome. Thus, further clinical studies are necessary to assess the clinical impact of NovaPCR's improved efficacy in detecting GBS serotypes.

In NovaPCR, specific probes are labeled with different fluorescence dyes: FAM, HEX, Quasar 705, and Quasar 670, and employ TOCE technology. This technology streamlines the PCR process for serotyping and effectively addresses the limitations associated with target-based probe real-time PCR methods. Furthermore, all the DNA extraction and PCR preparation steps were fully automated using the Microlab NIMBUS IVD platform, ensuring fast and reliable PCR preparation. The use of advanced knowledge-based technology in NovaPCR enhances the accuracy and reliability of GBS serotype detection. In this study, NovaPCR demonstrated higher accuracy in identifying serotypes compared to LA, particularly in distinguishing serotype IV and serotype V from serotype Ia. Additionally, NovaPCR includes a dedicated viewer that allows for easy and precise interpretation of the results. These unique features make NovaPCR a dependable tool for serotyping, minimizing intra- and inter-observer variability in data interpretation. Moreover, the introduction of NovaPCR has contributed to reducing assay costs.

The NovaPCR can be helpful for detecting GBS in newborns, particularly those at risk of early-onset disease (EOD) or late-onset disease (LOD), though we did not perform the tests with clinical samples. EOD occurs within the first week of life, often within the first 24 h, and can lead to severe conditions such as sepsis, pneumonia, and meningitis. LOD typically occurs between one week and three months of age. It also presents serious health risks, including meningitis and long-term neurological complications. In this context, the ability of NovaPCR to provide rapid and accurate detection of GBS is especially critical. During labor, time is of the essence; the prompt identification of GBS colonization in the mother or the presence of GBS in the newborn can significantly influence the timing and type of interventions administered. For instance, if GBS is detected in the mother during labor, appropriate antibiotic prophylaxis can be initiated to prevent vertical transmission of the bacteria to the newborn during delivery. This timely intervention is crucial for reducing the risk of EOD. Furthermore, in cases where a newborn is suspected of having LOD, rapid GBS detection allows for swift initiation of targeted antibiotic therapy, which can be lifesaving. Delayed or inaccurate diagnosis could result in inadequate treatment, increasing the risk of severe outcomes or complications. Thus, the NovaPCR's ability to deliver precise and fast results is essential for optimizing treatment strategies and improving clinical outcomes for both mothers and newborns.

Understanding the relationships between GBS serotypes, virulence genes, and antimicrobial resistance is critical for elucidating disease behavior and guiding treatment strategies. Specific combinations of serotypes and antimicrobial resistance patterns may enhance GBS invasiveness, complicating infection management and treatment. Previous reports suggest that a specific combination of virulence factors was predominant in invasive infection-related GBS (iGBS) [45,46]. These observations strongly indicate that these combinations may be major drivers in developing severe disease outcomes. Therefore, future investigations should target the specific combination to understand the relationship between disease and serotypes. Also, these investigations should be performed using clinical samples as they represent the actual clinical condition. However, in order to achieve success in these investigations, it is crucial to identify the serotype. NovaPCR has the ability to help with the precise identification of serotypes in various clinical samples. Collectively, NovaPCR offers a rapid, high-throughput, and reliable screening system for GBS. We acknowledge that our analysis is constrained to 131 samples and is obtained from a single hospital. Also, it needs representative clinical samples for serotypes IV, VII, and IX. Although it has shown promising results in clinical isolates, more validation utilizing clinical samples, particularly vaginal discharge or pus, is necessary before direct application.

5. Conclusions

NovaPCR is an advanced technique to detect GBS serotypes. It employs TOCE technology, which assists in navigating the existing technical constraints of target-based probe real-time PCR technology. Additionally, it maximizes the capabilities of real-time PCR in analyzing high multiplex data by utilizing novel components for melting temperature analysis and generating distinct signals. In this study, NovaPCR accurately identified serotypes IV and V, which were first classified as serotype Ia in the LA test and mPCR. This distinction in identification is crucial for achieving optimal clinical outcomes. Together, NovaPCR showed a reliable, fast, easy-to-interpret, and cost-efficient performance in GBS serotyping.

Author Contributions: Conceptualization, J.L.; methodology, J.L. and M.H.; validation, M.H.; formal analysis, J.L.; investigation, M.H.; resources, J.L.; data curation, J.L.; writing—original draft preparation, M.H.; writing—review and editing, J.L.; supervision, J.L.; project administration, J.L.; funding acquisition, J.L. All authors have read and agreed to the published version of the manuscript.

Funding: This paper was supported by research funds from Jeonbuk National University in 2022.

Data Availability Statement: The datasets generated during and/or analyzed during the study are available from the corresponding author upon reasonable request.

Acknowledgments: We would like to express our deepest gratitude to the staff members of the Department of Laboratory Medicine at Jeonbuk National University (JBNU) Hospital for their invaluable assistance and support throughout this study. We also thank Ran Kim, Ji Eun Kim, and Ga Gyo Jung from Jeonbuk National University Hospital Culture collection for pathogens, for her unwavering support. We are also immensely grateful to Seegene Inc., Seoul, Republic of Korea, for generously providing the NovaPCR kits for our research.

Conflicts of Interest: Some relevant information is withheld due to the fact that the NovaPCR is a commercial assay. The authors declare no conflicts of interest.

References

1. Farley, M.M. Group B streptococcal disease in nonpregnant adults. *Clin. Infect. Dis.* **2001**, *33*, 556–561. [CrossRef] [PubMed]
2. Ballard, M.S.; Schonheyder, H.C.; Knudsen, J.D.; Lyytikainen, O.; Dryden, M.; Kennedy, K.J.; Valiquette, L.; Pinholt, M.; Jacobsson, G.; Laupland, K.B.; et al. The changing epidemiology of group B streptococcus bloodstream infection: A multi-national population-based assessment. *Infect. Dis.* **2016**, *48*, 386–391. [CrossRef] [PubMed]
3. Brigtsen, A.K.; Dedi, L.; Melby, K.K.; Holberg-Petersen, M.; Radtke, A.; Lyng, R.V.; Andresen, L.L.; Jacobsen, A.F.; Fugelseth, D.; Whitelaw, A. Comparison of PCR and serotyping of Group B Streptococcus in pregnant women: The Oslo GBS-study. *J. Microbiol. Methods* **2015**, *108*, 31–35. [CrossRef] [PubMed]
4. Ip, M.; Ang, I.; Fung, K.; Liyanapathirana, V.; Luo, M.J.; Lai, R. Hypervirulent Clone of Group B Streptococcus Serotype III Sequence Type 283, Hong Kong, 1993–2012. *Emerg. Infect. Dis.* **2016**, *22*, 1800–1803. [CrossRef] [PubMed]
5. Rothen, J.; Sapugahawatte, D.N.; Li, C.; Lo, N.; Vogel, G.; Foucault, F.; Pfluger, V.; Pothier, J.F.; Blom, J.; Daubenberger, C.; et al. A simple, rapid typing method for *Streptococcus agalactiae* based on ribosomal subunit proteins by MALDI-TOF MS. *Sci. Rep.* **2020**, *10*, 8788. [CrossRef] [PubMed]
6. Le Doare, K.; Heath, P.T. An overview of global GBS epidemiology. *Vaccine* **2013**, *31* (Suppl. 4), D7–D12. [CrossRef]
7. Hsu, J.-F.; Lu, J.-J.; Lin, C.; Chu, S.-M.; Lin, L.-C.; Lai, M.-Y.; Huang, H.-R.; Chiang, M.-C.; Tsai, M.-H. Clustered regularly interspaced short palindromic repeat analysis of clonal complex 17 serotype iii group b streptococcus strains causing neonatal invasive diseases. *Int. J. Mol. Sci.* **2021**, *22*, 11626. [CrossRef]

8. Miselli, F.; Frabboni, I.; Di Martino, M.; Zinani, I.; Buttera, M.; Insalaco, A.; Stefanelli, F.; Lugli, L.; Berardi, A. Transmission of Group B Streptococcus in late-onset neonatal disease: A narrative review of current evidence. *Ther. Adv. Infect. Dis.* **2022**, *9*, 20499361221142732. [CrossRef]
9. Edwards, M.S.; Baker, C.J. Group B streptococcal infections in elderly adults. *Clin. Infect. Dis.* **2005**, *41*, 839–847. [CrossRef]
10. Lee, N.Y.; Yan, J.J.; Wu, J.J.; Lee, H.C.; Liu, K.H.; Ko, W.C. Group B streptococcal soft tissue infections in non-pregnant adults. *Clin. Microbiol. Infect.* **2005**, *11*, 577–579. [CrossRef]
11. Madhi, S.A.; Cutland, C.L.; Jose, L.; Koen, A.; Govender, N.; Wittke, F.; Olugbosi, M.; Meulen, A.S.; Baker, S.; Dull, P.M.; et al. Safety and immunogenicity of an investigational maternal trivalent group B streptococcus vaccine in healthy women and their infants: A randomised phase 1b/2 trial. *Lancet Infect. Dis.* **2016**, *16*, 923–934. [CrossRef]
12. Jin, Z.; Li, J.; Zhou, H.; Wang, Z.; Yi, L.; Liu, N.; Du, J.; Chang, C.Y.; Ji, W. Serotype Distribution, Virulence Determinants and Antimicrobial Susceptibility of *Streptococcus agalactiae* Isolated from Young Infants. *Pathogens* **2022**, *11*, 1355. [CrossRef] [PubMed]
13. Liu, Y.; Liu, J. Group B Streptococcus: Virulence Factors and Pathogenic Mechanism. *Microorganisms* **2022**, *10*, 2483. [CrossRef]
14. Schindler, Y.; Rahav, G.; Nissan, I.; Treygerman, O.; Prajgrod, G.; Attia, B.Z.; Raz, R.; Valenci, G.Z.; Tekes-Manova, D.; Maor, Y. Group B streptococcus virulence factors associated with different clinical syndromes: Asymptomatic carriage in pregnant women and early-onset disease in the newborn. *Front. Microbiol.* **2023**, *14*, 1093288. [CrossRef]
15. Slotved, H.-C.; Elliott, J.; Thompson, T.; Konradsen, H.B. Latex assay for serotyping of group B *Streptococcus* isolates. *J. Clin. Microbiol.* **2003**, *41*, 4445–4447. [CrossRef]
16. Slotved, H.C.; Sauer, S.; Konradsen, H.B. False-negative results in typing of group B streptococci by the standard lancefield antigen extraction method. *J. Clin. Microbiol.* **2002**, *40*, 1882–1883. [CrossRef] [PubMed]
17. Rosini, R.; Campisi, E.; De Chiara, M.; Tettelin, H.; Rinaudo, D.; Toniolo, C.; Metruccio, M.; Guidotti, S.; Sorensen, U.B.; Kilian, M.; et al. Genomic analysis reveals the molecular basis for capsule loss in the group B Streptococcus population. *PLoS ONE* **2015**, *10*, e0125985. [CrossRef]
18. Sheppard, A.E.; Vaughan, A.; Jones, N.; Turner, P.; Turner, C.; Efstratiou, A.; Patel, D.; Modernising Medical Microbiology Informatics, G.; Walker, A.S.; Berkley, J.A.; et al. Capsular Typing Method for *Streptococcus agalactiae* Using Whole-Genome Sequence Data. *J. Clin. Microbiol.* **2016**, *54*, 1388–1390. [CrossRef] [PubMed]
19. Centers for Disease Control and Prevention. *Streptococcus pneumoniae Detection and Serotyping Using PCR*; CDC Publication: New York, NY, USA, 2024.
20. Ivanov, I.G.; Bachvarov, D.R. Determination of plasmid copy number by the "boiling" method. *Anal. Biochem.* **1987**, *165*, 137–141. [CrossRef] [PubMed]
21. Imperi, M.; Pataracchia, M.; Alfarone, G.; Baldassarri, L.; Orefici, G.; Creti, R. A multiplex PCR assay for the direct identification of the capsular type (Ia to IX) of Streptococcus agalactiae. *J. Microbiol. Methods* **2010**, *80*, 212–214. [CrossRef]
22. Skoff, T.H.; Farley, M.M.; Petit, S.; Craig, A.S.; Schaffner, W.; Gershman, K.; Harrison, L.H.; Lynfield, R.; Mohle-Boetani, J.; Zansky, S.J. Increasing burden of invasive group B streptococcal disease in nonpregnant adults, 1990–2007. *Clin. Infect. Dis.* **2009**, *49*, 85–92. [CrossRef] [PubMed]
23. Phares, C.R.; Lynfield, R.; Farley, M.M.; Mohle-Boetani, J.; Harrison, L.H.; Petit, S.; Craig, A.S.; Schaffner, W.; Zansky, S.M.; Gershman, K.; et al. Epidemiology of invasive group B streptococcal disease in the United States, 1999–2005. *Jama* **2008**, *299*, 2056–2065. [CrossRef] [PubMed]
24. Wilson, C.B.; Nizet, V.; Maldonado, Y.; Remington, J.S.; Klein, J.O. *Remington and Klein's Infectious Diseases of the Fetus and Newborn Infant*; Elsevier: Amsterdam, The Netherlands, 2014; pp. 411–456.
25. Edmond, K.M.; Kortsalioudaki, C.; Scott, S.; Schrag, S.J.; Zaidi, A.K.; Cousens, S.; Heath, P.T. Group B streptococcal disease in infants aged younger than 3 months: Systematic review and meta-analysis. *Lancet* **2012**, *379*, 547–556. [CrossRef]
26. Lo, C.W.; Liu, H.C.; Lee, C.C.; Lin, C.L.; Chen, C.L.; Jeng, M.J.; Chiu, C.H. Serotype distribution and clinical correlation of *Streptococcus agalactiae* causing invasive disease in infants and children in Taiwan. *J. Microbiol. Immunol. Infect.* **2019**, *52*, 578–584. [CrossRef]
27. Ali, M.M.; Asrat, D.; Fenta, D.A.; Chaka, T.E.; Woldeamanuel, Y. Group B Streptococcus colonization rate and serotype distribution among pregnant women and their newborns at Adama Hospital Medical College, Ethiopia. *Sci. Rep.* **2020**, *10*, 9301. [CrossRef]
28. Madzivhandila, M.; Adrian, P.V.; Cutland, C.L.; Kuwanda, L.; Schrag, S.J.; Madhi, S.A. Serotype distribution and invasive potential of group B streptococcus isolates causing disease in infants and colonizing maternal-newborn dyads. *PLoS ONE* **2011**, *6*, e17861. [CrossRef]
29. van Kassel, M.N.; de Boer, G.; Teeri, S.A.; Jamrozy, D.; Bentley, S.D.; Brouwer, M.C.; van der Ende, A.; van de Beek, D.; Bijlsma, M.W. Molecular epidemiology and mortality of group B streptococcal meningitis and infant sepsis in the Netherlands: A 30-year nationwide surveillance study. *Lancet Microbe* **2021**, *2*, e32–e40. [CrossRef] [PubMed]
30. Yue, L.; Liu, H. Neonatal Late-Onset Meningitis Caused by Serotype III CC17 Group B Streptococci Aggregating in Two Families from Southern China. *Infect. Drug Resist.* **2023**, *16*, 3417–3424. [CrossRef]
31. Park, J.S.; Cho, D.H.; Yang, J.H.; Kim, M.Y.; Shin, S.M.; Kim, E.C.; Park, S.S.; Seong, M.W. Usefulness of a rapid real-time PCR assay in prenatal screening for group B streptococcus colonization. *Ann. Lab. Med.* **2013**, *33*, 39–44. [CrossRef]
32. Yao, K.; Poulsen, K.; Maione, D.; Rinaudo, C.D.; Baldassarri, L.; Telford, J.L.; Sorensen, U.B.; Members of the DEVANI Study Group; Kilian, M. Capsular gene typing of *Streptococcus agalactiae* compared to serotyping by latex agglutination. *J. Clin. Microbiol.* **2013**, *51*, 503–507. [CrossRef]

33. Gosiewski, T.; Brzychczy-Włoch, M.; Heczko, P.B. The application of multiplex PCR to detect seven different DNA targets in group B streptococci. *Folia Microbiol.* **2012**, *57*, 163–167. [CrossRef] [PubMed]
34. Ji, T.; Cai, Y.; Gao, Y.; Wang, G.; Miao, Y.; Gao, X. Establishment and application of a rapid visual diagnostic method for *Streptococcus agalactiae* based on recombinase polymerase amplification and lateral flow strips. *Sci. Rep.* **2024**, *14*, 10064. [CrossRef] [PubMed]
35. Breeding, K.M.; Ragipani, B.; Lee, K.D.; Malik, M.; Randis, T.M.; Ratner, A.J. Real-time PCR-based serotyping of Streptococcus agalactiae. *Sci. Rep.* **2016**, *6*, 38523. [CrossRef]
36. Eichinger, A.; Hagen, A.; Meyer-Bühn, M.; Huebner, J. Clinical benefits of introducing real-time multiplex PCR for cerebrospinal fluid as routine diagnostic at a tertiary care pediatric center. *Infection* **2019**, *47*, 51–58. [CrossRef]
37. Le Bars, H.; Madany, N.; Lamoureux, C.; Beauruelle, C.; Vallet, S.; Payan, C.; Pilorgé, L. Evaluation of the Performance Characteristics of a New POC Multiplex PCR Assay for the Diagnosis of Viral and Bacterial Neuromeningeal Infections. *Diagnostics* **2023**, *13*, 1110. [CrossRef]
38. Oeser, C.; Pond, M.; Butcher, P.; Bedford Russell, A.; Henneke, P.; Laing, K.; Planche, T.; Heath, P.T.; Harris, K. PCR for the detection of pathogens in neonatal early onset sepsis. *PLoS ONE* **2020**, *15*, e0226817. [CrossRef]
39. Otaguiri, E.S.; Morguette, A.E.B.; Morey, A.T.; Tavares, E.R.; Kerbauy, G.; de Almeida Torres, R.S.; Chaves Júnior, M.; Tognim, M.C.B.; Góes, V.M.; Krieger, M.A.; et al. Development of a melting-curve based multiplex real-time PCR assay for simultaneous detection of *Streptococcus agalactiae* and genes encoding resistance to macrolides and lincosamides. *BMC Pregnancy Childbirth* **2018**, *18*, 126. [CrossRef] [PubMed]
40. Mohamed, A.M.; Khan, M.A.; Faiz, A.; Ahmad, J.; Khidir, E.B.; Basalamah, M.A.; Aslam, A. Group B Streptococcus Colonization, Antibiotic Susceptibility, and Serotype Distribution among Saudi Pregnant Women. *Infect. Chemother.* **2020**, *52*, 70–81. [CrossRef]
41. Wang, P.; Tong, J.J.; Ma, X.H.; Song, F.L.; Fan, L.; Guo, C.M.; Shi, W.; Yu, S.J.; Yao, K.H.; Yang, Y.H. Serotypes, antibiotic susceptibilities, and multi-locus sequence type profiles of *Streptococcus agalactiae* isolates circulating in Beijing, China. *PLoS ONE* **2015**, *10*, e0120035. [CrossRef]
42. ACOG. Prevention of Group B Streptococcal Early-Onset Disease in Newborns: ACOG Committee Opinion, Number 797. *Obs. Gynecol.* **2020**, *135*, e51–e72. [CrossRef]
43. Lohrmann, F.; Hufnagel, M.; Kunze, M.; Afshar, B.; Creti, R.; Detcheva, A.; Kozakova, J.; Rodriguez-Granger, J.; Sørensen, U.B.S.; Margarit, I.; et al. Neonatal invasive disease caused by *Streptococcus agalactiae* in Europe: The DEVANI multi-center study. *Infection* **2023**, *51*, 981–991. [CrossRef] [PubMed]
44. Snoek, L.; van Kassel, M.N.; Krommenhoek, J.F.; Achten, N.B.; Plotz, F.B.; van Sorge, N.M.; Brouwer, M.C.; van de Beek, D.; Bijlsma, M.W.; the NOGBS study group. Neonatal early-onset infections: Comparing the sensitivity of the neonatal early-onset sepsis calculator to the Dutch and the updated NICE guidelines in an observational cohort of culture-positive cases. *eClinicalMedicine* **2022**, *44*, 101270. [CrossRef] [PubMed]
45. Gonçalves, B.P.; Procter, S.R.; Paul, P.; Chandna, J.; Lewin, A.; Seedat, F.; Koukounari, A.; Dangor, Z.; Leahy, S.; Santhanam, S.; et al. Group B streptococcus infection during pregnancy and infancy: Estimates of regional and global burden. *Lancet Glob. Health* **2022**, *10*, e807–e819. [CrossRef]
46. Choi, J.H.; Kim, T.H.; Kim, E.T.; Kim, Y.R.; Lee, H. Molecular epidemiology and virulence factors of group B Streptococcus in South Korea according to the invasiveness. *BMC Infect. Dis.* **2024**, *24*, 740. [CrossRef] [PubMed]

microorganisms

MDPI

Article

Pulmonary Tuberculosis Diagnosis Using an Intelligent Microscopy Scanner and Image Recognition Model for Improved Acid-Fast Bacilli Detection in Smears

Wei-Chuan Chen [1,2], Chi-Chuan Chang [1,3] and Yusen Eason Lin [3,*]

[1] Division of Teaching and Education, Teaching and Research Department, Kaohsiung Veterans General Hospital, Kaohsiung 813414, Taiwan; wcchen1027@vghks.gov.tw (W.-C.C.)
[2] Department of Pharmacy Master Program, Tajen University, Yanpu 907101, Taiwan
[3] Graduate Institute of Human Resource and Knowledge Management, National Kaohsiung Normal University, Kaohsiung 802561, Taiwan
[*] Correspondence: easonlin@nknu.edu.tw; Tel.: +886-77172-930

Abstract: Microscopic examination of acid-fast mycobacterial bacilli (AFB) in sputum smears remains the most economical and readily available method for laboratory diagnosis of pulmonary tuberculosis (TB). However, this conventional approach is low in sensitivity and labor-intensive. An automated microscopy system incorporating artificial intelligence and machine learning for AFB identification was evaluated. The study was conducted at an infectious disease hospital in Jiangsu Province, China, utilizing an intelligent microscope system. A total of 1000 sputum smears were included in the study, with the system capturing digital microscopic images and employing an image recognition model to automatically identify and classify AFBs. Referee technicians served as the gold standard for discrepant results. The automated system demonstrated an overall accuracy of 96.70% (967/1000), sensitivity of 91.94% (194/211), specificity of 97.97% (773/789), and negative predictive value (NPV) of 97.85% (773/790) at a prevalence of 21.1% (211/1000). Incorporating AI and machine learning into an automated microscopy system demonstrated the potential to enhance the sensitivity and efficiency of AFB detection in sputum smears compared to conventional manual microscopy. This approach holds promise for widespread application in TB diagnostics and potentially other fields requiring labor-intensive microscopic examination.

Keywords: TB smear; AI; machine learning; TB diagnosis

1. Introduction

Tuberculosis is treatable, preventable, and curable. Sustained declines in tuberculosis deaths in many countries during the past 50 years provide evidence that ending the pandemic is foreseeable [1]. However, tuberculosis, which has plagued humanity and has killed hundreds of millions of people over the past two centuries, remains a global public health threat. In 2023, 1.3 million people died from tuberculosis (95% UI: 1.18–1.43 m), including 167,000 people with HIV, representing more deaths than any other infectious disease [2]. World leaders in the most recent United Nations High-Level Meeting (UNHLM) on TB made commitments and requests to address the global tuberculosis crisis [1], which included providing comprehensive care to all people with TB, addressing the crisis of drug-resistant TB, strengthening the engagement of civil society and communities affected by TB, and enabling and strengthening TB research. It highlights the need for comprehensive care, addressing drug-resistant TB, engaging civil society and communities, and promoting TB research. The commitments made during the meeting provide a strong impetus to accelerate the TB response and work towards ending TB.

The World Health Organization (WHO) recommends the acid-fast stain method of sputum smears as the most robust and economical method for the first line of laboratory diagnosis of pulmonary tuberculosis. This method relies on the microscopic examination of sputum samples for acid-fast mycobacteria bacilli (AFB). However, it is important to note that the sensitivity and specificity of smear microscopy are poor, as it only detects 10 to 75% of pulmonary TB cases. Additionally, smear microscopy is labor-intensive and tedious. While new molecular-based methods like Xpert MTB/RIF have become available, they have not been widely deployed in rural areas due to substantially higher costs and infrastructure constraints, which may not be affordable in many countries with high TB burden in the foreseeable future [3,4]. Thus, despite advancements in molecular diagnostics, the acid-fast stain method remains the recommended first-line laboratory diagnosis for pulmonary tuberculosis due to its robustness and cost-effectiveness [5–7]. The WHO suggests the availability of 1.1 microscopy laboratories per every 100 thousand population to enhance the diagnostic capacity for tuberculosis [2].

The situation of unsatisfactory TB smear accuracy (sensitivity and specificity) seems to be the same scenario as pathology. For more than 100 years, pathologists have relied on manual microscopy, the same as microbiologists, for laboratory diagnosis. It seemed unsolvable until the development of artificial intelligence (AI), image recognition, and machine learning algorithms in the late 1990s. Machine learning (ML) is based on artificial neural networks, which mimic human brain processes by passing data through hidden layers by connected neurons, with the output layer providing the estimation or prediction. The key advantage of ML is its ability to automatically extract features of the input information from the iteration of calculation back and forth among input layers, the hidden layers, and the output layer(s). These developments have motivated several large clinical trials to use ML technologies in pathology. Digital pathology has become a trending movement in the so-called "Smart Hospitals", where pathology specimens can be digitalized, electronically transferred, diagnosed, reviewed, and the report issued. However, no "Digital Microbiology" products and services have been developed accordingly.

Recently, some automated TB smear microscopy systems have been developed that take advantage of artificial intelligence (AI) and big data analysis, which may significantly increase the sensitivity of TB smear microscopy [8–21]. However, most of the research focused on algorithms and deep learning model building, with less focus on system integration (e.g., evaluation of hardware and software together). Such an integrated system may include a motorized stage to load the smear slides into a bright-field microscope (hardware). Then, the system performs auto-focus, digitally captures the smear images, analyzes the images, and classifies smear slides as positive or negative (software). Although all these studies reported better performance than human examination, most are still in development or just "proof-of-concept" systems. Until 2022, an integrated microscopic system was commercialized for automatic detection of AFB, which has received medical device registration in several countries [22,23]. This is a continuation study to describe the performance characteristics and medical technician's workload of a diagnostic algorithm for the identification of AFB under a microscope using image recognition technology.

2. Materials and Methods

Study Hospital: The Study Hospital was formerly an infectious diseases specialty hospital located in Southern Jiangsu, China. The hospital has 900 beds, of which, 210 are in the respiratory department. An average of 80 smears are tested for mycobacteria in the laboratory. At least three technicians are on duty daily to perform TB smear microscopy. All specimens in the study were processed by liquid-base culture method for MTB identification.

Specimen: This study initially included 1150 smears. One hundred fifty smears were rejected due to incomplete stain removal (n = 60), smear location shift (n = 8), smear being too thick (n = 3), smear being too thin (14), smear dropped off (n = 4), and slide size too big or too small for the system (n = 21). The remaining 1000 smears were enrolled.

Smear Stain: We followed the standardized protocol for the modified Kinyoun acid-fast stain of smears. All specimens were processed with N-acetyl-L-cysteine-sodium hydroxide for decontamination. A smear was then made by spreading a thin layer of the processed sputum sample onto a glass slide and allowing it to air dry, followed by heat fixation 2 to 3 times. Then, the slide was flooded with Kinyoun carbolfuchsin stain for 5 min after 1 min with absolute methanol for 1 min. The slide was rinsed briefly (3 to 5 s) with 50% ethanol, followed by water rinsing. Moreover, the slide was decolorized with 1% sulfuric acid for 2 min or until no more color runs from the slide. Afterward, the slide was rinsed with water, counterstained with methylene blue for 1 min, and rinsed to air dry. After the technicians examined the smears with a manual microscope and issued the test results in the laboratory report, the same set of slides was transferred to another technician for comparison by the automated system.

Image Recognition Model for TB Bacillus: The machine learning model applied in this study for TB bacilli detection utilizes a hybrid approach, combining supervised and unsupervised learning algorithms. The model building started with supervised learning, where the system is trained to identify candidate TB objectives based on their morphological characteristics. The convolutional neural network (CNN), a class of deep learning models particularly effective in image recognition tasks, was trained on more than 100,000 TB smears, learning to distinguish the distinctive bacillus-shaped morphology of acid-fast bacilli (AFB) from other cellular debris and artifacts in the sputum smear, similar to approaches used in other medical imaging applications [24]. Once potential bacilli were identified, the model transitions to an unsupervised learning phase. This stage employed another CNN model to refine the classification. The unsupervised model is exposed to a diverse set of image objects containing TB-positive and TB-negative bacilli with labels by medical technicians. Through this process, the model learns to identify subtle features and patterns that distinguish positive TB bacilli from other similar-looking objects. This unsupervised approach is particularly valuable as it allows the model to discover complex, non-linear relationships in the data that might not be apparent to human observers or easily codified in rule-based systems. Following the unsupervised learning phase, the model undergoes a refinement step where the image objects classified as TB-negative by the unsupervised model are removed from further consideration. This step effectively prunes the candidate pool, leaving only the objects that the model considers highly likely to be TB bacilli. This refinement process significantly enhances the model's precision, reducing the likelihood of false positives in the final output, a technique that has shown promise in other medical imaging applications [25]. The overall architecture of this hybrid model allows for continuous improvement and adaptation. As new data become available, both the supervised and unsupervised components can be fine-tuned, enhancing the model's performance over time. The use of deep learning techniques, particularly in the unsupervised phase, enables the model to capture complex, high-dimensional features that may not be apparent to human observers, potentially leading to improved sensitivity compared to traditional manual microscopy.

Procedures for a Parallel Study: An automated intelligent medical microscope system ("system") (TB-Scan, Wellgen Medical, Kaohsiung, Taiwan) was installed in a negative pressured isolation laboratory. The system consists of two components: (1) microscopic imaging acquisition hardware with auto-focusing and slide-scanning capability to cover the 1 cm by 2 cm specimen area based on WHO recommendation (300 fields @1000× oil lens); (2) an image recognition algorithm for detection and classification of positive AFBs. The image acquisition hardware is designed to refocus every field of view to overcome the inconsistency of smear thickness. This procedure ensures that each image acquired is on focus, though the total acquisition time could be longer. After the microscopic images were digitally acquired and stored, candidate AFBs were detected and marked, and the marked bacilli were differentiated from other substances and tissues in the smear based on color and morphological features, as mentioned previously. Such a CNN model was pre-trained with a diverse set of specimen samples, more than 100,000 TB smears from across Asia, mostly coming from Taiwan and partially from China, India, and Japan, to minimize the potential overfitting problem [22,23]. The results were recorded as positive if any AFB was identified in the image of the slide. The laboratory technician supervisor served as the Gold Standard in evaluating the system's performance. The whole system was powered and controlled by a custom-made internal personal computer (CPU: Intel Gen10 Core i7-10700TE w/16 GB RAM and an Nvidia GTX 1650 GPU w/4 GB DDR5, Santa Clara, CA, USA).

Quality Control: All positive smears detected by TB-Scan were re-examined by a microscope (Olympus CX-21) under a 1000× oil lens for verification, and microscopic images were captured and stored by a cellphone (iPhone 13, Apple Inc., Cupertino, CA, USA).

Data Interpretation: Test performance evaluation is based on sensitivity and specificity. Sensitivity (also called the true positive rate) measures the proportion of positives correctly identified as such (e.g., the percentage of positive TB smears correctly identified from the true positives). Specificity (also called the true negative rate) measures the proportion of actual negatives correctly identified as such (e.g., the percentage of negative TB smears correctly identified as not having the condition). Negative predictive value (NPV) measures the ratio of true negative to all those identified as negative. NPV is an effective indicator for a screening test because its characteristics can predict how likely it is truly negative (e.g., healthy) in case of a negative test result.

3. Results

Specimen Characteristics: Of the 1150 smears for this study, 150 were rejected due to incomplete stain removal (n = 60), smear location shift (n = 8, see Figure 1), smear being too thick (n = 3), smear being too thin (14), smear dropped off (n = 4), and slide size too big or too small for the system (n = 21).

Figure 1. Examples of smear characteristics: #1 through #3 were acceptable. The #4 smear was too thin, and #5 had incomplete stain removal. The #6 smear was too thick, and both #5 and #6 smears were outside of the valid scanning target area.

Initial Results from the Automated System: The original hospital clinical records on acid-fast stains indicated that there were 194 AFB-positive smears and 806 AFB-negative smears. Based on TB-Scan's results, there were 210 AFB-positive smears and 790 AFB-negative smears. Of the 210 AFB-positive smears by TB-Scan, 198 smears contained AFB under microscope examination, and AFB was not found in the remaining 12 smears. Based on the results mentioned above, the confusion matrix is as follows in Table 1.

Table 1. Performance of automation system and manual smear microscopy to detect AFBs (before discrepancy resolution by gold standard).

Test Performance		AFB Record by Technicians	
		Positive	**Negative**
TB-Scan	Positive	177	33
	Negative	17	773

The accuracy was 95.00% (950/1000), with a sensitivity of 91.24% (177/194), specificity of 95.91% (773/806), false negative rate of 8.76% (17/194), and false positive rate of 4.09% (33/806). However, 21 smears that were previously reported as negative were found positive by TB-Scan. The microscopic images demonstrated scanty AFBs (Figure 2).

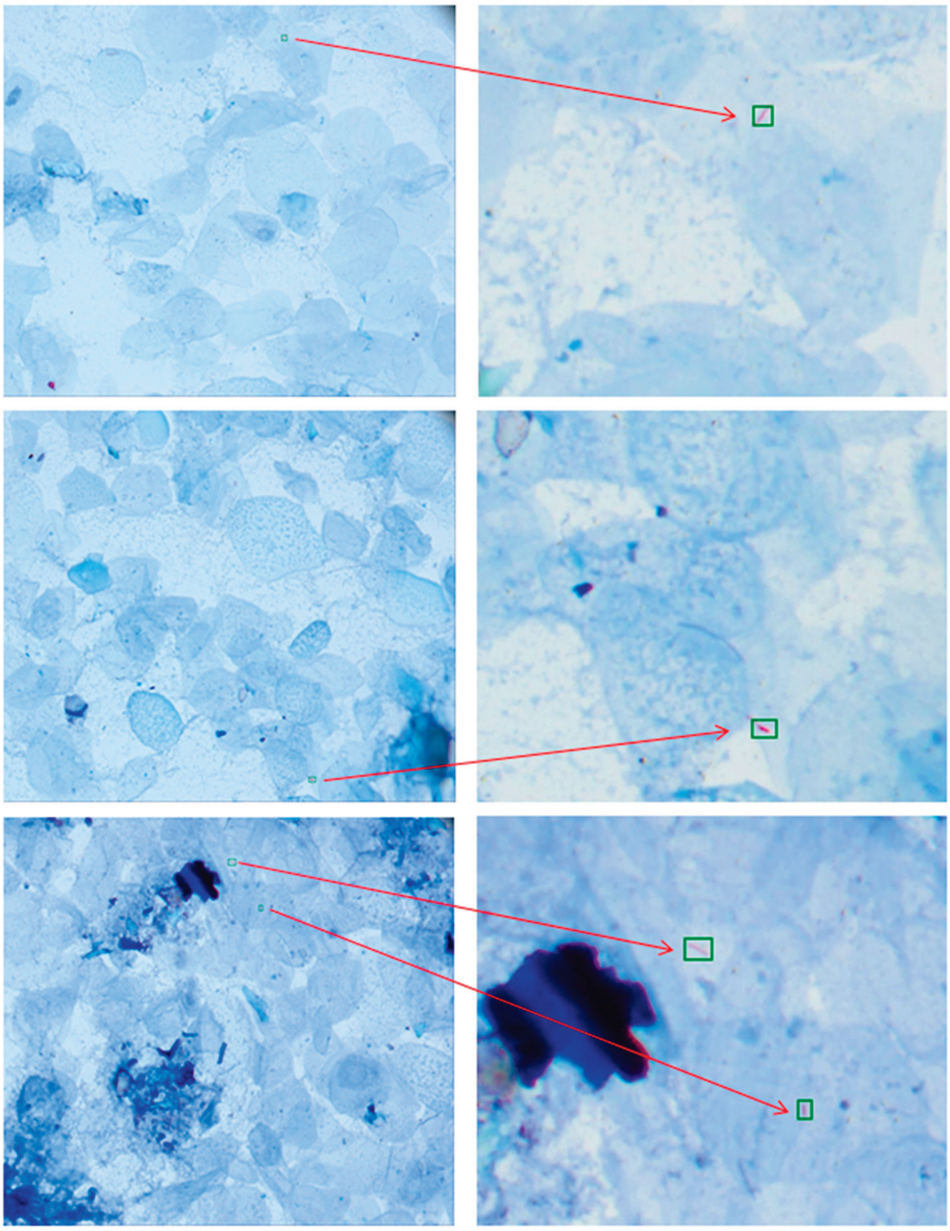

Figure 2. Examples of scanty AFBs detected by the automation system (each image is in 2448 × 2048 resolution with a pixel size of 0.173 µm).

Discrepancy Resolution and Updated Performance: After presenting the images to the medical technician in the study hospital (our gold standard), the technician ruled out four smears and maintained her judgment as negative, agreeing that the remaining 17 smears should have been recorded as positive. Therefore, the confusion matrix was re-calculated as follows in Table 2.

Table 2. Performance of the automation system and manual smear microscopy to detect AFBs (after discrepancy resolution by the gold standard).

Test Performance		Gold Standard	
		Positive	**Negative**
TB-Scan	Positive	194	16
	Negative	17	773

The accuracy was recalculated as 96.70% (967/1000), with a sensitivity of 91.94% (194/211), specificity of 97.97% (773/789), false negative rate of 8.06% (17/211), and false positive rate of 2.03% (16/789). The negative predictive value (NPV) was 97.8% at a prevalence of 21.1% (211/1000).

Among the 17 smears originally found negative, there were 8 recorded as scanty, 7 as 1+, 1 smear as 2+, and 1 smear as 3+.

User Feedback and Efficiency: During the study, we also interviewed the three laboratory technicians about the system's user-friendliness and the key benefit to them if they decide to apply such a system in their routine procedures. The technicians' reports ranged from "above average" (4 points) to "excellent" (5 points), yielding an average of 4.67 points in user-friendliness. The first key comment from the technicians was that the system can help them to eliminate more than 85% of negative smears and only focus on reviewing the remaining 15% of slides. Their average time spent in the manual microscopic examination per smear per person was reduced from 5 min to around 2 min if using the automated system based on a 100-smear workload every day. This is equivalent to a time saving of 5 person-hr per day that the technicians can work on other important laboratory errands while the automated system reads the smears in parallel. Secondly, the technicians were surprised how the image recognition software could detect scanty acid-fast bacilli (Figure 2), which was too difficult for human eyes. Lastly, reading TB smears under microscopy for 4 to 5 h per day is unhealthy for human eyes. The automated system can significantly reduce the eye fatigue associated with manual microscope examination.

One of the key obstacles to applying digital solutions in microscopic systems is the image/data size, which could be a major cost concern. In this study, images generated for each smear covering 300 fields @1000× oil lens is about 60 MB on average, which is significantly smaller than the images generated from the whole slide scanner (WSI), which could be as big as 4 to 6 GB.

4. Discussion

The most economical, rapid, and readily available method for laboratory diagnosis of TB is acid-fast staining of sputum smear to identify mycobacterial acid-fast bacilli (AFB). However, the sensitivity of smear microscopy is highly variable [26] due to less experienced or trained staff, long hours of workload, and no presence of quality assurance [27–31]. New technologies, such as the Xpert and TB-LAMP, based on molecular methods, are becoming available. In addition, the fluorescence in situ hybridization (FISH) tests were also used for directly detecting mycobacteria in sputum, which has been successfully implemented in India [32–34]. However, it is unlikely that these technologies will be affordable replacements for smear microscopy in many high-burden countries without subsidy from the WHO or Gates Foundations. Thus, if automation, AI, and machine learning can be applied to TB smears, such a system may significantly increase the sensitivity of TB smear microscopy. Then, one may re-evaluate the pros and cons of TB smear microscopy and TB molecular methods, given the trial data that the test sensitivity and specificity are equivalent between TB smear microscopy and TB molecular methods.

In this on-site test, the test system achieved an accuracy of 96.70% (967/1000), sensitivity of 91.94% (194/211), specificity of 97.97% (773/789), false negative rate of 8.06% (17/211), and false positive rate of 2.03% (16/789). The system performed more than 90% in both test sensitivity and specificity, well above previous studies. Due to more consistent specimen preparation, the overall detection performance was better than the previous two studies [22,23]. This is competitive with Xpert, which has a sensitivity of around 90% as well [2]. In addition, regardless of the costs and resource issues with molecular methods, TB smear microscopy continues to play a role in TB diagnosis in monitoring the treatment of TB cases [2,6,7]. It is noteworthy that 17 smears were false negatives based on TB-Scan analysis. After carefully examining each scanned image, both technicians in this study could not find images with AFB. A smear that contains AFB may be outside of the scan area. Thus, to minimize such false negative results, smear preparation should follow a standardized procedure, and the specimen area should be in accordance with TB-Scan's scan area.

One of the important pieces of feedback from the medical technicians in the study hospitals is that they spent significantly less time, an average reduction of 5 person-hour per work day, in reading the microscope. The literature has documented the health hazards of prolonged microscopic work [35–37]. In a study with 450 enrolled study pathologists, 84.8% complained of musculoskeletal disorders (MSD), with the neck being the most common location of pain [35]. Furthermore, 74.8% reported visual refractive errors, among which myopia took the highest place [36]. Another study, with 163 pathologists participating in the study, showed that 40% of responders reported musculoskeletal problems in the previous month [37]. Almost 90% of pathologists had visual refraction errors, mainly myopia [37]. Using the automated system in our study may save three-fifths of the time spent reading smears on the microscope, improving the medical technicians' work morale. Furthermore, the medical technicians in the study hospital reported that the system usability ranged from "above average" to "excellent". We would like to credit the company that hired our in-house medical technicians who participated in the user interface design process. It is important that our user interface is compatible with the laboratory's existing workflow and standard operating procedures as closely as possible, so no ambiguity and confusion occur.

Current guidelines and recommendations state that smear microscopy alone cannot differentiate *Mycobacterium tuberculosis* complex and non-tuberculous mycobacteria (NTM) [2,30,38]. While culture is considered the gold standard diagnostic method for TB due to its high specificity and sensitivity, it is not commonly used due to cost, infrastructure requirements, and the long turnaround time for results [39–41]. Huang et al. hypothesized that for performance evaluation of smear microscopy automation systems, the gold standard should be the consensus of expert technicians rather than culture [22]. The rationale behind this hypothesis is that smear microscopy inherently cannot distinguish between *M. tuberculosis* and NTM. Using culture as the gold standard for evaluating smear microscopy automation systems may lead to false negatives when NTM is present, which would be detected as positive by the automation system. Therefore, we support the hypothesis that the performance evaluation of smear microscopy automation systems should use a panel of experienced medical technicians as the reference standard rather than culture. This approach would provide a more accurate and fair assessment of the system's ability to detect TB bacilli in smear microscopy images, as it aligns with the inherent limitations of smear microscopy in differentiating between *M. tuberculosis* and NTM.

Lastly, when considering the field deployment of an automated microscope system for clinical laboratories, several issues are noteworthy and could be considered as weaknesses: (a) Slide size compatibility: While the slide tray design of the automated system can accommodate most commercial slides, some slides may be too large to fit into the tray slots or too small and prone to falling out of the slide tray. This could impact the system's ability to process certain slide formats effectively. (b) Stain quality: The quality of the manual staining technique can influence the performance of the automated system, as the recognition software relies on color as an important parameter for detecting acid-fast bacilli (AFB). Inconsistent or suboptimal staining may compromise the system's ability to accurately identify AFB. We suggest that the use of commercially available automatic stain systems may well resolve the problems. (c) Image size: Most studies use whole slide scanners (WSIs) from digital pathology trying to capture mycobacteria at 400×. Regardless of whether the image quality is acceptable for detecting mycobacteria, the image size could be an issue. The large image size of a WSI, ranging from 4 to 6 GB for the whole 1 cm by 2 cm area, could be costly in data storage and network transfer. In this study, the test system takes each field of view into a compressed image file (i.e., JPEG), and the total data size for one smear is only 60 MB on average, which is a cost advantage for users when considering the digital solution.

5. Conclusions

This study demonstrated the potential of an automated intelligent microscopy system incorporating deep learning to improve the diagnosis of pulmonary tuberculosis through the detection of acid-fast bacilli (AFB) in sputum smears. The system achieved an overall accuracy of 96.70%, with a sensitivity of 91.94% and specificity of 97.97%. These results indicate a significant improvement over conventional manual microscopy, particularly in detecting scanty AFB that may be missed by human observers. In addition, the negative predictive value (NPV) of 97.85% at a prevalence of 21.1% is particularly noteworthy. This suggests that the system could be an effective tool for screening, as it reliably identifies negative samples. In resource-limited settings with high TB burdens, this could reduce the workload on laboratory technicians by allowing them to focus their attention on the smaller number of potentially positive samples. The system's ability to detect previously missed positive cases (17 out of 211 total positives) highlights its potential to improve case detection rates. This is crucial in the global fight against TB, where early and accurate laboratory diagnosis is key to effective treatment and prevention of transmission.

From an operational perspective, the feedback from laboratory technicians regarding the system's user-friendliness and efficiency improvement is encouraging. The reported time savings of approximately 5 person-hours per day for a 100-smear workload represent a significant improvement in laboratory efficiency. This could allow for increased testing capacity or reallocation of human resources to other critical tasks. Moreover, the reduction in eye strain and fatigue for technicians is an important occupational health benefit that should not be overlooked. Prolonged microscopy work can lead to various health issues, and any system that can alleviate this burden is valuable. Furthermore, the relatively small file size of the digital images (average 60 MB per smear) compared to whole slide imaging (WSI) systems is another advantage. This makes the system more feasible for implementation in resource-limited settings where data storage and transfer capabilities may be constrained.

However, it is important to note this study's limitations. The rejection of 150 smears due to various quality issues highlights the need for standardized sample preparation and potential training requirements for optimal system use. Future studies should address these issues and explore ways to minimize sample rejection rates.

While the performance of this system is promising, it is crucial to consider its place within the broader context of TB diagnostics. Molecular methods like Xpert MTB/RIF and TB-LAMP offer rapid results and can detect drug resistance, which this system cannot. However, the cost and infrastructure requirements of these molecular methods may limit their widespread adoption in high-burden, low-resource settings. Thus, this automated system could potentially bridge the gap between conventional microscopy and molecular methods. It offers improved sensitivity over manual microscopy while being more cost-effective and easier to implement than molecular tests. In a tiered diagnostic approach, this system could serve as an enhanced initial screening tool, with positive or uncertain results then confirmed by molecular methods.

Looking forward, further research is needed to validate these results in diverse settings and populations. Multi-center studies comparing this system directly with both manual microscopy and molecular methods in terms of diagnostic accuracy, cost-effectiveness, and operational feasibility would be valuable. Additionally, exploring the potential of this technology for other diseases requiring microscopic examination could broaden its impact on global health.

Lastly, this automated intelligent microscopy system represents a significant advancement in TB diagnostics. By combining the traditional method of sputum smear microscopy with cutting-edge AI and deep learning technologies, it offers a promising solution to enhance TB detection, particularly in high-burden, resource-limited settings. As we strive to meet the ambitious goals set by the UN High-Level Meeting on TB, innovations like this may play a crucial role in improving TB case detection, reducing diagnostic delays and ultimately assisting in our global efforts to end the TB epidemic.

Author Contributions: Conceptualization and methodology, W.-C.C. and Y.E.L.; formal analysis and validation, C.-C.C. and Y.E.L.; investigation and data curation, W.-C.C. and C.-C.C.; writing—original draft preparation, W.-C.C.; writing—review and editing, C.-C.C.; final revision, supervision, and project administration, Y.E.L. All authors have read and agreed to the published version of the manuscript.

Funding: This study received no monetary funding from any agency. Wellgen Medical provided an intelligent microscopy system and supporting staff free of charge during the study.

Data Availability Statement: Validation image dataset can be found at “Lin, Y.E.; Wellgen Medical, (2024), “Detecting Mycobacterium tuberculosis Bacilli from TB Smear Images”, Mendeley Data, V1, doi:10.17632/yhybmfrmgs.1”.

Acknowledgments: The authors thank all personnel involved in this study as volunteers.

Conflicts of Interest: The corresponding author, Y.E.L., was the founder of Wellgen Medical but is retired from the company’s managerial position and now serves as a college professor. The automation system tested in this study is not for sale in China, and Wellgen Medical has neither a business subsidiary nor distributors and sales representatives in China.

References

1. Churchyard, G.; Kim, P.; Shah, N.S.; Rustomjee, R.; Gandhi, N.; Mathema, B.; Dowdy, D.; Kasmar, A.; Cardenas, V. What we know about tuberculosis transmission: An overview. *J. Infect. Dis.* **2017**, *216* (Suppl. 6), S629–S635. [CrossRef]
2. World Health Organization. *Global Tuberculosis Report 2023*; WTO: Geneva, Switzerland, 2023.
3. Das, P.K.; Ganguly, S.B.; Mandal, B. Sputum smear microscopy in tuberculosis: It is still relevant in the era of molecular diagnosis when seen from the public health perspective. *Biomed. Biotechnol. Res. J. (BBRJ)* **2019**, *3*, 77–79. [CrossRef]
4. Steingart, K.R.; Schiller, I.; Horne, D.J.; Pai, M.; Boehme, C.C.; Dendukuri, N. Xpert® MTB/RIF assay for pulmonary tuberculosis and rifampicin resistance in adults. *Cochrane Database Syst. Rev.* **2021**, *1*, CD012768. [CrossRef]
5. UN High-Level Meeting on TB 2018. 2018. Available online: https://www.stoptb.org/un-high-level-meeting-tb/un-high-level-meeting-tb-2018 (accessed on 9 May 2024).
6. World Health Organization. *Automated Real-Time Nucleic Acid Amplification Technology for Rapid and Simultaneous Detection of Tuberculosis and Rifampicin Resistance: Xpert MTB*; World Health Organization: Geneva, Switzerland, 2013.
7. Figueredo, L.J.d.A.; Miranda, S.S.d.; Santos, L.B.d.; Manso, C.G.G.; Soares, V.M.; Alves, S.; Vater, M.C.; Kritski, A.L.; Carvalho, W.d.S.; Pádua, C.M.d. Cost analysis of smear microscopy and the Xpert assay for tuberculosis diagnosis: Average turnaround time. *Rev. Soc. Bras. Med. Trop.* **2020**, *53*, e20200314. [CrossRef] [PubMed]
8. Lewis, J.J.; Chihota, V.N.; Van der Meulen, M.; Fourie, P.B.; Fielding, K.L.; Grant, A.D.; Dorman, S.E.; Churchyard, G.J. “Proof-of-concept” evaluation of an automated sputum smear microscopy system for tuberculosis diagnosis. *PLoS ONE* **2012**, *7*, e50173. [CrossRef]
9. Panicker, R.O.; Soman, B.; Saini, G.; Rajan, J. A review of automatic methods based on image processing techniques for tuberculosis detection from microscopic sputum smear images. *J. Med. Syst.* **2016**, *40*, 17. [CrossRef] [PubMed]
10. Xiong, Y.; Ba, X.; Hou, A.; Zhang, K.; Chen, L.; Li, T. Automatic detection of mycobacterium tuberculosis using artificial intelligence. *J. Thorac. Dis.* **2018**, *10*, 1936. [CrossRef]
11. Zingue, D.; Weber, P.; Soltani, F.; Raoult, D.; Drancourt, M. Automatic microscopic detection of mycobacteria in sputum: A proof-of-concept. *Sci. Rep.* **2018**, *8*, 11308. [CrossRef]
12. Lopez-Garnier, S.; Sheen, P.; Zimic, M. Automatic diagnostics of tuberculosis using convolutional neural networks analysis of MODS digital images. *PLoS ONE* **2019**, *14*, e0212094. [CrossRef]
13. El-Melegy, M.; Mohamed, D.; ElMelegy, T.; Abdelrahman, M. Identification of tuberculosis bacilli in ZN-stained sputum smear images: A deep learning approach. In Proceedings of the IEEE/CVF Conference on Computer Vision and Pattern Recognition Workshops, Long Beach, CA, USA, 15–20 June 2019.
14. Hu, M.; Liu, Y.; Zhang, Y.; Guan, T.; He, Y. Automatic detection of tuberculosis bacilli in sputum smear scans based on subgraph classification. In Proceedings of the 2019 International Conference on Medical Imaging Physics and Engineering (ICMIPE), Shenzhen, China, 22–24 September 2019; pp. 1–7.

15. Ibrahim, A.U.; Guler, E.; Guvenir, M.; Suer, K.; Serte, S.; Ozsoz, M. Automated detection of Mycobacterium tuberculosis using transfer learning. *J. Infect. Dev. Ctries.* **2021**, *15*, 678–686. [CrossRef]
16. Kuok, C.P.; Horng, M.H.; Liao, Y.M.; Chow, N.H.; Sun, Y.N. An effective and accurate identification system of Mycobacterium tuberculosis using convolution neural networks. *Microsc. Res. Tech.* **2019**, *82*, 709–719. [CrossRef]
17. López, Y.P.; Costa Filho, C.; Aguilera, L.; Costa, M. Automatic classification of light field smear microscopy patches using Convolutional Neural Networks for identifying Mycobacterium Tuberculosis. In Proceedings of the 2017 CHILEAN Conference on Electrical, Electronics Engineering, Information and Communication Technologies (CHILECON), Pucon, Chile, 18–20 October 2017; pp. 1–5.
18. Muyama, L.; Nakatumba-Nabende, J.; Mudali, D. Automated detection of tuberculosis from sputum smear microscopic images using transfer learning techniques. In Proceedings of the Intelligent Systems Design and Applications: 19th International Conference on Intelligent Systems Design and Applications (ISDA 2019), Auburn, WA, USA, 3–5 December 2019; Springer: Cham, Switzerland, 2021; pp. 59–68.
19. Pitchumani Angayarkanni, S.; Vanitha, V.; Karan, V.; Sivant, M. A novel architecture for improving tuberculosis detection from microscopic sputum smear images. In *International Conference on Image Processing and Capsule Networks*; Springer: Cham, Switzerland, 2022; pp. 51–62.
20. Serrão, M.; Costa, M.G.F.; Fujimoto, L.; Ogusku, M.M.; Costa Filho, C.F.F. Automatic bacillus detection in light field microscopy images using convolutional neural networks and mosaic imaging approach. In Proceedings of the 2020 42nd Annual International Conference of the IEEE Engineering in Medicine & Biology Society (EMBC), Montreal, QC, Canada, 20–24 July 2020; pp. 1903–1906.
21. Udegova, E.; Shelomentseva, I.; Chentsov, S. Optimizing Convolutional Neural Network Architecture for Microscopy Image Recognition for Tuberculosis Diagnosis. In *Advances in Neural Computation, Machine Learning, and Cognitive Research V: Selected Papers from the XXIII International Conference on Neuroinformatics, Moscow, Russia, 18–22 October 2021*; Springer: Cham, Switzerland, 2022; pp. 204–209.
22. Huang, H.-C.; Kuo, K.-L.; Lo, M.-H.; Chou, H.-Y.; Lin, Y.E. Novel TB smear microscopy automation system in detecting acid-fast bacilli for tuberculosis–A multi-center double blind study. *Tuberculosis* **2022**, *135*, 102212. [CrossRef] [PubMed]
23. Fu, H.-T.; Tu, H.-Z.; Lee, H.-S.; Lin, Y.E.; Lin, C.-W. Evaluation of an AI-based TB AFB smear screening system for laboratory diagnosis on routine practice. *Sensors* **2022**, *22*, 8497. [CrossRef] [PubMed]
24. Litjens, G.; Kooi, T.; Bejnordi, B.E.; Setio, A.A.A.; Ciompi, F.; Ghafoorian, M.; van der Laak, J.A.W.M.; van Ginneken, B.; Sánchez, C.I. A survey on deep learning in medical image analysis. *Med. Image Anal.* **2017**, *42*, 60–88. [CrossRef] [PubMed]
25. Bejnordi, B.E.; Veta, M.; Van Diest, P.J.; Van Ginneken, B.; Karssemeijer, N.; Litjens, G. Diagnostic Assessment of Deep Learning Algorithms for Detection of Lymph Node Metastases in Women with Breast Cancer. *JAMA* **2017**, *318*, 2199–2210. [CrossRef]
26. Steingart, K.R.; Henry, M.; Ng, V.; Hopewell, P.C.; Ramsay, A.; Cunningham, J.; Urbanczik, R.; Perkins, M.; Aziz, M.A.; Pai, M. Fluorescence versus conventional sputum smear microscopy for tuberculosis: A systematic review. *Lancet Infect. Dis.* **2006**, *6*, 570–581. [CrossRef]
27. Nguyen, T.; Wells, C.; Binkin, N.; Pham, D.; Nguyen, V. The importance of quality control of sputum smear microscopy: The effect of reading errors on treatment decisions and outcomes. *Int. J. Tuberc. Lung Dis.* **1999**, *3*, 483–487. [PubMed]
28. Van Deun, A.; Salim, A.H.; Cooreman, E.; Hossain, M.A.; Rema, A.; Chambugonj, N.; Hye, M.; Kawria, A.; Declercq, E. Optimal tuberculosis case detection by direct sputum smear microscopy: How much better is more? *Int. J. Tuberc. Lung Dis.* **2002**, *6*, 222–230.
29. Liang, Q.; Jiang, X.; Jia, J.; Zhao, L.; Li, Y.; Wang, F.; Dong, L.; Xue, Y.; Jiang, G.; Huang, H. An early and trustable indicator suggestive of non-tuberculosis mycobacteria isolation in a high tuberculosis burden setting. *J. Infect.* **2024**, *88*, 106149. [CrossRef]
30. Carvalho, T.F.M.; Santos, V.L.A.; Silva, J.C.F.; de Assis Figueredo, L.J.; de Miranda, S.S.; de Oliveira Duarte, R.; Guimarães, F.G. A systematic review and repeatability study on the use of deep learning for classifying and detecting tuberculosis bacilli in microscopic images. *Prog. Biophys. Mol. Biol.* **2023**, *180–181*, 1–18. [CrossRef]
31. Islam, M.R.; Khatun, R.; Uddin, M.K.M.; Khan, M.S.R.; Rahman, M.T.; Ahmed, T.; Banu, S. Yield of two consecutive sputum specimens for the effective diagnosis of pulmonary tuberculosis. *PLoS ONE* **2013**, *8*, e67678. [CrossRef]
32. Baliga, S.; Murphy, C.; Sharon, L.; Shenoy, S.; Biranthabail, D.; Weltman, H.; Miller, S.; Ramasamy, R.; Shah, J. Rapid method for detecting and differentiating Mycobacterium tuberculosis complex and non-tuberculous mycobacteria in sputum by fluorescence in situ hybridization with DNA probes. *Int. J. Infect. Dis.* **2018**, *75*, 1–7. [CrossRef]
33. Prabhu, V.; Coelho, S.; Achappa, B.; Baliga, S.; Sharon, L.; Shah, J. Role of fluorescence in situ hybridization in detecting Mycobacterium avium complex presenting as fever in treatment failure HIV. *J. Clin. Tuberc. Other Mycobact. Dis.* **2020**, *21*, 100188. [CrossRef] [PubMed]
34. Shah, J.S.; Ramasamy, R. Fluorescence In Situ Hybridization (FISH) Tests for Identifying Protozoan and Bacterial Pathogens in Infectious Diseases. *Diagnostics* **2022**, *12*, 1286. [CrossRef] [PubMed]
35. Khan, S. The dark side of being a pathologist: Unravelling the health hazards. *Indian J. Pathol. Microbiol.* **2024**, *67*, 46–50. [CrossRef] [PubMed]
36. Dervaux, A.; Vaysse, B.; Doutrellot-Philippon, C.; Couvreur, V.; Guilain, N.; Chatelain, D. Pathologist occupational hazards: Results of a survey for the French case. *Ann. Pathol.* **2020**, *40*, 2–11. [CrossRef] [PubMed]
37. Fritzsche, F.R.; Ramach, C.; Soldini, D.; Caduff, R.; Tinguely, M.; Cassoly, E.; Moch, H.; Stewart, A. Occupational health risks of pathologists—Results from a nationwide online questionnaire in Switzerland. *BMC Public Health* **2012**, *12*, 1054. [CrossRef]

38. Zhang, H.; Dai, X.; Hu, P.; Tian, L.; Li, C.; Ding, B.; Yang, X.; He, X. Comparison of targeted next-generation sequencing and the Xpert MTB/RIF assay for detection of Mycobacterium tuberculosis in clinical isolates and sputum specimens. *Microbiol. Spectr.* **2024**, *12*, e0409823. [CrossRef]
39. Munn-Mace, G.; Parmar, D. Treatment of tuberculosis in complex emergencies in developing countries: A scoping review. *Health Policy Plan.* **2018**, *33*, 247–257. [CrossRef]
40. Ngabonziza, J.C.S.; Ssengooba, W.; Mutua, F.; Torrea, G.; Dushime, A.; Gasana, M.; Andre, E.; Uwamungu, S.; Nyaruhirira, A.U.; Mwaengo, D.; et al. Diagnostic performance of smear microscopy and incremental yield of Xpert in detection of pulmonary tuberculosis in Rwanda. *BMC Infect. Dis.* **2016**, *16*, 660. [CrossRef]
41. Reid, M.J.; Arinaminpathy, N.; Bloom, A.; Bloom, B.R.; Boehme, C.; Chaisson, R.; Chin, D.P.; Churchyard, G.; Cox, H.; Ditiu, L.; et al. Building a tuberculosis-free world: The Lancet Commission on tuberculosis. *Lancet* **2019**, *393*, 1331–1384. [CrossRef] [PubMed]

microorganisms

MDPI

Article

Emergence of Recombinant Subclade D3/Y in Coxsackievirus A6 Strains in Hand-Foot-and-Mouth Disease (HFMD) Outbreak in India, 2022

Sanjaykumar Tikute [1], Pratik Deshmukh [1], Nutan Chavan [1], Anita Shete [2], Pooja Shinde [1], Pragya Yadav [2] and Mallika Lavania [1,*]

[1] Enteric Viruses Group, ICMR-National Institute of Virology, 20-A, Dr. Ambedkar Road, Pune 411001, Maharashtra, India; sanjaytikute@yahoo.co.in (S.T.); pratikdeshmukhdpd39@gmail.com (P.D.); nachavan@yahoo.in (N.C.)

[2] Maximum Containment Laboratory, ICMR-National Institute of Virology, 130, MCC, 1, Pashan—Sus Rd, Pashan, Pune 411021, Maharashtra, India; anitaaich2008@gmail.com (A.S.); hellopragya22@gmail.com (P.Y.)

* Correspondence: mallikalavania@gmail.com

Abstract: Coxsackievirus-A6 (CV-A6) is responsible for more severe dermatological manifestations compared to other enteroviruses such as CV-A10, CV-A16, and EV-A71, causing HFMD in children and adults. Between 2005 and 2007, the recombinant subclade D3/RF-A started to expand globally, and a CV-A6 pandemic started. The study aimed to conduct whole-genome sequencing (WGS) of an isolated CV-A6 strain from currently circulating HFMD cases from India in 2022. Gene-specific RT-PCR and sequencing were used to perform molecular characterization of the isolated virus. Confirmation of these isolates was also performed by transmission electron microscopy and WGS. Among eleven positive clinical enterovirus specimens, eight CV-A6 strains were successfully isolated in the RD cell line. Isolates confirmed the presence of the CV-A6 strain based on VP1 and VP2 gene-specific RT-PCR. Sequences of isolates were clustered and identified as the novel CV-A6 strain of the D3/Y sub-genotype in India. The studies revealed that the D3/Y sub-genotype is being introduced into Indian circulation. The predicted putative functional loops found in VP1 of CV-A6 showed that the nucleotide sequences of the amino acid were a remarkably conserved loop prediction compatible with neutralizing linear epitopes. Therefore, this strain represents a potential candidate for vaccine development and antiviral studies.

Keywords: HFMD; enteroviruses; CV-A6; RD cell line; TEM; nonsynonymous mutation

1. Introduction

HFMD is a common viral disease that infects young children below the age of five. The disease can be defined as an enterovirus (EV)-associated exanthem rash characterized by a febrile illness, oropharyngeal ulcers, and vesicular rashes on the hands, feet, palms, buttocks, knees, and soles [1]. In some cases, the disease may progress to cause neurological complications such as encephalomyelitis [2]; also, it may develop to cause aseptic meningitis, acute flaccid paralysis, and brainstem encephalitis.

Since 2008, atypical HFMD outbreaks have been primarily associated with the CV-A6 variant [3–7]. Contemporary surveillance data have demonstrated the potential of the CV-A6 virus for epidemic spread around the world, particularly in Brazil [8], China [9], France [10], Hong Kong [11], India [12], Japan [13], and Turkey [14]. CV-A6 has been associated with severe clinical symptoms in both children and adults in several nations, including Argentina [15], Brazil [16], China [17], Israel [18], Italy [19], and Japan [20]. These symptoms include a rash that resembles vasculitis and vesiculobullous exanthema.

CV-A6 is a non-enveloped positive-sense RNA virus and belongs to the genus Enterovirus, family *Picornaviridae*. It is a 7.4 kb long genome that contains one polyprotein, which viral proteases break to create suitable proteins. Structural proteins are essential for viral entry into host cells and immune evasion; the capsid protects the viral genome and makes it easier for the virus to attach to host cells during infection [21]. CV-A6 is spread by contact with respiratory or fecal fluids or other body fluids such as saliva, nasal mucus, blister fluid, and vesicles of infected individuals. Clinical manifestations of CV-A6-associated HFMD differ from traditional HFMD caused by EV-A71 or CV-A16. Atypical herpes and onychoptosis are the most common clinical symptoms of CV-A6-associated HFMD [22]. In some cases of patients with CV-A6, the symptom of Beau's lines occurs [23].

Due to limited data on the molecular characterization and whole-genome sequencing of CV-A6 strains from India, it is necessary to study the circulating lineages/clades of CV-A6 strains in the Indian population. By determining the circulating genotypes and recombinant strains of CV-A6 in India during the 2022 HFMD outbreak, we were able to investigate the evolutionary history of the disease. Using VP1/VP2 sequence analysis, we compared and analyzed the genetic characteristics of these recently sequenced CV-A6 variations as well as their evolutionary connections to other known worldwide strains. To better understand the prevalence of these recombinant strains, we also sequenced and characterized the almost complete genomes of eight typical CV-A6 strains circulating in India.

2. Materials and Methods

2.1. Sample Collection and Detection of EV RNA

Vesicular swabs (n = 225), throat swabs (n = 135), oral lesion swabs (n = 06), serum (n = 16), stool (n = 03), and urine (n = 40) specimens are among the 425 specimens, which were collected from symptomatic patients with HFMD from the referred hospitals and dispensaries.

All patients ranged in age from less than a year to more than twenty-one years, and their symptoms included fever; blisters on their hands, feet, and buttocks; and even mouth ulcers. One patient also had blisters in the genital region. The patient age distribution revealed that 23.9% of patients were between the ages of 11 and 35, and the male-to-female ratio was 1.92:1. Of the patients, 76.1% were under the age of 10.

Details about the patient including symptomatic conditions, type of clinical specimens, and a consent letter from the parents were obtained. All specimens were initially screened for pan-enterovirus qRT-PCR, followed by semi-nested RT-PCR targeting the VP1 region for typing. Among these characterized specimens, CV-A6-positive specimens were further selected for virus isolation based on the Ct values of qRT-PCR.

2.2. Virus Isolation

Throat swabs, serum, and vesicle swabs (vesicular fluid) were taken from HFMD patients. Those molecularly characterized as CV-A6 were selected for virus isolation. The procedure was carried out in a susceptible RD cell line. A total of eleven clinical specimens such as throat swabs, vesicular swabs, and serum were selected to attempt virus isolation. RD cells were prepared in Twenty-four-well plates using minimum essential medium (MEM Hi-Media, Thane, India) containing 10% fetal bovine serum, 100 μg/mL streptomycin, 100 U/mL penicillin, and a 37 °C incubation temperature with a supply of 5% CO_2. Clinical specimens were taken as undiluted (neat) and in a 1:10 dilution and inoculated onto the RD cell line, along with cell controls. At least twice a day, the cells were observed for morphological changes. The infected cells showing cytopathic effects (CPEs) were harvested and blind passages were carried out further.

2.3. Virus Propagation and Estimation of $TCID_{50}$

Among eight CV-A6 isolates passaged in the RD cell line using 24-well plates, one of the representative isolates was selected for propagation on a large scale. Scale-up was performed in T25, T75, and finally in T225 cm^2 tissue culture flasks. $TCID_{50}$ of the harvested isolate was further carried out in 96-well plates of the RD cell line by tenfold dilution. Cell sheet clearing indicated CPE, which represents cell death due to viruses. The Reed and Muench method was used for the calculation of titer.

2.4. Transmission Electron Microscopy (TEM)

Visualization of virus particles from virus isolates was acquired by transmission electron microscopy (TEM). For TEM analysis, negative staining of the sample was carried out with phosphotungstic acid as described earlier [24]. Samples were prefixed with 1% glutaraldehyde and negatively stained and a grid was examined under 100 KV in transmission electron microscopy (Tecnai 12 BioTwin $^{\text{TM}}$ (FEI, Eindhoven, The Netherlands)). Images were captured with a side-mounted 2 k × 2 k CCD camera (Megaview III, Olympus, Tokyo, Japan).

2.5. Confirmation of Enterovirus by Real-Time q-PCR from Isolates

RNA was extracted using QIAamp Viral RNA Mini Kit (Qiagen, Hilden, Germany) from the passaged viral lysate and subjected to real-time PCR (CFX96$^{\text{TM}}$ Real-Time System, Bio-RAD, Hercules, CA, USA) to confirm enterovirus positivity. Sanger sequencing was performed to determine the sequences of nucleotide bases. Reverse transcription polymerase chain reaction (RT-PCR) was performed to amplify the whole VP1 and VP2 genes using specific primers (Table 1) [25]. Cycle sequencing PCR was carried out using a BigDye direct cycle sequencing kit using specific primers for VP1 and VP2 genes. Using the BLAST search tool (http://www.ncbi.nlm.nih.gov/blast (accessed on 3 April 2023)), the sequence identity of the EV strains was determined. Molecular Evolutionary Genetics Analysis Version 6.0 (MEGA6) provided 1000 bootstrapping replicates for the phylogenetic analysis, which was conducted using the Maximum Likelihood approach.

Table 1. Primers used for VP1 and VP2 gene-specific RT-PCR and sequencing.

Primers	**Sequences (5′–3′)**	**Region**	**Nucleotide Positions (Range)**
224 Forward	GCIATGYTIGGIACICAYRT	VP1	1977–1996
222 Reverse	CICCIGGIGGIAYRWACAT	VP1	2969–2951
89 Forward	CCAGCACTGACAGCAGYNGARAYNGG	VP1	2602–2627
88 Reverse	TACTGGACCACCTGGNGGNAYRWACAT	VP1	2977–2951
12 Forward	ATGTAYGTICCICCIGGIGG	VP2	2917–2936
22 Forward	GCICCIGAYTGITGICCRAA	VP2	3408–3389
32 Reverse	GTYTGCCA	VP2	3009–3002

2.6. Whole-Genome Sequencing by Next-Generation Sequencing (NGS)

Whole-genome sequencing of the CV-A6 isolates was carried out using next-generation sequencing on the Illumina Miniseq platform. Using the Qubit RNA High Sensitivity (HS) kit (Thermo Fisher Scientific, Waltham, MA, USA), the concentration of extracted RNA was quantified using the Qubit® 2.0 Fluorometer (Invitrogen, Life Technologies, Carlsbad, CA, USA) and then kept at −80 °C until needed. Using the NEB/Next rRNA depletion kit (New England Biolabs, Ipswich, MA, USA) (human/mouse/rat), the host's ribosomal RNA was suppressed. Agencourt AMPure XP beads (Beckman Coulter, Brea, CA, USA) were used to further purify this RNA. The Qubit RNA High Sensitivity (HS) kit was used to quantify the depleted RNA. As recommended by the manufacturer for the depleted RNA, an RNA library was generated using the TruSeq Stranded mRNA LT Library preparation kit (llumina, San Diego, CA, USA). The Illumina Miniseq platform was loaded with the normalized library. After completion of the run, CLC Genomics. Workbench software Version 20 (CLC, Qiagen, Aarhus, Denmark) was used to import and analyze FASTQ data. A de novo method and reference mapping were both used to obtain the whole sequences of the etiological agent. Using MEGA software version 11, a Maximum Likelihood tree was constructed for the VP1 gene and the whole genome. A 1000-replication bootstrap was carried out. The reference-based assembly method in the workbench was used to retrieve the Coxsackievirus A6 sequences. OP896720.1 was used as the reference for CV-A6 strains.

Nucleotide substitution patterns and rates were estimated under the Tamura–Nei model (+G). A discrete Gamma distribution was used to model evolutionary rate differences among sites (5 categories, [+G]). The mean evolutionary rates in these categories were 0.00, 0.03, 0.20, 0.82, and 3.95 substitutions per site. The nucleotide frequencies are A = 27.81%, T/U = 24.93%, C = 23.52%, and G = 23.74%.

Each entry shows the probability of substitution (r) from one base (row) to another base (column). For simplicity, the sum of r values is made equal to 100. Rates of different transitional substitutions are shown in bold and those of transversion substitutions are shown in italics (Table 2). These evolutionary analyses were conducted in MEGA software version 11.

Table 2. The pattern of nucleotide substitution.

	A	**T**	**C**	**G**
A	-	*2.12*	*2.1*	**15.01**
T	*2.44*	-	**24.91**	*2.1*
C	*2.44*	**25.14**	-	*2.1*
G	**17.43**	*2.12*	2.1	-

2.7. Nucleotide Sequence Accession Numbers

All newly generated complete CV-A6 genome sequences obtained in this study have GenBank accession numbers from OR734733 to OR734740.

3. Results

3.1. Molecular Characterization of Enterovirus

A total of 425 clinical samples from 196 patients who had been diagnosed with HFMD were screened for pan-enterovirus using qRT-PCR. By using qRT-PCR, only 54.6% [107/196] of these patients showed evidence of EV RNA. Out of the patients who tested positive for human enterovirus, 42.0% [45/107] tested positive for CV-A16 and 28.97% [31/107] tested positive for CV-A6.

3.2. Virus Isolation

Based on Ct values (<25), eleven CV-A6-positive specimens (in duplicates) were inoculated onto a confluent monolayer of rhabdomyosarcoma (RD) cells. The infected cell lines were monitored daily for 5 to 6 days. The cells showed cytopathic effect (CPE) on day 4 postinfection. After 24 h of incubation, the cells begin to show morphological changes (Figure 1B). Virus-infected cells were harvested after showing CPE of 90 to 95% (Figure 1D). Another freeze–thaw process was performed and the inoculum was used for the next passage. The cells showed morphological changes from passage stage 3 (P-3) and a further blank passage was performed until passage stage 6 (P-6) and confirmed for the presence of CV-A6 using the VP1 and VP2 gene-specific RT-PCR cycle sequencing. Among eleven CV-A6-positive specimens, eight CV-A6 strains were successfully isolated in RD cell lines. A $TCID_{50}$ assay was performed on RD cells to estimate the viral titer of CV-A6. Cell sheet clearing indicates CPE, which represents cell death due to viral infectivity. From the experiment, 50% of wells showed CPE at the 10^{-10} dilution, which implies the titer is 10^{10}.

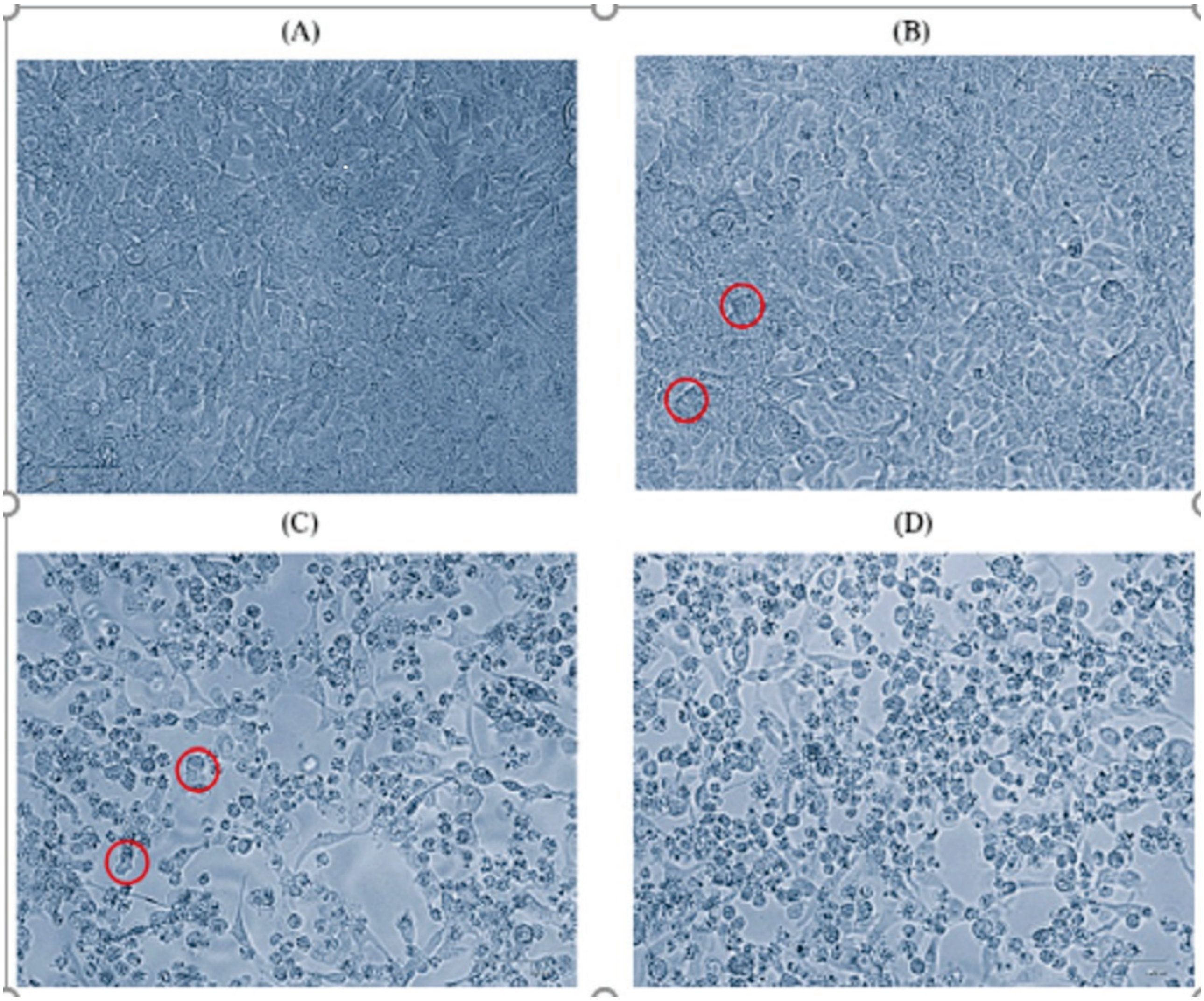

Figure 1. Microscopic images (40×) of RD cell line on day 4 of passage level 6. (**A**) Normal cells, (**B**) initiation of CPE, (**C**) 70% CPE, (**D**) 90% CPE (magnification 40×, EVOS XL core). Red circle indicates the CPE.

3.3. Confirmation of Virus Particles from Isolate by Transmission Electron Microscopy

TEM imaging of cleared and negatively stained isolates from individuals with CV-A6 (*n* = 05) revealed the various virus-like particles belonging to the *picornaviridae* family with a diameter of 30 nm (Figure 2). All HFMD patients were between 1 and 3.6 years old and had rashes on their hands and feet. Fever and mouth ulceration have been reported.

3.4. Confirmation of Isolates by q-Real-Time PCR and VP-1/VP-2 Sequencing

The data and Ct (cycle threshold) values generated from the CFX96^{TM} Real-Time System are arranged in ascending order. Ct values of CV-A6 isolates (783, 035, 722, 726, 273, 051, 064, 087, 274, and 085) were obtained by performing a real-time PCR assay for enterovirus and viral passages were confirmed. The Ct value of the isolates ranged between 11 and 27. Analysis of obtained data was further used for whole-genome sequencing experiments.

Molecular studies were conducted for the identification of CV-A6 strains and comparative analysis of the confirmed CV-A6 strains with other CV-A6 strains. Virus serotypes were identified using the BLASTn program from GenBank. The VP1 region of th confirmed strains CV-A6/087, CV-A6/051, CV-A6/722, CV-A6/726, CV-A6/274, and CV-A6/273 showed percentages of identity of 100%, 98.04%, 96.54%, 92.76%, 78%, 68.79% with OK635720.1, LC481419.1, OK635720.1, OP896720.1, MN233825.1, and OK635720.1, respectively. The VP2 region of the confirmed strains CV-A6/087, CV-A6/035, CV-A6/064, CV-A6/274, CV-A6/051, CV-A6/273, and CV-A6/783 showed percentages of identity of 98.19%, 97.46%, 96.52%, 96.04%, 95.27%, 94.41%, 85.80% with OP896719.1, OP896719.1, OP896719.1, MZ491032.1, MN845889.1, OL830040.1, and MN845859.1, respectively.

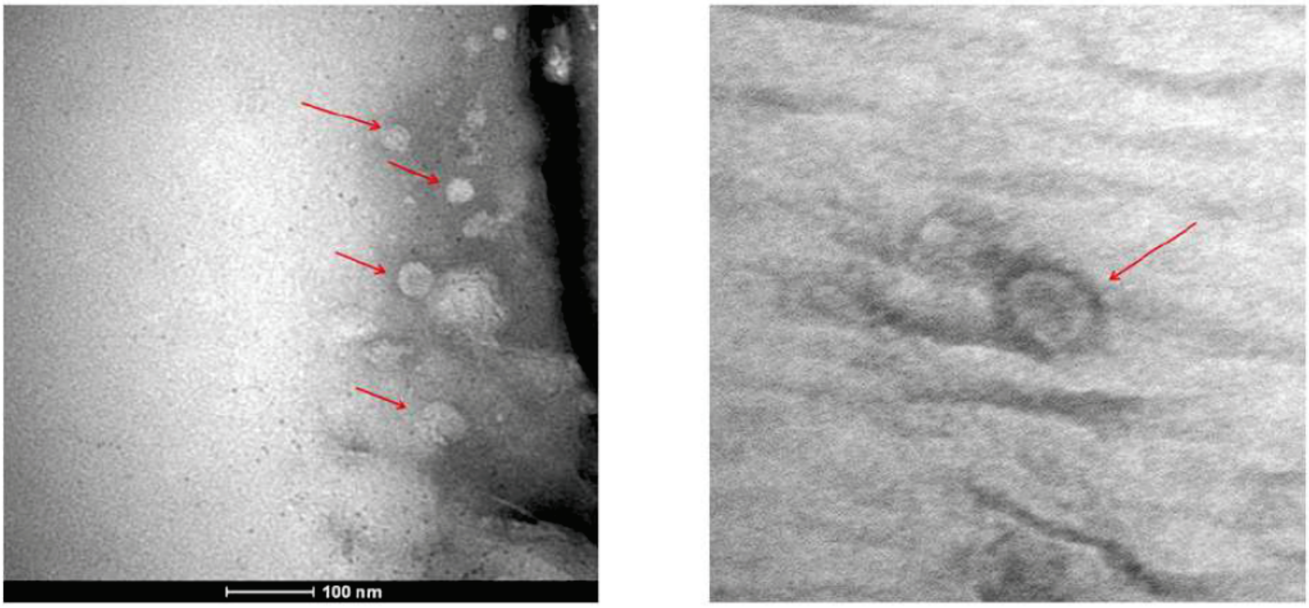

Specimen : CV-A6/051
Details : 30 nm virus like particles at very low frequency detected in fields scanned and suggested that virus belongs to family *picornaviridae*

Specimen : CV-A6/087
Details : 30 nm virus like particles at very low frequency detected in fields scanned and suggested that virus belongs to family *picornaviridae*

Figure 2. TEM imaging from the virus isolates from HFMD patients. Red arrows showing the 30 nm virus like particles.

3.5. Whole-Genome Sequencing by Next-Generation Sequencing (NGS)

To obtain new insights into the genetic diversity of CV-A6, we sequenced the whole genomes of eight isolates of CV-A6 strains with good CPE that were collected in 2022 (Table 3). All eight isolate sequences were derived from eight different patients. These sequences were then compared to GenBank reference sequences. The CV-A6 strains in this study had a nearly complete genome of 7435 nt, which included an ORF encoding a polyprotein precursor with 2201 amino acids and a portion of the 5′ UTR.

The whole genome of study isolates was aligned along with full whole-genome sequences of reference strains (OP896720, MN845848, OP896719, KM114057, MH780756, AB779614, JN203517, AY421764, JQ364886, KP143074, MN845781, MT814422, OL830039). All eight CV-A6 strains grouped together to form a clade, which was confirmed by the 5′ UTR, P1, and P2 regions having high bootstrap values (96–100%). Within the structural protein of the investigated strains, a strain belonging to subclade D3 that was identified in Thailand in 2022 had the most significant identity (97.7–99.5% nt identity). To elucidate the mutation in the VP1 gene (914 bp) of the D3/Y strains of CV-A6 compared the amino acid and nucleotide variation between the VP1 sequences of representative isolated strains and reference D3/Y strains, sequence alignment was performed and analyzed with reference CV-A6 strain (OP896720.1) by Needleman–Wunsch alignment and MEGA software version 11.

Table 3. Data was obtained from NGS with the percentage of identity and genome coverage as well as genomic length of all CV-A6 isolates. All isolates were mapped with OP896720.1 as aligned in the NCBI server, and it is taken as a reference strain.

Isolate ID	Percentage of Identity	Reference Strain	Consensus Length	Genome Coverage
CV-A6/726/NIV/IND/2023	98.25%	CV-A6 Isolate Thailand/2022 (OP896720.1)	7435	99%
CV-A6/274/NIV/IND/2023	98.20%		7435	99%
CV-A6/064/NIV/IND/2023	98.12%		7435	100%
CV-A6/035/NIV/IND/2023	97.87%		7435	100%
CV-A6/087/NIV/IND/2023	97.85%		7435	100%
CV-A6/783/NIV/IND/2023	97.82%		7435	100%
CV-A6/723/NIV/IND/2023	97.74%		7435	100%
CV-A6/051/NIV/IND/2023	97.00%		7435	99%

All CV-A6 isolates showed 97% to 98% identity with the reference strain with 2% to 3% nucleotide substitution in the VP1 region. The VP1-encoding gene of EVs is crucial in preventing the host immune response from being triggered. This study found 33 sites of nonsynonymous mutations in the VP1 gene of the isolates. Among them, 2456 (Q 578 P), 2465 (V 581 A), 2531 (L 603 P), 2657 (R 656 Q), 2666 (N 648 S), 2783 (V 687 A), 2813 (L 697 S), 2858 (R 712 H), 2870 (C 716 Y), 2888 (Y 722 C), 2897 (G 725 E), 2900 (L 726 P), 2906 (N 728 S), 2975 (I 751 T), 3077 (I 785 T), 3083 (N 787 S), 3164 (M 814 T), 3218 (S 832 F), 3221 (A 833 D), 3230 (L 836 P), 3272 (P 850 L), and 3290 (V 856 A) were present and more frequently seen in the isolates as compared to the reference strain from the D3/Y subclade (Supplementary Table S1).

The VP1 region sequences were categorized into clades A–D, and clade D was further subdivided into the D1–D3 subclades based on established classification criteria. This study found 33 types of non-synonymous mutations in the VP1 gene of the isolates. Based on the whole genomes of CV-A6 isolates and other reference strains, a phylogenetic tree was built using NGS data. Every significant functional area of the genome was analyzed separately. The evolutionary history was determined by the Neighbor-Joining method. The percentage of replicate trees with clustered taxa in the bootstrap test (1000 repetitions) is indicated above the branches (Figure 3). With branch lengths matching the evolutionary distances used to build the phylogenetic tree. The evolutionary distances are reported in base substitutions per site and have been derived using the Maximum Composite Likelihood method. The final dataset comprised 7439 locations. MEGA11 was used to carry out evolutionary analysis, with branch lengths matching the evolutionary distances used to build the phylogenetic tree. The evolutionary distances are reported in base substitutions per site and have been derived using the Maximum Composite Likelihood method.

Sequences of the isolates were clustered and identified to the new D3/Y sub-genotype, which exist in the dominant CV-A6 genotype that is currently in circulation in Thailand [26]. Most of the global outbreaks that have occurred were due to sub-genotype D3. The findings suggest that the persistent international circulation of CV-A6 may be due to the high transmission, infectivity, and virulence of sub-genotype D3 strains [27]. It can be suspected that the D3/Y sub-genotype has now been introduced into Indian circulation.

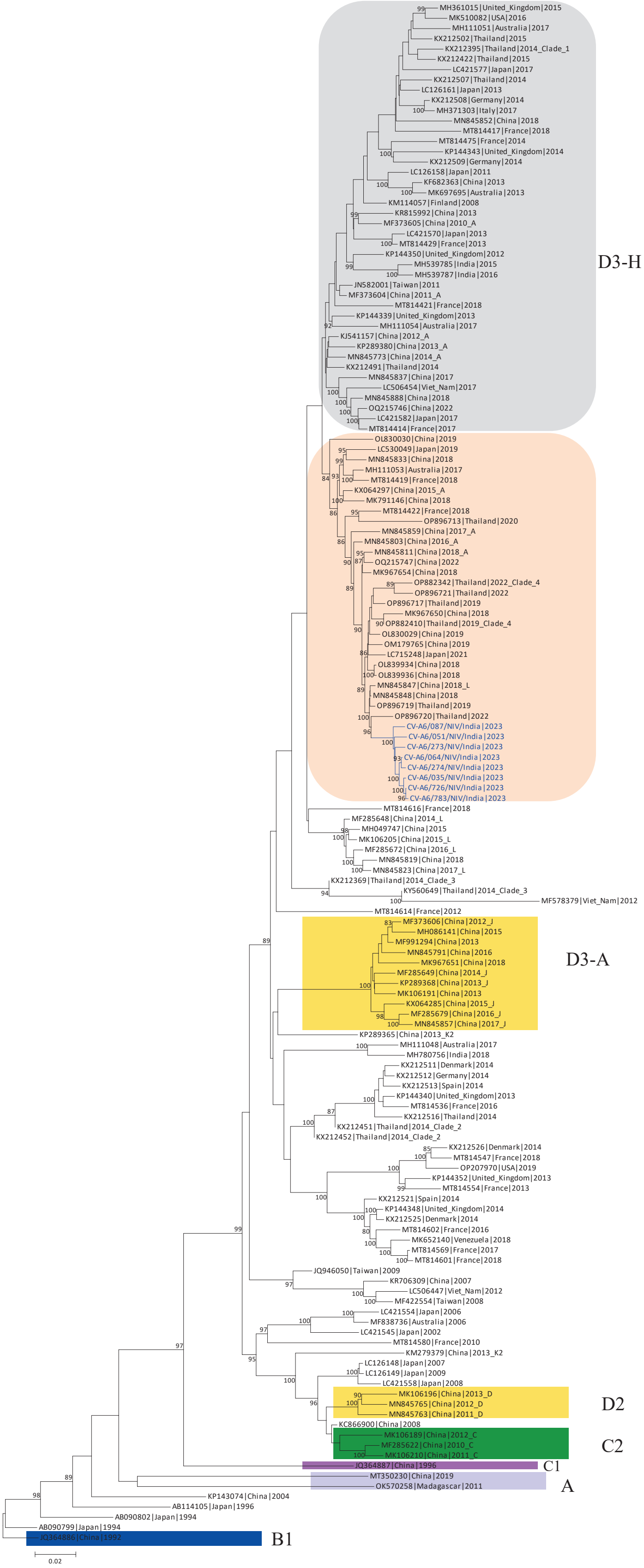

Figure 3. Time-scaled phylogenetic tree of sequences of coxsackievirus (CV)-A6 variants. The phylogenetic tree was generated using CV-A6 sequences characterized in this study (blue) and previously published sequences. Clades described in previous studies (A, B1, C1, C2, D2, and D3) are shown.

4. Discussion

Infection due to CV-A6 causes HFMD in both children and adults. Despite the major risk that CV-A6 illnesses represent to public health, our knowledge of the mechanisms by which new CV-A6 strains originate remains restricted [26]. Since 2008, CV-A6 strains have become the main genotype responsible for global epidemics of atypical HFMD [3]. Several sporadic cases of HFMD with high morbidity and death have occurred, mainly in Southeast Asian nations since 1997 and India after 2003 [23]. Multiple enterovirus serotypes were found to circulate simultaneously in HFMD patients from Bhubaneswar, Odisha, in 2009, southern and eastern India in 2009–2010 [22], and northern Kerala in 2015–2016. CV-A6 was the leading cause of HFMD in India from 2015 to 2017, followed by CV-A16 and CV-A10 [28]. Co-circulation of CV-A6 and CV-A16 was reported to cause HFMD in Mumbai in May–June 2018 [29]. It is essential to study the CV-A6 strains causing HFMD that are currently circulating in India. Due to limited data on the isolation of recent CV-A6 strains, its molecular characterizations and whole-genome sequencing will emphasize the genetic changes that occurred during this period. This study aimed to isolate, characterize, and perform whole-genome sequencing of the viral isolates causing HFMD in India. The study was based on three different research parameters, which comprise the isolation of the viral agents causing HFMD in the RD cell line. Molecular studies were conducted for identification, comparative analysis, and whole-genome sequencing by using next-generation sequencing using the Illumina platform for comparative studies. It provides knowledge of the genetic organization of the currently circulating CV-A6 viral strains. The study also provides information on the molecular characterizations of etiological agents and the evolutionary pattern of different CV-A6 isolates from various geographical locations in India.

Isolation of the clinically positive specimens was carried out in susceptible RD cell lines. The cell line was infected with the positive enterovirus samples. After 4 to 5 days of incubation, the cell line showed morphological changes in the form of cytopathic effect (CPE). Viral-infected cells with 90% CPE were collected, freeze–thawed, and utilized as an inoculum for subsequent passages. The cells showed morphological changes from passage level 3 (P-3) and further blind passaging was performed till passage level 6 (P-6) to get the best viral titer and confirm the presence of CV-A6 based on VP1 and VP2 gene-specific RT-PCR and cycle sequencing. Among eleven positive enterovirus specimens, eight CV-A6 strains were successfully isolated in RD cell lines. The representative viral agent was propagated on a large scale and further processed for virus titration. Virus titration was performed using tenfold dilutions of viral lysate and the titer was estimated in $TCID_{50}$. Isolated virus showed a 50% infectivity dose at a 10^{10} titer. VP1 and VP2 typing enables us to determine the sub-genotype of the viral strain. Sequences of isolates were clustered and identified to the new CV-A6 D3/Y sub-genotype, which existed in the dominant CV-A6 genotype circulating in Thailand [27]. Most of the global outbreaks that occurred thereafter were due to sub-genotype D3. The data show that ongoing international circulation of CV-A6 might be attributed to the high transmission, infectivity, and virulence of sub-genotype D3 viruses. It is suspected that the D3/Y sub-genotype is now emerging in India.

The phylogenetic tree was constructed using NGS data, and the whole genome of the study isolates was aligned along with whole genome sequences of reference strains. This study provided essential data, which will be useful for further studies. However, the VP1 gene is regarded as the most informative and sturdy region in evolutionary studies because of its wide range of diversity and lack of involvement in recombination. [29]. Human enteroviruses evolve by genetic drift and, over considerably longer periods, antigenic diversity in the structural gene region encoding the viral capsid, which includes VP1 [30]. When comparing strains with the reference strain (OP896720.1), nucleotide alterations and amino acid substitutions in the VP1 gene (914 bp) of representative isolates (CV-A6/087, CV-A6/274, CV-A6/051, CV-A6/783) were observed from the same subclade of isolates. All isolates showed 97% to 98% identity with the reference strain (OP896720.1) with 2% to 3% nucleotide substitution in the VP1 region. The VP1-encoding gene of EVs is crucial in preventing the host immune response from being triggered. This study found 33 sites of nonsynonymous mutations in the VP1 gene of the isolates. Among them, 22 mutations were at high frequencies in the isolates as compared to the reference strain (OP896720.1) from the D3/Y sub-genotype.

In previous studies, the amino acid changes between the four virus strains and the subclade D3/A strains from Thailand were compared to mutations in the subclade D3/Y strains from Thailand. There were fewer nonsynonymous mutations in the structural proteins (at the fifth position) than in the non-structural proteins. A crucial part of EVs' ability to elude the host immune response is their VP1-encoding gene. The VP1 gene of the sub-genotype CV-A6 D3/Y strains showed nine locations with nonsynonymous alterations. Among these, three mutations were present more frequently in the D3/Y sub-genotype [26]. The whole genome was analyzed using previous CV-A6 reference strains. Sequences of the isolates were clustered and identified to the new CV-A6 D3/Y sub-genotype, which was the predominant CV-A6 genotype circulating in Thailand. It can be suspected that the CV-A6 D3/Y sub-genotype is now in Indian circulation. Analysis of the complete VP1 gene revealed multiple nucleotide changes and amino acid substitutions and found 33 sites of nonsynonymous mutations in the VP1 gene of the isolates. Studies have shown that multiple protruding loops, such as the BC loop (residues 97–105), the EF loop (residues 163–177), and the GH loop (residues 208–225), and proximity of the C-terminus (residues 253–267) in VP1 have been identified as the significant antigenic proteins exposed on the viral surface. The host cell receptor for CV-A6 was found to be Kringle-Containing Transmembrane Protein 1 (KREMEN1). The BC, DE, EF, and HI loops on the surface of VP1 are the preferred binding sites for many short RNA viral receptors. Mutations in the 712th, 716th, 722nd, 725th, 751st, 785th, and 833rd amino acid positions of the VP1 region can change the structural characteristics of the capsid and alter the virus' ability to bind to the KREMEN1. Further studies can be conducted on how these amino acids alter the structural changes in the viral capsid and whether they help to bind the KREMEN1 receptor and the role of amino acids in causing infectivity. Predicted putative functional loops found in the VP1 of CV-A6 showed that the nucleotide sequences of the amino acid were remarkably conserved loops; this prediction is compatible with neutralizing linear epitopes. As a result, the D3/Y strains further represent a potential candidate for the development of a CV-A6 vaccine and antiviral studies.

5. Conclusions

This study provides further information on the molecular aspects and evolutionary patterns of different CV-A6 isolates from different geographical regions, revealing the importance of evolutionary relationships, as well as the genetic organization of the current circulating CV-A6 viral strains. The data will facilitate the development of effective diagnostic tools, antiviral therapies, and vaccines for the prevention and control of CV-A6-associated HFMD.

Supplementary Materials: The following supporting information can be downloaded at https://www.mdpi.com/article/10.3390/microorganisms12030490/s1. Supplementary Table S1: Nucleotide changes and amino acid substitutions identified in VP1 gene (914 bp) of the representative CV-A6 strains with the reference CV-A6 strain (OP896720.1) from Thailand.

Author Contributions: Conceptualization, M.L.; Methodology, S.T., N.C. and P.S.; Formal analysis, P.D. and M.L.; Investigation, S.T. and P.D.; Resources, A.S. and P.Y.; Data curation, S.T., P.D., N.C. and P.S.; Writing—original draft, S.T. and M.L.; Writing—review & editing, M.L.; Project administration, M.L. All authors have read and agreed to the published version of the manuscript.

Funding: The APC was funded by ICMR-National Institute of Virology, grant number ENV1301.

Institutional Review Board Statement: This study was approved by ICMR-National Institute of Virology Institutional Ethics Committee No: NIV/IEC/Oct/2023/D-4.

Informed Consent Statement: Informed consent was obtained from all subjects involved in the study.

Data Availability Statement: Data are contained within the article and Supplementary Materials.

Conflicts of Interest: The authors declare no conflict of interest.

References

1. Hubiche, T.; Schuffenecker, I.; Boralevi, F.; Léauté-Labrèze, C.; Bornebusch, L.; Chiaverini, C.; Phan, A.; Maruani, A.; Miquel, J.; Lafon, M.-E.; et al. Dermatological spectrum of hand, foot and mouth disease from classical to generalized exanthema. *Pediatr. Infect. Dis. J.* **2014**, *33*, e92–e98. [CrossRef] [PubMed]
2. Sabeena, S.; Bhat, K.G.; Bharani, K.C.; Ramachandran, S.; Arunkumar, G. Coxsackievirus A6 (CV-A6) Encephalomyelitis in an Immunocompromised Child: A Case Report and Brief Review of the Literature. *Jpn. J. Infect. Dis.* **2018**, *71*, 388–389. [CrossRef]
3. Österback, R.; Vuorinen, T.; Linna, M.; Susi, P.; Hyypiä, T.; Waris, M. Coxsackievirus A6 and hand, foot, and mouth disease, finland. *Emerg. Infect. Dis.* **2009**, *15*, 1485–1488. [CrossRef]
4. Flett, K.; Youngster, I.; Huang, J.; McAdam, A.; Sandora, T.J.; Rennick, M.; Smole, S.; Rogers, S.L.; Nix, W.A.; Oberste, M.S.; et al. Hand, foot, and mouth disease caused by Coxsackievirus A6. *Emerg. Infect. Dis.* **2012**, *18*, 1702–1704. [CrossRef] [PubMed]
5. Cabrerizo, M.; Tarragó, D.; Muñoz-Almagro, C.; del Amo, E.; Domínguez-Gil, M.; Eiros, J.M.; López-Miragaya, I.; Pérez, C.; Reina, J.; Otero, A.; et al. Molecular epidemiology of enterovirus 71, coxsackievirus A16 and A6 associated with hand, foot and mouth disease in Spain. *Clin. Microbiol. Infect.* **2014**, *20*, O150–O156. [CrossRef] [PubMed]
6. Song, Y.; Zhang, Y.; Ji, T.; Gu, X.; Yang, Q.; Zhu, S.; Xu, W.; Xu, Y.; Shi, Y.; Huang, X.; et al. Persistent circulation of Coxsackievirus A6 of genotype D3 in mainland of China between 2008 and 2015. *Sci. Rep.* **2017**, *7*, 5491. [CrossRef] [PubMed]
7. Gaunt, E.; Harvala, H.; Österback, R.; Sreenu, V.B.; Thomson, E.; Waris, M.; Simmonds, P. Genetic characterization of human coxsackievirus A6 variants associated with atypical hand, foot and mouth disease: A potential role of recombination in emergence and pathogenicity. *J. Gen. Virol.* **2015**, *96 Pt 5*, 1067–1079. [CrossRef]
8. Carmona, R.C.; Machado, B.C.; Reis, F.C.; Jorge, A.M.; Cilli, A.; Dias, A.M.; Morais, D.R.; Leme, L.; Yu, A.L.; Silva, M.R.; et al. Hand, foot, and mouth disease outbreak by Coxsackievirus A6 during COVID-19 pandemic in 2021, São Paulo, Brazil. *J. Clin. Virol.* **2022**, *154*, 105245. [CrossRef]
9. Zhang, M.; Chen, X.; Wang, W.; Li, Q.; Xie, Z. Genetic characteristics of Coxsackievirus A6 from children with hand, foot and mouth disease in Beijing, China, 2017–2019. *Infect. Genet. Evol.* **2022**, *106*, 105378. [CrossRef]
10. Mirand, A.; Cohen, R.; Bisseux, M.; Tomba, S.; Sellem, F.C.; Gelbert, N.; Béchet, S.; Frandji, B.; Archimbaud, C.; Brebion, A.; et al. A large-scale outbreak of hand, foot and mouth disease, France, as at 28 September 2021. *Eurosurveillance* **2021**, *26*, 2100978. [CrossRef]
11. Lau, S.K.; Zhao, P.S.; Sridhar, S.; Yip, C.C.; Aw-Yong, K.L.; Chow, E.Y.; Cheung, K.C.; Hui, R.W.; Leung, R.Y.; Lai, Y.S.; et al. Molecular epidemiology of coxsackievirus A6 circulating in Hong Kong reveals common neurological manifestations and emergence of novel recombinant groups. *J. Clin. Virol.* **2018**, *108*, 43–49. [CrossRef] [PubMed]
12. Saxena, V.K.; Pawar, S.D.; Qureshi, T.H.I.H.; Surve, P.; Yadav, P.; Nabi, F.; Mendadkar, R. Isolation and molecular characterization of coxsackievirus A6 and coxsackievirus A16 from a case of recurrent Hand, Foot and Mouth Disease in Mumbai, Maharashtra, India, 2018. *VirusDisease* **2020**, *31*, 56–60. [CrossRef] [PubMed]
13. Mizuta, K.; Tanaka, S.; Komabayashi, K.; Aoki, Y.; Itagaki, T.; Katsushima, F.; Katsushima, Y.; Yoshida, H.; Ito, S.; Matsuzaki, Y.; et al. Phylogenetic and antigenic analyses of coxsackievirus A6 isolates in Yamagata, Japan between 2001 and 2017. *Vaccine* **2019**, *37*, 1109–1117. [CrossRef] [PubMed]
14. Ceylan, A.N.; Turel, O.; Gultepe, B.S.; Inan, E.; Turkmen, A.V.; Doymaz, M.Z. Hand, Foot, and Mouth Disease Caused by Coxsackievirus A6: A Preliminary Report from Istanbul. *Pol. J. Microbiol.* **2019**, *68*, 165–171. [CrossRef]
15. Cisterna, D.M.; Lema, C.L.; Martinez, L.M.; Verón, E.; Contarino, L.P.; Acosta, D.; Freire, M.C. Atypical hand, foot, and mouth disease caused by Coxsackievirus A6 in Argentina in 2015. *Rev. Argent Microbiol.* **2019**, *51*, 140–143. [CrossRef]
16. Justino, M.C.A.; Mesquita, D.d.S.; Souza, M.F.; Farias, F.P.; Alves, J.C.d.S.; Ferreira, J.L.; Lopes, D.P.; Tavares, F.N. Atypical hand-foot-mouth disease in Belém, Amazon region, northern Brazil, with detection of coxsackievirus A6. *J. Clin. Virol.* **2020**, *126*, 104307. [CrossRef]
17. Gao, Y.; Ma, G.; Xiao, Y.; Cai, Q.; Chen, Y.; Shi, P.; Wang, K.; Shen, Y.; Shi, C. An Outbreak of Coxsackievirus A6 Infection in Adults of a Collective Unit, China, 2019. *Can. J. Infect. Dis. Med. Microbiol.* **2022**, *2022*, 6607294. [CrossRef]
18. Renert-Yuval, Y.; Marva, E.; Weil, M.; Shulman, L.; Gencylmaz, N.; Sheffer, S.; Wolf, D.; Molho-Pessach, V. Coxsackievirus A6 Polymorphic Exanthem in Israeli Children. *Acta Derm. Venereol.* **2016**, *96*, 546–549. [CrossRef] [PubMed]
19. Broccolo, F.; Drago, F.; Ciccarese, G.; Genoni, A.; Puggioni, A.; Rosa, G.M.; Parodi, A.; Manukyan, H.; Laassri, M.; Chumakov, K.; et al. Severe atypical hand-foot-and-mouth disease in adults due to coxsackievirus A6: Clinical presentation and phylogenesis of CV-A6 strains. *J. Clin. Virol.* **2019**, *110*, 1–6. [CrossRef] [PubMed]
20. No, T.-H.; Jo, K.M.; Jung, S.Y.; Kim, M.R.; Kim, J.Y.; Park, C.S.; Kym, S. Coxsackievirus A6-induced Hand-Foot-and-Mouth Disease Mimicking Stevens-Johnson Syndrome in an Immunocompetent Adult. *Infect. Chemother.* **2020**, *52*, 634–640. [CrossRef] [PubMed]
21. Büttner, C.R.; Spurný, R.; Füzik, T.; Plevka, P. Cryo-electron microscopy and image classification reveal the existence and structure of the coxsackievirus A6 virion. *Commun. Biol.* **2022**, *5*, 898. [CrossRef]
22. Chen, Y.-J.; Chang, S.-C.; Tsao, K.-C.; Shih, S.-R.; Yang, S.-L.; Lin, T.-Y.; Huang, Y.-C. Comparative genomic analysis of Coxsackievirus A6 strains of different clinical disease entities. *PLoS ONE* **2012**, *7*, e52432. [CrossRef] [PubMed]

23. Mahajan, V.; Sharma, A.; Mehta, K.; Chauhan, P.; Manvi, S.; Chauhan, A. Hand, Foot and Mouth Disease: A Single Centre Retrospective Study of 403 New Cases and Brief Review of Relevant Indian Literature to Understand Clinical, Epidemiological, and Virological Attributes of a Long-Lasting Indian Epidemic. *Indian Dermatol. Online J.* **2022**, *13*, 310–320. [CrossRef] [PubMed]
24. Brenner, S.; Horne, R.W. A negative staining method for high resolution electron microscopy of viruses. *Biochim. Biophys. Acta* **1959**, *34*, 103–110. [CrossRef] [PubMed]
25. Nix, W.A.; Oberste, M.S.; Pallansch, M.A. Sensitive, seminested PCR amplification of VP1 sequences for direct identification of all enterovirus serotypes from original clinical specimens. *J. Clin. Microbiol.* **2006**, *44*, 2698–2704. [CrossRef] [PubMed]
26. Puenpa, J.; Saengdao, N.; Khanarat, N.; Korkong, S.; Chansaenroj, J.; Yorsaeng, R.; Wanlapakorn, N.; Poovorawan, Y. Evolutionary and Genetic Recombination Analyses of Coxsackievirus A6 Variants Associated with Hand, Foot, and Mouth Disease Outbreaks in Thailand between 2019 and 2022. *Viruses* **2022**, *15*, 73. [CrossRef]
27. Zeng, H.; Lu, J.; Yang, F.; Liu, L.; Zheng, H.; Ke, C.; Song, T.; Li, H.; Sun, L. The increasing epidemic of hand, foot, and mouth disease caused by coxsackievirus-A6, Guangdong, China, 2017. *J. Infect.* **2018**, *76*, 220–223. [CrossRef]
28. Sanjay, R.E.; Josmi, J.; Sasidharanpillai, S.; Shahin, S.; Michael, C.J.; Sabeena, S.; Aswathyraj, S.; Kavitha, K.; Shilpa, C.; Prasada, S.V.; et al. Molecular epidemiology of enteroviruses associated with hand, foot, and mouth disease in South India from 2015 to 2017. *Arch. Virol.* **2022**, *167*, 2229–2238. [CrossRef]
29. Gopalkrishna, V.; Ganorkar, N. Epidemiological and molecular characteristics of circulating CVA16, CVA6 strains and genotype distribution in hand, foot and mouth disease cases in 2017 to 2018 from Western India. *J. Med. Virol.* **2021**, *93*, 3572–3580. [CrossRef]
30. Tee, K.K.; Lam, T.T.-Y.; Chan, Y.F.; Bible, J.M.; Kamarulzaman, A.; Tong, C.Y.W.; Takebe, Y.; Pybus, O.G. Evolutionary genetics of human enterovirus 71: Origin, population dynamics, natural selection, and seasonal periodicity of the VP1 gene. *J. Virol.* **2010**, *84*, 3339–3350. [CrossRef]

microorganisms

MDPI

Review

Using In Vitro Models to Study the Interactions Between Environmental Exposures and Human Microbiota

Qiwen Cheng [1,2] and Shengxi Chen [1,*]

[1] Biodesign Center for Bioenergetics, Arizona State University, Tempe, AZ 85281, USA
[2] Center for Big Data, Qilu Hospital of Shandong University, Jinan 250012, China
* Correspondence: shengxi.chen.1@asu.edu

Abstract: Research has demonstrated a close correlation between human microbiota and overall health, highlighting their intimate connection. Exposure to environmental factors, such as chemical contaminants and biological agents, has the potential to alter the composition and function of microbiota, thereby influencing health outcomes. Meanwhile, microbiota may contribute to host protection by degrading, or rendering harmless, exposures. Environmental exposures demonstrate significant diversity and dynamism; however, conventional methods for exposure–microbiota research, such as animal and epidemiological studies, are often both time-consuming and costly. Additionally, they may raise ethical concerns. This review aimed to examine the existing understanding of employing in vitro models to investigate the interactions between environmental exposures and human microbiota, particularly those located outside the large intestine. A comprehensive search was conducted across the Web of Science, PubMed, and Scopus databases, employing a range of keywords related to microbiota, exposures, and in vitro models. A total of 58 studies fulfilled the search criteria, revealing instances of microbial modulation of exposures and vice versa. It was observed that, although considerable research has been conducted on these interactions in vitro, there remains a pressing need for enhanced model designs and application contexts.

Keywords: human microbiota; in vitro models; environmental exposures; exposure-microbiota interactions

1. Introduction

Human microbiota, comprising trillions of microorganisms such as bacteria, archaea, fungi, and viruses, inhabit various body regions [1]. These microbial communities play critical roles in human health and disease. Gastrointestinal (GI) tract microbiota, particularly those in the large intestine, are crucial for nutrient metabolism, immune system development, and mental health [2,3]. Oral microbiota directly impact oral health and have been linked to conditions such as dental caries, periodontal diseases, and oral cancer [4]. Skin microbiota provide a defense against infections and inflammatory skin conditions, including acne, eczema, and psoriasis [5]. Vaginal microbiota create an acidic environment that inhibits the proliferation of opportunistic pathogens and prevents vaginal infections [6].

Imbalances within these microbial communities, often termed dysbiosis, can arise from environmental exposures. These exposures encompass chemical, biological, or physical agents that interact with humans and potentially lead to adverse health effects [7]. Exposure to chemical substances, such as heavy metals, pesticides, and antibiotics, can reduce microbial diversity, promote pathogen growth, and contribute to gut inflammation,

https://doi.org/10.3390/microorganisms13020247

increased intestinal permeability, and neurodevelopmental impairments [8–13]. Exposure to airborne pollutants, such as particulate matter, nitrogen dioxide, and ozone, can alter the composition and function of both respiratory and gut microbiota, increasing the risk of systemic inflammation and respiratory diseases [14,15]. Furthermore, contact with pathogens can interfere with microbial function, leading to either acute diseases or long-term health effects [1]. Despite these challenges, human microbiota possess remarkable defense mechanisms. Certain microorganisms can transform chemical toxins into less harmful forms, or bind and neutralize these toxins [16,17]. In addition, human microbiota can outcompete pathogens for nutrients and space, and create inhospitable environments by producing toxins or altering environmental pH [18,19]. Human microbiota can also modulate host immune responses, strengthen epithelial barrier integrity, and limit oxygen availability for facultative pathogens [18].

The continuous introduction of novel chemicals and the emergence of new pathogens underscore the importance of understanding the complex interactions between environmental exposures and human microbiota. Animal models, such as germ-free mice and traditional laboratory animals (e.g., rats), have played a crucial role in elucidating these interactions [20]. These models provide valuable insights into microbial and physiological responses to external stressors. Furthermore, genetically modified animal models enable researchers to explore specific host–microbiota interactions and the influence of host genetics on microbiota composition and function [21]. Nonetheless, the microbiota of laboratory animals may exhibit significant differences when compared to those of humans. For instance, animal vaginas lack key characteristics that are fundamental to the human vaginal environment, such as low pH and *Lactobacillus* dominance [22,23]. Such disparities can result in findings that may not be entirely applicable to human biology. Additionally, the ethical implications surrounding the treatment of animals in research, particularly in studies focusing on harmful exposures, raise important concerns that must be addressed [24–26]. Epidemiological studies offer another approach to directly investigating exposure–microbiota interactions in humans. Large-scale cohort studies can identify associations between exposures and health outcomes across diverse populations [27,28]. However, epidemiological studies often struggle to establish causal relationships, and it remains unclear whether changes in microbiota are a cause or consequence of disease. Additionally, human studies are subject to confounding factors like genetics, lifestyle, and socioeconomic status, which can complicate the interpretation of results.

To address these challenges, in vitro models have emerged as a valuable complementary approach. By enabling researchers to investigate exposure–microbiota interactions under controlled conditions, in vitro models circumvent the ethical and practical limitations of animal and human studies [24–26]. These models offer flexibility for high-throughput screening of individual or combined exposures, making them ideal for toxicity testing. Moreover, in vitro systems provide a stable and reproducible environment, facilitating the observation of sustained interactions without the complexities of animal or human studies. This review aimed to explore the role of in vitro models in elucidating the relationship between environmental exposures and human microbiota, with a particular focus on microbiota located outside the large intestine, an area that has received limited attention. An examination of the current in vitro models and the interactions between exposures and microbiota studied within these frameworks was conducted. Following this, the distinct advantages and drawbacks of existing research were analyzed, and recommendations for future efforts to enhance model application and tackle essential research inquiries were presented.

2. Methods

2.1. Search Strategy

The literature search was performed on 31 December 2024 across the Web of Science, PubMed, and Scopus databases, using a selection of keywords associated with oral, gastric, small intestinal, respiratory, skin, and vaginal microbiota, as well as exposures and in vitro models, in the abstract or title. A comprehensive list of query strings can be found in Table S1.

2.2. Eligibility Criteria

The inclusion criteria comprised: (1) original research articles, theses, and dissertations; (2) in vitro studies examining exposure–microbiota interactions, which include changes in microbial growth, abundance, and activity due to exposure, as well as modulation of exposure chemical structure and availability by microbiota; and (3) publications written in English and Chinese.

The exclusion criteria were as follows: (1) studies not involving human microbiota (e.g., animal microbiota); (2) studies not related to environmental exposures (e.g., nutrients, drugs), with the exception of antibiotic drugs, due to the significant number of reports regarding unintended dietary exposure to antibiotic residues [29–32]; (3) studies not utilizing in vitro models; (4) non-original research (e.g., review articles, perspectives, awarded grants, errata, patents); (5) preprints; and (6) studies published in languages other than English and Chinese.

2.3. Data Extraction and Synthesis

The two authors independently assessed each study for eligibility. Subsequently, one author (Q.C.) extracted descriptive information from the full text of each eligible study, and synthesized exposure type(s), in vitro model type(s), key findings on exposure–microbiota interactions (including alterations in microbiota and/or exposures), and methods to identify key findings. The other author (S.C.) independently verified the accuracy of the results to reduce the risk of bias, and discussed any discrepancies with Q.C.

3. Results

A total of 2147 records were retrieved from the three databases, with 1302 duplicate entries eliminated. The full texts of 16 out of the remaining 845 records were inaccessible and were therefore excluded from this review. Following the application of the inclusion and exclusion criteria, 58 studies were selected, which included 25 studies focusing on oral microbiota, one on gastric microbiota, one on small intestinal microbiota, seven on respiratory microbiota, 11 on skin microbiota, and 13 on vaginal microbiota (Table S1). These studies were subsequently categorized into "gastrointestinal tract microbiota" and "extraintestinal microbiota" according to their respective locations, and are discussed in the following sections. In addition to these studies, other research was referenced mainly to establish a foundational context and to suggest potential avenues for future investigation, offering essential insights for comprehending this review.

3.1. Gastrointestinal Tract Microbiota

The microbiota in the human GI tract, including bacteria, archaea, fungi, and viruses, play a crucial role in human health [1–3]. These microorganisms inhabit various regions of the GI tract, from the oral cavity to the colon, and their composition and function can be influenced by factors such as environmental exposures. Research into GI tract microbiota has increasingly turned to in vitro models, which offer controlled environments for studying microbial dynamics and their interactions with exposures. The various large intestinal models and the types of exposures examined in vitro have been thoroughly reviewed in other literature; therefore, this work focuses primarily on non-large intestinal microbiota (i.e., microorganisms living in the oral cavity, stomach, and small intestine). For a comprehensive overview of large intestinal microbiota research, readers are referred to specialized reviews [8–13,20,24–26,33–38] (Table 1).

3.1.1. Oral Microbiota

Oral microbiota, comprising over 1000 microbial species, are second in complexity only to the large intestinal microbiota [4,39]. Balanced oral microbiota contribute to dental health by preventing the overgrowth of pathogenic species that cause dental caries and periodontal diseases [4]. Multiple oral bacteria have also been linked to an increased risk of oral squamous cell carcinoma. Emerging research indicates a connection between oral microbiota and systemic health conditions, including cardiovascular diseases, diabetes, and respiratory infections [40]. A comprehensive understanding of oral microbiota can help inform strategies for maintaining oral and overall health, emphasizing the importance of good oral hygiene practices and regular dental care.

In vitro models designed to simulate oral microbiota range from simple single-species cultures to complex systems that closely resemble the physiological environment of the oral cavity. These models can be inoculated with either defined microbial species or actual samples obtained from human oral cavities, such as saliva, oral swabs, dental crowns, oral rinses, and toothbrushes [41–51]. Previous models aimed at investigating the interactions between oral microbiota and environmental factors encompass several innovative designs, including (1) the toothbrush model, which fosters biofilm development on nylon fibers (i.e., representative toothbrush material) [52]; (2) the hydroxyapatite disc biofilm reactor, which supports microbial biofilm growth on hydroxyapatite discs, effectively representing early supra-gingival plaques [42,53–55]; (3) the drip flow biofilm reactor, which allows a continuous drop-wise flow of medium over hydroxyapatite-coated slides, facilitating biofilms similar to supra-gingival plaques [42]; (4) the multiple sorbarod device, which enables the formation of biofilms similar to sub-gingival plaques [42]; and (5) the constant depth film fermenter, which simulates the oral environment by continuously supplying microbial media in a thin film of liquid flowing over the biofilm surface [43]. The last three models exhibit dynamic characteristics and are valuable for investigating the impact of mechanical forces on biofilms.

Previous research utilizing these models has primarily focused on examining the impact of oral hygiene products on microbial composition. For instance, fluoride, which is commonly utilized as an anti-caries agent in dental care products, showed minimal antimicrobial activity against biofilms consisting of *Candida albicans*, *Actinomyces oris*, *Fusobacterium nucleatum*, *Streptococcus oralis*, *Streptococcus sobrinus*, and *Veillonella dispar*, but decreased the formation of microbial extracellular polysaccharide (EPS) and the production of acids [54]. In a separate study, fluoride hindered the growth of *Streptococcus mutans* and *Streptococcus sanguinis* [44]. When used in conjunction with arginine, fluoride enhanced the growth of *S. sanguinis* and suppressed that of *S. mutans*, significantly reducing the demineralizing potential of oral biofilms derived from saliva. Other oral hygiene agents, including triclosan, chlorhexidine, traditional Chinese medicine, essential oils, and hypochlorite nanobubbles, could significantly reduce bacterial pathogens, including *Enterobacter*, *Streptococcus*, *Staphylococcus*, *Porphyromona*, and *Enterococcus*, as well as *C. albicans* in vitro [42,48,49,51,56–60]. However, it is important to note that certain agents might also hinder the growth of probiotics such as *Lactobacillus salivarius* and *Streptococcus salivarius* [51].

In addition to oral care products, previous in vitro research has linked oral microbiota to antibiotics and nanoparticles, two antimicrobial agents that can be unintentionally ingested. Studies on three antibiotics, namely, tetracycline, ampicillin, and amoxicillin, suggested that low concentrations of these antibiotics (e.g., less than 1 mg/L) had no impact or even a beneficial impact on the viability of oral biofilms, whereas elevated concentrations exhibited detrimental effects [43,45,46]. Furthermore, antibiotic resistance patterns within oral microbiota underwent significant changes following the introduction of antibiotics; however, the extent of these changes differed depending on the antibiotic types and concentrations, as well as the oral microbiota donors. Similar to antibiotics, nanoparticles possess the capability to modulate oral biofilm development. For instance, copper and zinc oxide nanoparticles could significantly reduce oral bacterial proliferation, EPS production, and biofilm formation [41].

Cigarette smoke and nonnutritive sweeteners are two additional chemical exposures linked to oral microbiota alterations in vitro. Cigarette smoking, associated with microbiota dysbiosis and periodontitis, could directly impact the abundance and function of *Fusobacterium*, a key player in oral biofilm development and disease progression [53]. Cigarette smoke could also enhance *S. mutans* biofilm formation [61]. Electronic cigarette vapor was capable of upregulating quorum sensing, enhancing oral biofilm surface area, increasing microbial alpha diversity, shifting metabolic pathways, and altering host response [55,62]. Nonnutritive sweeteners like acesulfame-K, aspartame, saccharin, and sucralose, were able to inhibit *S. mutans* and *S. sanguinis* biofilm development, reduce EPS production, lower *S. mutans*/*S. sanguinis* ratio, decrease acid production, and thereby lessen the cariogenic potential of oral biofilms [50].

Chemical factors are not the sole influences on oral microbiota; physical factors like radiation can also induce changes, as demonstrated in in vitro studies. For instance, low-dose gamma radiation (10 Gy) could reduce *Klebsiella oxytoca* biofilm formation, an effect potentially mitigated by the addition of mucins [63]. Additionally, heavy ion radiation could markedly reduce oral microbiota diversity, increase the relative abundance of *Streptococcus*, and upregulate *gtfC* and *gtfD* gene expression in *S. mutans*, indicative of enhanced cariogenic virulence [47].

The modulation of viral infections by oral microbiota is a burgeoning field of research. An in vitro assay for SARS-CoV-2 pseudovirus infection demonstrated that *Porphyromonas gingivalis* could significantly inhibit viral infection. This effect was mediated by *P. gingivalis*-related compounds, such as phosphoglycerol dihydroceramide and gingipains [64]. Similarly, in vitro studies involving *S. sanguinis* and Akata cells with Epstein-Barr virus (EBV) infection revealed that the metabolite of *S. sanguinis*, hydrogen peroxide, could induce EBV lytic activation [65].

3.1.2. Gastric and Small Intestinal Microbiota

Despite its acidic environment, the stomach harbors a unique microbial community, though significantly less diverse than that in the oral cavity. Acid-resistant bacteria such as *Helicobacter pylori* and *Lactobacillus* species can colonize the stomach [66]. *H. pylori* infection can lead to gastritis, peptic ulcers, and even gastric cancer, while *Lactobacillus* can contribute to a healthy stomach by lowering pH, aiding digestion, and supporting the immune system [67,68]. Based on the literature search, continuous fermenters are the primary tools used to simulate the gastric environment [66,68], with pH as the only factor investigated in vitro [66]. It was found that when inoculated with gastric and duodenal aspirates and subjected to pH changes from 6.0 to 3.0, *Candida* and *Lactobacillus* species exhibited acid tolerance [66]. *Escherichia* and *Klebsiella* populations decreased with decreasing pH, though they persisted at significant levels at pH 3.0.

Relative to the acidic gastric environment, the small intestine's more neutral pH facilitates diverse microbiota, composed of genera including *Lactobacillus*, *Bifidobacterium*, *Streptococcus*, *Enterococcus*, and *Escherichia* [69–75]. These bacteria aid digestion and nutrient absorption, regulate intestinal motility, and enhance mucosal immune function. Additionally, they may contribute to the gut–brain axis by producing metabolites like short-chain fatty acids (SCFAs), influencing mood and cognition [76]. Several recent investigations have sought to simulate small intestinal microbiota using batch cultures and in continuous reactors, the latter of which can function independently or be integrated into large intestinal models such as the Simulator of the Human Intestinal Microbial Ecosystem (SHIME) [69–74]. In one study, a dynamic in vitro model with four compartments, simulating the stomach, duodenum, jejunum, and ileum, was used to investigate and compare the impact of a bacteriophage cocktail and the antibiotic ampicillin on seven representative ileal microbial species and the foodborne pathogen *Listeria monocytogenes* [75]. While both treatments effectively inhibited *L. monocytogenes*, the bacteriophage cocktail demonstrated superior specificity, avoiding the microbiota dysbiosis-inducing effects associated with ampicillin.

Table 1. Interactions between intestinal microbiota and environmental exposures using in vitro methods.

Exposure	In Vitro Model	Key Findings [1]	Methodology [3]	Reference
Oral cavity microbiota				
Sodium fluoride	Six-species biofilm on sintered hydroxyapatite disks	Total bacteria (-)	Viable cell counting	[54]
Sodium fluoride	Saliva-derived mixed-species biofilm on saliva-coated human enamel discs	*Streptococcus mutans* (↓) *Streptococcus sanguinis* (↓)	qPCR	[44]
Stannous fluoride, triclosan + sodium fluoride	Saliva-derived mixed-species culture	Uncultured *Veillonella* sp. (↑) *Bulleidia extructa* (↑) *Veillonella atypica* and three *Veillonella* sp. (↓)	DGGE	[48]
Sodium fluoride + arginine	Saliva-derived mixed-species biofilm on saliva-coated human enamel discs	*Streptococcus mutans* (↓) *Streptococcus sanguinis* (↑)	qPCR	[44]
Sodium fluoride + stannous chloride	Oral isolate single-species culture	*Enterobacter hormaechei* (↓) *Streptococcus salivarius* (↓) *Staphylococcus aureus* (↓) *Enterobacter cloacae* (↓) *Enterococcus faecalis* (↓) *Lactobacillus salivarius* (↓) *Candida albicans* (↓)	Viable cell counting	[51]
Stannous fluoride + zinc lactate	Saliva-derived mixed-species biofilm in hydroxyapatite disc reactors	Total facultative anaerobes (↓) Total anaerobes (-) Total streptococci (-) Total Gram-negative anaerobes (↓)	Viable cell counting	[42]
Stannous fluoride + zinc lactate	Saliva-derived mixed-species biofilm in drip-flow biofilm reactors	Total facultative anaerobes (↓) Total anaerobes (↓) Total streptococci (↓) Total Gram-negative anaerobes (↓)	Viable cell counting	[42]
Stannous fluoride + zinc lactate	Saliva-derived mixed-species biofilm in multiple sorbarod devices	Total facultative anaerobes (-) Total anaerobes (-) Total streptococci (-) Total Gram-negative anaerobes (↓)	Viable cell counting	[42]
Triclosan	Saliva-derived mixed-species biofilm in hydroxyapatite disc reactors	Total facultative anaerobes (↓) Total anaerobes (↓) Total streptococci (↓) Total Gram-negative anaerobes (↓)	Viable cell counting	[42]
Triclosan	Saliva-derived mixed-species biofilm in drip-flow biofilm reactors	Total facultative anaerobes (↓) Total anaerobes (↓) Total streptococci (↓) Total Gram-negative anaerobes (↓)	Viable cell counting	[42]

Table 1. *Cont.*

Exposure	In Vitro Model	Key Findings [1]	Methodology [3]	Reference
Triclosan	Saliva-derived mixed-species biofilm in multiple sorbarod devices	Total facultative anaerobes (-) Total anaerobes (-) Total streptococci (↓) Total Gram-negative anaerobes (↓)	Viable cell counting	[42]
Traditional Chinese medicinal toothpaste	Oral cavity-derived isolate single-species culture	*Enterobacter hormaechei* (↓) *Streptococcus salivarius* (-) *Staphylococcus aureus* (↓) *Enterobacter cloacae* (-) *Enterococcus faecalis* (↓) *Lactobacillus salivarius* (-) *Candida albicans* (↓)	Viable cell counting	[51]
Chlorhexidine	Single-species culture and biofilm in culture plates; dual-species culture and biofilm in culture plates	*Streptococcus mutans* (↓) *Candida albicans* (↓) *Staphylococcus aureus* (↓) *Pseudomonas aeruginosa* (↓)	Viable cell counting	[57]
Chlorhexidine gluconate	Oral cavity-derived *Candida albicans* isolate single-species culture	*Candida albicans* (↓)	Cell counting, optical density measurement	[56]
Clove, oregano, thyme essential oils	Mixed-species biofilm in culture plates, and plates supplemented with nylon fibers	Mixtures of 5–6 species selected from *Actinomyces viscosus*, *Enterococcus faecalis*, *Streptococcus mutans*, *Streptococcus oralis*, *Streptococcus sanguinis*, and *Streptococcus salivarius* (↓)	Visual turbidity, viable cell counting, crystal violet staining	[52]
Two tulsi essential oils	Single-species culture on agar plates	*Porphyromonas gingivalis* (↓) *Prevotella intermedia* (↓) *Fusobacterium nucleatum* (↓) *Staphylococcus aureus* (↓) *Streptococcus mutans* (↓)	Agar well diffusion assay	[58]
Eleven essential oils from plant rhizome, leaf and bark	Single-species culture on agar plates	*Streptococcus mutans* (↓) *Streptococcus sanguinis* (↓) *Staphylococcus aureus* (↓) *Candida albicans* (↓)	Disc diffusion assay	[59]
Hypochlorite nanobubbles	Saliva-derived mixed-species culture	*Porphyromonas pasteri* (↓)	16S rRNA gene sequencing	[49]
Denture cleanser	Nine-species biofilm on polymethylmethacrylate discs	Total aerobes (↓) Total anaerobes (↓) *Candida* (↓)	qPCR	[60]
Copper oxide nanoparticles, zinc oxide nanoparticles	Teeth crown surface-derived mixed-species culture	Total bacterial counts (↓)	Viable cell counting	[41]
Tetracycline	Saliva-derived mixed-species biofilm in Constant Depth Film Fermenters	Total anaerobic count (↓) *Lactobacillus* (-) *Streptococcus* (↓) *Actinomyces* (↓)	Viable cell counting	[43]
Ampicillin	Saliva-derived mixed-species biofilm in culture plates pre-coated with saliva pellicle	*Veillonella atypica* (↑) *Veillonella infantium* (↑) *Veillonella dispar* (↑) *Veillonella parvula* (↓) *Prevotella jejuni* (↑) *Prevotella histicola* (↑) *Prevotella salivae* (↑) *Prevotella melaninogenica* (↑) *Streptococcus oralis* (↓) *Streptococcus mitis* (↓) *Streptococcus parasanguinis* (↓) *Streptococcus sanguinis* (↓) *Streptococcus salivarius* (↑) *Streptococcus pneumoniae* (-) *Staphylococcus aureus* (-)	Metagenomic shotgun sequencing	[45]

Table 1. *Cont.*

Exposure	In Vitro Model	Key Findings [1]	Methodology [3]	Reference
Amoxicillin	Saliva-derived mixed-species biofilm in culture plates	Total viable cells (-) *Streptococcus salivarius* (↑) *Streptococcus pneumoniae* (↑) *Lactobacillus fermentum* (↓)	Viable cell counting, metagenomic shotgun sequencing	[46]
Cigarette smoke	Mixed-species biofilm in sintered hydroxyapatite disc reactors	*Fusobacterium nucleatum* was associated with carbohydrate metabolism (↑), cofactors, vitamins, prosthetic groups and pigments (↑), amino acid metabolism (↑), virulence mechanisms (↑), respiration (↓)	Metatranscriptomic sequencing	[53]
Cigarette smoke	Single-species biofilm in culture plates	*Streptococcus mutans* biofilm (↑)	Crystal violet staining	[61]
Electronic cigarette vapor	Mixed-species biofilm on sintered hydroxyapatite disks, with or without organoid tissue overlay	Without overlay: quorum-sensing regulated gene expression (↑), biofilm surface area (↑) With overlay: keratin thickness (↑), host response to pathogen-rich biofilms (↓)	NMR spectroscopy, TIMS-TOF, CLSM	[55]
Electronic cigarette vapor	Saliva-derived mixed species culture in 3D oral mucosa models	Alpha diversity (↑) *Clostridium* (↑) *Prevotella* (↑) *Veillonellaceae* (↑) *Bacteroides* (↑) Multiple glucose and energy metabolic pathways (↑)	16S rRNA gene sequecning, GC-MS	[62]
Nonnutritive sweeteners including acesulfame-K, aspartame, saccharin, and sucralose	Single-species culture and biofilm in culture plates; dual-species biofilm on glass coverslips pre-coated with saliva; saliva-derived mixed-species biofilm on glass coverslips pre-coated with saliva	*Streptococcus sanguinis* (↓) *Streptococcus mutans* (↓) *Streptococcus mutans*/*Streptococcus sanguinis* ratio (↓)	Optical density meansurement, FISH, EPS staining	[50]
Gamma radiation	*Candida albicans*, *Candida glabrata*, *Streptococcus salivarius*, and *Klebsiella oxytoca* single-species culture and biofilm in culture plates	Planktonic cell growth (-) *Klebsiella oxytoca* and *Candida glabrata* biofilms exhibited varying responses to different culture conditions	Optical density meansurement, crystal violet staining, calcofluor white staining	[63]
Heavy ion radiation	Single-, dual-, and saliva-derived mixed-species culture	*Streptococcus* (↑) *Streptococcus mutans*/*Streptococcus sanguinis* ratio (↑)	Viable cell counting, qPCR, FISH, MTT assay, crystal violet staining, EPS staining, RNA sequencing	[47]
SARS-CoV-2	*Porphyromonas gingivalis*, *Actinobacillus actinomycetemcomitans*, *Actinomyces odontilyticus* single-species culture supernatant, co-cultured with ACE2 + 293 T cells	SARS-CoV-2 pseudoviral infection (↓)	Luciferase activity measurement	[64]
Epstein-Barr virus (EBV)	*Streptococcus sanguinis* and Akata cell co-culture	EBV lytic activation (↑)	Flow cytometry, qPCR	[65]
Gastric microbiota				
pH (6.0 to 3.0)	Eleven-species culture in chemostats	*Candida* (-) *Lactobacillus* (-) *Escherichia* (↓) *Klebsiella* (↓)	Viable cell counting	[66]

Table 1. *Cont.*

Exposure	**In Vitro Model**	**Key Findings** [1]	**Methodology** [3]	**Reference**
Small intestinal microbiota				
Bacteriophage cocktail	Seven-species culture in the Smallest Intestine (TSI) model inoculated with *Listeria monocytogenes*	*Streptococcus* (-) *Enterococcus faecalis* (-) *Listeria monocytogenes* (↓) *Escherichia coli* (-)	Viable cell counting	[75]
Ampicillin	Seven-species culture in the Smallest Intestine (TSI) model inoculated with *Listeria monocytogenes*	*Streptococcus* (-) *Enterococcus faecalis* (↓) *Listeria monocytogenes* (-) *Escherichia coli* (↓)	Viable cell counting	[75]
Large intestinal microbiota [2]				
Reviews on types of in vitro models				[24–26,33]
Reviews including exposure-microbiota interactions using in vitro models:				
Heavy metals				[8,9]
Antibiotics				[10,11]
Nanomaterials				[34,35]
Persistent organic pollutants				[12,13]
Food additives				[36,37]
Pathogens				[20,38]

[1] The symbols (↑), (↓) and (-) represent significant increases, decreases, and no significant changes in microbial growth, abundance, or activity, respectively, as observed after exposure. [2] Numerous reviews on large intestinal microbiota are already available, and a selection of these reviews is listed in this table. [3] qPCR: quantitative polymerase chain reaction; DGGE: denaturing gradient gel electrophoresis; FISH: fluorescence in situ hybridization; EPS: extracellular polysaccharide; MTT: 3-(4,5-dimethylthiazol-2-yl)-2,5-diphenyltetrazolium bromide; NMR: nuclear magnetic resonance; TIMS-TOF: trapped ion mobility spectrometry time-of-flight mass spectrometry; CLSM: confocal laser scanning microscopy; GC-MS: gas chromatography coupled to mass spectrometry.

3.2. Extraintestinal Microbiota

Beyond the GI tract, microbial communities reside in diverse body sites, including the respiratory tract, skin, and vagina, where they play critical roles in maintaining health and influencing disease outcomes. In vitro models have become a valuable tool for advancing the understanding of extraintestinal microbiota, a field that remains less explored compared to the well-studied intestinal microbiota. The literature search yielded only 31 studies investigating in vitro interactions between extraintestinal microbiota, including the respiratory tract, skin, and vaginal microbiota, and various environmental exposures (Tables 2 and S1). In contrast, 25 studies focused solely on oral microbiota, while hundreds examined the large intestinal microbiota. Therefore, a comprehensive overview of current research on extraintestinal microbiota and their interactions with exposures in vitro is presented, along with the identification of research domains that necessitate further exploration.

3.2.1. Respiratory Microbiota

The respiratory tract harbors a diverse community of microorganisms, collectively known as respiratory microbiota. Key bacterial genera found in this ecosystem include *Staphylococcus*, *Corynebacterium*, *Streptococcus*, *Haemophilus*, and *Prevotella* [77–79]. These microorganisms play a crucial role in respiratory health by influencing immune responses and pulmonary function. Disruptions to this delicate balance can lead to various respiratory conditions, such as pneumonia, chronic obstructive pulmonary disease, and asthma [77,80]. Additionally, interactions between the gut and respiratory microbiota, often referred to as the gut–lung axis, can influence systemic immune responses and inflammation, impacting respiratory health [80].

Despite its importance, research into respiratory microbiota is still emerging. Current in vitro studies often rely on conventional culturing methods to investigate specific bacterial isolates, but a few more complicated models have been developed. For example, the simultaneous utilization of a filter plate alongside a standard multi-well plate (receiver) facilitates the examination of the effects of soluble microbial metabolites that can transfer from the filter plate to the receiver [81]. The nasal epithelial cell model allows microbial colonization of a cultured host mucosa in vitro, providing a platform for investigating the intricate dynamics of host–microbe and microbe–microbe interactions [82]. The three-dimensional (3D) lung epithelial model demonstrates the ability to replicate bacterial invasion and host pro-inflammatory response [82]. The air-liquid interface (ALI) culture model, often using cell lines like Calu-3, simulates the respiratory tract by creating an interface between air and liquid, allowing for the differentiation of cells into a functional, mucus-secreting epithelium, which can then be co-cultured with various respiratory microbiota [77].

Using microbial cultures, previous studies have isolated *Staphylococcus* [78,83], *Haemophilus* [84], *Prevotella* [79], *Moraxella catarrhalis* [85], and *Streptococcus pneumoniae* [85] from nasal or throat swabs and examined their antibiotic susceptibility on agar plates. Furthermore, one study cultured sputum microbiota in a batch model and investigated the impact of excessive oxygen on microbiota composition and function [86]. Results from this study indicated that hyperoxia reduced the overall microbial load and diversity, as well as the abundance of specific bacteria, including *Rothia mucilaginosa* and various *Streptococcus* species. In contrast, *Pseudomonas aeruginosa* and *Staphylococcus aureus*, which are commonly associated with cystic fibrosis, were minimally affected. In addition, the ALI model was used to study the impact of microbial changes in response to human rhinovirus (HRV) infection, and it was discovered that a combination of *Corynebacterium pseudodiphtheriticum* and *Haemophilus influenzae* significantly reduced HRV copy number, highlighting the potential protective role of these bacteria against viral infections [77].

3.2.2. Skin Microbiota

Skin microbiota are a diverse community of microorganisms, including bacteria, fungi, viruses, and archaea, that reside on and within the skin. Common inhabitants include *Staphylococcus*, *Cutibacterium*, *Micrococcus*, *Propionibacterium*, *Corynebacterium*, and *Malassezia* species [5,87]. These microorganisms play a vital role in maintaining skin health by protecting against pathogens, regulating the immune response, and contributing to overall skin homeostasis. Balanced skin microbiota support wound healing, prevents infections, and reduces inflammation, while dysbiosis has been associated with dermatological conditions such as acne, eczema, psoriasis, and atopic dermatitis [5].

Currently, the majority of in vitro studies on skin microbiota rely on traditional culturing techniques, whereas advanced models designed to replicate the physical architecture and function of the skin do not typically integrate the microbial ecosystem. According to our knowledge, a limited number of studies have attempted to inoculate skin microorganisms into skin models, with a maximum of two species being introduced simultaneously [87,88]. One of these models, the microbially competent 3D skin model, was utilized to study the impact of polycyclic aromatic hydrocarbons, such as benzo[a]pyrene (B[a]P), on skin microorganisms *Micrococcus luteus* and *Pseudomonas oleovorans* [87]. This research demonstrated that B[a]P had the potential to function as the exclusive carbon and energy source for the two microorganisms, with its metabolites experiencing modified rates of skin penetration and diffusion.

In single-species cultures, the most-studied environmental factor affecting skin microbiota is the use of skincare and cosmetic products. The presence of diverse ferments and plant extracts in cosmetics could influence the production of SCFAs by *Staphylococcus epidermidis* [89]. Additionally, certain sunscreen components, including butyl methoxydibenzoylmethane, ethylhexyl salicylate, and octocrylene, along with their combinations, were able to enhance the viability of the probiotic *Lactobacillus crispatus* while diminishing the presence of the pathogenic *Cutibacterium acnes* upon UV exposure [90]. Conversely, skin microorganisms such as *Deinococcus grandis* and the genus *Stenotrophomonas* were capable of metabolizing some of these ingredients [91]. In addition to chemical products, ultraviolet radiation (UVR) is a common skin exposure. Under UVR, *Sphingomonas mucosissima* demonstrated significant resistance and the ability to lower reactive oxygen species levels in human keratinocyte cell lines, suggesting its potential role in safeguarding human skin from UV-induced damage [92]. In addition, UVA strongly inhibited the growth of *M. luteus*, *Corynebacterium stearicum*, *Moraxella osloensis*, and a few *Staphylococcus* species, while UVB only delayed the exponential phase or showed insignificant impact [93]. In a separate study, UVB substantially inhibited the proliferation of *C. acnes* and *Lactobacillus fermentum* [94].

Other forms of exposure have also been explored in vitro. Mycolactones produced by *Mycobacterium ulcerans*, the causative agent of Buruli ulcer, could significantly stimulate spore germination of *Aspergillus flavus* and *Aspergillus niger* while inhibiting *Penicillium rubens*, highlighting intricate interactions between mycobacteria and fungi [95]. Moreover, two types of azo dyes, namely methyl red and orange II, were effectively reduced by skin bacteria such as *Staphylococcus*, *Micrococcus*, and *Kocuria* [96]. Finally, antimicrobial agents, such as antibiotics and green tea extracts, were co-cultured with prevalent skin microorganisms to determine their inhibitory effects [97,98].

3.2.3. Vaginal Microbiota

Vaginal microbiota are essential for sustaining both vaginal and reproductive health, serving as a defense against infections and impacting a range of health outcomes [99,100]. Healthy vaginal microbiota are predominantly composed of *Lactobacillus* species, which foster an acidic environment via production of lactic acid, thereby inhibiting the proliferation of pathogens. Key species within this group include *L. crispatus*, *L. jensenii*, and *L. gasseri*, though the dominance of these species can vary among individuals [100,101]. An imbalance in vaginal microbiota has been linked to conditions like bacterial vaginosis (BV) and an increased risk of sexually transmitted infections [99,102–104], highlighting the importance of this microbial community in maintaining health.

In vitro investigations concerning vaginal microbiota primarily depend on microbial cultures, with a few models established within more intricate systems. For instance, in an ALI culture model, vaginal bacteria and vaginal epithelial cells were co-cultured to mimic the morphological and functional characteristics of the vaginal mucosa and the production of microbial metabolites, as well as viral infection [100,102,105]. In a vagina-on-a-chip microfluidic model, the probiotic *L. crispatus* and disease-associated *Gardnerella vaginalis* were able to colonize the vagina chip, leading to alterations in epithelial cell viability, pH, lactic acid accumulation and pro-inflammatory cytokine levels [101]. A key area of research utilizing these models is dedicated to exploring the intricate interplay between invasive pathogens and vaginal microbiota. For instance, research has discovered that microbiota dominated by *Lactobacillus iners* and group B *Streptococcus* could significantly suppress the replication of human immunodeficiency virus type 1 (HIV-1) in the ALI model, while microbiota containing *Ruminococcaceae* sp., *Aerococcus* sp., *Sneathia sanguinegens*, and *Atopobium vaginae* could potentially enhance HIV-1 replication [102]. Similarly, vaginal microbiota were found to significantly alter the replication of Zika virus (ZIKV) and

Herpes Simplex Virus type 2 (HSV-2), with higher levels of *S. epidermidis* associated with significantly decreased titers of both viruses [105].

Culture-based studies also provide valuable insights into pathogen–microbiota interactions. For instance, multiple strains of *L. crispatus* exhibited antibacterial activity against 11 human vaginal pathogens through the production of bacteriocins and other antimicrobial agents like lactic acid [106]. *Lactobacillus* strains isolated from vaginal swabs hindered the growth of *Escherichia coli*, *S. aureus*, *Enterococcus* species, and *Candida* species [107]. Additionally, in one study, the protozoan parasite *Trichomonas vaginalis* (TV) inhibited the growth of *L. iners* and promoted the growth of *Streptococcus agalactiae* upon initial exposure [108]. The same study also suggested that *L. iners* was capable of surviving from TV after prolonged exposure. In addition to *Lactobacillus* species, the probiotic *Lacticaseibacillus rhamnosus*, isolated from vaginal fluid, suppressed the growth of *Mycobacterium tuberculosis* in co-culture experiments, suggesting its anti-tuberculosis effect [109]. Beyond single-species isolates, cultured cervicovaginal secretions from healthy donors have shown the ability to inhibit the growth of dysbiosis-associated *Gardnerella*, making them a promising source for vaginal microbiota transplantation [110].

Other exposures studied in vitro include antibiotics, tea tree oil, and vaginal hygiene products, all of which possess antimicrobial properties. For instance, the antibiotic metronidazole effectively targeted bacterial vaginosis-associated pathogens like *G. vaginalis* and *Prevotella bivia*, but had limited impact on *A. vaginae* [103]. Moreover, the efficacy of metronidazole against *G. vaginalis* could be compromised by *L. iners*, which potentially sequestered this antibiotic [99]. Antibiotic susceptibility testing of vaginal microbiota isolates, including multiple *Lactobacillus* and *Bifidobacterium* species and *G. vaginalis*, revealed species-specific resistance traits [104,107,111]. In addition to antibiotics, tea tree oil, a potent antimicrobial compound, demonstrated fungicidal activity against multiple *Candida* strains at low concentrations (1% *v*/*v*), while minimally affecting beneficial vaginal species like *Lactobacillus* [112]. This offers a potential strategy to combat chronic vaginal *Candida* infections. However, vaginal douche products, which can suppress the growth of *Lactobacillus*, should be used with caution [113].

Table 2. Interactions between extraintestinal microbiota and environmental exposures using in vitro methods.

Exposure	In Vitro Model	Key Findings [1]	Methodology [2]	Reference
Respiratory tract microbiota				
Fluoroquinolone, meticillin, penicillin, oxacillin, kanamycin, tobramycin, gentamicin, erythromycin, lincomycin, tetracycline, fusidic acid, fosfomycin, rifampicin, trimethoprim/ sulfamethoxazole	Nose-derived *Staphylococcus* isolates on agar plates	87 out of 88 fluoroquinolone- resistant staphylococci carried co-resistance, and 75 carried co-resistance specifically to meticillin	Disc diffusion assay	[78]
Penicillin, cefoxitin	Nose-derived *Staphylococcus* isolates on agar plates	24 out of 27 *Staphylococcus* carried resistance to penicillin and/or cefoxitin	Viable cell counting	[83]
Ampicillin, amoxicillin/ clavulanate, ampicillin/sulbactam, cefuroxime, cefotaxime, imipenem, meropenem, azithromycin, tetracycline, chloramphenicol, thrimetoprim/sulfametoxazole	Throat- and nose-derived *Haemophilus parainfluenzae* isolates on agar plates	Isolates showed different resistance patterns based on two different guidelines	Disc diffusion assay	[84]

Table 2. *Cont.*

Exposure	In Vitro Model	Key Findings [1]	Methodology [2]	Reference
Ceftazidime, amoxicillin, cefotaxime, ceftazidime	Respiratory tract-derived *Prevotella* isolates on agar plates	38 out of 50 *Prevotella* isolates produced extended-spectrum β-lactamases and had higher resistance to amoxicillin and ceftazidime	Disc diffusion assay, Etest	[79]
Amoxicillin, amoxicillin/clavulanate, azithromycin, trimethoprim/sulfamethoxazole (TMP/SMX), ceftriaxone, levofloxacin	Nose-derived single-species isolates on agar plates	6 out of 8 *Moraxella catarrhalis* isolates carried resistance to amoxicillin and TMP/SMX, 2 of these 6 exhibited ceftriaxone resistance, and 1 exhibited azithromycin resistance 12 our of 45 *Streptococcus pneumoniae* isolates demonstrated azithromycin resistance, and 14 showed resistance to TMP/SMX	Etest	[85]
Supplemental oxygen	Sputum-derived mixed-species culture	*Candida albicans* (↓) *Aspergillus fumigatus* (↓) *Actinomyces oris* (↓) *Schaalia odontolytica* (↓) *Rothia mucilaginosa* (↓) Multiple *Streptococcus* species (↓) *Pseudomonas aeruginosa* (-) *Staphylococcus aureus* (-)	Metagenomic shotgun sequencing	[86]
Human rhinovirus (HRV)	*Corynebacterium*, *Haemophilus influenzae*, Calu-3 cell co-culture in the air-liquid interface (ALI) model	HRV copy number (↓) by *Corynebacterium pseudodiphtheriticum* + *Haemophilus influenzae*	qRT-PCR	[77]
Skin microbiota				
Nine cosmetics	*Staphylococcus epidermidis* single-species culture	Yields of short-chain fatty acids depended on different cosmetics	HPLC	[89]
Ultraviolet (UV) filters in sunscreens	*Lactobacillus crispatus*, *Staphylococcus epidermidis*, and *Cutibacterium acnes* single-species culture in a culture plate exposed to UV light	*Lactobacillus crispatus* (↑) *Cutibacterium acnes* (↓)	Viable cell counting	[90]
Octocrylene	Skin-derived single-species culture	*Deinococcus grandis* and *Stenotrophomonas* grew by metabolizing octocrylene	Optical density measurement	[91]
Ultraviolet radiation (UVR) at 254 nm or 312 nm	*Sphingomonas mucosissima* single-species culture on agar plates	*Sphingomonas mucosissima* was resistant to UVR at both wavelengths	Visual observation	[92]
Ultraviolet A (UVA), ultraviolet B (UVB), or combination	Skin-derived *Staphylococcus aureus*, *Staphylococcus epidermidis*, *Staphylococcus hominis*, *Micrococcus luteus*, *Corynebacterium stearicum*, and *Moraxella osloensis* single-species culture	UVA: complete inhibition of all microorganisms UVB: strain-dependent inhibition Combination: similar to UVA	Optical density measurement	[93]
Ultraviolet B (UVB)	*Cutibacterium acnes* and *Lactobacillus fermentum* single-species culture	Both microorganisms (↓)	Viable cell counting	[94]
Mycolactones	Skin-derived single-species fungal spores on agar plates	*Aspergillus flavus* (↑) *Aspergillus niger* (↑) *Penicillium rubens* (↓)	Germinated spore quantification	[95]
Benzo[a]pyrene	Skin-derived *Micrococcus luteus* and *Pseudomonas oleovorans* co-culture in a microbially competent 3D skin model	Benzo[a]pyrene degradation to various metabolites	GC-MS	[87]

Table 2. *Cont.*

Exposure	**In Vitro Model**	**Key Findings** [1]	**Methodology** [2]	**Reference**
Methyl Red, Orange II	Single-species culture	*Staphylococcus*, *Corynebacterium*, *Micrococcus*, *Dermacoccus*, *and Kocuria* species metabolized Methyl Red with various rates, and all but *Corynebacterium xerosis* metabolized Orange II	Spectrophotometry	[96]
Doxycycline, ciprofloxacin, erythromycin, cefalexin, amoxicillin, trimethoprim, clarithromycin, linezolid, metronidazole, azithromycin, co-amoxiclav	*Staphylococcus epidermidis* single-species culture on agar plates	*Staphylococcus epidermidis* exhibited resistance to various antibiotics, and antibiotic-adapted strains showed cross-resistance	Disc diffusion assay	[97]
Green tea extracts	Single-species culture on agar plates	*Micrococcus luteus* (↓) *Staphylococcus epidermidis* (↓) *Clostridium xerosis* (↓) *Bacillus subtilis* (↓)	Optical density measurement	[98]
Vaginal microbiota				
Human immunodeficiency virus type 1 (HIV-1)	Vagina-derived single species or mixed species co-cultured with vaginal epithelial cells and HIV-1-susceptible cells in the air-liquid interface (ALI) model	HIV-1 replication (↓) by *Lactobacillus iners* and group B *streptococcus*-dominated culture	qRT-PCR	[102]
Zika virus (ZIKV), Herpes Simplex Virus type 2 (HSV-2)	Vagina-derived single species or mixed species co-cultured with vaginal epithelial cells in the air-liquid interface (ALI) model	ZIKV titers (↓) by *Staphylococcus epidermidis*-dominated culture ZIKV titers (↑) by *Lactobacillus crispatus*-dominated culture HSV- HSV-2 (↑) by *Lactobacillus jensenii*-dominated, *Mobiluncus mulieris*-containing culture	qPCR	[105]
Human vaginal pathogens including *Enterococcus faecalis*, *Staphylococcus aureus*, *Staphylococcus epidermidis*, *Streptococcus agalactiae*, *Escherichia coli*, *Klebsiella pneumoniae*, *Pseudomonas aeruginosa*, *Gardnerella vaginalis*, and *Mobiluncus curtisii*	*Lactobacillus* single-species culture on agar plates	Pathogens (↓) by *Lactobacillus* species except for *L. iners*, with strain-specific differences	Zone of inhibition surrounding *Lactobacillus*	[106]
Human vaginal pathogens including *Escherichia coli*, *Staphylococcus aureus*, *Enterococcus*, and *Candida albicans*	Vagina-derived *Lactobacillus* single-species culture on agar plates	Pathogens (↓), with strain-specific differences	Spots-on-lawn test	[107]
Trichomonas vaginalis (TV)	*Streptococcus agalactiae* and *Lactobacillus iners* single-species culture	*Lactobacillus iners* (↓) upon TV exposure, and (-) six hours later *Streptococcus agalactiae* (↑)	Viable cell counting	[108]
Mycobacterium tuberculosis	Vagina-derived *Lacticaseibacillus rhamnosus* single-species culture	*Mycobacterium tuberculosis* (↓)	Viable cell counting	[109]
Gardnerella	Vagina-derived mixed-species culture on agar plates	*Gardnerella* (↓)	Zone of inhibition surrounding mixed-species culture	[110]
Metronidazole	*Lactobacillus crispatus*, *Lactobacillus iners*, *Gardnerella vaginalis*, *Prevotella bivia*, and *Atopobium vaginae* co-culture	*Gardnerella vaginalis* (↓) *Prevotella bivia* (↓) *Atopobium vaginae* (↓) *Lactobacillus crispatus* (-) *Lactobacillus iners* (-)	Optical density measurement	[103]

Table 2. *Cont.*

Exposure	In Vitro Model	Key Findings [1]	Methodology [2]	Reference
Metronidazole	*Gardnerella* vaginalis and *Lactobacillus iners* co-culture	*Gardnerella vaginalis* (-) due to metronidazole sequestration by *Lactobacillus iners*	Viable cell counting	[99]
Metronidazole, clindamycin	Vagina-derived *Bifidobacterium* single-species culture on agar plates	*Bifidobacterium* exhibited different susceptibility to metronidazole and clindamycin, with species-specific patterns	Etest	[104]
β-lactamines, aminoglycosides, tetracyclines, macrolides, glycopeptides, sulfamides, diaminopyrimidine, rifamycines, aminosides	Vagina-derived *Lactobacillus* single-species culture on agar plates	*Lactobacillus* showed species- and strain-dependent antibiotic resistance patterns	Disc diffusion assay	[107]
Clindamycin, erythromycin, metronidazole, tinidazole, dequalinium	*Gardnerella vaginalis* single-species culture	*Gardnerella vaginalis* showed strain-dependent antibiotic resistance patterns	Optical density measurement	[111]
Tea tree oil	Vagina-derived single-species culture	*Candida* (↓) at low oil concentration *Bifidobacterium* (↓) at intermediate concentration *Lactobacillus* (↓) at high concentration	Agar well diffusion assay	[112]
Three vaginal douche products	*Lactobacillus* single-species culture	*Lactobacillus* (↓)	Minimal inhibiting concentration measurement	[113]

[1] The symbols (↑), (↓) and (-) represent significant increases, decreases, and no significant changes in microbial growth, abundance, or activity, respectively, as observed after exposure. [2] qRT-PCR: quantitative reverse transcription polymerase chain reaction; HPLC: high-performance liquid chromatography; GC-MS: gas chromatography coupled to mass spectrometry; qPCR: quantitative polymerase chain reaction.

4. Discussion

One benefit of current in vitro models lies in their ability to support the establishment of accurate dose–response relationships between various exposures and microbiota. This functionality can aid in clarifying the molecular mechanisms through which microorganisms influence exposures and vice versa. Such insights are particularly valuable for investigating microbial susceptibility and resistance to antimicrobial agents [43,78,79,83,84,97,98,104,107,111]. In contrast, in animal models or human subjects, exposures are frequently altered by the host prior to or during interaction with the microbiota, complicating the control of this process due to the intricate nature of host interactions. By gaining a deeper understanding of the molecular mechanisms, researchers can enhance their ability to forecast health outcomes linked to environmental exposures and devise targeted strategies to preserve healthy microbiota.

Moreover, in vitro models serve as valuable tools for screening and expanding potential probiotics aimed at reducing risks associated with various exposures. For example, *Bifidobacterium* strains isolated from healthy vaginal microbiota, traditionally thought to be predominantly composed of *Lactobacillus*, possessed the ability to produce lactic acid and withstand low pH levels, thus providing a protective role similar to that of *Lactobacillus* [104]. *L. rhamnosus*, also obtained from vaginal microbiota, could inhibit the growth of *M. tuberculosis*, thereby presenting itself as a potential candidate for anti-tuberculosis drug development [109].

Additionally, in vitro models can be personalized to rapidly investigate the unique microbiota of each individual and their responses to environmental exposures, as shown in previous studies [42,45,49]. This capability is particularly useful for precision medicine, as it enables predictions of individual reactions before clinical interventions or treatments, and eliminates concerns regarding interpersonal variability. A possible application lies within the domain of microbiota transplantation, wherein microbiota from prospective donors may be tested against pathogens obtained from particular patients to identify the most appropriate donor [110].

Finally, in vitro, lab-based models can yield data that either support or validate computational models simulating the interactions between microbiota and various exposures, as well as interactions between microorganisms. For instance, one multispecies computational model was created to simulate the transitions between BV-associated bacteria and *Lactobacillus* species following exposure to metronidazole, and the association was later validated in an in vitro co-culture setting [99].

In vitro studies have provided valuable insights into the interactions between environmental exposures and the human microbiota. However, these models often overlook the host's role in modifying exposures before they reach the microbiota, especially those in the lower GI tract. While models like SHIME simulate digestion and enzymatic reactions, they cannot fully replicate host-mediated processes like absorption in the small intestine, limiting their ability to accurately mimic real-world exposure scenarios. Furthermore, these models do not adequately consider the metabolic interactions between the host and microbiota, nor do they incorporate other host-related elements such as immune responses and systemic feedback mechanisms. Additionally, many in vitro systems tend to oversimply conditions for microbial growth, disregarding factors such as nutrient flow, mechanical forces, and oxygen gradients that influence microbial behavior in vivo. Organ-on-a-chip technology, which integrates various cell types and microenvironments, shows promise for addressing these limitations [114]. By replicating the complex physiology of target organs, including the epithelium, immune cells, and microbiota, this technology can enable more comprehensive investigations into the interplay between host cells, microorganisms, and environmental exposures, ultimately leading to a more comprehensive understanding of exposure outcomes and effects. Nevertheless, it can be challenging to simulate long-term microbial adaptation patterns and host systemic responses on chips, which is crucial for comprehending the effects of chronic exposures.

Another limitation of current studies is the lack of research on how multiple exposures combine to affect the microbiota. In real-world scenarios, individuals encounter complex mixtures of chemicals and conditions. In vitro models are ideal for studying these combined effects, including potential interactions between exposures and their overall impact on the microbiota. Additionally, such models can generate data for developing computational tools that predict how the microbiota respond to new exposure combinations. Nevertheless, this review found very limited studies of this nature. This type of research is crucial for informing regulations and risk assessments, allowing the prioritization of the most concerning mixtures for further investigation in vivo and in clinical trials.

Furthermore, a significant number of existing studies are primarily observational or merely indicate associations, without thoroughly elucidating the mechanisms underlying microbial alterations induced by exposure. To address this gap, omics methodologies offer a comprehensive approach to investigating the intricate microbiota. Whole-genome sequencing can facilitate the identification of genetic factors influencing exposure metabolism, while RNA sequencing can be employed to examine gene expression patterns in relation to varying exposure levels. Although these techniques have been effectively applied in certain studies [45,46,53], there is a necessity for broader implementation for a deeper understanding of the complex interplay between exposure and microbiota.

Finally, in-depth in vitro studies of the stomach and small intestinal microbiota are lacking. A significant challenge is their relative inaccessibility. Unlike the colon, oral cavity, skin and vagina, which can be sampled non-invasively through swabs, the stomach and small intestine typically require invasive procedures like endoscopy or ileostomy [73,74].

These methods are costly, uncomfortable for patients, and carry a risk of contamination. A potentially less invasive approach is to adapt capsule endoscopy for collecting fluid or tissue samples for more comprehensive analysis [115,116].

5. Conclusions

In vitro models have emerged as valuable tools for studying the intricate interactions between environmental exposures and human microbiota. These models offer advantages over conventional animal and epidemiological studies by providing a controlled, reproducible, and ethically sound environment to investigate exposure–microbiota dynamics. While research has predominantly focused on large intestinal microbiota, growing attention to microbiota in other body regions, such as oral, gastric, small intestinal, skin, respiratory, and vaginal microbiota, has revealed promising findings. However, current limitations, including a lack of clarity surrounding host–microbiota interactions, insufficient exploration of multi-exposure effects, and a deficiency in mechanistic studies, highlight opportunities for improvement. Future advancements in organ-on-a-chip technologies, multi-exposure studies, and omics approaches will be crucial in bridging existing knowledge gaps. Ultimately, the continued development and application of in vitro models will enhance the understanding of microbiota-mediated health outcomes, paving the way for precision medicine strategies and improved risk assessment frameworks.

Supplementary Materials: The following supporting information can be downloaded at: https://www.mdpi.com/article/10.3390/microorganisms13020247/s1. Table S1: Query criteria.

Author Contributions: Conceptualization, Q.C. and S.C.; Writing—original draft preparation, Q.C.; Writing—review and editing, S.C. All authors have read and agreed to the published version of the manuscript.

Funding: This research received no external funding.

Data Availability Statement: The original contributions are presented in the article; further inquiries can be sent to the corresponding author.

Conflicts of Interest: The authors declare no conflicts of interest.

References

1. Hou, K.; Wu, Z.-X.; Chen, X.-Y.; Wang, J.-Q.; Zhang, D.; Xiao, C.; Zhu, D.; Koya, J.B.; Wei, L.; Li, J.; et al. Microbiota in Health and Diseases. *Signal Transduct. Target. Ther.* **2022**, *7*, 135. [CrossRef] [PubMed]
2. Thursby, E.; Juge, N. Introduction to the Human Gut Microbiota. *Biochem. J.* **2017**, *474*, 1823–1836. [CrossRef] [PubMed]
3. Dieterich, W.; Schink, M.; Zopf, Y. Microbiota in the Gastrointestinal Tract. *Med. Sci.* **2018**, *6*, 116. [CrossRef]
4. Lamont, R.J.; Koo, H.; Hajishengallis, G. The Oral Microbiota: Dynamic Communities and Host Interactions. *Nat. Rev. Microbiol.* **2018**, *16*, 745–759. [CrossRef] [PubMed]
5. Byrd, A.L.; Belkaid, Y.; Segre, J.A. The Human Skin Microbiome. *Nat. Rev. Microbiol.* **2018**, *16*, 143–155. [CrossRef]
6. France, M.; Alizadeh, M.; Brown, S.; Ma, B.; Ravel, J. Towards a Deeper Understanding of the Vaginal Microbiota. *Nat. Microbiol.* **2022**, *7*, 367–378. [CrossRef]
7. Gutvirtz, G.; Sheiner, E. Airway Pollution and Smoking in Reproductive Health. *Best Pract. Res. Clin. Obstet. Gynaecol.* **2022**, *85*, 81–93. [CrossRef] [PubMed]
8. Giambò, F.; Italia, S.; Teodoro, M.; Briguglio, G.; Furnari, N.; Catanoso, R.; Costa, C.; Fenga, C. Influence of Toxic Metal Exposure on the Gut Microbiota (Review). *World Acad. Sci. J.* **2021**, *3*, 19. [CrossRef]
9. Duan, H.; Yu, L.; Tian, F.; Zhai, Q.; Fan, L.; Chen, W. Gut Microbiota: A Target for Heavy Metal Toxicity and a Probiotic Protective Strategy. *Sci. Total Environ.* **2020**, *742*, 140429. [CrossRef] [PubMed]
10. Sadighara, P.; Rostami, S.; Shafaroodi, H.; Sarshogi, A.; Mazaheri, Y.; Sadighara, M. The Effect of Residual Antibiotics in Food on Intestinal Microbiota: A Systematic Review. *Front. Sustain. Food Syst.* **2023**, *7*, 1163885. [CrossRef]
11. Guzman-Rodriguez, M.; McDonald, J.A.K.; Hyde, R.; Allen-Vercoe, E.; Claud, E.C.; Sheth, P.M.; Petrof, E.O. Using Bioreactors to Study the Effects of Drugs on the Human Microbiota. *Methods* **2018**, *149*, 31–41. [CrossRef]

12. Lu, M.; Li, G.; Yang, Y.; Yu, Y. A Review on in-Vitro Oral Bioaccessibility of Organic Pollutants and Its Application in Human Exposure Assessment. *Sci. Total Environ.* **2021**, *752*, 142001. [CrossRef] [PubMed]
13. Tsiaoussis, J.; Antoniou, M.N.; Koliarakis, I.; Mesnage, R.; Vardavas, C.I.; Izotov, B.N.; Psaroulaki, A.; Tsatsakis, A. Effects of Single and Combined Toxic Exposures on the Gut Microbiome: Current Knowledge and Future Directions. *Toxicol. Lett.* **2019**, *312*, 72–97. [CrossRef] [PubMed]
14. Klimkaite, L.; Liveikis, T.; Kaspute, G.; Armalyte, J.; Aldonyte, R. Air Pollution-Associated Shifts in the Human Airway Microbiome and Exposure-Associated Molecular Events. *Future Microbiol.* **2023**, *18*, 607–623. [CrossRef] [PubMed]
15. Pulliero, A.; Traversi, D.; Franchitti, E.; Barchitta, M.; Izzotti, A.; Agodi, A. The Interaction among Microbiota, Epigenetic Regulation, and Air Pollutants in Disease Prevention. *J. Pers. Med.* **2022**, *12*, 14. [CrossRef] [PubMed]
16. Średnicka, P.; Juszczuk-Kubiak, E.; Wójcicki, M.; Akimowicz, M.; Roszko, M.Ł. Probiotics as a Biological Detoxification Tool of Food Chemical Contamination: A Review. *Food Chem. Toxicol.* **2021**, *153*, 112306. [CrossRef] [PubMed]
17. Afshar, P.; Shokrzadeh, M.; Raeisi, S.N.; Ghorbani-HasanSaraei, A.; Nasiraii, L.R. Aflatoxins Biodetoxification Strategies Based on Probiotic Bacteria. *Toxicon* **2020**, *178*, 50–58. [CrossRef] [PubMed]
18. Caballero-Flores, G.; Pickard, J.M.; Núñez, G. Microbiota-Mediated Colonization Resistance: Mechanisms and Regulation. *Nat. Rev. Microbiol.* **2023**, *21*, 347–360. [CrossRef]
19. Khan, I.; Bai, Y.; Zha, L.; Ullah, N.; Ullah, H.; Shah, S.R.H.; Sun, H.; Zhang, C. Mechanism of the Gut Microbiota Colonization Resistance and Enteric Pathogen Infection. *Front. Cell. Infect. Microbiol.* **2021**, *11*, 716299. [CrossRef]
20. Calvigioni, M.; Mazzantini, D.; Celandroni, F.; Ghelardi, E. Animal and In Vitro Models as Powerful Tools to Decipher the Effects of Enteric Pathogens on the Human Gut Microbiota. *Microorganisms* **2024**, *12*, 67. [CrossRef]
21. Zhang, C.; Franklin, C.L.; Ericsson, A.C. Consideration of Gut Microbiome in Murine Models of Diseases. *Microorganisms* **2021**, *9*, 1062. [CrossRef] [PubMed]
22. Miller, E.A.; Beasley, D.E.; Dunn, R.R.; Archie, E.A. Lactobacilli Dominance and Vaginal pH: Why Is the Human Vaginal Microbiome Unique? *Front. Microbiol.* **2016**, *7*, 1936. [CrossRef] [PubMed]
23. Yildirim, S.; Yeoman, C.J.; Janga, S.C.; Thomas, S.M.; Ho, M.; Leigh, S.R.; Consortium, P.M.; White, B.A.; Wilson, B.A.; Stumpf, R.M. Primate Vaginal Microbiomes Exhibit Species Specificity without Universal Lactobacillus Dominance. *ISME J.* **2014**, *8*, 2431–2444. [CrossRef]
24. Yadav, A.; Ahlawat, S.; Sharma, K.K. Culturing the Unculturables: Strategies, Challenges, and Opportunities for Gut Microbiome Study. *J. Appl. Microbiol.* **2023**, *134*, lxad280. [CrossRef]
25. Isenring, J.; Bircher, L.; Geirnaert, A.; Lacroix, C. In Vitro Human Gut Microbiota Fermentation Models: Opportunities, Challenges, and Pitfalls. *Microbiome Res. Rep.* **2023**, *2*, 2. [CrossRef] [PubMed]
26. Qi, Y.; Yu, L.; Tian, F.; Zhao, J.; Zhai, Q. In Vitro Models to Study Human Gut-Microbiota Interactions: Applications, Advances, and Limitations. *Microbiol. Res.* **2023**, *270*, 127336. [CrossRef] [PubMed]
27. Thompson, K.N.; Oulhote, Y.; Weihe, P.; Wilkinson, J.E.; Ma, S.; Zhong, H.; Li, J.; Kristiansen, K.; Huttenhower, C.; Grandjean, P. Effects of Lifetime Exposures to Environmental Contaminants on the Adult Gut Microbiome. *Environ. Sci. Technol.* **2022**, *56*, 16985–16995. [CrossRef]
28. Vignal, C.; Guilloteau, E.; Gower-Rousseau, C.; Body-Malapel, M. Review Article: Epidemiological and Animal Evidence for the Role of Air Pollution in Intestinal Diseases. *Sci. Total Environ.* **2021**, *757*, 143718. [CrossRef]
29. Ben, Y.; Hu, M.; Zhong, F.; Du, E.; Li, Y.; Zhang, H.; Andrews, C.B.; Zheng, C. Human Daily Dietary Intakes of Antibiotic Residues: Dominant Sources and Health Risks. *Environ. Res.* **2022**, *212*, 113387. [CrossRef] [PubMed]
30. Seo, J.; Kloprogge, F.; Smith, A.M.; Karu, K.; Ciric, L. Antibiotic Residues in UK Foods: Exploring the Exposure Pathways and Associated Health Risks. *Toxics* **2024**, *12*, 174. [CrossRef] [PubMed]
31. Arsène, M.M.J.; Davares, A.K.L.; Viktorovna, P.I.; Andreevna, S.L.; Sarra, S.; Khelifi, I.; Sergueïevna, D.M. The Public Health Issue of Antibiotic Residues in Food and Feed: Causes, Consequences, and Potential Solutions. *Vet. World* **2022**, *15*, 662–671. [CrossRef]
32. Subirats, J.; Domingues, A.; Topp, E. Does Dietary Consumption of Antibiotics by Humans Promote Antibiotic Resistance in the Gut Microbiome? *J. Food Prot.* **2019**, *82*, 1636–1642. [CrossRef] [PubMed]
33. Biagini, F.; Daddi, C.; Calvigioni, M.; De Maria, C.; Zhang, Y.S.; Ghelardi, E.; Vozzi, G. Designs and Methodologies to Recreate in Vitro Human Gut Microbiota Models. *Bio-Des. Manuf.* **2023**, *6*, 298–318. [CrossRef]
34. Utembe, W.; Tlotleng, N.; Kamng'ona, A. A Systematic Review on the Effects of Nanomaterials on Gut Microbiota. *Curr. Res. Microb. Sci.* **2022**, *3*, 100118. [CrossRef] [PubMed]
35. Wojciechowska, O.; Costabile, A.; Kujawska, M. The Gut Microbiome Meets Nanomaterials: Exposure and Interplay with Graphene Nanoparticles. *Nanoscale Adv.* **2023**, *5*, 6349–6364. [CrossRef]
36. Li, P.; Qu, R.; Li, M.; Sheng, P.; Jin, L.; Huang, X.; Xu, Z.Z. Impacts of Food Additives on Gut Microbiota and Host Health. *Food Res. Int.* **2024**, *196*, 114998. [CrossRef]
37. Cao, Y.; Liu, H.; Qin, N.; Ren, X.; Zhu, B.; Xia, X. Impact of Food Additives on the Composition and Function of Gut Microbiota: A Review. *Trends Food Sci. Technol.* **2020**, *99*, 295–310. [CrossRef]

38. Vogt, S.L.; Peña-Díaz, J.; Finlay, B.B. Chemical Communication in the Gut: Effects of Microbiota-Generated Metabolites on Gastrointestinal Bacterial Pathogens. *Anaerobe* **2015**, *34*, 106–115. [CrossRef] [PubMed]
39. Dewhirst, F.E.; Chen, T.; Izard, J.; Paster, B.J.; Tanner, A.C.R.; Yu, W.-H.; Lakshmanan, A.; Wade, W.G. The Human Oral Microbiome. *J. Bacteriol.* **2010**, *192*, 5002–5017. [CrossRef]
40. Sampaio-Maia, B.; Caldas, I.M.; Pereira, M.L.; Pérez-Mongiovi, D.; Araujo, R. Chapter Four—The Oral Microbiome in Health and Its Implication in Oral and Systemic Diseases. In *Advances in Applied Microbiology*; Sariaslani, S., Michael Gadd, G., Eds.; Academic Press: Cambridge, MA, USA, 2016; Volume 97, pp. 171–210.
41. Tabrez Khan, S.; Ahamed, M.; Al-Khedhairy, A.; Musarrat, J. Biocidal Effect of Copper and Zinc Oxide Nanoparticles on Human Oral Microbiome and Biofilm Formation. *Mater. Lett.* **2013**, *97*, 67–70. [CrossRef]
42. Ledder, R.G.; McBain, A.J. An in Vitro Comparison of Dentifrice Formulations in Three Distinct Oral Microbiotas. *Arch. Oral Biol.* **2012**, *57*, 139–147. [CrossRef] [PubMed]
43. Ready, D.R. Antibiotic and Mercury Resistance in the Cultivable Oral Microbiota of Children. Ph.D. Thesis, University of London and University College London, London, UK, 2005.
44. Zheng, X.; He, J.; Wang, L.; Zhou, S.; Peng, X.; Huang, S.; Zheng, L.; Cheng, L.; Hao, Y.; Li, J.; et al. Ecological Effect of Arginine on Oral Microbiota. *Sci. Rep.* **2017**, *7*, 7206. [CrossRef] [PubMed]
45. Brar, N.K.; Dhariwal, A.; Åmdal, H.A.; Junges, R.; Salvadori, G.; Baker, J.L.; Edlund, A.; Petersen, F.C. Exploring Ex Vivo Biofilm Dynamics: Consequences of Low Ampicillin Concentrations on the Human Oral Microbiome. *npj Biofilms Microbiomes* **2024**, *10*, 37. [CrossRef]
46. Brar, N.K.; Dhariwal, A.; Shekhar, S.; Junges, R.; Hakansson, A.P.; Petersen, F.C. HAMLET, a Human Milk Protein-Lipid Complex, Modulates Amoxicillin Induced Changes in an Ex Vivo Biofilm Model of the Oral Microbiome. *Front. Microbiol.* **2024**, *15*, 1406190. [CrossRef]
47. Wang, Z.; Yang, G.; Zhou, X.; Peng, X.; Li, M.; Zhang, M.; Lu, D.; Yang, D.; Cheng, L.; Ren, B. Heavy Ion Radiation Directly Induced the Shift of Oral Microbiota and Increased the Cariogenicity of Streptococcus Mutans. *Microbiol. Spectr.* **2023**, *11*, e01322-23. [CrossRef] [PubMed]
48. Glancey, A.S.G. Selection, Interaction and Adaptation in the Oral Microbiota. Ph.D. Thesis, The University of Manchester, Manchester, UK, 2011.
49. Sagara, K.; Kataoka, S.; Yoshida, A.; Ansai, T. The Effects of Exposure to O_2- and HOCl-Nanobubble Water on Human Salivary Microbiota. *Sci. Rep.* **2023**, *13*, 21125. [CrossRef] [PubMed]
50. Zhu, J.; Liu, J.; Li, Z.; Xi, R.; Li, Y.; Peng, X.; Xu, X.; Zheng, X.; Zhou, X. The Effects of Nonnutritive Sweeteners on the Cariogenic Potential of Oral Microbiome. *BioMed Res. Int.* **2021**, *2021*, 9967035. [CrossRef] [PubMed]
51. Shang, Q.; Gao, Y.; Qin, T.; Wang, S.; Shi, Y.; Chen, T. Interaction of Oral and Toothbrush Microbiota Affects Oral Cavity Health. *Front. Cell. Infect. Microbiol.* **2020**, *10*, 17. [CrossRef] [PubMed]
52. Aires, A.; Barreto, A.S.; Semedo-Lemsaddek, T. Antimicrobial Effects of Essential Oils on Oral Microbiota Biofilms: The Toothbrush In Vitro Model. *Antibiotics* **2021**, *10*, 21. [CrossRef] [PubMed]
53. Ganesan, S.M. Relative Contributions of Tobacco Associated Factors and Diabetes to Shaping the Oral Microbiome. Ph.D. Thesis, The Ohio State University, Columbus, OH, USA, 2018.
54. Thurnheer, T.; Belibasakis, G.N. Effect of Sodium Fluoride on Oral Biofilm Microbiota and Enamel Demineralization. *Arch. Oral Biol.* **2018**, *89*, 77–83. [CrossRef]
55. Beverly, M.L.-S. The Exposomal Impacts of E-Cigarettes on the Oral Microbiome. Ph.D. Thesis, The Ohio State University, Columbus, OH, USA, 2024.
56. Ellepola, A.; Samaranayake, L. The Effect of Brief Exposure to Sub-Therapeutic Concentrations of Chlorhexidine Gluconate on the Germ Tube Formation of Oral Candida Albicans and Its Relationship to Post-Antifungal Effect. *Oral Dis.* **2000**, *6*, 166–171. [CrossRef]
57. Marino, P.J. Interaction of the Oral Microbiota with Respiratory Pathogens in Biofilms of Mechanically Ventilated Patients. Ph.D. Thesis, Cardiff University, Cardiff, UK, 2017.
58. Kalra, K.; Vasthare, R.; Shenoy, P.A.; Vishwanath, S.; Singhal, D.K. Antibacterial Efficacy of Essential Oil of Two Different Varieties of Ocimum (Tulsi) on Oral Microbiota—An Invitro Study. *Indian J. Public Health Res. Dev.* **2019**, *10*, 188. [CrossRef]
59. Somantri, R.U.; Sugiarto; Iriani, E.S.; Sunarti, T.C. In Vitro Study on the Antimicrobial Activity of Eleven Essential Oils against Oral Cavity Microbiota. *IOP Conf. Ser. Earth Environ. Sci.* **2022**, *1063*, 012025. [CrossRef]
60. O'Donnell, L.E. The Impact of Denture Related Disease on the Oral Microbiome of Denture Wearers. Ph.D. Thesis, University of Glasgow, Glasgow, UK, 2016.
61. Walsh, M. The Effects of Smoking and Vaping on the Growth of *P. gingivalis*, *S. mutans*, and *Aa*: A Comparative Study of the Oral Microbiome. Master's Thesis, Southern Illinois University at Edwardsville, Edwardsville, IL, USA, 2024.
62. Maan, M.; Pillai, J.; Mohamed, D.A.; Jalaleddine, N.; Abuzayeda, M.; Khamis, A.H.; Dutta, M.; Moharamzadeh, K. The Effects of Electronic Cigarettes on Oral Microbiome and Metabolome in 3D Tissue-Engineered Models. *Int. Dent. J.* **2024**. [CrossRef]

63. Vanhoecke, B.W.; De Ryck, T.R.; De Boel, K.; Wiles, S.; Boterberg, T.; Van de Wiele, T.; Swift, S. Low-Dose Irradiation Affects the Functional Behavior of Oral Microbiota in the Context of Mucositis. *Exp. Biol. Med.* **2016**, *241*, 60–70. [CrossRef] [PubMed]
64. Bontempo, A.; Chirino, A.; Heidari, A.; Lugo, A.; Shindo, S.; Pastore, M.R.; Madonia, R.; Antonson, S.A.; Godoy, C.; Nichols, F.C.; et al. Inhibition of SARS-CoV-2 Infection by Porphyromonas Gingivalis and the Oral Microbiome. *Microbiol. Spectr.* **2024**, *12*, e0059924. [CrossRef] [PubMed]
65. Liao, Y.; Zhang, J.-B.; Lu, L.-X.; Jia, Y.-J.; Zheng, M.-Q.; Debelius, J.W.; He, Y.-Q.; Wang, T.-M.; Deng, C.-M.; Tong, X.-T.; et al. Oral Microbiota Alteration and Roles in Epstein-Barr Virus Reactivation in Nasopharyngeal Carcinoma. *Microbiol. Spectr.* **2023**, *11*, e03448-22. [CrossRef]
66. O'May, G.A.; Reynolds, N.; Macfarlane, G.T. Effect of pH on an In Vitro Model of Gastric Microbiota in Enteral Nutrition Patients. *Appl. Environ. Microbiol.* **2005**, *71*, 4777–4783. [CrossRef] [PubMed]
67. Pereira-Marques, J.; Ferreira, R.M.; Pinto-Ribeiro, I.; Figueiredo, C. Helicobacter Pylori Infection, the Gastric Microbiome and Gastric Cancer. In *Helicobacter Pylori in Human Diseases: Advances in Microbiology, Infectious Diseases and Public Health Volume 11*; Kamiya, S., Backert, S., Eds.; Springer International Publishing: Cham, Switzerland, 2019; pp. 195–210, ISBN 978-3-030-21916-1.
68. Smith, A.R.; Macfarlane, G.T.; Reynolds, N.; O'May, G.A.; Bahrami, B.; Macfarlane, S. Effect of a Synbiotic on Microbial Community Structure in a Continuous Culture Model of the Gastric Microbiota in Enteral Nutrition Patients. *FEMS Microbiol. Ecol.* **2012**, *80*, 135–145. [CrossRef] [PubMed]
69. Akritidou, T.; Smet, C.; Akkermans, S.; Tonti, M.; Williams, J.; Van de Wiele, T.; Van Impe, J.F.M. A Protocol for the Cultivation and Monitoring of Ileal Gut Microbiota Surrogates. *J. Appl. Microbiol.* **2022**, *133*, 1919–1939. [CrossRef] [PubMed]
70. Firrman, J.; Friedman, E.S.; Hecht, A.; Strange, W.C.; Narrowe, A.B.; Mahalak, K.; Wu, G.D.; Liu, L. Preservation of Conjugated Primary Bile Acids by Oxygenation of the Small Intestinal Microbiota in Vitro. *mBio* **2024**, *15*, e00943-24. [CrossRef] [PubMed]
71. Stolaki, M.; Minekus, M.; Venema, K.; Lahti, L.; Smid, E.J.; Kleerebezem, M.; Zoetendal, E.G. Microbial Communities in a Dynamic in Vitro Model for the Human Ileum Resemble the Human Ileal Microbiota. *FEMS Microbiol. Ecol.* **2019**, *95*, fiz096. [CrossRef]
72. van Trijp, M.P.H.; Rösch, C.; An, R.; Keshtkar, S.; Logtenberg, M.J.; Hermes, G.D.A.; Zoetendal, E.G.; Schols, H.A.; Hooiveld, G.J.E.J. Fermentation Kinetics of Selected Dietary Fibers by Human Small Intestinal Microbiota Depend on the Type of Fiber and Subject. *Mol. Nutr. Food Res.* **2020**, *64*, 2000455. [CrossRef] [PubMed]
73. Deyaert, S.; Moens, F.; Pirovano, W.; van den Bogert, B.; Klaassens, E.S.; Marzorati, M.; Van de Wiele, T.; Kleerebezem, M.; Van den Abbeele, P. Development of a Reproducible Small Intestinal Microbiota Model and Its Integration into the SHIME®-System, a Dynamic in Vitro Gut Model. *Front. Microbiol.* **2023**, *13*, 1054061. [CrossRef] [PubMed]
74. Takada, T.; Chinda, D.; Mikami, T.; Shimizu, K.; Oana, K.; Hayamizu, S.; Miyazawa, K.; Arai, T.; Katto, M.; Nagara, Y.; et al. Dynamic Analysis of Human Small Intestinal Microbiota after an Ingestion of Fermented Milk by Small-Intestinal Fluid Perfusion Using an Endoscopic Retrograde Bowel Insertion Technique. *Gut Microbes* **2020**, *11*, 1662–1676. [CrossRef] [PubMed]
75. Jakobsen, R.R.; Trinh, J.T.; Bomholtz, L.; Brok-Lauridsen, S.K.; Sulakvelidze, A.; Nielsen, D.S. A Bacteriophage Cocktail Significantly Reduces Listeria Monocytogenes without Deleterious Impact on the Commensal Gut Microbiota under Simulated Gastrointestinal Conditions. *Viruses* **2022**, *14*, 190. [CrossRef] [PubMed]
76. O'Riordan, K.J.; Collins, M.K.; Moloney, G.M.; Knox, E.G.; Aburto, M.R.; Fülling, C.; Morley, S.J.; Clarke, G.; Schellekens, H.; Cryan, J.F. Short Chain Fatty Acids: Microbial Metabolites for Gut-Brain Axis Signalling. *Mol. Cell. Endocrinol.* **2022**, *546*, 111572. [CrossRef] [PubMed]
77. Narang, P. Development of In-Vitro Model Systems to Study the Effect of the Human Microbiota in Respiratory Diseases. Ph.D. Thesis, University of Technology Sydney, Ultimo, Australia, 2023.
78. Munier, A.-L.; de Lastours, V.; Barbier, F.; Chau, F.; Fantin, B.; Ruimy, R. Comparative Dynamics of the Emergence of Fluoroquinolone Resistance in Staphylococci from the Nasal Microbiota of Patients Treated with Fluoroquinolones According to Their Environment. *Int. J. Antimicrob. Agents* **2015**, *46*, 653–659. [CrossRef]
79. Sherrard, L.J.; McGrath, S.J.; McIlreavey, L.; Hatch, J.; Wolfgang, M.C.; Muhlebach, M.S.; Gilpin, D.F.; Elborn, J.S.; Tunney, M.M. Production of Extended-Spectrum *β*-Lactamases and the Potential Indirect Pathogenic Role of *Prevotella* Isolates from the Cystic Fibrosis Respiratory Microbiota. *Int. J. Antimicrob. Agents* **2016**, *47*, 140–145. [CrossRef]
80. Enaud, R.; Prevel, R.; Ciarlo, E.; Beaufils, F.; Wieërs, G.; Guery, B.; Delhaes, L. The Gut-Lung Axis in Health and Respiratory Diseases: A Place for Inter-Organ and Inter-Kingdom Crosstalks. *Front. Cell. Infect. Microbiol.* **2020**, *10*, 9. [CrossRef] [PubMed]
81. Vandeplassche, E.; Sass, A.; Lemarcq, A.; Dandekar, A.A.; Coenye, T.; Crabbé, A. In Vitro Evolution of Pseudomonas Aeruginosa AA2 Biofilms in the Presence of Cystic Fibrosis Lung Microbiome Members. *Sci. Rep.* **2019**, *9*, 12859. [CrossRef]
82. Charles, D.D.; Fisher, J.R.; Hoskinson, S.M.; Medina-Colorado, A.A.; Shen, Y.C.; Chaaban, M.R.; Widen, S.G.; Eaves-Pyles, T.D.; Maxwell, C.A.; Miller, A.L.; et al. Development of a Novel Ex Vivo Nasal Epithelial Cell Model Supporting Colonization With Human Nasal Microbiota. *Front. Cell. Infect. Microbiol.* **2019**, *9*, 165. [CrossRef]
83. Scarlat, I.P.; Stroe, R.; Diţu, L.-M.; Curuţiu, C.; Chiurtu, E.R.; Stănculescu, I.; Chifiriuc, M.C.; Lazăr, V. Evaluating the Role of the Working Environment on to Skin and Upper Respiratory Tract Microbiota of Museum Workers. *Romanian Biotechnol. Lett.* **2020**, *25*, 2103–2106. [CrossRef]

84. Kosikowska, U.; Andrzejczuk, S.; Grywalska, E.; Chwiejczak, E.; Winiarczyk, S.; Pietras-Ożga, D.; Stępień-Pyśniak, D. Prevalence of Susceptibility Patterns of Opportunistic Bacteria in Line with CLSI or EUCAST among Haemophilus Parainfluenzae Isolated from Respiratory Microbiota. *Sci. Rep.* **2020**, *10*, 11512. [CrossRef] [PubMed]
85. Zelasko, S.; Swaney, M.H.; Sandstrom, S.; Lee, K.E.; Dixon, J.; Riley, C.; Watson, L.; Godfrey, J.J.; Ledrowski, N.; Rey, F.; et al. Early-Life Upper Airway Microbiota Are Associated with Decreased Lower Respiratory Tract Infections. *J. Allergy Clin. Immunol.* **2024**. [CrossRef] [PubMed]
86. Vieira, J.; Jesudasen, S.; Bringhurst, L.; Sui, H.-Y.; McIver, L.; Whiteson, K.; Hanselmann, K.; O'Toole, G.A.; Richards, C.J.; Sicilian, L.; et al. Supplemental Oxygen Alters the Airway Microbiome in Cystic Fibrosis. *mSystems* **2022**, *7*, e00364-22. [CrossRef]
87. Lemoine, L. Modulation of Polycyclic Aromatic Hydrocarbon Toxicity by the Human Skin Microbiome. Ph.D. Thesis, Freie Universitaet Berlin, Berlin, Germany, 2021.
88. Holland, D.B.; Bojar, R.A.; Jeremy, A.H.T.; Ingham, E.; Holland, K.T. Microbial Colonization of an in Vitro Model of a Tissue Engineered Human Skin Equivalent—A Novel Approach. *FEMS Microbiol. Lett.* **2008**, *279*, 110–115. [CrossRef] [PubMed]
89. Tanabe, K.; Moriguchi, C.; Fujiyama, N.; Shigematsu, Y.; Haraguchi, N.; Hirano, Y.; Dai, H.; Inaba, S.; Tokudome, Y.; Kitagaki, H. A Trial for the Construction of a Cosmetic Pattern Map Considering Their Effects on Skin Microbiota—Principal Component Analysis of the Effects on Short-Chain Fatty Acid Production by Skin Microbiota Staphylococcus Epidermidis. *Fermentation* **2023**, *9*, 647. [CrossRef]
90. Schuetz, R.; Claypool, J.; Sfriso, R.; Vollhardt, J.H. Sunscreens Can Preserve Human Skin Microbiome upon Erythemal UV Exposure. *Int. J. Cosmet. Sci.* **2024**, *46*, 71–84. [CrossRef]
91. Timm, C.M.; Loomis, K.; Stone, W.; Mehoke, T.; Brensinger, B.; Pellicore, M.; Staniczenko, P.P.A.; Charles, C.; Nayak, S.; Karig, D.K. Isolation and Characterization of Diverse Microbial Representatives from the Human Skin Microbiome. *Microbiome* **2020**, *8*, 58. [CrossRef]
92. Harel, N.; Ogen-Shtern, N.; Reshef, L.; Biran, D.; Ron, E.Z.; Gophna, U. Skin Microbiome Bacteria Enriched Following Long Sun Exposure Can Reduce Oxidative Damage. *Res. Microbiol.* **2023**, *174*, 104138. [CrossRef]
93. Amar, Y.; Niedermeier, S.; Silva, R.; Kublik, S.; Schloter, M.; Biedermann, T.; Köberle, M.; Eberlein, B. Skin Microbiome Dynamics in Patients with Polymorphic Light Eruption in Response to UV Radiations. *Br. J. Dermatol.* **2024**, ljae464. [CrossRef] [PubMed]
94. Alarcón-Guijo, P.; Garcés, V.; González, A.; Delgado-López, J.M.; Ullah, R.; Bansal, V.; Dominguez-Vera, J.M. Bacterial Cellulose as a UVB Filter to Protect the Skin Microbiota. *Macromol. Biosci.* **2024**, e2400269. [CrossRef]
95. Hammoudi, N.; Cassagne, C.; Million, M.; Ranque, S.; Kabore, O.; Drancourt, M.; Zingue, D.; Bouam, A. Investigation of Skin Microbiota Reveals *Mycobacterium Ulcerans-Aspergillus* Sp. Trans-Kingdom Communication. *Sci. Rep.* **2021**, *11*, 3777. [CrossRef]
96. Stingley, R.L.; Zou, W.; Heinze, T.M.; Chen, H.; Cerniglia, C.E. Metabolism of Azo Dyes by Human Skin Microbiota. *J. Med. Microbiol.* **2010**, *59*, 108–114. [CrossRef] [PubMed]
97. Khan, R. Does the Human Skin Microbiome Adapt to Antibiotic Exposure? Master's Thesis, University of Salford, Salford, UK, 2019.
98. Al-Talib, H.; Mohd Kasim, N.A.; Al-khateeb, A.; Murugaiah, C.; Abdul Aziz, A.; Rashid, N.N.; Azizan, N.; Ridzuan, S. Antimicrobial Effect of Malaysian Green Tea Leaves (*Camellia sinensis*) on the Skin Microbiota. *Malays. J. Microbiol.* **2016**, *12*, 423–427. [CrossRef]
99. Lee, C.Y. A Systems Approach to Characterize Drivers of Vaginal Microbiome Composition and Bacterial Vaginosis Treatment Efficacy. Ph.D. Thesis, University of Michigan, Ann Arbor, MI, USA, 2023.
100. Zahra, A.; Menon, R.; Bento, G.F.C.; Selim, J.; Taylor, B.D.; Vincent, K.L.; Pyles, R.B.; Richardson, L.S. Validation of Vaginal Microbiome Proxies for in Vitro Experiments That Biomimic Lactobacillus-Dominant Vaginal Cultures. *Am. J. Reprod. Immunol.* **2023**, *90*, e13797. [CrossRef] [PubMed]
101. Mahajan, G.; Doherty, E.; To, T.; Sutherland, A.; Grant, J.; Junaid, A.; Gulati, A.; LoGrande, N.; Izadifar, Z.; Timilsina, S.S.; et al. Vaginal Microbiome-Host Interactions Modeled in a Human Vagina-on-a-Chip. *Microbiome* **2022**, *10*, 201. [CrossRef] [PubMed]
102. Pyles, R.B.; Vincent, K.L.; Baum, M.M.; Elsom, B.; Miller, A.L.; Maxwell, C.; Eaves-Pyles, T.D.; Li, G.; Popov, V.L.; Nusbaum, R.J.; et al. Cultivated Vaginal Microbiomes Alter HIV-1 Infection and Antiretroviral Efficacy in Colonized Epithelial Multilayer Cultures. *PLoS ONE* **2014**, *9*, e93419. [CrossRef] [PubMed]
103. Bloom, S.M.; Mafunda, N.A.; Woolston, B.M.; Hayward, M.R.; Frempong, J.F.; Abai, A.B.; Xu, J.; Mitchell, A.J.; Westergaard, X.; Hussain, F.A.; et al. Cysteine Dependence of Lactobacillus Iners Is a Potential Therapeutic Target for Vaginal Microbiota Modulation. *Nat. Microbiol.* **2022**, *7*, 434–450. [CrossRef]
104. Freitas, A.C.; Hill, J.E. Quantification, Isolation and Characterization of *Bifidobacterium* from the Vaginal Microbiomes of Reproductive Aged Women. *Anaerobe* **2017**, *47*, 145–156. [CrossRef] [PubMed]
105. Amerson-Brown, M.H.; Miller, A.L.; Maxwell, C.A.; White, M.M.; Vincent, K.L.; Bourne, N.; Pyles, R.B. Cultivated Human Vaginal Microbiome Communities Impact Zika and Herpes Simplex Virus Replication in Ex Vivo Vaginal Mucosal Cultures. *Front. Microbiol.* **2019**, *9*, 3340. [CrossRef] [PubMed]
106. Argentini, C.; Fontana, F.; Alessandri, G.; Lugli, G.A.; Mancabelli, L.; Ossiprandi, M.C.; van Sinderen, D.; Ventura, M.; Milani, C.; Turroni, F. Evaluation of Modulatory Activities of Lactobacillus Crispatus Strains in the Context of the Vaginal Microbiota. *Microbiol. Spectr.* **2022**, *10*, e02733-21. [CrossRef] [PubMed]

107. Ouarabi, L.; Chait, Y.A.; Seddik, H.A.; Drider, D.; Bendali, F. Newly Isolated Lactobacilli Strains from Algerian Human Vaginal Microbiota: Lactobacillus Fermentum Strains Relevant Probiotic's Candidates. *Probiotics Antimicrob. Proteins* **2019**, *11*, 43–54. [CrossRef] [PubMed]
108. Chiu, S.-F.; Huang, P.-J.; Cheng, W.-H.; Huang, C.-Y.; Chu, L.J.; Lee, C.-C.; Lin, H.-C.; Chen, L.-C.; Lin, W.-N.; Tsao, C.-H.; et al. Vaginal Microbiota of the Sexually Transmitted Infections Caused by Chlamydia Trachomatis and Trichomonas Vaginalis in Women with Vaginitis in Taiwan. *Microorganisms* **2021**, *9*, 1864. [CrossRef] [PubMed]
109. Rahim, M.A.; Seo, H.; Kim, S.; Tajdozian, H.; Barman, I.; Lee, Y.; Lee, S.; Song, H.-Y. In Vitro Anti-Tuberculosis Effect of Probiotic *Lacticaseibacillus Rhamnosus* PMC203 Isolated from Vaginal Microbiota. *Sci. Rep.* **2022**, *12*, 8290. [CrossRef]
110. Wrønding, T.; Vomstein, K.; Bosma, E.F.; Mortensen, B.; Westh, H.; Heintz, J.E.; Mollerup, S.; Petersen, A.M.; Ensign, L.M.; DeLong, K.; et al. Antibiotic-Free Vaginal Microbiota Transplant with Donor Engraftment, Dysbiosis Resolution and Live Birth after Recurrent Pregnancy Loss: A Proof of Concept Case Study. *eClinicalMedicine* **2023**, *61*, 102070. [CrossRef] [PubMed]
111. Horrocks, V. NMR Metabolomics to Understand Behaviour and Symbiosis between Isolates of the Vaginal Microbiota. Ph.D. Thesis, King's College London, London, UK, 2022.
112. Di Vito, M.; Mattarelli, P.; Modesto, M.; Girolamo, A.; Ballardini, M.; Tamburro, A.; Meledandri, M.; Mondello, F. In Vitro Activity of Tea Tree Oil Vaginal Suppositories against Candida Spp. and Probiotic Vaginal Microbiota. *Phytother. Res.* **2015**, *29*, 1628–1633. [CrossRef] [PubMed]
113. Aslan, E.; Bechelaghem, N. To 'Douche' or Not to 'Douche': Hygiene Habits May Have Detrimental Effects on Vaginal Microbiota. *J. Obstet. Gynaecol.* **2018**, *38*, 678–681. [CrossRef] [PubMed]
114. Thomas, D.P.; Zhang, J.; Nguyen, N.-T.; Ta, H.T. Microfluidic Gut-on-a-Chip: Fundamentals and Challenges. *Biosensors* **2023**, *13*, 136. [CrossRef]
115. Ding, Z.; Wang, W.; Zhang, K.; Ming, F.; Yangdai, T.; Xu, T.; Shi, H.; Bao, Y.; Yao, H.; Peng, H.; et al. Novel Scheme for Non-Invasive Gut Bioinformation Acquisition with a Magnetically Controlled Sampling Capsule Endoscope. *Gut* **2021**, *70*, 2297–2306. [CrossRef] [PubMed]
116. Nejati, S.; Wang, J.; Sedaghat, S.; Balog, N.K.; Long, A.M.; Rivera, U.H.; Kasi, V.; Park, K.; Johnson, J.S.; Verma, M.S.; et al. Smart Capsule for Targeted Proximal Colon Microbiome Sampling. *Acta Biomater.* **2022**, *154*, 83–96. [CrossRef] [PubMed]

microorganisms

Case Report

Case Report: Fatal Necrotizing Pneumonia by Exfoliative Toxin *etE2*-Producing *Staphylococcus aureus* Belonging to MLST ST152 in The Netherlands

Wouter J. van Steen [1], Monika A. Fliss [2], Ethel Metz [1], Klaus Filoda [3], Charlotte H. S. B. van den Berg [1], Bhanu Sinha [2,†] and Erik Bathoorn [2,*,†]

[1] Department of Intensive Care, University Medical Center Groningen, University of Groningen, 9713 GZ Groningen, The Netherlands
[2] Department of Medical Microbiology and Infection Prevention, University Medical Center Groningen, University of Groningen, 9713 GZ Groningen, The Netherlands; b.sinha@umcg.nl (B.S.)
[3] Department of Intensive Care, Ommelander Ziekenhuis Groningen, 9679 BJ Scheemda, The Netherlands
[*] Correspondence: d.bathoorn@umcg.nl
[†] These authors contributed equally to this work and share last authorship.

Abstract: We present a case of fatal necrotizing *Staphylococcus aureus* pneumonia with underlying influenza A (H3) infection. Next-generation-sequencing-based analysis revealed that the *S. aureus* isolate harbored the newly recognized exfoliative toxin *etE2* gene. Molecular epidemiologic analysis showed that the isolate belonged to the MSSA ST152 lineage, harboring PVL genes and *edinB* co-located to *etE2* as distinctive virulence factors. The *etE2* gene is present in all isolates of this lineage co-located to the exotoxin gene *edinB*, both implicated in the destruction of tissue integrity. We alert as to the global emergence of this lineage causing serious infections in patients.

Keywords: *Staphylococcus aureus*; PVL; exfoliative toxin; molecular epidemiology; surveillance

1. Introduction

This study illustrates the case of a previously healthy young adult who was hospitalized in the Netherlands for the treatment of a community-acquired necrotizing *Staphylococcus aureus* (MSSA) pneumonia with an underlying influenza A (H3) infection. Necrotizing pneumonia is a disease entity with a high mortality rate that is characterized by a rapidly deteriorating clinical course, leukopenia, airway hemorrhages, severe respiratory failure, and the necrotic destruction of wide areas of the lung [1]. The course of disease was fulminant, and the patient deceased on the second day of hospitalization on the intensive care unit. Molecular evaluation revealed that the isolate belonged to Multi-Locus Sequencing Type (MLST) ST152 and was positive for an extensive repertoire of virulence genes, including genes encoding for the cytotoxin Panton–Valentine leukocidine (PVL; *lukS* PV and *lukF* PV), the exotoxin *edinB*, and the recently identified exfoliative toxin E allelic variant *etE2*, identified in a case of severe necrotizing fasciitis [2].

This communication should raise awareness of the emergence of the MSSA ST152 lineage, which is associated with severe necrotizing pneumonia accompanied by bacteremia, and deep-seated soft-tissue infections as frequent presentations. In all isolates of this lineage, the newly identified exfoliative toxin gene *etE2* is present. The global dissemination of this high-risk PVL-positive community lineage, which harbors the exotoxin genes *edinB* and *etE2* implicated in the destruction of tissue integrity, is a potential threat to public health and warrants monitoring.

Microorganisms **2025**, *13*, 1618 https://doi.org/10.3390/microorganisms13071618

2. Case Description

A 25-year-old previously healthy male presented with tachypnea and hypoxemia to the emergency department of a regional hospital in the Netherlands in 2024. The patient had been experiencing malaise for one week prior to presentation and had been prescribed amoxicillin for a respiratory infection one day prior to admission. Upon admission, he was diagnosed with pneumosepsis and bilateral severe pneumonia, necessitating high-flow nasal cannula oxygen therapy in the intensive care unit. A nasopharyngeal swab and PCR tested positive for influenza A. Later subtyping showed that the virus belonged to H3. Blood tests revealed no leucocytosis but showed an elevated C-reactive protein level of 108 mg/L (normal range: <5 mg/L) and an arterial lactate of 6.4 mmol/L (normal range: <2 mmol/L) on admission. Given the suspicion of bacterial superinfection, empirical antibiotic therapy with cefuroxime (1.5 g three-times daily) and ciprofloxacin (400 mg twice daily) was initiated after obtaining blood and sputum cultures.

Despite treatment, the patient's condition deteriorated rapidly, requiring endotracheal intubation and mechanical ventilation in the prone position. Hemodynamic support with escalating doses of norepinephrine and vasopressin were started, along with continuous hydrocortisone (200 mg once daily) due to the severity of septic shock.

The following day, the patient was transferred to our tertiary intensive care unit. Shortly after arrival, he suffered cardiac arrest, prompting cardiopulmonary resuscitation for approximately 20 min. During resuscitation, large amounts of pink, watery sputum were drained from the lungs. After achieving the return of spontaneous circulation, veno-venous extracorporeal membrane oxygenation and continuous renal replacement therapy were initiated. The antibiotic regimen was escalated to cefotaxime (4 g continuous daily), levofloxacin (500 mg twice daily, and clindamycin (900 mg three-times daily). Despite these interventions, the patient's condition continued to deteriorate, with the development of liver failure, coagulopathy, refractory hyperlactatemia, heart failure, pericardial effusion, and loss of brain function, with dilated non-reactive pupils. Bronchoscopy revealed diffusely swollen bronchial mucosa and significant watery secretions. Extensive transfusions led to worsening pulmonary edema.

Given the lack of clinical stabilization, the medical team concluded that recovery was unlikely. The best supportive care was initiated, and the patient passed away later that day. *Post mortem*, the blood and sputum cultures identified *S. aureus*.

Isolate Characterization

The *S. aureus* isolate UMCG-ST152-2024-1 grew from a blood culture and in pure culture from sputum samples. Analysis of short-read sequencing (MiSeq, Ilumina, San Diego, CA, USA), as described previously [3], revealed that the isolate belonged to MLST ST152. The isolate was susceptible to all antibiotics tested by Vitek2 (Biomerieux, Marcy l'Etoile, France) except for trimethoprim and penicillin G, interpreted by EUCAST v.13.1. The resistance was confirmed by agar diffusion disk testing with a zone of 6 mm to trimethoprim and 10 mm to penicillin, and the associated resistance genes *blaZ* and *dfrG* were detected by sequencing. In Table 1, we present the repertoire of virulence genes identified by SeqSphere [4]. The list of virulence factors is extensive. However, we emphasize the presence of PVL-encoding genes (*lukS* PV and *lukF* PV), *edinB*, and *etE2* since they are epidemiologically important molecular markers. Figure 1 shows that the toxin genes *etE2* and *edinB* were detected in a co-located position on a previously described genomic island [2]. The *lukF-PV* and *lukS-PV* genes were located on the ΦSa2 phage. In Figure 2, the phylogenetic relation of the isolate is presented using public sequencing data of isolates from clonal complex (CC) 152 [5]. The clinical isolate is in a clade that consists mostly of MSSA strains. The MSSA isolate ERR3861662 obtained from the Democratic Republic of the Congo is the most recent common ancestor of UMCG-ST152-2024-1, and it clusters with isolates that have been isolated from Nigeria (*n* = 3), Gabon (*n* = 2), Reunion, France (*n* = 2), and one isolate from Denmark which was identified as MRSA. The co-located virulence genes *etE2* and *edinB* were present in the same nucleotide composition in all isolates of the CC152 lineage.

Table 1. Major virulence genes in isolate *S. aureus* UMCG-ST152-2024-1.

Gene	Virulence Factor
aur	ACME
cap5H	capsule
cap5J	capsule
cap5K	capsule
ebpS	adhesion
edinB	exotoxin
etE2	exfoliative toxin
eno	adhesion
hla	hemolysin
hlb-intact	hemolysin
hlgA	hemolysin
hlgB	hemolysin
hlIII	hemolysin
icaA	adhesion
icaD	biofilm
isaB	immunodominant antigen
isdA	MSCRAMM
lukF-PV	leukotoxin (PVL)
lukS-PV	leukotoxin (PVL)
sak	immune-evasion
scn	immune-evasion
setB1	superantigen-like
setB3	superantigen-like
ssl01	superantigen-like
ssl02	superantigen-like
ssl10	superantigen-like
sspA	serine protease
sspB	cystein protease
sspP	cystein protease

Virulence genes were detected using SeqSphere+ v9.0.8. The exfoliative toxin *etE2* was manually detected and submitted to the Virulence Factor Database. ACME: arginine catabolic mobile element; MSCRAMM: Microbial Surface Components Recognizing Adhesive Matrix Molecules; PVL: Panton–Valentine leukocidine. Superantigen-like: A family of virulence factors with homology to superantigens, associated with host–pathogen interactions and immune evasion.

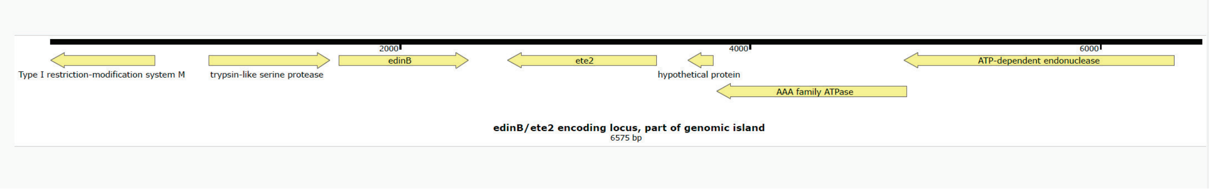

Figure 1. A genetic map of the part of the genomic island which integrates *etE2* and *edinB* in the chromosome of *S. aureus* UMCG-ST152-2024-1. Figure legend: The genetic map was visualized using Snapgene V 5.1.7.

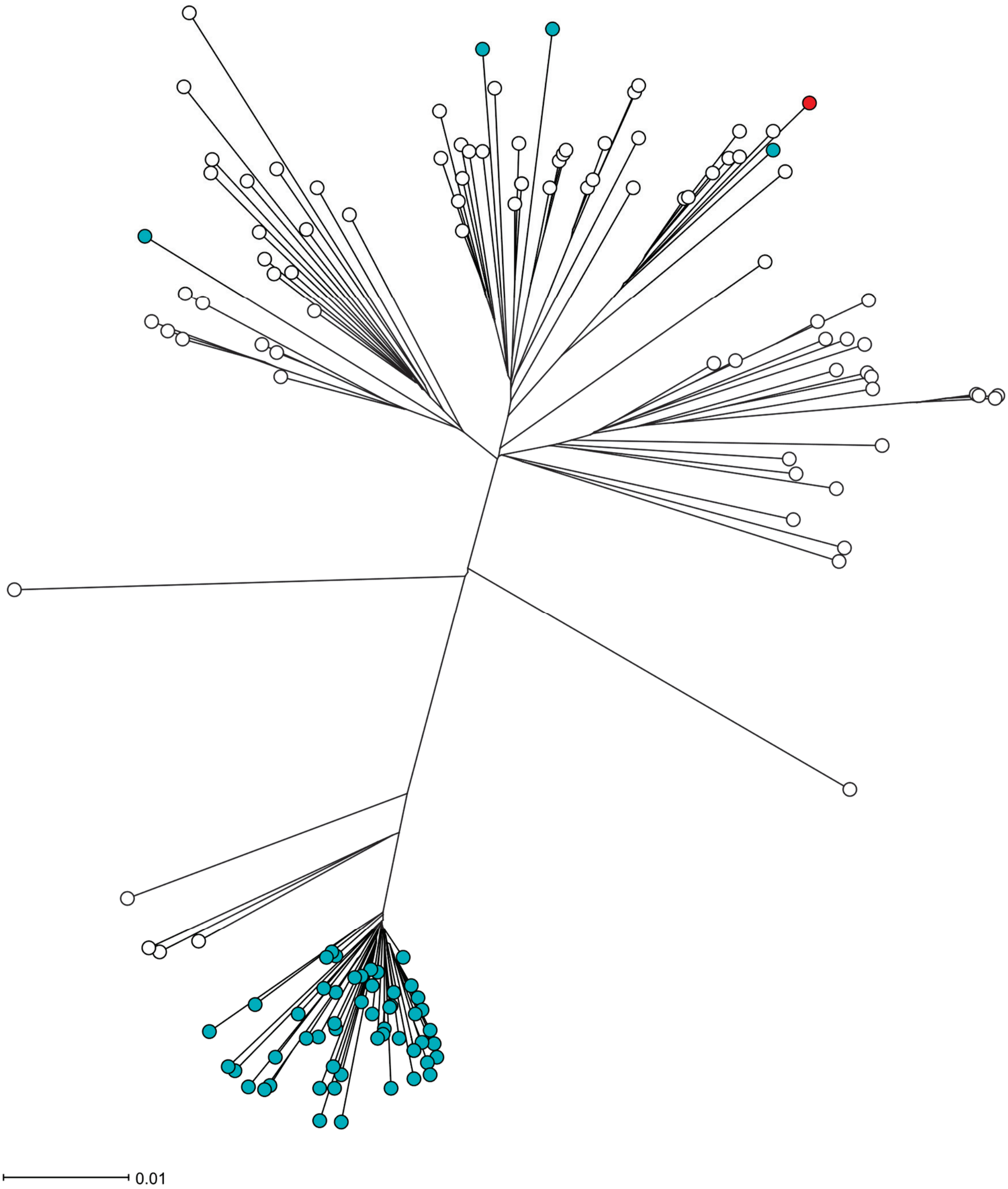

Figure 2. The phylogeny of the *S. aureus* isolate UMCG-ST152-2024-1 in the CC152 lineage. Figure legend: The radial neighbor-joining tree of S. aureus was generated by SeqSphere+ v9.0.8, analyzing 140 genomes. In this analysis, 1861 genes were compared using published schema. The red dot represents isolate UMCG-ST152-2024-1, the white dots are MSSA isolates, and the blue dots are MRSA isolates.

3. Discussion

We present the case of a fatal community-acquired necrotizing pneumoniae caused by *S. aureus* in a young adult with underlying influenza A infection. At the University Medical Center Groningen (UMCG), severe necrotizing *S aureus* infections had sporadically been seen before. When we encounter such infections, we sequence the isolates to determine the sequence type of the *S aureus* isolate and explore if (exo-)toxins are present that could have contributed to the severity of the infection. Although disease presentation and severity of infection generally depend on combinations of virulence and host factors, some specific well-characterized virulence factors are associated with typical disease presentations.

Remarkably, when comparing the genomic data in the UMCG database, we found a closest match with a case of severe necrotizing *S. aureus* infection by MSSA ST152 presenting in 2022 [2]. This patient had been admitted to the intensive care suffering from severe necrotizing cellulitis. The isolate in that study showed a similar virulence factor profile to the present case. In that study, we reported the identification of a genomic island encoding the exotoxins *edinB* and *etE2* in the isolate's genome. Both toxins encoded by these genes are directly associated with tissue destruction. The gene *etE2* is a novel exfoliative toxin encoding gene variant of *etE*. The *etE* gene has been detected in ovine *S. aureus* isolates, whereas we have exclusively detected *etE2* in human *S. aureus* isolates [6]. Degradation experiments of epidermal cells have shown the host-specificity of *etE*, which may explain why the toxin variants have consistently been detected in different species. Exfoliative toxins, in general, are very specific serine proteases, causing lesions in tissue by cutting desmosomes, which are cell-adherence molecules. The typical presentations of disease are bullous impetigo and staphylococcal scalded skin syndrome [7]. Future experimental studies are required to gain more insight into the contribution of the ETE2 exotoxin to the virulence of the MSSA ST152 lineage.

Our study shows that *edinB* and the co-located *etE2* are consistently present in the CC152 lineage. EDIN-B is a C3-like ADP-ribosyltransferase that catalyzes the ribosylation of Rho GTPases. The inhibition of Rho GTPases results in the modification of the actin cytoskeleton of the host cells and devastates stress fibers, which are involved in cell contractility [8]. The exposure of cells to EDIN-B results in the loss of tissue integrity through the formation of large transcellular tunnels by this exotoxin [9]. In a mouse model of *S aureus* pneumonia, the role of EDIN-B was identified as an important factor in the translocation of *S aureus* to the bloodstream by comparing wildtype and knock-out strains [10]. Also, clinical reports suggest that EDIN-B is a virulence factor associated with invasive infection. In diabetic ulcers, *edinB*-positive *S aureus* is prevalent at a much higher rate in deep-seated ulcer infections compared to low-grade infections. In addition, several studies have reported increased percentages of *edinB*-positive *S aureus* in deep-seated or bloodstream infection [11]. However, since *edinB* is co-located on a genomic island with exfoliative exotoxins, as we and others have shown [12], it is unclear if EDIN-B acts independently as a causative factor in deep-seated infections.

The PVL-positive MSSA ST152 is a hyperepidemic lineage, predominantly circulating in Africa and the Caribbean. Reports of MSSA ST152 in Europe are uncommon so far, in contrast to the MRSA clade of ST152, which is most prevalent in Europe [5]. This MRSA clade probably emerged from a common ancestor in the 1990s. This clonal expansion is similar to other hyperepidemic MRSA lineages in the community, such as CC80 and USA300. In addition, numerous sporadic acquisitions of methicillin resistance have occurred in MSSA ST152, without clonal expansion, as shown in Figure 2. The MSSA ST152 lineage is commonly associated with wound infections [13,14]. In our study, we show that MSSA ST152 is also associated with necrotizing pneumoniae.

Necrotizing pneumonia is often caused by a *S. aureus* superinfection upon a viral airway infection, most prominently influenza A and B. If the infection is caused by PVL positive isolates, the course of disease can be severe, even in young, otherwise healthy adults [1,15]. In 2022, two cases of severe necrotizing pneumonia PVL-positive MSSA ST152 requiring intensive care treatment were reported in the Indian Ocean region [16]. In both cases, an underlying SARS-CoV-2 respiratory infection had been detected, but no other immuno-compromising disease. Like our case, both the patients had concurrent bacteremia with *S. aureus*. In 2021, in a case of severe necrotizing pneumonia and bloodstream infection from the Faroe Islands, PVL-positive MSSA ST152, was reported as causative pathogen. This patient had an underlying influenza B infection, was 47 years old, and was previously healthy [17].

The pathological association between preceding influenza infection and PVL-positive *S. aureus* causing necrotizing pneumonia has already been proposed, in 2014. The proposed theory for this association is that the lungs are infiltrated by inflammatory cells during viral infection. Subsequently, PVL produced by *S. aureus* forms membrane pores, causing massive destruction of leukocytes with the subsequent release of neutrophile serine proteases that destroy human tissue [18]. While experimental data supports this theory, there are other membrane-active toxins, such as the family of small membrane-active peptides (phenol-soluble modulins, PSMs) that are pathogenetically relevant in severe soft-tissue infections, and pore-forming toxins, such as alpha-toxin, that cause the lysis of leukocytes and red blood cells [19]. Furthermore, the synergistic effect of *S. aureus* alpha-toxin Hla and PVL was shown in the pathogenesis of necrotizing pneumonia [20]. PVL could be one factor in a multifactorial etiology of disease contributed to by the numerous virulence factors that are produced by *S. aureus* implicated in the lysis of leukocytes, tissue destruction, and immune evasion. While the exact contribution to the severity of disease of each virulence factor separately is difficult to establish in humans, it is certain that the PVL-positive MSSA ST152 lineage is outstanding in its plentitude of virulence factors.

In conclusion, severe infections caused by MSSA ST152 positive for an extensive repertoire of virulence factors including PVL, *edinB*, and *etE2* appear to be an emerging issue in Europe and other regions. The presented cases and other recent casuistic studies report that isolates of this lineage cause life-threatening necrotizing pneumonia with concurrent bacteremia in previously healthy persons suffering from underlying influenza or SARS-CoV2 infections. In future surveillance projects, the typing of MSSA isolated from blood cultures could be considered for the risk assessment of this lineage. On our request, the characterized exfoliative toxin gene *etE*, which had thus far been exclusively detected in animals, and its allelic variant *etE2*, have been included in the Virulence Factor Database so that they can be detected by NGS-based analysis tools.

Author Contributions: W.J.v.S. collected the data and drafted the manuscript; M.A.F. supervised the molecular research and analysis; E.M., K.F. and C.H.S.B.v.d.B. participated in the writing and editing of the manuscript; B.S. identified the case and participated in the conception and editing of the manuscript; E.B. coordinated and edited the manuscript. All authors have read and agreed to the published version of the manuscript.

Funding: This research received no external funding.

Institutional Review Board Statement: No ethical approval was necessary for this case study. The conduct and reporting of this study were in line with the Declaration of Helsinki, as revised in 2013.

Informed Consent Statement: Written informed consent was obtained from the parents of the patient.

Data Availability Statement: The sequences of the isolates are available from the European Nucleotide Archive (ENA) under project number: PRJEB88875. [European Nucleotide Archive] URL (accessed on 15 June 2025) [https://www.ebi.ac.uk] [PRJEB88875].

Conflicts of Interest: The authors declare no conflicts of interest.

References

1. Gillet, Y.; Issartel, B.; Vanhems, P.; Fournet, J.-C.; Lina, G.; Bes, M.; Vandenesch, F.; Piémont, Y.; Brousse, N.; Floret, D.; et al. Association between Staphylococcus aureus strains carrying gene for Panton-Valentine leukocidin and highly lethal necrotising pneumonia in young immunocompetent patients. *Lancet* **2002**, *359*, 753–759. [PubMed]
2. Sabat, A.J.; Wouthuyzen-Bakker, M.; Rondags, A.; Hughes, L.; Akkerboom, V.; Koutsopetra, O.; Friedrich, A.W.; Bathoorn, E. Case Report: Necrotizing fasciitis caused by *Staphylococcus aureus* positive for a new sequence variant of exfoliative toxin E. *Front. Genet.* **2002**, *13*, 964358.
3. Lisotto, P.; Raangs, E.C.; Couto, N.; Rosema, S.; Lokate, M.; Zhou, X.; Friedrich, A.W.; Rossen, J.W.A.; Harmsen, H.J.M.; Bathoorn, E.; et al. Long-read sequencing-based in silico phage typing of vancomycin-resistant Enterococcus faecium. *BMC Genom.* **2021**, *22*, 758.
4. Strauß, L.; Ruffing, U.; Abdulla, S.; Alabi, A.; Akulenko, R.; Garrine, M.; Germann, A.; Grobusch, M.P.; Helms, V.; Herrmann, M.; et al. Detecting Staphylococcus aureus Virulence and Resistance Genes: A Comparison of Whole-Genome Sequencing and DNA Microarray Technology. *J. Clin. Microbiol.* **2016**, *54*, 1008–1016. [PubMed]
5. Baig, S.; Larsen, A.R.; Simões, P.M.; Laurent, F.; Johannesen, T.B.; Lilje, B.; Tristan, A.; Schaumburg, F.; Egyir, B.; Cirkovic, I.; et al. Evolution and Population Dynamics of Clonal Complex 152 Community-Associated Methicillin-Resistant *Staphylococcus aureus*. *mSphere* **2020**, *5*, e00226-20. [PubMed]
6. Imanishi, I.; Nicolas, A.; Caetano, A.B.; Castro, T.L.P.; Tartaglia, N.R.; Mariutti, R.; Guédon, E.; Even, S.; Berkova, N.; Arni, R.K.; et al. Exfoliative toxin E, a new Staphylococcus aureus virulence factor with host-specific activity. *Sci. Rep.* **2019**, *9*, 16336.
7. Bukowski, M.; Wladyka, B.; Dubin, G. Exfoliative toxins of Staphylococcus aureus. *Toxins* **2010**, *2*, 1148–1165. [CrossRef] [PubMed]
8. Wiegers, W.; Just, I.; Müller, H.; Hellwig, A.; Traub, P.; Aktories, K. Alteration of the cytoskeleton of mammalian cells cultured in vitro by Clostridium botulinum C2 toxin and C3 ADP-ribosyltransferase. *Eur. J. Cell Biol.* **1991**, *54*, 237–245. [PubMed]
9. Boyer, L.; Doye, A.; Rolando, M.; Flatau, G.; Munro, P.; Gounon, P.; ClémEnt, R.; Pulcini, C.; Popoff, M.R.; Mettouchi, A.; et al. Induction of transient macroapertures in endothelial cells through RhoA inhibition by Staphylococcus aureus factors. *J. Cell Biol.* **2006**, *173*, 809–819. [PubMed]
10. Courjon, J.; Munro, P.; Benito, Y.; Visvikis, O.; Bouchiat, C.; Boyer, L.; Doye, A.; Lepidi, H.; Ghigo, E.; Lavigne, J.P.; et al. EDIN-B Promotes the Translocation of Staphylococcus aureus to the Bloodstream in the Course of Pneumonia. *Toxins* **2015**, *7*, 4131–4142. [CrossRef] [PubMed]
11. Czech, A.; Yamaguchi, T.; Bader, L.; Linder, S.; Kaminski, K.; Sugai, M.; Aepfelbacher, M. Prevalence of Rho-inactivating epidermal cell differentiation inhibitor toxins in clinical Staphylococcus aureus isolates. *J. Infect. Dis.* **2001**, *184*, 785–788. [PubMed]
12. Yamaguchi, T.; Nishifuji, K.; Sasaki, M.; Fudaba, Y.; Aepfelbacher, M.; Takata, T.; Ohara, M.; Komatsuzawa, H.; Amagai, M.; Sugai, M.; et al. Identification of the Staphylococcus aureus etd pathogenicity island which encodes a novel exfoliative toxin, ETD, and EDIN-B. *Infect. Immun.* **2002**, *70*, 5835–5845. [PubMed]
13. Egyir, B.; Owusu-Nyantakyi, C.; Bortey, A.; Amuasi, G.R.; Owusu, F.A.; Boateng, W.; Ahmed, H.; Danso, J.K.; Oclu, A.A.G.; Mohktar, Q.; et al. Whole genome sequencing revealed high proportions of ST152 MRSA among clinical *Staphylococcus aureus* isolates from ten hospitals in Ghana. *mSphere* **2024**, *9*, e00446-24. [PubMed]
14. Shittu, A.O.; Okon, K.; Adesida, S.; Oyedara, O.; Witte, W.; Strommenger, B.; Layer, F.; Nübel, U. Antibiotic resistance and molecular epidemiology of Staphylococcus aureus in Nigeria. *BMC Microbiol.* **2011**, *11*, 92.
15. Newell, R.; El-Shakankery, K.; Bhowmik, A.; Rajakulasingam, R.K. Panton–Valentine leucocidin Staphylococcus aureus necrotising pneumonia in a clinically well patient. *Br. J. Hosp. Med.* **2023**, *29*, 1–4.
16. Allou, N.; Allyn, J.; Traversier, N.; Baron, M.; Blondé, R.; Dupieux, C.; Coolen-Allou, N.; Jabot, J.; Miltgen, G. SARS-CoV-2 with Panton-Valentine leukocidin-producing *Staphylococcus aureus* healthcare-associated pneumonia in the Indian Ocean. *Heliyon* **2022**, *8*, e10422. [PubMed]
17. Larsen, S.A.H.; Kyhl, K.; Baig, S.; Petersen, A.; Av Steinum, M.R.; Clemmensen, S.; Jensen, E.; Á Steig, T.; Gaini, S. Life-Threatening Necrotizing Pneumonia with Panton-Valentine Leukocidin-Producing, Methicillin-Sensitive Staphylococcus aureus in a Healthy Male Co-Infected with Influenza B. *Infect. Dis. Rep.* **2021**, *14*, 12–19. [PubMed]
18. Löffler, B.; Niemann, S.; Ehrhardt, C.; Horn, D.; Lanckohr, C.; Lina, G.; Ludwig, S.; Peters, G. Pathogenesis of Staphylococcus aureus necrotizing pneumonia: The role of PVL and an influenza coinfection. *Expert. Rev. Anti Infect. Ther.* **2013**, *11*, 1041–1051. [PubMed]

19. Otto, M. Staphylococcus aureus toxins. *Curr. Opin. Microbiol.* **2014**, *17*, 32–37. [PubMed]
20. Ragle, B.E.; Bubeck Wardenburg, J. Anti-alpha-hemolysin monoclonal antibodies mediate protection against Staphylococcus aureus pneumonia. *Infect. Immun.* **2009**, *77*, 2712–2718. [PubMed]

microorganisms

MDPI

Systematic Review

Unraveling Pediatric Group A Streptococcus Meningitis: Lessons from Two Case Reports and a Systematic Review

Lavinia Di Meglio [1,*], Maia De Luca [2,*], Laura Cursi [2], Lorenza Romani [2], Mara Pisani [3], Anna Maria Musolino [3], Stefania Mercadante [2], Venere Cortazzo [4], Gianluca Vrenna [4], Paola Bernaschi [4], Roberto Bianchi [5] and Laura Lancella [2]

[1] School of Pediatrics, University of Rome Tor Vergata, 00133 Rome, Italy
[2] Infectious Diseases Unit, Bambino Gesù Children's Hospital, IRCCS, 00165 Rome, Italy; laura.cursi@opbg.net (L.C.); lorenza.romani@opbg.net (L.R.); stefania.mercadante@opbg.net (S.M.); laura.lancella@opbg.net (L.L.)
[3] Hospital University Pediatrics Clinical Area, Bambino Gesù Children's Hospital, IRCCS, 00165 Rome, Italy; mara.pisani@opbg.net (M.P.); amcaterina.musolino@opbg.net (A.M.M.)
[4] Unit of Microbiology and Diagnostic Immunology, Bambino Gesù Children's Hospital, IRCCS, 00165 Rome, Italy; venere.cortazzo@opbg.net (V.C.); gianluca.vrenna@opbg.net (G.V.); paola.bernaschi@opbg.net (P.B.)
[5] Anaesthesia, Emergency and Pediatric Intensive Care Unit, Bambino Gesù Children Hospital, IRCCS, 00165 Rome, Italy; roberto.bianchi@opbg.net
* Correspondence: laviniadimeglio@gmail.com (L.D.M.); maia.deluca@opbg.net (M.D.L.); Tel.: +39-3357017645 (ext. 80127) (L.D.M.)

Abstract: *Streptococcus pyogenes* meningitis is a rare invasive disease, accounting for less than 2% of bacterial meningitis. We presented two case reports and conducted a systematic review using PUBMED, covering the database from its inception up to 31 December 2024, of pediatric cases of Streptococcus pyogenes meningitis. Only case reports and case series were included. Differences in clinical and laboratory parameters were compared between uneventful course and complicated admissions. A total of 57 cases were included. The median age at diagnosis was 4 years. A primary infection focus outside the brain was identified in 61.39% of cases. *S. pyogenes* was identified from cerebrospinal fluid in 66.66% of cases and from blood in 15.79%. Septic shock occurred in 24.56% of cases, and 36.84% had brain anatomical anomalies. All patients received broad-spectrum empiric antibiotics, while protein-synthesis inhibitors were administered in 26.31% of cases. A total of 17% of patients died, and 28.07% experienced sequelae. The identification of *S. pyogenes* from blood and a Phoenix Sepsis Score ≥ 2 were significantly associated with a complicated clinical course. Our findings may offer useful insights for the clinical management of Streptococcus pyogenes meningitis.

Keywords: *Streptococcus pyogenes*; meningitis; children; pediatrics; group A streptococcus; GAS

1. Introduction

Group A streptococcus (GAS), also known as *Streptococcus pyogenes*, is a Gram-positive bacterium and one of the leading human-restricted pathogens affecting children worldwide [1]. This pathogen can cause both non-invasive disease—pharyngitis, scarlet fever, impetigo—as well as life-threatening invasive diseases [1–3]. The most common invasive GAS (iGAS) infections are toxic shock syndrome and necrotizing fasciitis [1–3]. The main virulence factors of *S. pyogenes* are the M protein and secreted pyogenic exotoxins (SPE). The M protein is the pivotal virulence factor, functioning as an epithelial adhesion

https://doi.org/10.3390/microorganisms13051100

factor and inhibiting bacterial phagocytosis. It is encoded by the *emm* gene, with more than 180 M protein variants detected to date. In iGAS infections, an association with *emm 1*, *emm 3*, SPE A, and SPE B has been described [1–4]. *S. pyogenes* meningitis is a rare invasive disease, accounting for less than 2% of iGAS cases [5]. Since 2022, an increase in iGAS infections has been reported in many European countries, with a subsequent rise in GAS meningitis cases [6]. We present two case reports and a systematic review to:

- highlight the key clinical features, common complications, and outcomes of GAS meningitis;
- identify factors associated with a complicated course of disease.

2. Case Reports

Case 1:

A fully immunized 4 years and 8 months old girl presented to our Pediatric Emergency Department (ED) with fever, left earache within the previous 48 h, and incoercible vomiting over the preceding 24 h. Her past medical history was unremarkable. On physical examination, she was alert and reactive but appeared unwell with meningeal signs. Vital parameters showed normal blood pressure 108/83 mmHg, mild tachycardia 105 bpm, and mild tachypnea 40/min. Otoscopy showed left acute otitis media (AOM), while the rest of the examination was normal. Therapy with ceftriaxone and acyclovir was initiated, and blood tests, a head CT, and a lumbar puncture were performed (Table 1). Blood tests revealed neutrophilic leukocytosis and elevated C-reactive protein (CRP). Cerebrospinal fluid (CSF) analysis was compatible with bacterial meningitis (Table 1), and the head CT revealed left mastoiditis with a hypodense fluid collection (maximum thickness: 5 mm), involving the temporal and occipital lobes. Blood and CSF cultures were collected, and a rapid multiplex PCR panel for viruses and bacteria on CSF was negative. Seven hours later, the patient developed focal seizures and worsening neurological status. On examination, she was unresponsive, presenting with anisocoria, right fixed mydriasis, decerebrate posturing, and a positive Babinski sign. The patient was intubated, and an emergent head CT revealed cerebral edema. Dexamethasone and mannitol were administered, and an urgent decompressive craniotomy was performed. Vital parameters showed hypotension (80/50 mmHg), tachycardia 170, and tachypnea 40/min. The CSF culture became positive for *Streptococcus pyogenes* after 10 h, and therapy was adjusted with the addition of linezolid, while acyclovir was discontinued. Despite those interventions, the patient developed hypotensive shock, and an electroencephalogram (EEG) showed the absence of electrical activity. The patient was declared brain dead 48 h after admission.

Table 1. Clinical and laboratory features of the two case reports.

	Case One	**Case Two**
Age Sex	4 years and 8 months Female	5 years and 9 months Female
Comorbidities	No	No
Local infection	AOM	No
Blood exams		
White blood cells	32,280/m^3	18,370/m^3
Neutrophils	95.54%	94%
Lymphocytes	1.1%	3.0%
Hemoglobin	11.5 g/dL	9.7 g/dL

Table 1. *Cont.*

	Case One	**Case Two**
Platelets	450,000/m^3	137,000/m^3
CRP	16.76 mg/dL	26.74 mg/dL
Procalcitonin	28.6 ng/mL	24.3 ng/mL
Glucose	95 mg/dL	140 mg/dL
Cerebrospinal fluid		
Appearance	turbid	turbid
Color	xanthochrome	xanthochrome
White blood cells	296/m^3	49/m^3
Glucose	2 mg/dL	58 mg/dL
Proteins	511 mg/dL	125 mg/dL
Treatment and Outcome		
Therapy	Ceftriaxone, Linezolid	Ceftriaxone, Vancomycin, Linezolid, Immunoglobulins
Surgery	Craniectomy	Craniectomy
Length of stay	2 days	21 days
Outcome	Death	Full recovery

Case 2:

A fully immunized 5 year and 9 months old girl presented to a peripheral ED with a 48 h history of fever and lethargy. On examination, she exhibited meningeal signs. Therapy with ceftriaxone and vancomycin was initiated, and the girl was transferred to our pediatric intensive care unit. Upon arrival, she was lethargic with meningeal signs, but no evidence of localized infection was detected. Vital parameters showed normal blood pressure 105/70 mmHg, tachycardia 112 bpm, and mild tachypnea 42/min. Blood tests revealed neutrophilic leukocytosis and elevated CRP. Blood and CSF cultures were collected. CSF analysis was consistent with bacterial meningitis (Table 1). An initial head CT showed a fluid collection (maximum thickness: 4 mm) in the right frontal and parietal regions. BIOFIRE® FILMARRAY® Meningitis/Encephalitis Panel for viruses and bacteria on CSF was negative. After consultation with microbiologists, given the strong suspicion of bacterial meningitis, the Biofire Blood Culture Identification (BCID) Panel designed for blood—which includes a larger number of bacterial targets—was performed on the CSF, yielding a positive result for *Streptococcus pyogenes*. Therapy with dexamethasone was initiated and therapy with immunoglobulin for 3 days at 400 mg/kg was implemented, while vancomycin was discontinued. After five days, the patient was afebrile but continued to exhibit meningeal signs and developed left hemiparesis; BP was stable 98/75 mmHg, and at lower limit the heart rate was 60 bpm. An EEG revealed asymmetrical brain activity, and a brain MRI showed an enlargement of the fluid collection, now involving the entire right hemisphere with a thickness of 6 mm. Antibiotic treatment was remodulated with addition of linezolid, and an urgent decompressive craniotomy was performed. From that moment, the patient showed a slow but progressive improvement. Physiotherapy was started, and after 10 days, the neurological examination was normal. Audiometry performed prior to discharge was also normal. The patient was discharged home after 21 days in good clinical condition, continuing a tapering of steroid therapy at home. Two years after the event, she remains in good health, with no neurological sequelae.

3. Materials and Methods

A systematic review following the PRISMA 2020 statement was conducted from the inception of the database up to 31 December 2024, using PUBMED. The following keywords were used: Streptococcus pyogenes meningitis, Group A Streptococcus meningitis, and invasive Streptococcus pyogenes disease. The inclusion criteria were as follows: a diagnosis of bacterial meningitis based on CSF features and clinical conditions, along with culture or PCR (from either CSF or blood) positive for *S. pyogenes*, and patients aged < 18 years. Only case reports and case series were included. Cases from all selected studies were evaluated and analyzed. Study selection followed the PRISMA flow diagram (Figure 1). Two researchers independently assessed the eligibility of the studies. Data extraction from individual studies was performed in duplicate. Any discrepancies in data extraction were discussed and resolved among the authors.

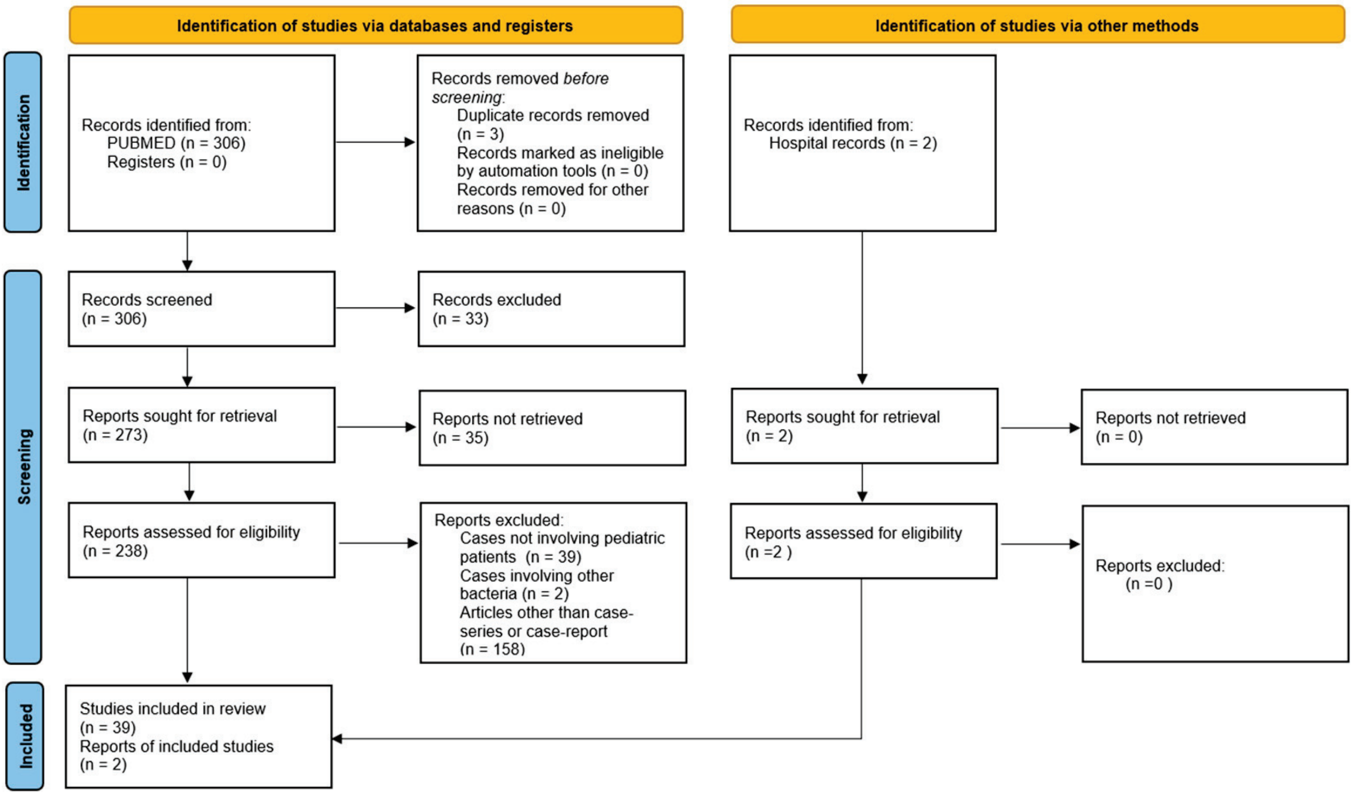

Figure 1. Prima flowchart.

A total of 306 manuscripts were initially identified. After reviewing titles and abstracts and eliminating duplicates, 238 full-text articles were assessed. Ultimately, 39 papers were selected and included in the review. We analyzed each of the retained studies, as well as our two case reports, to create our own database. The following variables were collected: age, sex, medical history (both past and present), prior *S. pyogenes* localized infections, laboratory results, CT/MRI findings, treatment regimens, and clinical outcomes. In each study, all categories and variables were analyzed. Data were entered into a dedicated database. Categorical data are presented as frequencies and percentages, while continuous data are expressed as means/medians with ranges, depending on the statistical distribution.

Patients were classified into two groups: those with a uneventful meningitis course, defined as patients who did not experience septic shock, neurological deterioration, or brain involvement on CT/MRI, and those with a complicated course, defined as patients who developed septic shock, neurological instability, brain involvement on CT/MRI, sequelae (including nerve palsy, deafness, neurological impairment), or death. The following variables were compared between the two groups: age, female sex, focus of infection outside the brain, CSF white blood cell (WBC) count, CSF protein levels, CSF glucose levels, WBC blood count, identification of *S. pyogenes* on blood, Phoenix Sepsis Score $\geq$ 2 [7], use of antibiotics with activity on protein synthesis inhibition, dexamethasone therapy, and length of hospital stay. A univariate analysis was initially performed to assess the associations between each independent variable and the outcome. The Chi-square (χ^2) test was used for nominal variables, with a significance threshold set at 0.05. For independent numerical variables following a normal distribution, comparisons between the two groups were made using a one-tailed *t*-test, with a significance level of 0.05. Subsequently, a multivariate analysis using logistic regression was conducted, adjusted for age and sex, accounting for potential confounding factors. Odds ratios (OR) were calculated, along with 95% confidence intervals (CI), to assess the strength of the associations. All statistical analyses were performed using Jamovi version 2.6.44.

4. Results

Here, we report the results of a systematic review of the literature and the description of two cases of *S. pyogenes* meningitis. In total, 39 papers reporting a total of 55 cases were included in the analysis, and we also added 2 cases admitted to our hospital for a total of 57 cases (Figure 1) [8–46]. Results are summarized in Table 2 and Figure 2.

Table 2. Characteristics of the two patients admitted to our hospital and of the patients derived from the systematic review.

Variable	Variable Subclassification	Results	Variable	Variable Subclassification	Results
Predisposing conditions	HIV VPS Cochlear implant Prematurity	1.75% (1/57) 1.75% (1/57) 1.75% (1/57) 1.75% (1/57)	Cerebral TC/RMN findings	Cerebral collection Hydrocephalus Cerebral edema Vasculopathy Necrosis Ventriculitis Myelitis	21.04% (12/57) 5.26% (3/57) 8.77% (12/57) 21.04% (12/57) 8.77% (5/57) 7.01% (4/57) 1.75% (1/57)
Empiric antibiotic therapy	Cephalosporin Cephalosporin plus glycopeptides Other regimes Overall use of protein-synthesis inhibitors	66.66% (38/57) 17.54% (10/57) 15.78 (9/57) 26.31% (15/57)	Additional treatment/ therapies	Steroids Immunoglobulins Surgery	33.33% (19/57) 5.26% (3/57) 22.80% (13/57)
Overall complications	Status epilepticus Nerve involvement Hydrocephalus Brain collection Vasculopathy Hygroma Cerebral edema Coma Phoenix Sepsis Score $\geq$ 2	21.04% (12/57) 7.01% (4/57) 5.26% (3/57) 21.04% (12/57) 12.28% (7/57) 7.01% (4/57) 24.56% (14/57) 33.33% (19/57) 45.61% (26/57)	Outcome	Full recovery Death Sequelae: -NSHL -Third nerve palsy -Moderate disability -Severe disability	62.39% (31/57) 17.54% (10/57) 28.07% (16/57) 5.26% (3/57) 1.75% (1/57) 5.26% (3/57) 15.80% (9/57)

VPS: ventricular peritoneal shunt, NSHL: sensorineural hearing loss.

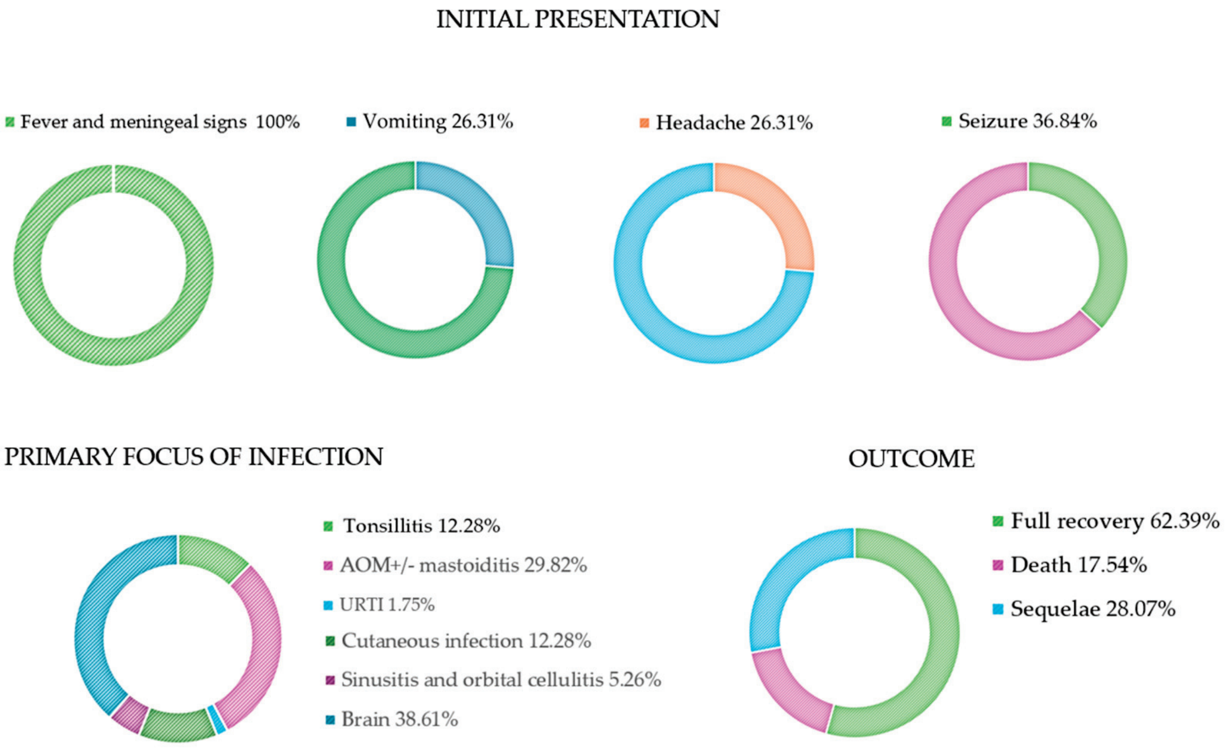

Figure 2. Initial presentation, primary focus of infection and clinical outcome. AOM: acute otitis media; URTI: upper respiratory tract infections.

The median age at diagnosis was 4 years (range: 1 day–15 years); 54.38% (31/57) were female. Seven percent (4/57) of the cases reported previous predisposing conditions for bacterial meningitis, such as medical devices, HIV infection, and prematurity [10,15,17,28]. A primary focus of infection outside the brain was identified in 61.39% (35/57) of cases, with otitis and skin infections being the most common. Six patients (10.52%) had received a course of *S. pyogenes* sensitive antibiotics for at least 48 h before admission, including azithromycin, amoxicillin, and cephalexin [14,17,32,37,38,40]. All patients presented with fever and meningeal signs, including altered mental status. Most of them also had vomiting, headache, and seizures. The diagnosis was confirmed by CSF features (turbid CSF, low glucose, high protein, high white blood cells) in all cases. GAS was identified from CSF in 66.66% (38/57) of cases, and in three of those cases, only by PCR. In 15.79% (9/57), *S. pyogenes* was isolated from blood, while in 17.55% (10/57), *S. pyogenes* was detected from both CSF and blood. In nine cases, *S. pyogenes* was detected in other tissues, including ear cultures in patients with otitis, skin vesicles in patients with skin infections, and tonsillar exudates in patients with tonsillitis. In one case, *S. pyogenes* was detected on the cervix of the newborn's mother [45].

Forty-seven percent (27/57) of patients were admitted to the pediatric intensive care unit (PICU). Forty-five percent (26/57) had a Phenix sepsis score > 2. The clinical course was uneventful in 38.59% (22/57). However, 24.56% (14/57) experienced septic shock requiring inotropic support, 33.33% (19/57) entered a coma, 21.05% (12/57) experienced status epilepticus, 8.7% (5/57) had cranial nerve impairments, and 36.84% (24/57) had brain anatomical anomalies detected by cerebral imaging.

A cerebral CT was performed during admission or later in 56.14% (32/57) of cases, with negative results in 25% (8/32) of patients. Brain involvement was detected in 75% (24/32), including 12 cases with an intracranial fluid collection (extra-axial collection $n = 8$, intra-axial collection $n = 4$), 7 cases with vascular involvement, 12 cases of brain edema, 5 cases of brain tissue necrosis, 3 cases of ventriculomegaly, 4 cases of cerebritis/ventriculitis, and

1 case of myelitis [9,12–14,16–20,23–27,30,32,35–37,39,42,46]. All patients received a broad-spectrum empiric antibiotic therapy with third-generation cephalosporins alone in 66.66% (38/57) of cases. Seventeen percent (10/57) received third-generation cephalosporins plus a glycopeptide, mainly vancomycin. The remaining cases received different antibiotic regimens, including meropenem alone or in combination with linezolid, third-generation cephalosporins plus clindamycin, or cephalosporins/penicillin combined with rifampicin or linezolid. In 50.87% (29/57) of cases, therapy was targeted after GAS identification. In 31.67% (18/57) of cases, therapy was de-escalated to intravenous penicillin based on susceptibility testing. Other regimens included the addition of clindamycin, rifampicin, or linezolid to cephalosporins/penicillin or the substitution of the previous therapy with meropenem. Overall, protein-synthesis inhibitors (clindamycin, linezolid, or rifampicin) were used in 26.31% (15/57) of cases. The median length of therapy was 18 days (range: 10–42 days, $n = 36$). Dexamethasone with or without mannitol was used in 33.33% (19/57) of cases [9,12,17,23,25,27,30–33,35,36,39]. Other treatments included anticonvulsant therapy for patients with seizures, heparin for those with thrombosis, and supportive care for patients in critical conditions. Immunoglobulins were used in three patients (3.50%) [30,36].

Surgical procedures were performed in 13 patients (22.80%). In particular, three patients had a liquor derivation, two underwent myringotomy/tympanostomy, two had mastoidectomy, two required abscess drainage, two had craniectomy, one had both mastectomy and abscess drainage, and one patient had a combination of mastoidectomy, myringotomy, and craniectomy [9,11,12,16,17,27,32,35,37,42,46].

Seventeen percent (10/57) of patients died, all within the first 48 h of hospitalization, while 28.07% (16/57) had sequelae, including hearing loss, nerve palsy, and varying degrees of neurological impairment defined according to Pediatric Cerebral Performance Category [9–14,16,17,19,20,27,28,33–37,39,41–43,46]. Sixty-two percent (31/57) had a complete recovery. Table 3 shows the univariate analysis of the comparisons between patients with an uneventful course versus those with a complicated course. Age, sex, presence of predisposing conditions, the primary non-invasive *S. pyogenes* focus, use of dexamethasone, and antibiotics that interfere with protein synthesis were not statistically significantly different between the comparison groups in the statistical analysis. The presence of *S. pyogenes* on blood and a Phoenix Sepsis Score ≥ 2 were significantly associated with a complicated course. Regarding laboratory exams, patients with a complicated course had significantly higher levels of WBC and proteins in the CSF. CSF glucose and blood WBC were not statistically different between the groups. Table 4 reports the logistic regression analysis conducted to identify factors associated with a complicated course adjusted for age and sex: the presence of *S. pyogenes* on blood was significantly associated with a complicated course (OR: 6.101, $p = 0.01$), indicating a more than 6-fold increase in the likelihood of a complicated course in patients with GAS bacteremia. Similarly, a Phoenix Sepsis Score ≥ 2 was strongly associated with a complicated course (OR: 68.570, $p < 0.001$), suggesting that this subset of patients have an higher risk of sequelae and/or death.

Table 3. Comparison between patients with uneventful and complicated course of disease.

Variable	Uneventful Course N = 22	Complicated Course N = 35	*p*-Value
Age (y)	5.5	5.21	0.41
Age below 1 y	4/22	11/35	0.26
Female sex	12/22	19/35	0.98
Predisposing conditions	2/22	2/35	0.62

Table 3. *Cont.*

Variable	Uneventful Course N = 22	Complicated Course N = 35	*p*-Value
Other focus of infection beside the brain	13/22	22/35	0.77
CSF WBC (mg/dL)	1350.3	2586	0.03
CSF proteins (mg/dL)	126.26	252.42	0.02
CSF glucose (mg/dL)	29.25	20.33	0.12
WBC on blood (mmc)	18,836.36	20,216.4	0.35
S. pyogenes on blood	3/22	18/35	<0.01
Phoenix Sepsis Score ≥ 2	1/22	25/35	<0.01
Use of protein-synthesis inhibitors	3/22	12/35	0.064
Dexamethasone therapy	4/22	15/35	0.054
Length of stay (d)	17	24	0.02

WBC: white blood cells: CSF: cerebrospinal fluid.

Table 4. Logistic regression between patients with uneventful and complicated course of disease adjusted for age and sex.

Variable	*p*-Value	Odds Ratio	CI 95%
Predisposing conditions	0.618	0.595	0.0771–4.59
Other focus of infection beside the brain	0.712	1.247	0.386–4.02
S. pyogenes on blood	0.01	6.101	1.512–24.62
Phoenix Sepsis Score ≥ 2	<0.001	68.570	7.3733–637.68
Use of protein-synthesis inhibitors	0.06	3.846	0.915–16.16
Dexamethasone therapy	0.05	3.763	0.999–14.18

5. Discussion

Bacterial meningitis is a life-threatening condition that causes high morbidity and mortality in children. The most common pathogens involved are *Streptococcus pneumoniae*, *Neisseria meningitidis*, and *Haemophilus influenzae* type B [47]. *GAS* is responsible for fewer than 2% of bacterial meningitis [5].

Since 2022, the WHO has reported an increase in iGAS infections in at least five European countries, particularly in the age group from 0 to 5 years old [6,48–53]. In our tertiary pediatric hospital, between April 2023 and July 2024, we recorded 2 cases of GAS meningitis out of 34 cases of iGAS infections.

S. pyogenes meningitis exhibits peculiar features. According to our study and previous reports, in half of the patients, the primary focus of infection was not the brain, with otitis and skin infections being the most common sources of bacterial spread. Meningitis may occur through brain invasion via the hematogenous route or by direct spread through continuity. The hematogenous route could be responsible for dissemination from the skin and the nasopharyngeal mucosa, while direct spread seems to be involved in GAS infections of the ear and mastoid bone [5,9,16,23,54].

The main *S. pyogenes* virulence factors involved in adhesion and bacterial dissemination are the M protein, Streptolysin O, streptococcal DNases, and the IL-8 protease SpyCEP. So far, studies have failed to demonstrate differential expression of these factors in patients with GAS meningitis compared with those with otitis or oropharyngeal colonization. Therefore, host characteristics may represent the key discriminant in this process [55].

To better define the pathogenesis and risk factors for local infection spreading, more studies are advocated [54,55].

Based on our findings and those of previous studies, we recommend some specific diagnostic and therapeutic steps in cases of *S. pyogenes* meningitis.

The initial approach is the same for all bacterial meningitis. In case of suspicion of meningitis, a thorough examination is mandatory, especially to recognize meningeal signs and any source of peripheral infection [47,56–58]. It is crucial to collect blood samples and cultures, as well as perform lumbar puncture for the CSF analysis and culture. Broad-spectrum antibiotics should be initiated as soon as cultures are collected; however, the execution of head CT/MRI, blood tests, and lumbar puncture should not delay the administration of antibiotics [47,56–58]. If possible, we recommend using molecular techniques, especially in patients who received antibiotics before blood and CSF collection [59]. The most common rapid multiplex PCR panel does not include GAS, but in cases of high suspicion—such as concomitant tonsillitis, otitis, or skin impetigo—a more comprehensive panel should be considered [16]. At our center, when rapid multiplex PCR results on CSF are negative and bacterial meningitis is highly suspected, a more comprehensive panel designed for blood testing on cerebrospinal fluid is performed. This approach has also been suggested in other studies [60,61].

Empiric therapy typically involves ceftriaxone plus vancomycin, depending on local resistance patterns [47,56–58]. Once *S. pyogenes* is isolated, the approach should be personalized for each case and involve a multidisciplinary team, including pediatricians, intensivists, neurosurgeons, and infectious disease specialists. The antibiotic regimen should be targeted based on the antibiogram. Penicillin G is usually the antibiotic of choice [56]. *S. pyogenes* meningitis has been associated with specific M types and exotoxin production, particularly SPEA, SPEB, and SPEC. Based on these virulence features, there is a growing trend of using protein-synthesis inhibitors (such as linezolid, rifampicin, and clindamycin) in combination with penicillin or cephalosporins [4,16,20,35,62,63]. In both our patients, we decided to add linezolid, an oxazolidinone that inhibits bacterial protein synthesis by binding to the bacterial 23S ribosomial RNA of the 50S subunit, based on its good cerebral penetration, more favorable pharmacokinetic properties compared to vancomycin, and a theoretical activity against the production of pyrogenic exotoxins A and B [64]. In our study, 26% of patients were treated with this approach. Clindamycin has been reported to have poor CSF penetration, and therefore its role in the management of CNS infections is debated [65,66]. Nowadays, no comparative studies have been conducted comparing beta-lactam monotherapy with beta-lactam plus protein-synthesis inhibitors in *S. pyogenes* meningitis, and further research is needed to define the most effective strategy [67,68].

Dexamethasone may play a positive role in reducing brain edema and the inflammatory cascade. The results of its use in Streptococcus pneumoniae meningitis encourage its administration in *S. pyogenes* meningitis as well. In a 2015 Cochrane meta-analysis and systematic review regarding corticosteroid use for acute bacterial meningitis, the use of steroids in Streptococcus pneumoniae meningitis was proven to be protective against death but it had no significant beneficial effect on hearing loss sequelae [69]. In our analysis, steroid use was not statistically different between patients with an uneventful course and those with a complicated course [35,70–72]. Of note, our results cannot define the efficacy of steroids in this setting, primary because of the small sample size and secondly because in many cases, steroids were introduced only after the evidence of brain edema at the MRI, rather than immediately after the detection of the bacteria. Additionally, the efficacy demonstrated in Streptococcus pneumoniae is not enough to advise its use in *S. pyogenes* meningitis. Even if they belong to the same genus (Streptococcus), they are distinct species with different pathogenic profiles. Based on the current literature, GAS meningitis exhibits a higher rate of brain anomalies on brain CT/MRI (17% vs. 36.84%), death (13% vs. 17.54%), and sequelae (23% vs. 28.07%) compared to *S. pneumoniae* meningitis [41,42]. Our results align with previous studies [5,9,29,35,38,72–74].

We recommend continuous monitoring of the patient during the first 48–72 h, particularly for those with elevated WBC or protein levels in the CSF, as well as those with GAS bacteremia or signs of sepsis, as these factors have been associated with a complicated course, sequelae, or death in our study. Fatal complications occurred in 17% of our cohort, all of them within the first 48 h; thus an intensive setting should be considered at the time of admission. In the event of worsening of the clinical condition or lack of improvement, we recommend performing additional tests based on the clinical presentation, including imaging, as cerebral parenchyma involvement or vascular alterations are common in *S. pyogenes* meningitis [4,16,20,35,45,73,74]. Surgical intervention should be considered, especially in cases of brain anomalies (e.g., hydrocephalus or fluid collections) or when otitis or mastoiditis is the source of infection. In cases of thrombosis, the use of heparin and high doses of steroids has been proposed [12,37].

Looking to the future, some considerations need to be done in terms of possible concerns in the management of *S. pyogenes* meningitis. In the last three years, studies in the Netherlands have reported a concerning increase not only in iGAS infections but also specifically in GAS meningitis. Moreover, while molecular studies before 2022 showed that approximately 35% of isolated strains belonged to the emm1 subtype, after 2022, nearly 90% of cases were associated with the emm1 subtype, and of these, 80% were identified as the toxigenic M1uk variant, known to be associated with more severe clinical courses [75].

Interestingly, the current concern is not limited to the emergence of *S. pyogenes* strains with additional virulence factors but also includes the rise in antibiotic resistance. Penicillin remains the antibiotic of choice; however, over the last 20 years, there has been a troubling trend of reduced penicillin susceptibility, not yet a case of resistance [76]. Several mechanisms have been proposed for this phenomenon: (1) intracellular persistence of *S. pyogenes* within tonsillar tissues, where poor antibiotic penetration reduces treatment efficacy, and (2) beta-lactamase-mediated inactivation, where co-infecting bacteria produce extracellular beta-lactamase that degrades penicillin in the absence of an inhibitor. One of the latest discoveries as mechanisms of resistance involves mutations in the *pbp2x* gene, which encodes a key enzyme in peptidoglycan synthesis [76,77]. These mutations have been linked to reduced susceptibility to penicillins and cephalosporins and are associated with multiple emm types exhibiting high mortality rates. Even more concerning is the growing resistance to macrolides. Over the past decade, the incidence of macrolide resistance has increased dramatically, reaching rates as high as 20–40%. The mechanisms behind this resistance typically involves the methylation of the 23S rRNA target by *erm* (erythromycin ribosomal methylase) genes (ermA and ermB) [76–78].

Finally, despite global advances, a reliable vaccination is still not yet available, but a number of vaccine candidates are in early human trials [79].

The limitations of our study include, primarily, the small sample size, mainly due to the rarity of the disease. Another significant limitation is that the data were derived from retrospective studies, each focusing on different aspects of the disease. As a result, some data may have been omitted by the original authors based on the focus they chose for their paper. Additionally, it is important to consider that severe cases may be overrepresented, as they might have been more likely to be published compared to milder cases, introducing a significant bias. Furthermore, the length of follow-up varied across case reports which could have influenced the reporting of sequelae.

6. Conclusions

Our study reviewed the management of *S. pyogenes* meningitis. No guidelines or unique approaches to this invasive infection are available yet. Our study may help clinicians quickly identify high-risk patients with *S. pyogenes* meningitis who require more intensive monitoring during hospitalization to reduce morbidity and mortality associated with this infection. Further studies are needed to enhance knowledge for the management of iGAS infections.

Author Contributions: Conceptualization M.D.L., L.C. and M.P.; methodology M.D.L., L.R., L.C., L.L., R.B. and P.B.; formal analysis L.D.M. and S.M.; investigation A.M.M. and L.L.; resources, A.M.M., M.P., V.C. and G.V.; data curation, M.P. and S.M.; writing—original draft preparation, L.D.M., M.D.L. and L.R.; writing—review and editing, M.D.L., L.C., P.B., L.L. and M.P. All authors have read and agreed to the published version of the manuscript.

Funding: This work was supported by the Italian Ministry of Health with Current Research funds.

Institutional Review Board Statement: "The study was conducted in accordance with the Declaration of Helsinki, and approved by the Institutional Review Board (or Ethics Committee) of Bambino Gesù Pediatric Hospital code Prot. n. 201; Pratica n° 3596/2025 and date of approval 8 May 2025)." for studies involving humans.

Informed Consent Statement: Informed consent statement was obtained from all subjects involved in the study.

Data Availability Statement: The original contributions presented in this study are included in the article. Further inquiries can be directed to the corresponding author. The raw data supporting the conclusions of this article will be made available by the authors on request.

Acknowledgments: All the authors acknowledge ChatGPT version 4o-mini (OpenAI) for helping improve the clarity and accuracy of the English language in this article. The AI was not used for content generation or any other purpose.

Conflicts of Interest: The authors declare no conflicts of interest.

Abbreviations

The following abbreviations are used in this manuscript:

GAS	Group A streptococcus
iGAS	Invasive GAS
SPE	Secreted pyogenic exotoxins
ED	Emergency Department
AOM	Acute Otitis Media
CRP	C-reactive protein
CSF	Cerebrospinal fluid
WBC	White blood cell
OR	Odds Ratio
PICU	Pediatric Intensive Care Unit

References

1. Brouwer, S.; Rivera-Hernandez, T.; Curren, B.F.; Harbison-Price, N.; De Oliveira, D.M.P.; Jespersen, M.G.; Davies, M.R.; Walker, M.J. Pathogenesis, epidemiology and control of Group A *Streptococcus* infection. *Nat. Rev. Microbiol.* **2023**, *21*, 431–447. [CrossRef]
2. Cunningham, M.W. Pathogenesis of group a streptococcal infections. *Clin. Microbiol. Rev.* **2000**, *13*, 470–511. [CrossRef] [PubMed] [PubMed Central]
3. Carapetis, J.R.; Steer, A.C.; Mulholland, E.K.; Weber, M. The global burden of group A streptococcal diseases. *Lancet Infect. Dis.* **2005**, *5*, 685–694. [CrossRef]
4. Waddington, C.S.; Snelling, T.L.; Carapetis, J.R. Management of invasive group A streptococcal infections. *J. Infect.* **2014**, *69* (Suppl. S1), S63–S69. [CrossRef] [PubMed]
5. Link-Gelles, R.; Toews, K.-A.; Schaffner, W.; Edwards, K.M.; Wright, C.; Beall, B.; Barnes, B.; Jewell, B.; Harrison, L.H.; Kirley, P.D.; et al. Characteristics of Intracranial Group A Streptococcal Infections in US Children, 1997–2014. *J. Pediatr. Infect. Dis. Soc.* **2020**, *9*, 30–35. [CrossRef]
6. World Health Organization Disease Outbreak News; Increased Incidence of Scarlet Fever and Invasive Group A Streptococcus Infection—Multi-Country. Available online: https://www.who.int/emergencies/disease-outbreak-news/item/2022-DON429 (accessed on 15 December 2022).
7. Schlapbach, L.J.; Watson, R.S.; Sorce, L.R.; Argent, A.C.; Menon, K.; Hall, M.W.; Akech, S.; Albers, D.J.; Alpern, E.R.; Balamuth, F.; et al. International Consensus Criteria for Pediatric Sepsis and Septic Shock. *JAMA* **2024**, *331*, 665–674. [CrossRef]
8. Abuhammour, W.; Hasan, R.A.; Unuvar, E. Group A beta-hemolytic streptococcal bacteremia. *Indian J. Pediatr.* **2004**, *71*, 915–919. [CrossRef]
9. Arnoni, M.V.; Berezin, E.N.; Sáfadi, M.A.; Almeida, F.J.; Lopes, C.R. *Streptococcus pyogenes* meningitis in children: Report of two cases and literature review. *Braz. J. Infect. Dis.* **2007**, *11*, 375–377. [CrossRef] [PubMed]
10. Givner, L.B. Invasive disease due to group A beta-hemolytic streptococci: Continued occurrence in children in North Carolina. *South. Med. J.* **1998**, *91*, 333–337. [CrossRef]
11. Harnden, A.; Lennon, D. Serious suppurative group A streptococcal infections in previously well children. *Pediatr. Infect. Dis. J.* **1988**, *7*, 714–718. [CrossRef]
12. Hummel, B.A.; Blackburn, J.; Pham-Huy, A.; Muir, K. High-dose steroid and heparin: A novel therapy for cerebral vasculitis associated with presumed group A *Streptococcus meningitis*. *BMJ Case Rep.* **2021**, *14*, e239618. [CrossRef]
13. Lee, J.; Blackburn, J.; Pham-Huy, A. Uncommon clinical presentation of a common bug: Group A *Streptococcus meningitis*. *Paediatr. Child Health* **2020**, *26*, e129–e131. [CrossRef] [PubMed]
14. Levy, E.N.; Griffith, J.A.; Carvajal, H.F. Localized meningoencephalitis and group A streptococcal bacteremia. *Clin. Pediatr.* **1992**, *31*, 438–441. [CrossRef] [PubMed]
15. Marshall, G.S.; Patel, C.C.; Buck, G. Meningitis caused by toxigenic group a beta-hemolytic streptococcus in a pediatric patient with acquired immunodeficiency syndrome. *Pediatr. Infect. Dis. J.* **1991**, *10*, 339–340. [CrossRef]
16. Paul, S.P.; Jerwood, S. Group A streptococcal septicemia, meningitis and cerebral abscess: Case report and literature review. *Turk. J. Pediatr.* **2012**, *54*, 180–183. [PubMed]
17. Pettersen, G.; Ovetchkine, P.; Tapiero, B. Group a streptococcal meningitis in a pediatric patient following cochlear implantation: Report of the first case and review of the literature. *J. Clin. Microbiol.* **2005**, *43*, 5816–5818. [CrossRef] [PubMed] [PubMed Central]
18. Ruvinsky, R.O.; Schindler, Y.; Urman, G.; Lopera, L.C.; Carrano, J.; Paolillo, A.L.; Grosman, A. Meningitis por *Streptococcus pyogenes*: Informe de un caso pediátrico. [Streptococcus pyogenes meningitis: A pediatric case report]. *Arch. Argent. Pediatr.* **2020**, *118*, e309–e312. [CrossRef]
19. Rezvani, M.; Yager, J.Y.; Hartfield, D.S. Group A streptococcal meningitis as a complication of an infected capillary haemangioma. *Eur. J. Pediatr.* **2004**, *163*, 19–21. [CrossRef]
20. Shetty, A.K.; Frankel, L.R.; Maldonado, Y.; Falco, D.A.; Lewis, D.B. Group A streptococcal meningitis: Report of a case and review of literature since 1976. *Pediatr. Emerg. Care* **2001**, *17*, 430–434. [CrossRef]
21. van Zitteren, L.M.; Arents, N.L.; Halbertsma, F. Group-A-streptococcal meningitis in a 7-year-old child—A rare pathogen in a non-immune compromised patient. *BMJ Case Rep.* **2011**, *2011*, bcr1020114896corr1. [CrossRef]
22. Walsh, M.; Chodock, R.; Quinn, C.; Peglow, S. Group A beta-hemolytic streptococcal meningitis associated with uncomplicated varicella. *Am. J. Emerg. Med.* **1994**, *12*, 602–603. [CrossRef] [PubMed]
23. Berner, R.; Herdeg, S.; Gordjani, N.; Brandis, M. *Streptococcus pyogenes* meningitis: Report of a case and review of the literature. *Eur. J. Pediatr.* **2000**, *159*, 527–529. [CrossRef]
24. González, E.J.; Gutiérrez, P.B.; Villán, E.A.; Aguado, I.C. Meningitis y *Streptococcus pyogenes*: Un cruce de caminos poco frecuente [Meningitis and Streptococcus pyogenes: A rare cross-roads]. *An. Pediatr.* **2013**, *80*, 65–66. [CrossRef]
25. Brandt, C.M.; Kitz, R.; Lütticken, R.; Brade, V. *Streptococcus pyogenes* meningitis complicating varicella in a 3-month-old child. *Scand. J. Infect. Dis.* **2003**, *35*, 876–878. [CrossRef]

26. Núñez Ramiro, A.G.; Adell Sales, A.; Calderón Fernández, R.J.; Frasquet, J.; Pérez Tamarit, A. Meningitis bacteriana aguda por *Streptococcus pyogenes* [Acute bacterial meningitis caused by *Streptococcus pyogenes*]. *An. Pediatr.* **2013**, *78*, 135. [CrossRef]
27. Steppberger, K.; Adams, I.; Deutscher, J.; Müller, H.; Kiess, W. Meningitis in a girl with recurrent otitis media caused by *Streptococcus pyogenes*—Otitis media has to be treated appropriately. *Infection* **2001**, *29*, 286–288. [CrossRef] [PubMed]
28. Jouhadi, Z.; Sadiki, H.; Lehlimi, M.; Honsali, Z.; Najib, J.; Zerouali, K.; Belabess, H.; Mdaghri, N. Meningites à streptocoque du groupe A. *Med. Mal. Infect.* **2012**, *42*, 615–618. [CrossRef] [PubMed]
29. Perera, N.; Abulhoul, L.; Green, M.; Swann, R. Group A streptococcal meningitis: Case report and review of the literature. *J. Infect.* **2005**, *51*, E1–E4. [CrossRef]
30. Moses, A.; Beeri, M.; Engelhard, D. Group A streptococcal meningitis: Report of two cases. *J. Infect.* **1998**, *36*, 116–118. [CrossRef]
31. Busetti, M.; Marchetti, F.; Croci, E.; L'Erario, I.; Creti, R.; D'Agaro, P. Group A streptococcal meningitis: A case report. *New Microbiol.* **2013**, *36*, 419–422.
32. Fanella, S.; Embree, J. Group A Streptococcal Meningitis in a Pediatric Patient. *Can. J. Infect. Dis. Med. Microbiol.* **2008**, *19*, 306–308. [CrossRef] [PubMed]
33. Brown, C.C.; Pickering, L.K.; Baker, C.J. Group A streptococcal meningitis without predisposing factors. *South. Med. J.* **1981**, *74*, 1029–1030. [CrossRef]
34. Jevon, G.P.; Dunne, W.M.; Hawkins, H.K.; Armstrong, D.L.; Musser, J.M. Fatal group a streptococcal meningitis and toxic shock-like syndrome: Case report. *Clin. Infect. Dis.* **1994**, *18*, 91–93. [CrossRef]
35. Bruun, T.; Kittang, B.R.; Mylvaganam, H.; Lund-Johansen, M.; Skrede, S. Clinical, microbiological and molecular characteristics of six cases of group A streptococcal meningitis in western Norway. *Scand. J. Infect. Dis.* **2010**, *42*, 665–671. [CrossRef]
36. González, L.A.; Peñaranda, N.A.D.; Fernández, J.M.R.; Alonso, J.M.C. Post-infective transverse myelitis following *Streptococcus pyogenes* meningitis. *An. Pediatr.* **2024**, *101*, 224–225. [CrossRef]
37. Hutton, D.; Kameda-Smith, M.; Afshari, F.T.; Elawadly, A.; Hogg, F.; Mehta, S.; Samarasekara, J.; Aquilina, K.; Jeelani, N.U.O.; Tahir, M.Z.; et al. Intracranial invasive group A *Streptococcus*: A neurosurgical emergency in children. *J. Neurosurg. Pediatr.* **2023**, *32*, 478–487. [CrossRef]
38. Torres, L.; Rodrigues, A.M.; Francisco, C.; Santos, S.; Carvalho, P. *Streptococcus pyogenes* Meningitis in a Pediatric Patient: Case Report. *Acta Medica Port.* **2024**, *37*, 142–144. [CrossRef] [PubMed]
39. Krebs, V.L.J.; Chieffi, L.N.; Ceccon, M.E.J.R.; Diniz, E.M.D.A.; Feferbaum, R.; Takeuchi, C.A.; Marques-Dias, M.J.; Carneiro, J.D.A.; Vaz, F.A.C. Meningite neonatal por *Streptococcus pyogenes* e trombose de seio sagital: Relato de caso. [Neonatal Streptococcus pyogenes meningitis and sagittal sinus thrombosis: Case report]. *Arq. Neuro Psiquiatr.* **1998**, *56*, 829–832. [CrossRef]
40. Bacalhau, S.; Zarcos, M.M.; Rezende, T. *Meningite bacteriana*. Uma etiologia pouco frequente [Bacterial meningitis. A rare cause]. *Acta Med. Port.* **2011**, *24* (Suppl. S3), 627–630.
41. Gupta, V.; Jain, S. Meningitis with bilateral acute suppurative otitis media caused by Group A *Streptococcus*. *Indian Pediatr.* **2005**, *42*, 79–80.
42. Hmami, F.; Oulmaati, A.; Mahmoud, M.; Boubou, M.; Tizniti, S.; Bouharrou, A. Méningite néonatale à streptocoque A et thrombose porte: Une association fortuite ? [Neonatal group A streptococcal meningitis and portal vein thrombosis: A casual association? *Arch. Pediatr.* **2014**, *21*, 1020–1023. [CrossRef]
43. Gertner, M.; Rodriguez, L.; Barnett, S.H.; Shah, K. Group A beta-hemolytic Streptococcus and Waterhouse-Friderichsen syndrome. *Pediatr. Infect. Dis. J.* **1992**, *11*, 595–596. [CrossRef]
44. Nutman, J.; Henig, E.; Wilunsky, E.; Reisner, S.H. Acute necrotising fasciitis due to streptococcal infection in a newborn infant. *Arch. Dis. Child.* **1979**, *54*, 637–639. [CrossRef] [PubMed]
45. Yagupsky, P.; Giladi, Y. Group A beta-hemolytic streptococcal septicemia complicating infected hemangioma in children. *Pediatr. Dermatol.* **1987**, *4*, 24–26. [CrossRef] [PubMed]
46. Dou, Z.-Z.; Li, W.; Hu, H.-L.; Guo, X.; Hu, B.; Chen, T.-M.; Chen, H.-Y.; Guo, L.-Y.; Liu, G. Group A Streptococcal meningitis in children: A short case series and systematic review. *Eur. J. Clin. Microbiol. Infect. Dis.* **2024**, *43*, 1517–1531. [CrossRef] [PubMed]
47. Kim, K.S. Acute bacterial meningitis in infants and children. *Lancet Infect. Dis.* **2010**, *10*, 32–42. [CrossRef]
48. de Gier, B.; Marchal, N.; de Beer-Schuurman, I.; Wierik, M.T.; Hooiveld, M.; ISIS-AR Study Group; GAS Study group; de Melker, H.E.; van Sorge, N.M. Increase in invasive group A streptococcal (*Streptococcus pyogenes*) infections (iGAS) in young children in The Netherlands, 2022. *Euro. Surveill.* **2023**, *28*, 2200941. [CrossRef]
49. Guy, R.; Henderson, K.L.; Coelho, J.; Hughes, H.; Mason, E.L.; Gerver, S.M.; Demirjian, A.; Watson, C.; Sharp, A.; Brown, C.S.; et al. Increase in invasive group A streptococcal infection notifications, England, 2022. *Euro. Surveill.* **2023**, *28*, 2200942. [CrossRef]
50. Lassoued, Y.; Assad, Z.; Ouldali, N.; Caseris, M.; Mariani, P.; Birgy, A.; Bonacorsi, S.; Bidet, P.; Faye, A. Unexpected Increase in Invasive Group A Streptococcal Infections in Children After Respiratory Viruses Outbreak in France: A 15-Year Time-Series Analysis. *Open Forum. Infect. Dis.* **2023**, *10*, ofad188. [CrossRef]

51. Cobo-Vázquez, E.; Aguilera-Alonso, D.; Carrasco-Colom, J.; Calvo, C.; Saavedra-Lozano, J.; Mellado, I.; Grandioso, D.; Rincón, E.; Jové, A.; Cercenado, E.; et al. Increasing incidence and severity of invasive Group A streptococcal disease in Spanish children in 2019–2022. *Lancet Reg. Health Eur.* **2023**, *27*, 100597. [CrossRef]
52. van Kempen, E.B.; Bruijning-Verhagen, P.C.J.; Borensztajn, D.M.; Vermont, C.L.; Quaak, M.S.W.; Janson, J.-A.; Maat, I.; Stol, K.; Vlaminckx, B.J.M.; Wieringa, J.W.; et al. Increase in Invasive Group a Streptococcal Infections in Children in the Netherlands, A Survey Among 7 Hospitals in 2022. *Pediatr. Infect. Dis. J.* **2023**, *42*, e122–e124. [CrossRef] [PubMed]
53. Mercadante, S.; Ficari, A.; Romani, L.; De Luca, M.; Tripiciano, C.; Chiurchiù, S.; Carducci, F.I.C.; Cursi, L.; Di Giuseppe, M.; Krzysztofiak, A.; et al. The Thousand Faces of Invasive Group A Streptococcal Infections: Update on Epidemiology, Symptoms, and Therapy. *Children* **2024**, *11*, 383. [CrossRef]
54. Aznar, S.L.; Martinez, C.V.; Fonz, R.B.; Lobera, I.B.; Alonso, M.B. Mastoiditis aguda con complicación intracraneal. Reporte de un caso pediátrico. *Arch. Argent. Pediatr.* **2020**, *118*, e166–e169. [CrossRef]
55. Marquardt, L.; Andreoni, F.; Boumasmoud, M.; Schweizer, T.A.; Heuberger, D.M.; Parietti, E.; Hertegonne, S.; Epprecht, J.; Mattle, D.; Raez, A.K.; et al. Group A *Streptococcus* strains causing meningitis without distinct invasive phenotype. *Microbiologyopen* **2024**, *13*, e1394. [CrossRef]
56. de Almeida Torres, R.S.; Fedalto, L.E.; Steer, A.C.; Smeesters, P.R. Group A *Streptococcus meningitis* in Children. *Pediatr. Infect. Dis. J.* **2013**, *32*, 110–114. [CrossRef] [PubMed]
57. Griffiths, M.J.; McGill, F.; Solomon, T. Management of acute meningitis. *Clin. Med.* **2018**, *18*, 164–169. [CrossRef] [PubMed] [PubMed Central]
58. Alamarat, Z.; Hasbun, R. Management of Acute Bacterial Meningitis in Children. *Infect. Drug Resist.* **2020**, *13*, 4077–4089. [CrossRef] [PubMed] [PubMed Central]
59. Trujillo-Gómez, J.; Tsokani, S.; Arango-Ferreira, C.; Atehortúa-Muñoz, S.; Jimenez-Villegas, M.J.; Serrano-Tabares, C.; Veroniki, A.-A.; Florez, I.D. Biofire FilmArray Meningitis/Encephalitis panel for the aetiological diagnosis of central nervous system infections: A systematic review and diagnostic test accuracy meta-analysis. *eClinicalMedicine* **2022**, *44*, 101275. [CrossRef]
60. López-Amor, L.; García-Prieto, E.; Fernández-Suárez, J.; Escudero, D.; Vázquez, F.; Fernández, J. Evaluation of a commercial multiplex PCR for diagnosis of central nervous system (CNS) nosocomial infections. *J. Microbiol. Methods* **2020**, *171*, 105865. [CrossRef]
61. Leitner, E.; Hoenigl, M.; Wagner, B.; Krause, R.; Feierl, G.; Grisold, A.J. Performance of the FilmArray Blood culture identification panel in positive blood culture bottles and cerebrospinal fluid for the diagnosis of sepsis and meningitis. *GMS Infect. Dis.* **2016**, *4*, Doc06. [CrossRef]
62. Rezahosseini, O.; Roed, C.; Holler, J.G.; Frimodt-Møller, N.; Harboe, Z.B. Adjunctive antibiotic therapy with clindamycin or linezolid in patients with group A streptococcus (GAS) meningitis. *Infect. Dis.* **2023**, *55*, 751–753. [CrossRef] [PubMed]
63. Bergsten, H.; Medina, L.M.P.; Morgan, M.; Moll, K.; Skutlaberg, D.H.; Skrede, S.; Wajima, T.; Svensson, M.; Norrby-Teglund, A. Adjunctive Rifampicin Increases Antibiotic Efficacy in Group A Streptococcal Tissue Infection Models. *Antimicrob. Agents Chemother.* **2021**, *65*, e0065821. [CrossRef]
64. Cascone, A.; De Luca, M.; Simeoli, R.; Goffredo, B.M.; Cursi, L.; Tripiciano, C.; Romani, L.; Mercadante, S.; Di Giuseppe, M.; Carducci, F.I.C.; et al. Therapeutic Drug Monitoring-Guided Linezolid Therapy for the Treatment of Multiple Staphylococcal Brain Abscesses in a 3-Month-Old Infant. *Pathogens* **2024**, *14*, 4. [CrossRef]
65. Meesters, K.; Alemayehu, T.; Benou, S.; Buonsenso, D.; Decloedt, E.H.; Lorente, V.P.-F.; Downes, K.J.; Allegaert, K. Pharmacokinetics of Antimicrobials in Children with Emphasis on Challenges Faced by Low and Middle Income Countries, a Clinical Review. *Antibiotics* **2022**, *12*, 17. [CrossRef]
66. Sullins, A.K.; Abdel-Rahman, S.M. Pharmacokinetics of Antibacterial Agents in the CSF of Children and Adolescents. *Pediatr. Drugs* **2013**, *15*, 93–117. [CrossRef]
67. Coyle, E.A. Targeting Bacterial Virulence: The role of protein synthesis inhibitors in severe infections. *Pharmacother. J. Hum. Pharmacol. Drug Ther.* **2003**, *23*, 638–642. [CrossRef] [PubMed]
68. Andreoni, F.; Zürcher, C.; Tarnutzer, A.; Schilcher, K.; Neff, A.; Keller, N.; Maggio, E.M.; Poyart, C.; Schuepbach, R.A.; Zinkernagel, A.S. Clindamycin Affects Group A Streptococcus Virulence Factors and Improves Clinical Outcome. *J. Infect. Dis.* **2016**, *215*, 269–277. [CrossRef]
69. Brouwer, M.C.; McIntyre, P.; Prasad, K.; van de Beek, D. Corticosteroids for acute bacterial meningitis. *Cochrane Database Syst. Rev.* **2015**, *2018*, CD004405. [CrossRef]
70. Schaad, U.; Wedgwood, J.; Lips, U.; Gnehm, H.; Heinzer, I.; Blumberg, A. Dexamethasone therapy for bacterial meningitis in children. *Lancet* **1993**, *342*, 457–461. [CrossRef]
71. Girgis, N.I.; Farid, Z.; Mikhail, I.A.; Farrag, I.; Sultan, Y.; Kilpatrick, M.E. Dexamethasone treatment for bacterial meningitis in children and adults. *Pediatr. Infect. Dis. J.* **1989**, *8*, 848–851. [CrossRef]

72. McIntyre, P.B.; MacIntyre, C.R.; Gilmour, R.; Wang, H. A population based study of the impact of corticosteroid therapy and delayed diagnosis on the outcome of childhood pneumococcal meningitis. *Arch. Dis. Child.* **2005**, *90*, 391–396. [CrossRef] [PubMed]
73. Pagliano, P.; Fusco, U.; Attanasio, V.; Rossi, M.; Pantosti, A.; Conte, M.; Faella, F.S. Pneumococcal meningitis in childhood: A longitudinal prospective study. *FEMS Immunol. Med. Microbiol.* **2007**, *51*, 488–495. [CrossRef] [PubMed]
74. Pelton, S.I.; Yogev, R. Improving the outcome of pneumococcal meningitis. *Arch. Dis. Child.* **2005**, *90*, 333–334. [CrossRef] [PubMed]
75. van der Putten, B.C.L.; Vlaminckx, B.J.M.; de Gier, B.; Graaf, W.F.-D.; van Sorge, N.M. Group A Streptococcal Meningitis With the $M1_{UK}$ Variant in the Netherlands. *JAMA* **2023**, *329*, 1791–1792. [CrossRef]
76. Gergova, R.; Boyanov, V.; Muhtarova, A.; Alexandrova, A. A Review of the Impact of Streptococcal Infections and Antimicrobial Resistance on Human Health. *Antibiotics* **2024**, *13*, 360. [CrossRef]
77. Rubio-López, V.; Valdezate, S.; Álvarez, D.; Villalón, P.; Medina, M.J.; Salcedo, C.; Sáez-Nieto, J.-A. Molecular epidemiology, antimicrobial susceptibilities and resistance mechanisms of *Streptococcus pyogenes* isolates resistant to erythromycin and tetracycline in Spain (1994–2006). *BMC Microbiol.* **2012**, *12*, 215. [CrossRef]
78. Berbel, D.; González-Díaz, A.; de Egea, G.L.; Càmara, J.; Ardanuy, C. An Overview of Macrolide Resistance in Streptococci: Prevalence, Mobile Elements and Dynamics. *Microorganisms* **2022**, *10*, 2316. [CrossRef]
79. Castro, S.A.; Dorfmueller, H.C. Update on the development of Group A Streptococcus vaccines. *npj Vaccines* **2023**, *8*, 135. [CrossRef]

microorganisms

MDPI

Case Report

First Case of Candida Auris Sepsis in Southern Italy: Antifungal Susceptibility and Genomic Characterisation of a Difficult-to-Treat Emerging Yeast

Stefania Stolfa [1,†], Giuseppina Caggiano [2,3,†], Luigi Ronga [1], Lidia Dalfino [4], Francesca Centrone [3], Anna Sallustio [3], Davide Sacco [2], Adriana Mosca [1], Monica Stufano [4], Annalisa Saracino [5], Nicolo' De Gennaro [5], Daniele Casulli [3], Nicola Netti [3], Savino Soldano [6], Maria Faggiano [7], Daniela Loconsole [2,3], Silvio Tafuri [2,3], Salvatore Grasso [4] and Maria Chironna [1,2,3,*]

[1] Microbiology and Virology Unit, Department of Interdisciplinary Medicine, University of Bari "A. Moro", 70124 Bari, Italy; stefania.stolfa@policlinico.ba.it (S.S.); luigi.ronga@policlinico.ba.it (L.R.); adriana.mosca@uniba.it (A.M.)

[2] Hygiene Section, Department of Interdisciplinary Medicine, University of Bari "A. Moro", 70124 Bari, Italy; giuseppina.caggiano@uniba.it (G.C.); sacco.davide19@gmail.com (D.S.); daniela.loconsole@uniba.it (D.L.); silvio.tafuri@uniba.it (S.T.)

[3] Hygiene Unit, Bari Policlinico University Hospital, 70124 Bari, Italy; francesca.centrone@policlinico.ba.it (F.C.); annasallustio@libero.it (A.S.); daniele.casulli@hotmail.com (D.C.); nettinicola@icloud.com (N.N.)

[4] Intensive Care Unit II, Department of Precision Medicine, Ionic Area, University of Bari "A. Moro", 70124 Bari, Italy; lidia.dalfino@yahoo.com (L.D.); monistufa@gmail.com (M.S.); salvatore.grasso@uniba.it (S.G.)

[5] Clinic of Infectious Diseases, Department of Biomedical Sciences and Human Oncology, University of Bari "A. Moro", 70124 Bari, Italy; annalisa.saracino@uniba.it (A.S.); nico84degennaro@gmail.com (N.D.G.)

[6] Policlinico Hospital Sanitary Direction, Bari Policlinico University Hospital, 70124 Bari, Italy; savino.soldano@policlinico.ba.it

[7] Pharmacy Unit, Bari Policlinico University Hospital, 70124 Bari, Italy; maria.faggiano@policlinico.ba.it

[*] Correspondence: maria.chironna@uniba.it; Tel.: +39-0805592328

[†] These authors contributed equally to this work.

Abstract: *Candida auris* is an emerging yeast considered a serious threat to global health. We report the first case of *C. auris* candidemia in Southern Italy, characterized using whole genome sequencing (WGS), and compared with a second strain isolated from a patient who presented as *C. auris*-colonized following screening. The *C. auris* strain was isolated from clinical samples, identified via MALDI-TOF, and subjected to WGS. Antifungal susceptibility testing was performed using commercial broth microdilution plates, and resistance protein sequences were evaluated with TBLASTN-2.15.0. Following the initial *C. auris* isolation from patient A, active surveillance and environmental investigations were implemented for all ICU patients. Of the 26 ICU surfaces sampled, 46.1% tested positive for *C. auris* via real-time PCR. Screening identified a second patient (patient B) as *C. auris*-colonized. The phylogenetic characterization of strains from patients A and B, based on the D1/D2 region of the 28s rDNA and the internal transcribed spacer (ITS) region, showed high similarity with strains from Lebanon. SNP analysis revealed high clonality, assigning both strains to clade I, indicating a significant similarity with Lebanese strains. This case confirms the alarming spread of *C. auris* infections and highlights the need for stringent infection control measures to manage outbreaks.

Keywords: *Candida auris*; whole-genome sequencing; infection control; phylogenesis

1. Introduction

Candida auris is a multidrug-resistant (MDR) yeast of public health concern. Hospital-acquired infections (HAI) across five continents have been reported [1]. *C. auris* causes invasive infections particularly in immunocompromised patients, with high mortality rates

Microorganisms **2024**, *12*, 1962. https://doi.org/10.3390/microorganisms12101962

mainly attributed to laboratory misidentification and MDR profiles. Furthermore, hospital outbreaks have been reported, probably due to its ability to create biofilms, making it resistant to antiseptics and persistent on environmental surfaces [2]. In 2019–2021, a large outbreak was reported in northern Italy with at least 277 cases [3] and a case fatality rate of 40.4% [4].

Six distinct clades of *C auris* have recently been reported [5]. These clades were distinguished on the basis of the analyses of whole genome sequencing (WGS) data and single nucleotide polymorphism (SNP) variation. Furthermore, these clades diverged in terms of antifungal susceptibility profiles, epidemic potential, and clinical manifestations [5].

We report the first case of *C. auris* candidemia in a critically ill patient admitted to a Intensive Care Unit (ICU) of southern Italy. The patient had not travelled abroad or had any other recent hospitalizations.

In April 2024, a critically ill patient was admitted to the ICU of the University Hospital Policlinico of Bari (patient A). One week later, he developed a bloodstream infection by New Delhi metallo-beta-lactamase (NDM) *Klebsiella pneumoniae* carbapenemase (KPC) and, despite prompt active antimicrobial treatment, refractory septic shock ensued. Daptomycin and caspofungin were empirically added but, unfortunately, the patient died within 48 h. Two days later, *C. auris* was isolated from their blood cultures.

Immediately, active surveillance of patients and ICU environmental surfaces was started, and infection control measures were strongly implemented. One of the sixteen screened patients (patient B) turned out to be colonized by *C. auris* in endotracheal aspirate, skin, and rectal swabs. He was admitted 2 weeks before patient A from an Albanian ICU and remained in good clinical condition until his last clinical evaluation in June 2024.

2. Materials and Methods

Blood cultures from patient A were performed as part of standard procedure for patients with sepsis. *C. auris* strain was isolated from blood culture after incubation on Sabouraud Dextrose agar (Biomerieux Inc., Lyon, France) for 48 h at 37 °C. Skin surveillance swabs (particularly of the axilla and groin) were collected by vigorously rubbing the tip of the swab over the indicated site at least 3–5 times. Skin, rectal swabs, and tracheobronchial aspirate (TBA) were inoculated on Sabouraud dextrose agar and incubated at 37 °C for 72 h. The identification of *C. auris* was performed through MALDI-TOF. Isolates of *C. auris* from patient A and patient B were subjected to WGS (whole genome sequencing) using the MiniSeq platform (Illumina Inc., San Diego, CA, USA). DNA was extracted and purified with QIAamp DNA Mini kit, according to the recommendations of the manufacturer. Purified DNA was measured with a Qubit 4.0 Fluorometer (Invitrogen by ThermoFisher Scientific, Waltham, MA; USA) using the double-stranded DNA (dsDNA). Nextera XT paired-end sequencing with a paired-end run of 2 × 150 bp was performed for library preparation. FastQC V0.12.1 software was used to perform quality control checks on the raw sequence data [6,7].

Read data were aligned against the reference genome of *C. auris* B8441 (GenBank assembly accession GCA_002759435.2) using BWA-MEM [8]. The consensus was generated using Samtools (version 1.20) and consensus was generated from BAM file based on the contents of the alignment records. The consensus was written as FASTA file [9]. BLAST was used to retrieve sequences with >90% identity from NCBI database, which were then added to the background genomic dataset after manual curation. The alignment of the core genome, the detection of recombination events, and the detection of single nucleotide polymorphisms (SNPs) were performed using Parsnp v1.2 [10]. Phylogenetic analysis was performed using RaxML8 and the TVM evolutionary model [11]. The phylogenetic tree was constructed using Mega 11.0.13 software with the neighbor-joining algorithm and annotated in iTOL [12].

Antifungal susceptibility testing was performed using commercial broth microdilution plates (Sensititre YeastOne, ThermoScientific, Waltham, MA, USA) according to the manufacturer's instructions. As there are currently no established *C. auris*-specific susceptibility breakpoints, tentative breakpoints proposed by the CDC [13] were selected to define the clinical category of susceptibility.

A total of 26 surfaces in the ICU were sampled. Specifically, high-touch patient-area surfaces (multi-parameter touch screen monitors, assisted ventilation touch screen monitors, bed rails, infusion pumps, bed keypad, drug preparation shelf) and common ward surfaces (computer keyboards, ultrasound probes, telephone) were evaluated. The surfaces were sampled using sterile swabs soaked in distilled water. All swabs were transported to the laboratory in refrigerated containers at a temperature of +4 °C and were analyzed immediately upon arrival.

3. Results

C. auris strains from patient A (BA02) and patient B (BA03) were phylogenetically characterized on the basis of the D1/D2 region of the 28s rDNA and the internal transcribed spacer (ITS) region (Figures 1 and 2).

The analysis showed a high degree of similarity of BA02 and BA03 with strains isolated in Lebanon (Bioproject PRJNA736600). Single nucleotide polymorphism (SNP) analysis showed that BA02 and BA03 had a high degree of clonality showing only 125 SNPs and were assigned to clade I, confirming a high rate of similarity with the strains collected in Lebanon (Figure 3). The difference in the number of SNPs between the BA03 strain of the present study and the Lebanon strain GCA019039495 was 381.

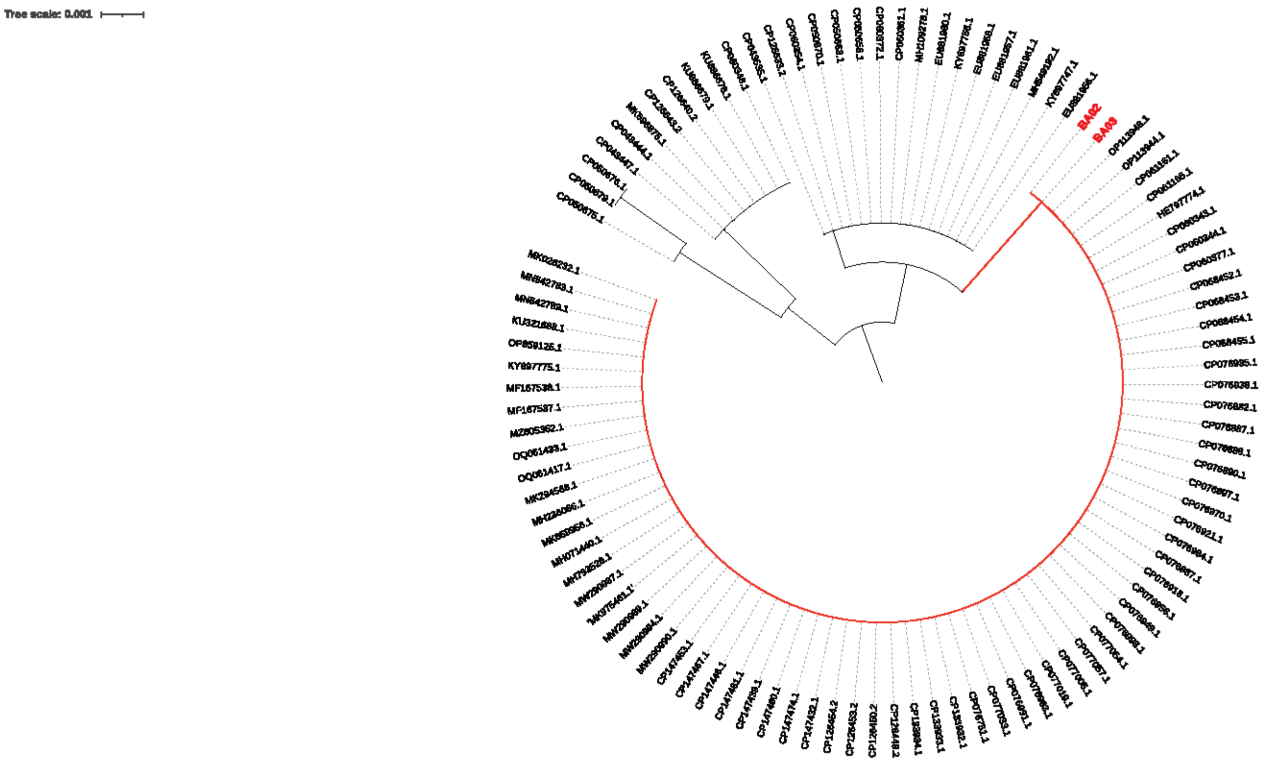

Figure 1. Neighbor-joining phylogenetic tree (max. seq. difference 0.75) on the partial D1/D2 large subunit (LSU) rDNA sequence of *C. auris* was constructed using 101 sequences. Sequences BA02 (from patient A) and BA03 (from patient B) are shown in red.

The sequences of the original clinical specimens described here have been deposited in the Genebank sequence database (accession number: SAMN41379019, SAMN41379020).

The isolates were both resistant to fluconazole and amphotericin B and susceptible to caspofungin, anidulafungin and, micafungin.

The evaluation of resistance protein sequences was performed using TBLASTN-2.15.0 [14]. Compared with the reference genome, the isolates BA02 and BA03 harbored

Y132F azole resistance-associated mutation in ERG11 and mutations M192I in ERG4, K74E in CIS2, K52N in SNQ2, and S70R in FCY1. Finally, A583S in TAC1b and K719N in STE6 were detected (Table 1). Both isolates also expressed flucytosine resistance harboring, a single mutation in the FCY1 gene [14].

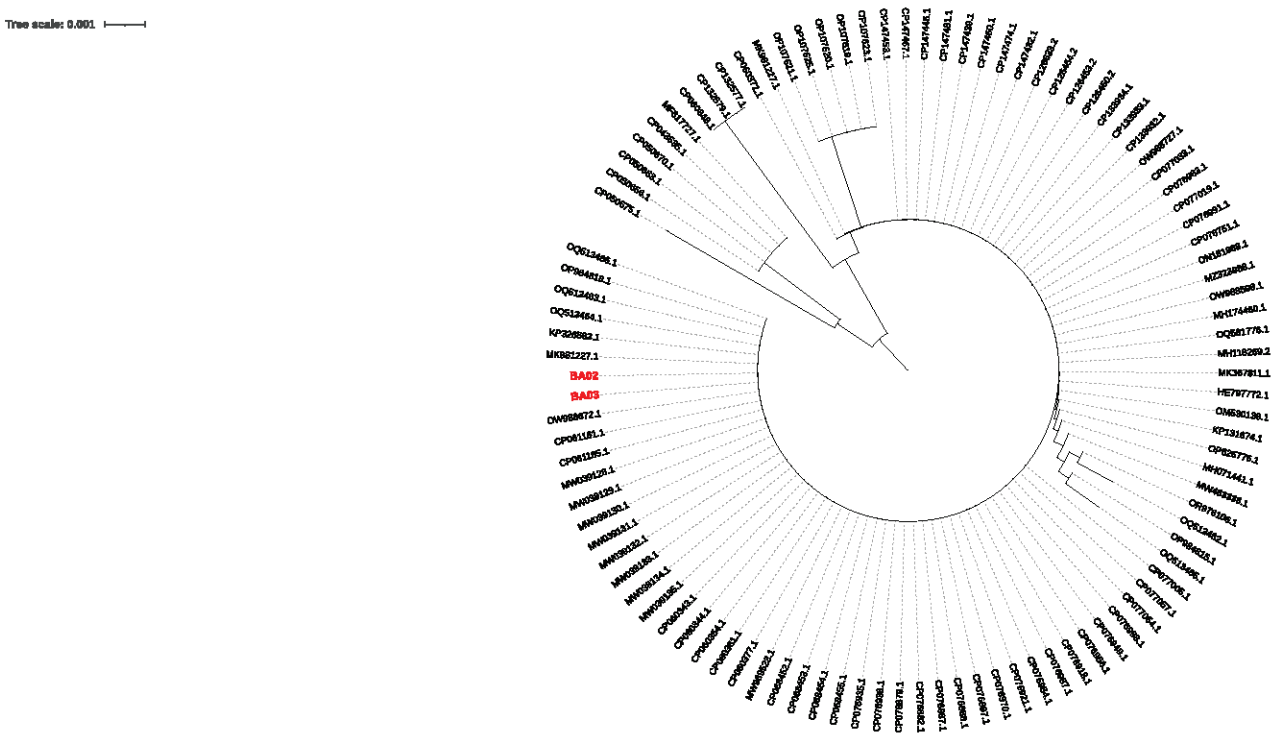

Figure 2. Neighbor-joining phylogenetic tree (max. seq. difference 0.75) on the internal transcribed spacer (ITS) sequence of *C. auris* was constructed using 101 sequences. Sequences BA02 (from patient A) and BA03 (from patient B) are shown in red.

Table 1. Antifungal susceptibility testing of the two *C. auris* isolates (upper part) and the mutations detected (lower part). * N/A: data not available.

MIC	**Patient A**		**Patient B**		**CDC's Tentative MIC Breakpoints**
Amphotericin B	2	R	4	R	≥2
Anidulafungin	0.12	S	0.12	S	≥4
Caspofungin	0.12	S	0.12	S	≥2
Fluconazole	128	R	256	R	≥32
Isavuconazole	0.06	N/A *	0.12	N/A	N/A
Itraconazole	0.12	N/A	0.25	N/A	N/A
Micafungin	0.12	S	0.12	S	≥4
Posaconazole	0.06	N/A	0.06	N/A	N/A
Voriconazole	0.5	N/A	0.5	N/A	N/A

Mutations		
Gene	Gene ID	Substitution
CIS2	B9J08_01093	K74E
ERG4	B9J08_00711	M192I
SNQ2	B9J08_03375	K52N
STE6	B9J08_05399	K719N
ERG11	B9J08_03698	Y132F+
TAC1B	B9J08_04780	A583S
FCY1	PIS48695.1	S70R+

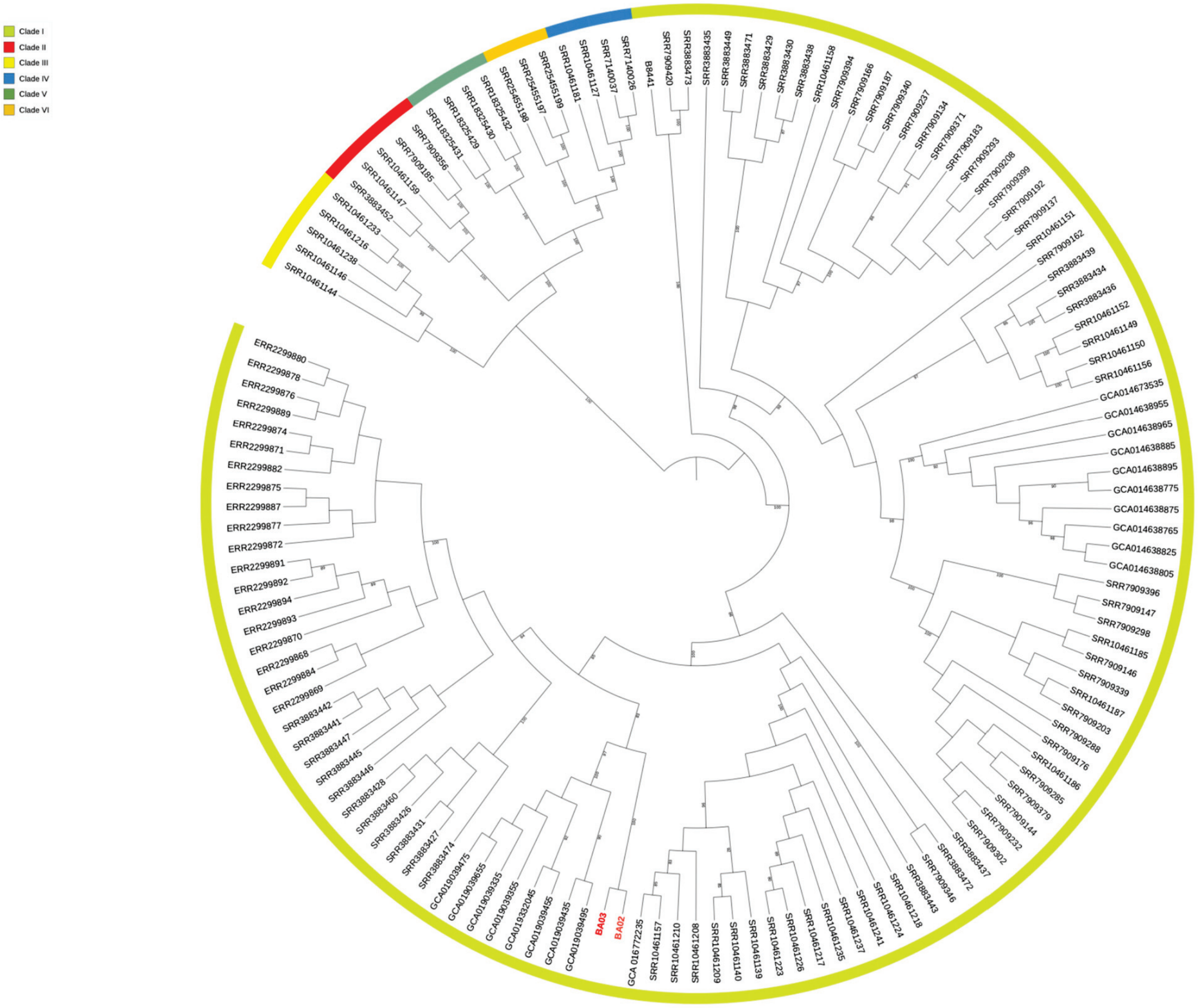

Figure 3. Six-clade population structure of *C. auris* using 139 genomes represented in the phylogenetic tree. The tree was generated by the maximum-likelihood method and annotated in iTOL. Numbers above branches are bootstrap values (only values >80 are shown). The strains of the present study are indicated in red.

The detection of *C. auris* from surfaces was performed by the commercial *Auris* ID detection real-time PCR kit according to the instructions for use (Olm Diagnostics, Braintree, UK, distributed by LionDx, Pordenone, Italy). Samples were considered positive when they showed a ct value $\leq$ 40. Of the 26 environmental samples, 12 (46.1%) were positive for *C. auris*, in particular, swabs from multi-parameter monitors, infusion pumps, bed rails, and telephones.

4. Discussion

C. auris infections represent a major challenge due to its unfavorable antifungal resistance profile, with more than 40% expressing combined resistance to two or more classes of antifungals, severely limiting therapeutic options [15]. This characteristic may complicate the management of invasive *C. auris* infections such as candidemia, potentially contributing to high mortality and transmissibility. *C. auris* candidemia usually follows colonization; therefore, the early identification of colonized patients is critical to prevent invasive infection through interventions on modifiable predictors.

To our knowledge, this is the first isolation of *C. auris* in the whole of southern Italy. Similar cases of *C. auris* importation into Italy have been described previously [16], but this result confirms its alarming spread, especially in hospital settings worldwide. The cases of *C. auris* importation are united by prolonged hospitalization in countries with a high rate of multi-resistant organisms and the need for invasive medical procedures (central venous catheter, urinary catheter recent surgical procedure, mechanical ventilation).

The high rate of similarity of the two analyzed strains, showing only 125 SNPS, clearly suggests an epidemiological link between patient A and patient B. On the other hand, it was not possible to establish an epidemiological link between the strains of the present study and the Lebanese strains, with which the strains of the present study showed a high degree of similarity, nor to identify the source of patient B colonization. In fact, the spread of *C. auris* in Albania is not known, nor are the sequences of the strains isolated in that country available. It also remains undefined through which routes strains of Lebanese origin may have caused the fatal case and the colonization of the patient admitted from the Albanian ICU. It is of note that Y132F in the Erg11 gene was detected in both isolates, reflecting the resistance to azoles. Y132F is commonly detected among South Asian isolates, particularly Indian, Pakistani, and Chinese, and it is considered a clade-I-specific marker of resistance against fluconazole as well as in other Candida species, such as *C. parapsilosis* strains, which have the same Y132F mutation in the ERG 11 gene [15,17,18].

The mutations in ERG4 may be linked to reduced susceptibility to amphotericin B in *C. auris*, although their impact on structural changes and gene expression has not been investigated [14].

K74E was reported in all susceptible and resistant isolates, suggesting this may represent a polymorphism not connected with resistance and may not be under selective pressure from antifungals. TAC1b is a transcription factor controlling CDR1 expression in Candida species. Mutations in TAC1b were associated with increased azole resistance [19,20]. Finally, STE6 is an a-pheromone ABC family transporter that showed antimycotic responses [21].

Antifungal susceptibility testing confirmed resistance to fluconazole and amphotericin B, as well as susceptibility to echinocandins, which are still the first choice of treatment. This demonstrates that the combination of molecular characterization and antimycotic susceptibility testing represents the best possible strategy to address the challenge of diagnosis and the treatment of both symptomatic infections and asymptomatic colonization.

5. Conclusions

In conclusion, our data suggest the hypothesis of a strain imported from Albania/Lebanon. It is notable that the strain has different characteristics from the Greek one collected by Rimoldi et al. since the common mutations detected are S70R on gene FCY1 and Y132F on gene ERG11 [16]. This suggests the likely different origins and dynamics of the strains. The high transmissibility, the ability of *C. auris* to cause outbreaks, and the high frequency of antifungal resistance among clinical isolates highlight the need for the early identification and implementation of global surveillance programs. Monitoring resistance, coordinating local and international antifungal surveillance protocols, and developing novel diagnostic tests and antifungal drugs may play a crucial role in improving the clinical outcome of ICU patients. After the first *C. auris* isolation, immediate and accurate environmental investigation and disinfection, in combination with timely clinical surveillance and updated HAI prevention bundles, controlled the spread of *C. auris* and quickly extinguished the epidemic outbreak.

Author Contributions: S.S. (Stefania Stolfa), L.R., F.C. and M.C. conceptualized, defined the aims and wrote the first draft of the article. S.S. (Stefania Stolfa), L.R. and A.M. isolated *C. auris* and analyzed and interpreted patient's primary cultures and antifungal susceptibility. G.C. performed all environmental analysis and contributed to drafting the manuscript. L.D., M.S., A.S. (Annalisa Saracino), N.D.G. and S.G. were responsible for the clinical aspects of the work as the physicians responsible for the patients and the administration of antimicrobial and antifungal therapy and also contributed to the drafting and revising of the manuscript. A.S. (Anna Sallustio) and D.S. coordinated

and performed genomic analysis. D.C. and N.N. collected the samples, analyzed the data, and critically discussed the results. D.L., S.S. (Savino Soldano) and S.T. conducted the epidemiological investigation and infection control interventions and analyzed and critically discussed the results and the final version of the paper. M.F. contributed to the study and the selection of disinfectants for infection control. M.C., S.T. and S.G. coordinated the study and analyzed and critically discussed the results and the final version of the article. All authors have read and agreed to the published version of the manuscript.

Funding: This research was supported by EU funding within the NextGenerationEU-MUR PNRR Extended Partnership initiative on Emerging Infectious Diseases (project no. PE00000007, INF-ACT).

Data Availability Statement: Data will be available upon reasonable request by e-mail to Maria Chironna (maria.chironna@uniba.it).

Conflicts of Interest: The authors declare no conflicts of interest.

References

1. Kohlenberg, A.; Monnet, D.L.; Plachouras, D.; Candida auris survey collaborative group. Candida auris survey collaborative group includes the following national experts. Increasing number of cases and outbreaks caused by Candida auris in the EU/EEA, 2020 to 2021. *Eurosurveillance* **2022**, *27*, 2200846. [CrossRef] [PubMed]
2. Welsh, R.M.; Bentz, M.L.; Shams, A.; Houston, H.; Lyons, A.; Rose, L.J.; Litvintseva, A.P. Survival, Persistence, and Isolation of the Emerging Multidrug-Resistant Pathogenic Yeast Candida auris on a Plastic Health Care Surface. *J. Clin. Microbiol.* **2017**, *55*, 2996–3005. [CrossRef] [PubMed] [PubMed Central]
3. European Centre for Disease Control and Prevention. Candida Auris Outbreak in Healthcare Facilities in Northern Italy, 2019–2021. Available online: https://www.ecdc.europa.eu/sites/default/files/documents/RRA-candida-auris-Feb2022.pdf (accessed on 30 May 2024).
4. Sticchi, C.; Raso, R.; Ferrara, L.; Vecchi, E.; Ferrero, L.; Filippi, D.; Finotto, G.; Frassinelli, E.; Silvestre, C.; Zozzoli, S. Increasing Number of Cases Due to Candida auris in North Italy, July 2019–December 2022. *J. Clin. Med.* **2023**, *12*, 1912. [CrossRef] [PubMed] [PubMed Central]
5. Suphavilai, C.; Ko, K.K.K.; Lim, K.M.; Tan, M.G.; Boonsimma, P.; Chu, J.J.K.; Goh, S.S.; Rajandran, P.; Lee, L.C.; Tan, K.Y.; et al. Detection and characterisation of a sixth Candida auris clade in Singapore: A genomic and phenotypic study. *Lancet Microbe* **2024**, *5*, 100878. [CrossRef] [PubMed]
6. Schoch, C.L.; Seifert, K.A.; Huhndorf, S.; Robert, V.; Spouge, J.L.; Levesque, C.A.; Chen, W.; Consortium, F.B. Nuclear ribosomal internal transcribed spacer (ITS) region as a universal DNA barcode marker for Fungi. *Proc. Natl. Acad. Sci. USA* **2012**, *109*, 6241–6246. [CrossRef] [PubMed] [PubMed Central]
7. Černáková, L.; Roudbary, M.; Brás, S.; Tafaj, S.; Rodrigues, C.F. Candida auris: A Quick Review on Identification, Current Treatments, and Challenges. *Int. J. Mol. Sci.* **2021**, *22*, 4470. [CrossRef] [PubMed] [PubMed Central]
8. Li, H.; Durbin, R. Fast and accurate long-read alignment with Burrows-Wheeler transform. *Bioinformatics* **2010**, *26*, 589–595. [CrossRef] [PubMed] [PubMed Central]
9. Danecek, P.; Bonfield, J.K.; Liddle, J.; Marshall, J.; Ohan, V.; Pollard, M.O.; Whitwham, A.; Keane, T.; McCarthy, S.A.; Davies, R.M.; et al. Twelve years of SAMtools and BCFtools. *Gigascience* **2021**, *10*, giab008. [CrossRef] [PubMed] [PubMed Central]
10. Treangen, T.J.; Ondov, B.D.; Koren, S.; Phillippy, A.M. The Harvest suite for rapid core-genome alignment and visualization of thousands of intraspecific microbial genomes. *Genome Biol.* **2014**, *15*, 524. [CrossRef] [PubMed] [PubMed Central]
11. Stamatakis, A. RAxML version 8: A tool for phylogenetic analysis and post-analysis of large phylogenies. *Bioinformatics* **2014**, *30*, 1312–1313. [CrossRef] [PubMed] [PubMed Central]
12. Letunic, I.; Bork, P. Interactive Tree of Life (iTOL) v6: Recent updates to the phylogenetic tree display and annotation tool. *Nucleic Acids Res.* **2024**, *52*, W78–W82. [CrossRef] [PubMed]
13. Centers for Disease Control and Prevention. *C. auris* Screening: Patient Swab Collection. Available online: https://www.cdc.gov/candida-auris/hcp/screening-hcp/c-auris-screening-patient-swab-collection-1.html (accessed on 30 May 2024).
14. Ben Abid, F.; Salah, H.; Sundararaju, S.; Dalil, L.; Abdelwahab, A.H.; Salameh, S.; Ibrahim, E.B.; Almaslmani, M.A.; Tang, P.; Perez-Lopez, A.; et al. Molecular characterization of Candida auris outbreak isolates in Qatar from patients with COVID-19 reveals the emergence of isolates resistant to three classes of antifungal drugs. *Clin. Microbiol. Infect.* **2023**, *29*, 1083.e1–1083.e7. [CrossRef] [PubMed]
15. Lockhart, S.R.; Etienne, K.A.; Vallabhaneni, S.; Farooqi, J.; Chowdhary, A.; Govender, N.P.; Colombo, A.L.; Calvo, B.; Cuomo, C.A.; Desjardins, C.A.; et al. Simultaneous Emergence of Multidrug-Resistant Candida auris on 3 Continents Confirmed by Whole-Genome Sequencing and Epidemiological Analyses. *Clin. Infect. Dis.* **2017**, *64*, 134–140, Erratum in *Clin. Infect. Dis.* **2018**, *67*, 987. [CrossRef] [PubMed] [PubMed Central]
16. Rimoldi, S.G.; Nodari, R.; Rizzo, A.; Tamoni, A.; Longobardi, C.; Pagani, C.; Grosso, S.; Salari, F.; Galimberti, L.; Olivieri, P.; et al. First imported case of Candida auris infection in Milan, Italy: Genomic characterisation. *Infection* **2024**, *52*, 1633–1638. [CrossRef] [PubMed]

17. Chen, X.F.; Zhang, H.; Liu, L.L.; Guo, L.N.; Liu, W.J.; Liu, Y.L.; Li, D.-D.; Zhao, Y.; Zhu, R.-Y.; Li, Y.; et al. Genome-wide analysis of in vivo-evolved Candida auris reveals multidrug-resistance mechanisms. *Mycopathologia* **2024**, *189*, 35. [CrossRef] [PubMed]
18. Caggiano, G.; Fioriti, S.; Morroni, G.; Apollonio, F.; Triggiano, F.; D'Achille, G.; Stefanizzi, P.; Dalfino, L.; Ronga, L.; Mosca, A.; et al. Genotypic and phenotypic characteristics of Candida parapsilosis bloodstream isolates: Health Care Associated Infections in a teaching Hospital in Italy. *J. Infect. Public Health* **2024**, *17*, 967–974. [CrossRef] [PubMed]
19. Rybak, J.M.; Muñoz, J.F.; Barker, K.S.; Parker, J.E.; Esquivel, B.D.; Berkow, E.L.; Lockhart, S.R.; Gade, L.; Palmer, G.E.; White, T.C.; et al. Mutations in TAC1B: A Novel Genetic Determinant of Clinical Fluconazole Resistance in Candida auris. *mBio* **2020**, *11*, e00365-20. [CrossRef] [PubMed] [PubMed Central]
20. Li, J.; Coste, A.T.; Liechti, M.; Bachmann, D.; Sanglard, D.; Lamoth, F. Novel ERG11 and TAC1b mutations associated with azole resistance in Candida auris. *Antimicrob. Agents Chemother.* **2023**, *65*, e02663-20. [CrossRef] [PubMed] [PubMed Central]
21. Yadav, A.; Singh, A.; Wang, Y.; Haren, M.H.V.; Singh, A.; de Groot, T.; Meis, J.F.; Xu, J.; Chowdhary, A. Colonisation and Transmission Dynamics of Candida auris among Chronic Respiratory Diseases Patients Hospitalised in a Chest Hospital, Delhi, India: A Comparative Analysis of Whole Genome Sequencing and Microsatellite Typing. *J. Fungi* **2021**, *7*, 81. [CrossRef] [PubMed] [PubMed Central]

MDPI AG
Grosspeteranlage 5
4052 Basel
Switzerland
Tel.: +41 61 683 77 34

Microorganisms Editorial Office
E-mail: microorganisms@mdpi.com
www.mdpi.com/journal/microorganisms

Academic Open
Access Publishing

mdpi.com

ISBN 978-3-7258-5974-0